DESIGN AND ANALYSIS OF DYNAMIC ANTENNA ARRAYS
FOR RADAR AND REMOTE SENSING APPLICATIONS

By

Daniel S. Chen

A DISSERTATION

Submitted to
Michigan State University
in partial fulfillment of the requirements
for the degree of

Electrical and Computer Engineering—Doctor of Philosophy

2024

ABSTRACT

The need for fast and reliable sensing at millimeter-wave frequencies has been increasing dramatically in recent years for a wide range of applications including non-destructive evaluation, medical imaging, and security screening such as concealed contraband detection. Imaging based approaches have been of particular interest since the wavelengths at millimeter-wave frequencies provide good resolution and are capable of propagating through clothing with negligible attenuation allowing the identification of concealed contraband. While various implementations for millimeter-wave imaging have been developed, the new technique of active incoherent millimeter-wave (AIM) imaging, developed in our research group, is of particular interest because it solves fundamental limitations inherent in other approaches. Furthermore, AIM enables imaging with significantly fewer elements than phased arrays and costs less than passive imagers. This is enabled by actively transmitting noise signals, allowing the system to capture scene information in the spatial Fourier domain. When the received signal at each of the array elements are spatio-temporally incoherent, the spatial coherence function of the captured signals represent samples of the measured visibility which can be further processed via an inverse Fourier transformation to recover the measured scene. With a good quality recovered image, additional processing can be applied for detection and/or classification on specific spatial features. However, images often contain more than the required information necessary for effective classification results which means that unnecessary resources are used for the collection and processing of redundant information.

In this dissertation, I present on the design and analysis of array dynamics for radar and remote sensing applications. Specifically, I investigate approaches to measure specific spatial Fourier information which can be useful for direct classification therefore eliminating the need of full image recovery. I present an adapted formulation of the spatial coherence function by considering individual antenna trajectories within a dynamic antenna array. The measured visibility, hence, becomes a function of array trajectory over a slow time dimension. The use of array dynamics further reduces the hardware requirements in the AIM technique by introducing a new degree of freedom in the array design. By allowing the receiving elements of the antenna array to dynamically

move across the measurement plane, the spatial Fourier domain can be efficiently sampled using as few as two receiving antennas. Discussion of the effects of trajectory approaches on the measured spatial Fourier information are presented. Furthermore, I expand on a specific array trajectory where as few as two antennas can generate a ring filter (i.e., spatial Fourier sampling function exhibiting a form of a ring) that can efficiently identify spatial Fourier artifacts pertaining to sharp edges in the scene. This approach enables an imageless approach to differentiate scenes containing objects with sharp-edge that are generally made artificially. I then present a real-time rotational dynamic antenna array operating at $75\,$GHz with two noise-transmitting sources as required by the AIM technique and two receivers to generate the ring filter. Compared to traditional millimeter-wave imaging, this non-imaging approach further reduces the required number of antennas. Experimental measurements using the AIM based rotational dynamic antenna array demonstrate the possibility of detecting concealed contraband via the direct measured spatial Fourier domain information.

業精於勤，荒於嬉；

行成於思，毀於隨。

《進學解》

ACKNOWLEDGEMENTS

TABLE OF CONTENTS

CHAPTER 1

INTRODUCTION

1.1 Radar and Remote Sensing

The concept of remote sensing describes the process where systems with integrated sensors, without making physical contact, can detect and/or monitor physical attributes within its coverage by acquiring the reflected and/or the emitted radiation at a distant location [1]. Implementations of remote sensing systems are derived from application specific requirements. For underwater detection and mapping, remote sensing systems are designed to respond to acoustic waves (i.e., longitudinal waves) [2]. In addition to the use of acoustic waves, sensing can also be achieved via measuring electromagnetic waves such as using radar systems that typically operate in the microwave (3 GHz–30 GHz) and millimeter-wave region (30 GHz–300 GHz) [1]. Furthermore, electromagnetic based remote sensing systems can also operate at much higher frequencies such as in the infrared region (300 GHz–400 THz) [3] and optical region (300 GHz–3000 THz) [4] for specific application scenarios. Leveraging electromagnetic waves for remote sensing has gained traction since the 17th century after Christiaan Huygens' studies in optics where light exhibits the properties of waves [5]. Approximately two centuries later, James Clerk Maxwell formulated the theory of electromagnetism that corresponded to the characteristics between light and electromagnetic waves [6]. Later that century, experimental demonstration of Maxwell's prediction was presented by Heinrich Hertz where the electromagnetic propagation speed is equivalent to that of light [7]. Inevitably, radar systems operating and microwave and millimeter-wave frequencies came out during World War II and have since been used for both military and commercial purposes.

Radar, originated as an acronym for radio detection and ranging [8], generally refers to a system that leverages radio waves (i.e., electromagnetic waves) to determine the relative range, direction and velocity of objects that are within its coverage. Given the characteristic that radar systems do not make physical contact with the objects that are distant to their position, it is also considered to be within the framework of remote sensing. In modern times, radar systems can be found in various applications such as non-destructively evaluating the fruit quality [9], detection

for breast cancer [10, 11], remote sensing of the Earth [12, 13, 14], and detection of concealed contraband [15, 16, 17]. In particular, radar systems operating in the microwave and millimeter-wave frequencies are especially desirable as wavelength within this spectrum is sufficiently small which can provide good resolution while also being sufficiently large which exhibits good propagation characteristics. For example, materials such as fog, smoke, clothing, among others can manifest high propagation attenuation at higher frequencies such as infrared and optical region, which in contrast, are low, if not minimal at microwave and millimeter-wave frequencies [18, 1]. Besides, recent advancements in hardware design and fabrication techniques represent opportunities for microwave and/or millimeter-wave radar systems to be implemented in a cost-effective manner as components are becoming significantly more efficient and affordable [19, 20]. Therefore, it is natural that the exploration using radar systems for remote sensing applications have gained significant interest both in the research and commercial communities.

A typical radar system is complex by nature and generally involves a diverse pool of expertise to identify use cases, overcome challenges and constraints, and solidify requirements which brings the system from concept to realization. The design considerations for a radar system's architecture can be generalized into the following two categories:

1. Hardware and physics, which include antennas, transmitters, receivers, propagation, target scattering, mechanical structure, and power distribution, etc.

2. Software and algorithms, which represent the developments that range from the coordination of various subsystems and signal processing where the latter can be further dissected into waveform designs, data acquisition, signal conditioning, detection, classification, and imaging, etc.

Each of the aforementioned design considerations are not necessarily independent from each other representing various complicated design trade-offs during development. Therefore, advancements in one particular area of radar development are extremely valuable as the improvement in one area could lead to significantly fewer, if not eliminate the constraints of others.

2

1.1.1 Radar Applications

Since the deployment in World War II, radar systems have been used in various applications and have become an integrated part of many aspects of society. Primarily stimulated by military use cases, radar was employed for surveillance, navigation, and weapon control in the early days [21]. One such application is the moving target indication (MTI) radars that transmit pulsed waveform, and that the return signals are processed to identify Doppler frequency shift which exploit the fact that shift in frequency are produced by moving targets and stationary clutters will appear to have exceedingly small spectral content near zero frequency [22, 23]. Similarly, tracking radars can provide the range, angle, and Doppler frequency shift of targets within coverage [24, 25]. Weather radar is another specific application that takes advantage of Doppler frequency shift to determine the motion and intensity of atmospheric objects enabling the classification of precipitation type varying from hail, snow, or rain [26, 27].

Besides detection and classification, synthetic aperture radar (SAR) systems are used to image the environment such as landscapes [28, 29]. The concept of SAR systems leverages motion of the radar antenna, mounted on moving platforms such as aircraft or spacecraft, which moves across a region of interest to provide finer spatial resolution over conventional stationary scanning radar. Directed outwardly from the Earth, radio astronomers utilize radar imaging systems to recover images of celestial objects such as the Very Large Array (VLA) in Socorro, New Mexico [30, 31, 32]. The VLA is an example of a sparse antenna array in contrast to a fully populated filled array, which benefits from using significantly fewer receiving antennas and the subsequent radio frequency components while achieving the same resolution.

In modern days, radar systems have also thrived on civilian applications. Notably, enabling the possibility of autonomous driving and life-saving vehicular functionalities where cars utilize multiple compact automotive radars to detect and identify on-road objects, hence mitigate collisions [33, 34, 35]. Given the recent advancements in electronics design and fabrication, radar systems have also be deployed for many indoor use cases ranging from evaluating fruit quality in a non-destructive manner that can help improving efficiency of logistical facilities [9]; reconstructing

medical imageries to assist early detection of breast cancer [10, 11]; monitoring of human activities where micro-Doppler signatures are used track the location of a person and/or determine a person's activity based on the classification of Doppler associated gait patterns [36, 37, 38]; and the detection of concealed contraband beneath clothing by either recovering imageries for human recognition or classification based on the range-Doppler mapping [15, 16, 17].

1.1.2 Radar System Architectures

As observed above, radar systems are complex and exist for a remarkably diverse range of applications. While the realization of radar system architectures can differ drastically, the general building blocks are similar and are illustrated in Figure 1.1. The five important pillars of a typical radar system architecture are: signal processing, modulation and demodulation of the signals, transmission and reception of electromagnetic waves carrying the information, accurate modeling of the propagating environment, and prediction of the scatter responses from a group of expected targets or sources external to the radar systems that produce radiation sensitive to the radar. Each of them is highly dependent on the others which can increase the complexity of design trade-offs and system requirements.

The signal processing component involves the generation of information, or waveforms that are suitable for the specific radar functionality such as using pulsed waveforms to exploit the Doppler frequency shift of potentially moving targets. Other types of waveforms that are commonly used are continuous waveform, linear frequency modulated waveform (i.e., chirp or de-chirp) and even noise waveform. Furthermore, acquiring the received signal requires sampling rate that is efficient based on the defined signal types where too low of a rate means the possibility of losing useful information (i.e., under-sampled) and too high of a rate represents unnecessary resources being allocated for capturing signals (i.e., over-sampled). Upon successful data sampling, the received information can be further processed enabling:

1. Detection, such as evaluation for Doppler frequency shift or change in signal amplitude when compared to preceding measurements;

2. Classification, where the processed information is compared against classes of known signatures to determine the likelihood of specific event monitored by the radar systems; or

3. Imaging, where aggregated information from the measured scene is used to spatially recover imagery of the scene.

It is important to note that detection, classification, imaging, and other functionalities of a radar system are not necessarily unrelated to each other. For example, detection based on tracking over a radar's coverage could lead to a more comprehensive imaging of the radar's field of view. For another example, classification algorithms can be applied to either the measured signals, processed signals, or the reconstructed images [39, 40].

Given that it is economically efficient to generate information at baseband (i.e., generally under 2 GHz), modulation and demodulation becomes inevitable part of radar system architectures as it enables information generated at lower frequency to be up-converted to, and down-converted from the desirable frequency spectrum such as in the case of automotive radars that typically operate around 77 GHz[41]. Once the signals are at the desirable frequency on transmission, it is common that they are fed through a cascade of components that condition the signal to ensure that they only appear in the correct frequency region and that their power does not exceed ratings of neighboring components to ensure dependable and reliable operation. Lastly, the modulated and conditioned signals are radiated through either a single antenna or an array of antennas. Similarly, on reception, the receiver captures electromagnetic radiation arriving at its aperture and the measured signals are conditioned and subsequently demodulated before sampled and further processed.
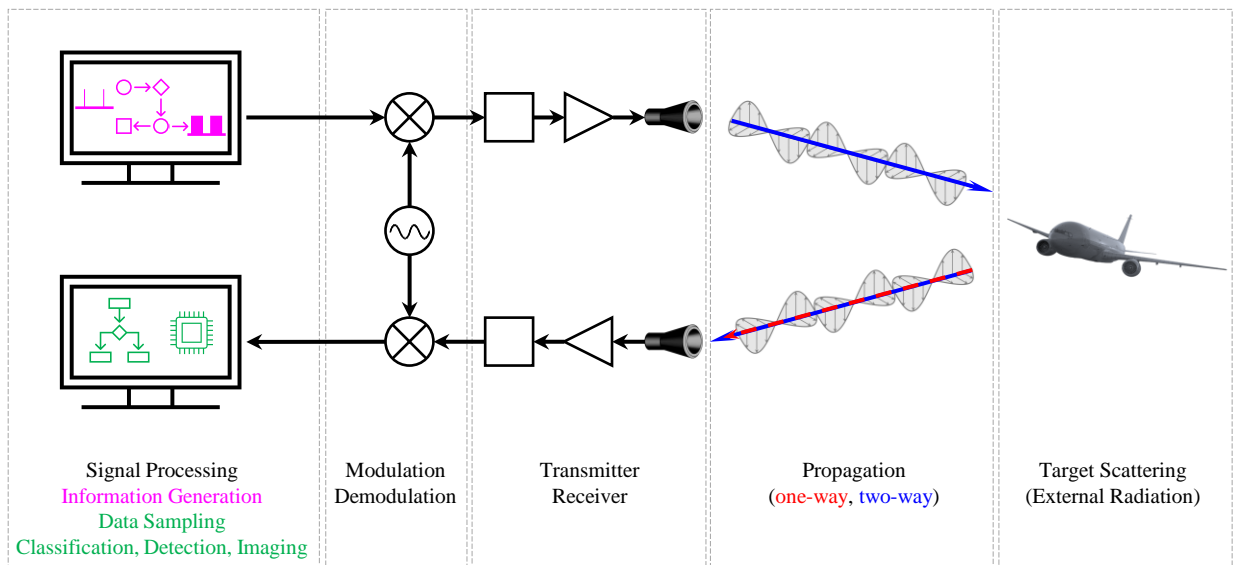
Figure 1.1 General architecture of a radar system. Information such as waveforms are generated before being modulated, conditioned, and transmitted out of an antenna (or array of antennas). Propagation of the transmitted waves (or waves generated from other unknown sources) are reflected from target(s) within the radar's coverage. The receiving antenna (or array of antennas) captures the reflected waves. The captured signals are then conditioned, demodulated before being acquired by computational device(s) that performs subsequent detection, classification, and/or image reconstruction.

The last two pillars of radar system architecture as shown in Figure 1.1 represents factors that are external to the physical realization. However, they drive the majority of early design decisions. For example, a practical propagation environment requires the consideration of many factors that can potentially degrade the performance of radar systems such as multipath, attenuation due to propagation, unwanted interfering signals and/or refraction. Lastly, understanding the types of possible scattering targets can help define the requirements for proper signal transmission and reception throughout the radar systems. On the other hand, some radar systems do not have transmission capability but can still process radiation arriving at its receiving aperture due to external sources.

The first three pillars of radar system architecture as shown in Figure 1.1 usually represent the physical realization of the system implementation. Depending on the configuration, the architecture of radar systems can be grouped in ways such as mono-static versus bi-static, active versus passive, and scanning versus staring. Mono-static radar systems compose a single set of transmitter, receiver, and antenna. In contrast, bi-static radar systems compose multiple mono-static radars operating at the same frequency that can also be physically separated at larger distances depending on the use cases. Active radar systems can both transmit and receive while passive radar systems only receive. Scanning radars have system beams (i.e., due to antenna or array configuration) that are adjustable to achieve certain spatial coverage while staring radars are designed to operate at specific spatial direction.

1.1.3 Scanning Radar Systems

Scanning radar systems are common for detection, tracking and imaging use cases with examples shown in Figure 1.2. The scanning can be accomplished either by electrical and/or mechanical implementation where the antenna/array responses are redirected within the radar systems' coverage (i.e., field of view). Depending on the implementation, scanning radar systems might support only a confined spatial coverage due to component limitation which can also dictate the scanning effectiveness (i.e., undesirable reset motion between subsequent scanning).

Electronically-based scanning radar systems (top left of Figure 1.2) leverage multiple radiating

elements each with independent phase shifting capability to form an array where the beam can be steered to a specific spatial direction based on the control of phases. A common implementation of electronically scanning radar is the use of a phased array that utilizes phase shifters located behind each antenna element to alter the overall array response [42, 43]. In general, the scanning rate of an electronically-based scanning radar is much higher than its mechanical counterpart as a result of no physical moving components and that the control of phases can be accomplished digitally. However, the cost of such electronically scanning radar can increase significantly when the number of antennas within the array is large because each radiating element represent additional cascaded active and/or passive components such as amplifiers, phase shifters, filters, among others which can themselves becoming challenging engineering tasks to design and fabricate at higher frequencies.

Mechanically based scanning radar systems (bottom left of Figure 1.2) utilize motors to raster scan the system beam (of the antenna/array) by either rotating the aperture or by rotating reflective surfaces that help direct the beam from a static aperture to the desired spatial direction [21]. The reflecting surfaces can take the form of different geometry such as using a mirror to direct the beam of high-gain aperture, or a parabolic reflector to focus the beam of low-gain aperture. Furthermore, either the aperture or the entire front end of the radar systems can be mechanically moved to facilitate scanning. Generally, only a single antenna and receiver is required for mechanically scanning radar making it a cost-effective implementation over other radar architectures. However, vibrations due to mechanical movements can contribute to the noise problem from transient signals which can be problematic for radar systems operating at higher frequencies. In addition, mechanical scanning is rather slow when compared to the aforementioned electrical scanning method making it prohibitive for certain applications such as real-time imaging of moving targets.
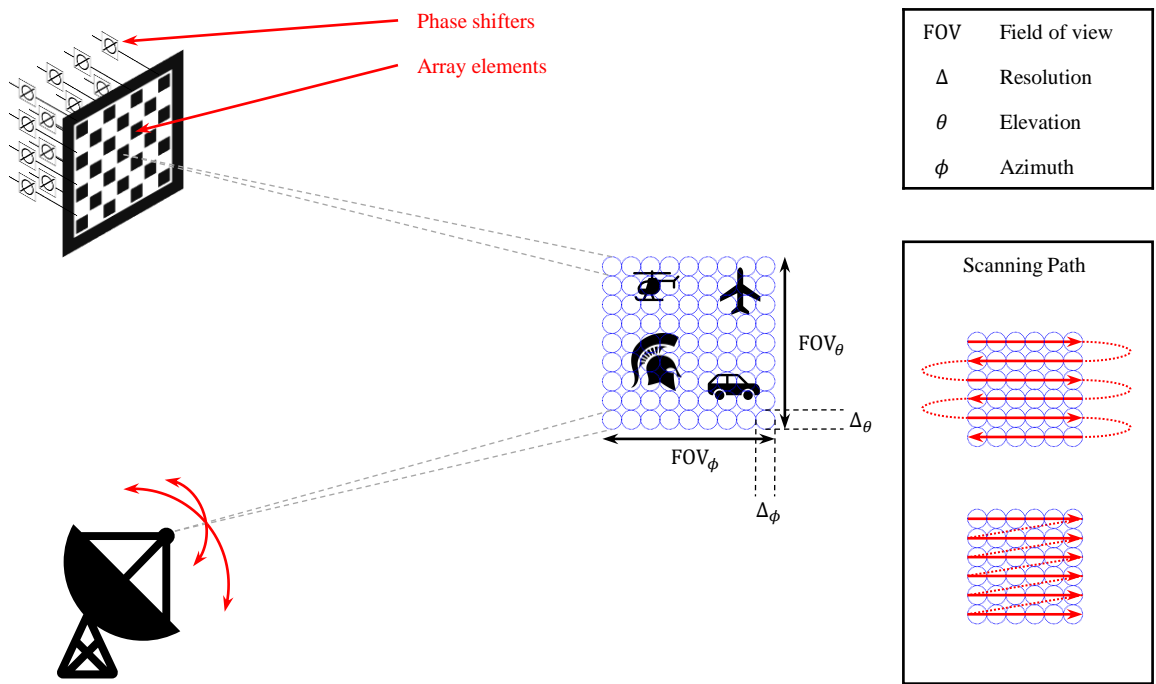
Figure 1.2 Examples of scanning systems where the beam can be steered towards a specific direction that is within the total system coverage (i.e., field of view). Scanning can be achieved electronically such as using a phased array (top left), mechanically such as mounting the antenna on an adjustable platform (bottom left), or compositely using a hybrid approach.

1.1.4 Staring Radar Systems

Unlike scanning radar systems that seek to cover a spatial region overtime, staring radar systems are optimized for specific spatial direction which drives the importance of array configuration. An example of a staring radar system is an interferometric imaging system which is shown in Figure 1.3. One appreciable design consideration of such imaging radar systems is the concept of using a sparse array where the resolution can be achieved using significantly fewer antenna elements when compared to a fully populated phased array with equivalent dimensions. As illustrated in Figure 1.3, the resolution of an interferometric imaging radar is determined by the largest antenna spacing (in both spatial dimensions) within the array and the field of view of an interferometric imaging radar is determined by the smallest antenna spacing (in both spatial dimensions) within the array. The result of using significantly fewer receiving antennas represents a radar system that is more cost-effective, lighter in weight, and consumes less energy to operate.

Interferometric imaging radar systems were developed for radio astronomical observations around the mid-twentieth century with the objective to map the radio frequency emission coming from celestial objects [44, 45, 32]. It was discovered by radio astronomers that the result of cross-correlating the outputs of two antennas is a representation of the radiating scene and that by using an array configuration that produces the most diverse cross-correlating pair will improve the reconstruction of the measured scene. Given the nature of radio astronomy, the associated interferometric systems are considered passive which means that there is no active transmission of signals towards the scene. Recently, the interferometric imaging technique was made possible with active incoherent illumination where active transmission of noise signals are used to illuminate the scene of interest [46, 47, 48]. Furthermore, the particular interferometric radar imaging system was implemented at millimeter-wave frequency making it compact and suitable for indoor use cases. This technique not only improves the receive signal power at the interferometric array but also enables a computationally cost-effective imaging radar that can be used for applications such as conceal contraband detection.

FOV	Field of view
Δ	Resolution
θ	Elevation
ϕ	Azimuth
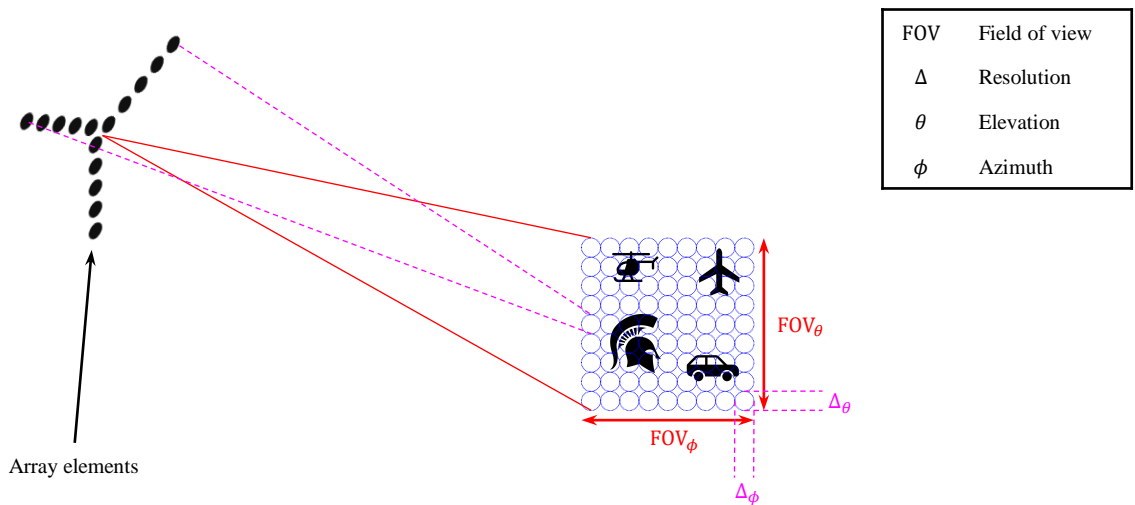
Figure 1.3 Example of a 15-element interferometric imaging system (staring system). The field of view of the imaging system is determined by the smallest element spacing within the array. The resolution of the imaging system is determined by the largest element separation within the array.

1.2 Fourier-Domain Imaging Using Incoherent Signals

1.2.1 Fundamentals on Interferometric Imaging

Interferometric imaging system measures information in the spatial Fourier domain, or spatial frequency domain to recover spatial information of the measured scene which can be represented as two-dimensional images. As shown in the top of Figure 1.4, a two-dimensional image can be also considered as the superposition of an infinite series of spatial varying sinusoidal signals that are related to different spatial frequencies and orientations (i.e., spatial Fourier domain information) [49]. Spatial Fourier domain information is captured by the unique correlation pair within the antenna array of interferometric imagers, which can be treated as the electromagnetic information that corresponds to a specific set of spatial frequencies. By carefully designing the placements of individual antennas of the interferometric array, the unique combination of spacing and orientation (i.e., baseline) of all possible pairs map to a specific spatial frequency when the received signals of the particular antenna pair are correlated upon capturing.

The most basic element of any interferometric imaging array is the correlation pair of two antennas. Considering a two-element correlation pair observing a distant radiating point source as shown in the bottom right of Figure 1.4, the measured signals in terms of voltage response at each of the antennas can be represented as follows [50, 46, 1]:

$$V_1(t) = \cos(2\pi f t) + n_1(t)$$
$$V_2(t) = \cos[2\pi f (t - \tau_g)] + n_2(t)$$

$$(1.1)$$

where the subscripts 1 and 2 indicate the two antennas, f is the operating frequency of the correlation pair, $\tau_g = \frac{D}{c} \cdot \sin\theta$ is the geometric time delay representing the time difference of wavefront reaching the two antennas that are separated by the baseline D considering a wavefront propagation speed of c, and the terms $n_1(t)$ and $n_2(t)$ each describes the additive noise as part of the measured signal of the corresponding antenna. Based on (1.1), the response, or correlation output of the two-element

12

interferometric array is

$$r(\theta) = \langle V_1(t)V_2(t) \rangle$$

$$r(\theta) = \langle \cos(2\pi f t) \cos[2\pi f(t - \tau_g)] \rangle + \langle \cos(2\pi f t) n_2(t) \rangle \tag{1.2}$$

$$+ \langle \cos[2\pi f(t - \tau_g)] n_1(t) \rangle + \langle n_1(t) n_2(t) \rangle$$

where the angle brackets $\langle \cdot \rangle$ represent time averaging. Because the signal from the considered point source is statistically independent from each of the measured noise and the two measured noises in each antenna are also uncorrelated, the time averaging operation applied to the last three terms of (1.2) will become zero, hence reduces (1.2) to

$$r(\theta) = \langle \cos(2\pi f t) \cos[2\pi f(t - \tau_g)] \rangle$$

$$r(\theta) = \langle \frac{1}{2} \cos[2\pi f(2t - \tau_g)] + \frac{1}{2} \cos(2\pi f \tau_g) \rangle \tag{1.3}$$

where the details of derivation on (1.3) are included in Appendix B. Lastly, the higher frequency component term (i.e., $\cos[2\pi f(2t - \tau_g)]$) can be dropped due to integration of low pass filtering at the correlator output, hence,

$$r(\theta) = \frac{1}{2} \cos(2\pi f \tau_g) \tag{1.4}$$

Recall that $\tau_g = \frac{D}{c} \cdot \sin \theta$,

$$r(\theta) = \frac{1}{2} \cos(2\pi f \frac{D}{c} \cdot \sin \theta)$$

$$r(\theta) = \frac{1}{2} \cos(2\pi \frac{D}{\lambda} \cdot \sin \theta) \tag{1.5}$$

$$r(\theta) = \frac{1}{2} \cos(2\pi D_\lambda \cdot \sin \theta)$$

where $\lambda = \frac{f}{c}$ is the wavelength and D_λ is the baseline in the unit of wavelength. It can be seen from the result of (1.5) that the correlation interferometer output is associated with an oscillatory response relative to $\sin \theta$. This is also the spatial pattern comprising grating lobes mapping to a specific spatial frequency which are dependent on the electrical baseline (i.e., D_λ) of a given correlation pair. Furthermore, this spatial pattern is multiplicative to the antenna beam pattern yielding the system beam pattern as illustrated in the bottom left of Figure 1.4.

13
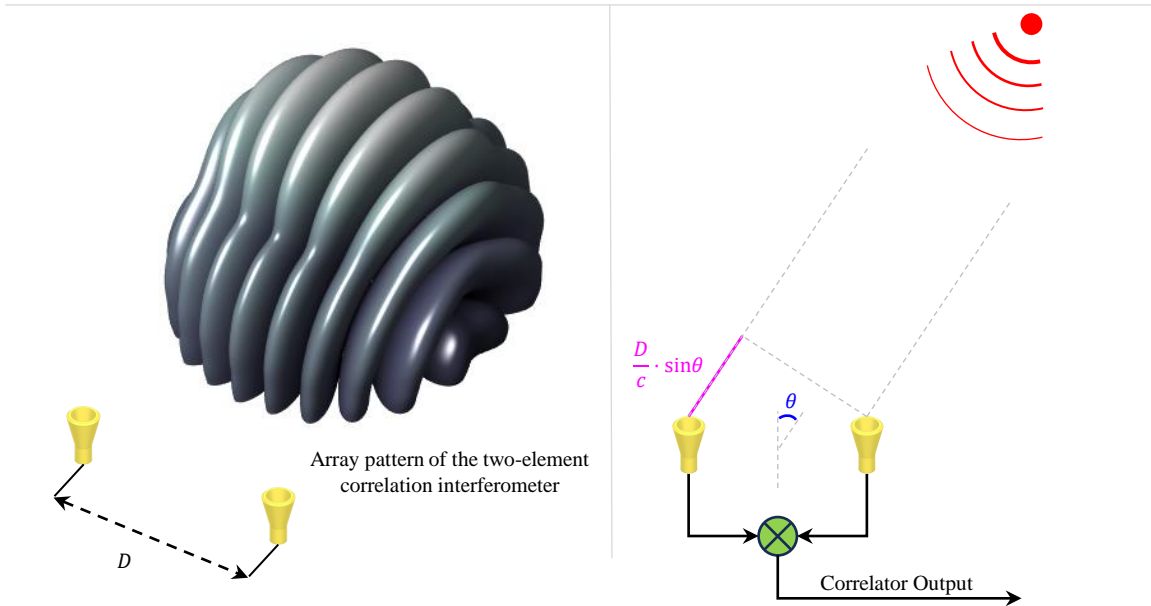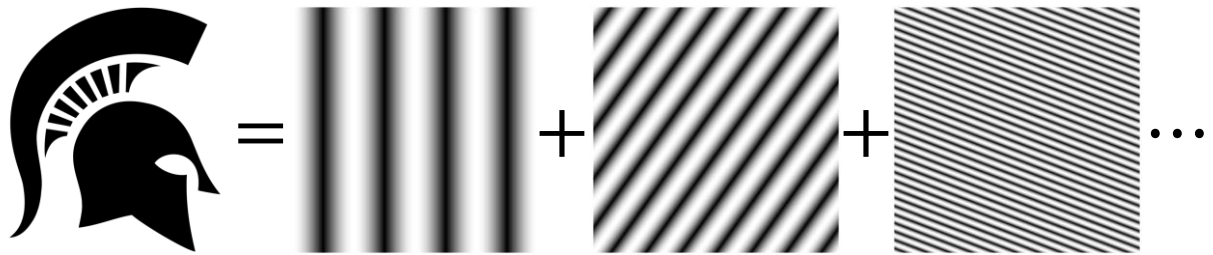
Figure 1.4 Top: A two-dimensional image can be considered as the superposition of an infinite series of spatially varying sinusoidal signals that are related to different spatial frequencies and orientations [49]. Bottom left: Illustration of the two-element correlation pair's array pattern that is due to the multiplicative relationship of antenna pattern and array factor. Bottom right: Example of a two-element correlation pair observing a distant radiating point source [1].

1.2.2 The Van Cittert-Zernike Theorem: Signals Incoherence

One important prerequisite for the interferometric imaging radar to successfully recover spatial scene information forming images is the van Cittert-Zernike theorem which requires that the signals emanating from the measured scene shall be spatially and temporally incoherent [51, 52]. For radio astronomy application, radiation emanating from celestial objects generally satisfies the incoherence requirement except the occurrences of pulsars and masers [53, 32]. Radiation that is thermally induced can also be considered as incoherent for the purpose of recovering images of measured scenes. However, challenges arise for designing interferometric radar with the intention of imaging humans for application such as security screening. This is because thermally induced radiations from humans have exceedingly low power at microwave and millimeter-wave frequencies mandating a high sensitivity requirement for passive interferometric systems. In which, represent systems that can require exceedingly high gain amplification circuitry while also minimizing noise figure, supporting wide bandwidth, and/or long integration time which are not necessarily cost-effective nor feasible. Addressing these challenges, the active incoherent millimeter-wave (AIM) technique introduced recently leverages properly placed independent noise transmitters to illuminate the measured scene enabling Fourier domain sampling with commercially available components [48, 54, 55]. A photo of the latest iteration on the AIM radar imager is included in Appendix A.

To understand the importance of the van Cittert-Zernike theorem, let's first consider two antennas observing signals emanating from a distant distributed source as shown in Figure 1.5. The mutual spatial coherence function, as defined in optics for an electric field $E(t)$ measured by the two antennas is given by [56]

$$\Gamma_{12}(u, v, w, \tau) = \lim_{T \to \infty} \frac{1}{2T} \int_{-T}^{T} E_1(t) E_2^*(t - \tau) \, dt \tag{1.6}$$

where $u = \frac{x_2 - x_1}{\lambda}$, $v = \frac{y_2 - y_1}{\lambda}$ and, $w = \frac{z_2 - z_1}{\lambda}$ are the three-dimensional spacing between the two measurement points expressed in wavelength, and λ is the considered wavelength. Following a similar approach as in [32], when the distance between the radiating distributed source and the

15

antennas are significant than the separation of the antennas ($R \gg D$ shown in Figure 1.5), it is convenient to specify a single radiating element in the XYZ-space using direction cosines (l, m, n) which are with respect to the x, y, and z axes of the antenna space. Note that both $\vec{R}_1$ and $\vec{R}_2$ point toward the (l, m, n) direction of any point within the distributed source and will be the same when measured at the two antennas given they are at large distance from the distributed source.

It can be assumed that the amplitude of the electric fields arriving at both antennas to be approximately the same when the distributed source is at a larger distance away while being close to the broadside of the antenna pair. In contrast, the phases of the two considered electric fields will undergo different phase shifts due to the actual difference in the absolute distance traveled from the source to each antenna. Furthermore, let's assume the electric fields are propagating in vacuum. With these considerations, the electric fields arriving at Antenna 1 and Antenna 2 that originated from a single element of the distributed source (l, m, n) can be written as

$$
\begin{aligned}
E_1(l, m, n, t) &= \mathcal{E}\left(l, m, n, t - \frac{R_1}{c}\right) \frac{e^{-j\omega(t - R_1/c)}}{R_1} \\
E_2(l, m, n, t) &= \mathcal{E}\left(l, m, n, t - \frac{R_2}{c}\right) \frac{e^{-j\omega(t - R_2/c)}}{R_2}
\end{aligned}
\tag{1.7}
$$

where c is the speed of wavefront propagation, $\omega = 2\pi f$ where f is the frequency, $\mathcal{E}$ is the electric field originated from the considered element of the distributed source, R_1 and R_2 account for the propagation attenuation, and the exponential terms represent the phase changes due to the corresponding propagation paths. Considering that (1.6) is the time-averaged product between the two electric fields at the two antennas, the spatial coherence function of the fields can be computed using the complex cross-correlation between the signals in (1.7) as

$$
\left\langle E_1(l, m, n, t) E_2^*(l, m, n, t) \right\rangle
\tag{1.8}
$$

where the superscript asterisk denotes the complex conjugate and the angle brackets $\langle \cdot \rangle$ represent time averaging, or

$$
\begin{aligned}
&\left\langle E_1(l, m, n, t) E_2^*(l, m, n, t) \right\rangle \\
&= \left\langle \mathcal{E}(l, m, n, t)\, \mathcal{E}^*\left(l, m, n, t - \left(\frac{R_2 - R_1}{c}\right)\right) \right\rangle \cdot \left(\frac{e^{-j\omega(R_2 - R_1)/c}}{R_1 R_2}\right)
\end{aligned}
\tag{1.9}
$$

16

with detail derivation from (1.8) to (1.9) included in Appendix C. (1.9) represent the mutual spatial coherence function due to a single element of the distributed source at the two antennas. To account for all radiating points from the distributed source, one can consider the expression as an integration over the entire source, hence,

$$\Gamma_{21}(u, v, n, \tau)$$
$$= \int\limits_{\text{dist.source}} \left\langle \mathcal{E}(l, m, n, t)\, \mathcal{E}^*\left(l, m, n, t - \left(\frac{R_2 - R_1}{c}\right)\right) \right\rangle \cdot \left(\frac{e^{-j\omega(R_2 - R_1)/c}}{R_1 R_2}\right) \frac{R^2 dl\, dm}{n} \qquad (1.10)$$

where R denotes the distance between the origins of the two coordinate systems as illustrated in Figure 1.5 (i.e., xyz and XYZ). Considering the assumption that the fields from the source subtend a small angle, the direction cosines l and m can be approximated by small angles where the direction cosine n can be approximated by unity. Furthermore, the quantity $(R_2 - R_1)$ can also be expressed as the quantity $\lambda(ul + vm + wn)$. (1.10) then becomes

$$\Gamma_{21}(u, v, w, \tau)$$
$$= \int\limits_{\text{dist.source}} \left\langle \mathcal{E}(l, m, 1, t)\, \mathcal{E}^*\left(l, m, 1, t - \left(\frac{R_2 - R_1}{c}\right)\right) \right\rangle \cdot \left(\frac{e^{-j2\pi(ul+vm+w)}}{R_1 R_2}\right) R^2 dl\, dm \qquad (1.11)$$

Given that the electric field from the distributed source is constant with regard to variable n, the (1.11) can be further reduce by dropping w and $n = 1$,

$$\Gamma_{21}(u, v, \tau)$$
$$= \int\limits_{\text{dist.source}} \left\langle \mathcal{E}(l, m, t)\, \mathcal{E}^*\left(l, m, t - \left(\frac{R_2 - R_1}{c}\right)\right) \right\rangle \cdot \left(\frac{e^{-j2\pi(ul+vm)}}{R_1 R_2}\right) R^2 dl\, dm \qquad (1.12)$$

Recall that for (1.6), it is assumed that $R \gg D$ (as shown in Figure 1.5), hence, R_1 and R_2 can be approximate as R,

$$\Gamma_{21}(u, v, \tau)$$
$$= \int\limits_{\text{dist.source}} \left\langle \mathcal{E}(l, m, t)\, \mathcal{E}^*\left(l, m, t - \left(\frac{R_2 - R_1}{c}\right)\right) \right\rangle \cdot e^{-j2\pi(ul+vm)}\, dl\, dm \qquad (1.13)$$

Subsequently, the limits of the integral can be considered as extending to $\pm\infty$ because the integrand is effectively zero when accounting for location outside the distributed source boundary,

and the term $\frac{R_2 - R_1}{c}$ can be neglected if is less than the reciprocal receiver bandwidth, hence,

$$\Gamma_{21}(u, v, \tau) = \iint\limits_{l,m=-\infty}^{\infty} \langle \mathcal{E}(l, m, t) \mathcal{E}^*(l, m, t) \rangle \cdot e^{-j2\pi(ul+vm)} \, dl\,dm \tag{1.14}$$

Assume that the distributed source satisfies the incoherence property, then the time-averaged quantity due to different elements of the source, are zero. Therefore, the two quantities within the angle bracket in (1.14) is equivalent to that of the time-averaged intensity of the considered distributed source, or $\langle \mathcal{E}(l, m, t) \mathcal{E}^*(l, m, t) \rangle = I(l, m)$. Thus,

$$\Gamma_{21}(u, v, \tau) = \iint\limits_{l,m=-\infty}^{\infty} I(l, m) e^{-j2\pi(ul+vm)} \, dl\,dm \tag{1.15}$$

For zero time offset, $\tau = 0$, the mutual spatial coherence function $\Gamma_{21}(u, v, 0)$ is equivalent to the complex visibility $V(u, v)$ which both are the Fourier transformation of the scene intensity (i.e., property of the van Cittert-Zernike theorem),

$$V(u, v) = \Gamma_{21}(u, v, 0) = \iint\limits_{l,m=-\infty}^{\infty} I(l, m) e^{-j2\pi(ul+vm)} \, dl\,dm \tag{1.16}$$
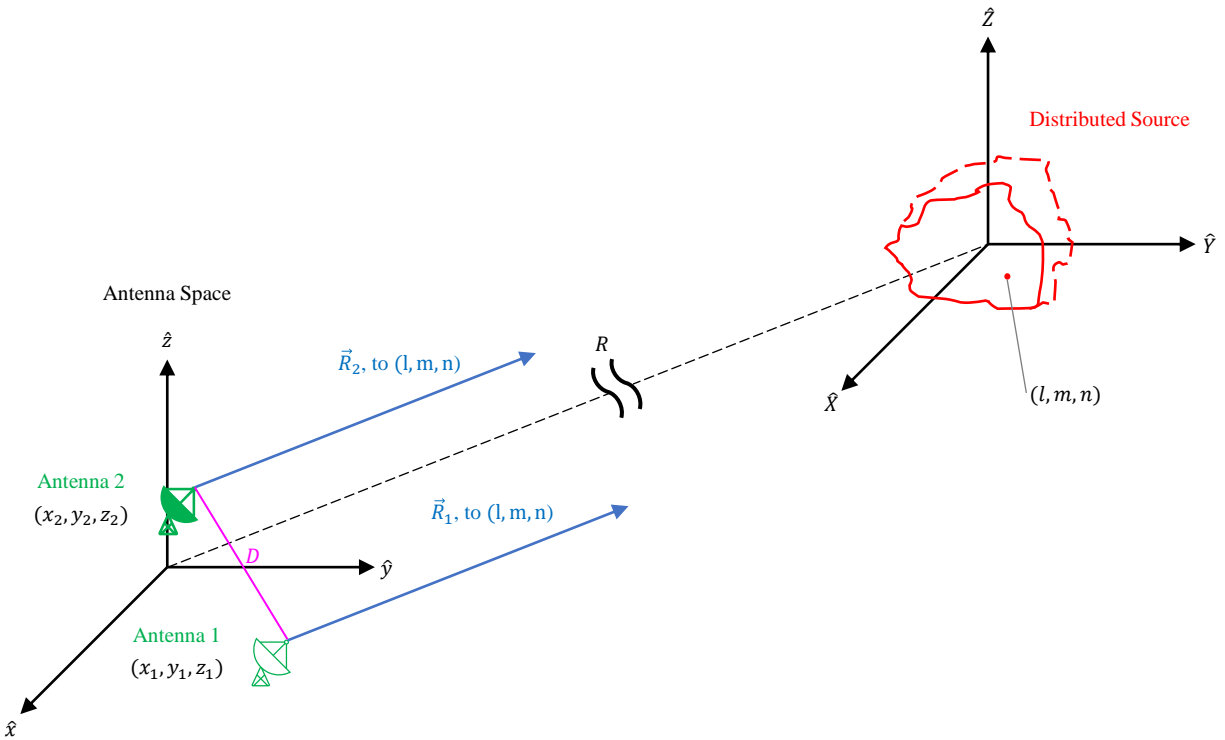
Figure 1.5 Two antennas observing signals emanating from a distant distributed source.

1.2.3 Fourier Relationships and Array Design Considerations

Based on the observation in (1.16), the Fourier relationships between the interferometric measuring domain (i.e., spatial Fourier domain) and the scene intensity's domain (i.e., spatial domain) can be summarized as shown in Figure 1.6 where the visibility $V(u,v)$ is the Fourier transformation of the scene intensity $I(l,m)$,

$$I(l,m) = \iint\limits_{l,m=-\infty}^{\infty} V(u,v)e^{j2\pi(ul+vm)}\,dl\,dm \tag{1.17}$$

In the second column of Figure 1.6, the star pattern of the sampling function is the result of an interferometric array configuration that uses 28 receiving antennas arranged in a "**Y**" layout with a maximum dimension of 36λ and an inter-element spacing of 2λ with λ being the considered wavelength. As introduced in Figure 1.3, these two array design parameters determine the spatial resolution and the usable unambiguous field of view, respectively. Furthermore, for a specific interferometric array configuration, a sampling function $S(u,v)$ can be synthesized where its inverse Fourier transform is the point spread function $PSF(l,m)$,

$$PSF(l,m) = \iint\limits_{l,m=-\infty}^{\infty} S(u,v)e^{j2\pi(ul+vm)}\,dl\,dm \tag{1.18}$$

The point spread function can be used as a metric to evaluate the performance of a specific sampling function (i.e., array configuration). An ideal sampling function measures all spatial frequency information representing an inverse Fourier transform yielding a Dirac delta function, or a point. In the point spread function example shown in Figure 1.6, it can be seen at the location $(l=0, m=0)$ that a slight spread from an ideal point is a result of the spatial frequencies that the considered sampling function can measure. Furthermore, one can also observe the spatial aliasing extending outward from $(l=0, m=0)$ which is due to the under-sampling of the spatial Fourier domain (i.e., result of the smallest inter-element spacing of the array).

In the third column of Figure 1.6, the sampled visibility can be considered as the multiplicative product in the spatial Fourier domain between the visibility and the sampling function, $V_{\text{s}}(u,v) = V(u,v)S(u,v)$ and that the inverse Fourier transform of the sampled visibility yields the

reconstructed scene intensity $I_r(l, m)$. It is evident that the quantity $I_r(l, m)$ is not a fully recovered copy of $I(l, m)$ which is expected as not all spatial frequencies are measured by the considered sampling function. Furthermore, the multiplicative operation in the spatial Fourier domain represents a convolution in the spatial domain, hence, the spatial aliasing appearing in reconstructed intensity reducing the usable or unambiguous field of view. A dense sampling function can be synthesized enabling high-resolution image reconstruction using sparse antenna arrays with judicious placement of a small number of antennas (compared to a filled aperture) [57, 49, 32, 58]. In general, an interferometric array's performance can be improved by increasing the number of elements with the objective to synthesize additional sampling points in the spatial Fourier domain (i.e., as a result of new unique baselines). However, this can become a challenge as the number of receiving antennas in the array is large.
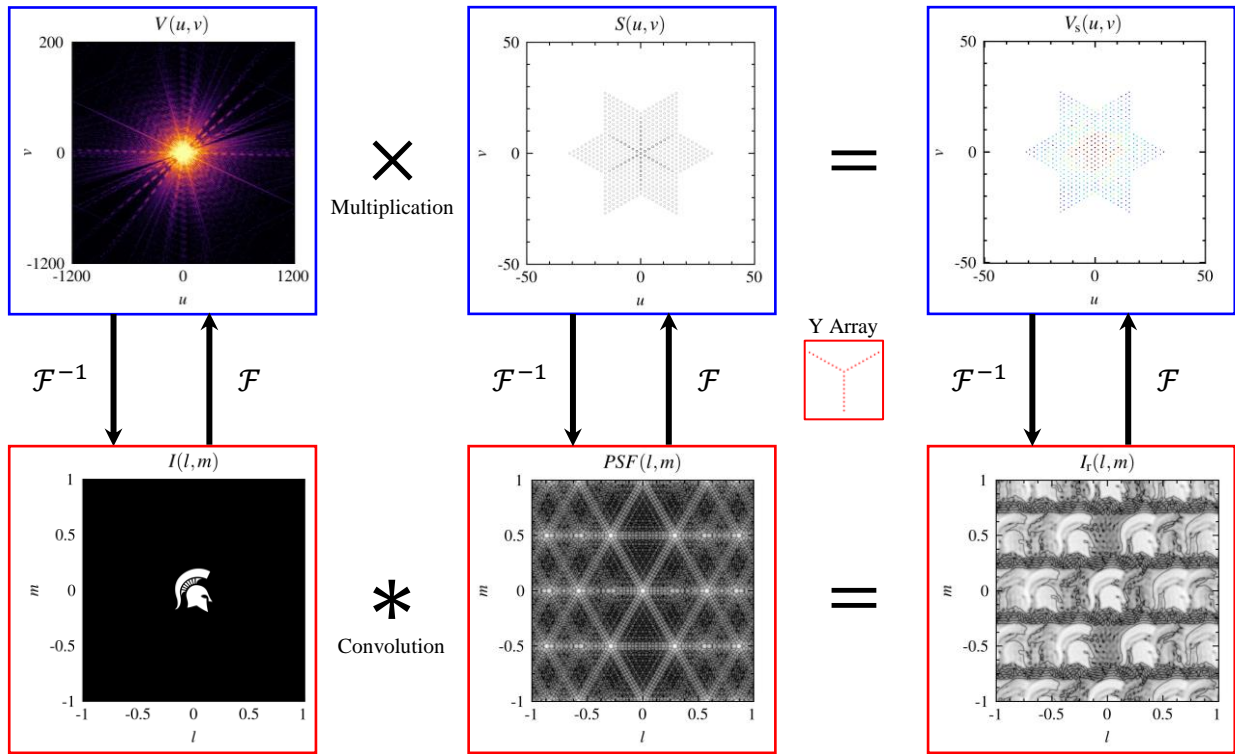
Figure 1.6 Visual example showing the Fourier relationship between the spatial Fourier domain and the spatial domain. The visibility $V(u, v)$ is the Fourier transform of the scene intensity $I(l, m)$ when the van Cittert-Zernike theorem is satisfied. The sampling function $S(u, v)$ is determined by the interferometric array configuration and is the Fourier transform of the point spread function $PSF(l, m)$. The sampled visibility $V_s(u, v)$ is the multiplicative product between the sampling function and the visibility, and its inverse Fourier transform yields the reconstructed scene intensity $I_r(l, m)$ which can also be considered as the convolution between the point spread function and the scene intensity.

1.3 Significance of this Dissertation

The work included in this dissertation demonstrates an unconventional way of designing radar systems. Scanning based radar systems leverage relative motion of the antenna/array to obtain additional information of the measured scene. In contrast, staring based radar systems utilize specific antenna/array configuration to improve the measured scene information. The concept of dynamic antenna array inherits both design considerations of scanning and staring based radar systems; fast array dynamics are being applied to individual receiving elements within the dynamic antenna array to measure additional information of the scene over a period of time due to the antennas' trajectories while the line of sight of the system remains unchanged (i.e., staring). Information measured using the dynamic antenna array technique can be combined with various signal processing techniques enabling its applicability to different use cases providing the possibility to be considered alternative solutions to radar applications such as imaging radar, remote sensing of the Earth, or concealed contraband detection.

Airport security screening is a specific application that can benefit from this work. At the time of drafting this dissertation, Quarter 1 of 2024, air travel numbers have already returned to pre-pandemic level. Furthermore, it is estimated that we will see a record number of 4.7 billion air travelers in the year 2024. This can represent a challenge at the airport security checkpoints when the number of travelers is beyond the capacity of security screener. Common airport security personnel screener such as the ProVision®2 requires less than six seconds total processing time from scan to decision with upgrades and future iterations focusing on reducing this time to further improve the throughput of screened travelers [59]. By using a dynamic antenna array I designed and implemented, imaging of the screened person is not necessary, hence enabling privacy preservation of the person. All of this, from data acquisition, signal processing, and classification only account for a fraction of a second which presents itself as a potential viable approach.

CHAPTER 2

SPATIAL FOURIER DOMAIN SAMPLING USING ARRAY WITH DYNAMICS

In this chapter, I discuss the concept and theory of spatial Fourier domain sampling starting with a conventional static array followed by the expansion to account for array dynamics. For the context of this work, the *synthesized* sampling function refers to the collection of *uv*-points based on the array configuration at a given fast time instance as described by (2.3); and the *integrated* sampling function refers to the aggregated measured *uv*-points integrated over a slow time duration T as a result of each individual antenna's trajectory yielding varying array configurations at various times as described by (2.14). Subsequently, I present a remote sensing scenario considering two different types of array trajectories with discussion on the trades and design constraints.

This chapter is, in part, a reprint or adaptation of materials with permission in "A Remote Sensing Approach Using Dynamic Distributed Interferometric Array" submitted to the *IEEE Transactions on Geoscience and Remote Sensing*, March 2024 and "Imageless Contraband Detection Using a Millimeter-Wave Dynamic Antenna Array via Spatial Fourier Domain Sampling" submitted to the *IEEE Access*, April 2024.

2.1 Spatial Fourier Domain Sampling

As discussed in the previous chapter, an interferometric imaging array measures the scene information in the spatial Fourier domain by cross-correlating the receive signals among individual antenna pairs within the array, and relies on the assumption that the signals emanating from the measured scene are spatially and temporally incoherent which satisfies the van Cittert-Zernike theorem [51, 52]. When the spatio-temporal incoherent requirement is maintained, the visibility function can be expressed as the two-dimensional (2D) Fourier transform of the scene intensity function [32] as previously given in (1.16),

$$V(u, v) = \iint\limits_{l,m=-\infty}^{\infty} I(l, m) e^{-j2\pi(ul+vm)} \, dl\,dm$$

where $l = \sin\theta\cos\phi$ and $m = \sin\theta\sin\phi$ are the direction cosines relative to the two spatial Fourier domain dimensions u and v in unit of cycles·rad^{-1}, respectively. This formulation can be further

expanded to include array design consideration such as antenna pattern and/or placement given by

$$\left[V(u,v) * * \bar{A}_N(u,v)\right] S(u,v) = \iint\limits_{l,m=-\infty}^{\infty} \left[I(l,m)A_N(l,m)\right] * * PSF(l,m)e^{-j2\pi(ul+vm)} \, dl \, dm$$

(2.1)

where the double-asterisk $**$ represents 2D convolution, $\bar{A}_N(u,v)$ is the 2D Fourier transform of the normalized antenna patterns $A_N(l,m)$, and $S(u,v)$ is the synthesized sampling function with its 2D Fourier transform pair being the point spread function $PSF(l,m)$.

2.1.1 Synthesized Sampling Function and the Measured Visibility

The sampling function can be thought of as the 2D auto-correlation function among the distributed electric fields $\mathcal{E}(x_\lambda, y_\lambda)$ across the considered array aperture,

$$S(u,v) = \mathcal{E}(x_\lambda, y_\lambda) \star\star \mathcal{E}^*(x_\lambda, y_\lambda) = \iint\limits_{x_\lambda, y_\lambda=-\infty}^{\infty} \mathcal{E}(x_\lambda, y_\lambda)\mathcal{E}^*(x_\lambda - u, y_\lambda - v) \, dx_\lambda dy_\lambda \qquad (2.2)$$

where the double-star symbol $\star\star$ represents 2D auto-correlation and (x_λ, y_λ) represent the co-ordinates of the array aperture plane in wavelength. In practice, however, electric fields among individual coordinates of a single antenna cannot be measured separately, hence the output response of a receiving antenna accounts for only one sampling coordinate that usually represents the location of the phase center of the antenna. With such consideration, (2.2) can be formulated considering coordinates of individual antennas' phase center within the array aperture $\mathcal{A}(x_\lambda, y_\lambda)$ as

$$S(u,v) = \mathcal{A}(x_\lambda, y_\lambda) \star\star \mathcal{A}^*(x_\lambda, y_\lambda) \qquad (2.3)$$

An example of a linear array (i.e., array aperture) is shown in the top of Figure 2.1 with two identical horn antennas located at $(x_{1\lambda}, y_{1\lambda})$ and $(x_{2\lambda}, y_{2\lambda})$, respectively resulting in a separation of D_λ, and that both have an antenna aperture dimension of $x_\lambda \times y_\lambda$. The resulting sampling function is shown in the bottom of Figure 2.1 where the rectangles in the uv-space represent the sampling function formulation in (2.2) and the points on the uv-space (i.e., 0 and $\pm|D_\lambda|$) represent the formulation in (2.3).
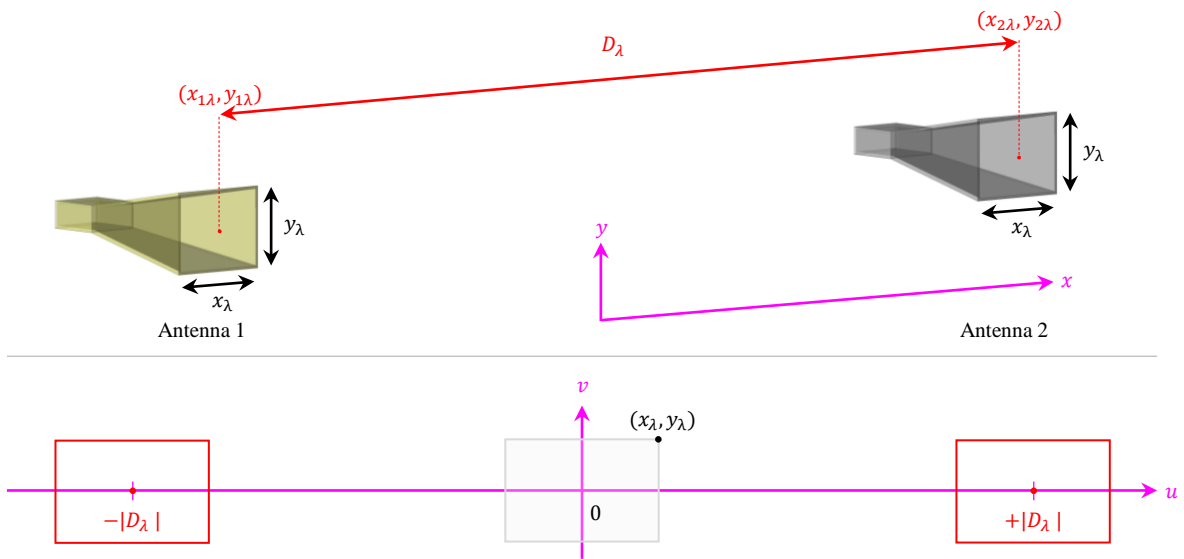
Figure 2.1 **Top**: Example of a linear array (i.e., array aperture) with two identical horn antennas located at $(x_{1\lambda}, y_{1\lambda})$ and $(x_{2\lambda}, y_{2\lambda})$, respectively resulting in a separation of D_λ, and that both have an antenna aperture dimension of $x_\lambda \times y_\lambda$. **Bottom**: The sampling function can be considered as the 2D auto-correlation of the array aperture resulting in cross-correlation among individual antennas (i.e., sampling points at $\pm|D_\lambda|$ in and auto-correlation of individual antenna with itself (i.e., sampling point at 0) where the former maps a specific pair of antenna's baseline $D_\lambda = (D_{\lambda x} = x_{\lambda 1} - x_{\lambda 2}, D_{\lambda y} = y_{\lambda 1} - y_{\lambda 2})$ to specific sampled uv-points such that $(u, v) = \pm(D_{\lambda x}, D_{\lambda y})$, and the latter yielding the sampling point $(u = 0, v = 0)$.

Note that the consideration of 2D auto-correlation of the array aperture in (2.3) results in cross-correlation among individual antennas (i.e., sampling points at $\pm|D_\lambda|$ in Figure 2.1) and auto-correlation of individual antenna with itself (i.e., sampling point at 0 in Figure 2.1) where the former maps a specific pair of antenna's baseline $D_\lambda = (D_{\lambda x} = x_{\lambda 1} - x_{\lambda 2}, D_{\lambda y} = y_{\lambda 1} - y_{\lambda 2})$ to specific sampled uv-points such that $(u, v) = \pm(D_{\lambda x}, D_{\lambda y})$, and the latter yielding the sampling point $(u = 0, v = 0)$ assuming the two antennas are located at $(x_{\lambda 1}, y_{\lambda 1})$ and $(x_{\lambda 2}, y_{\lambda 2})$, respectively.

The design of an interferometric array mainly considers the number of available antennas and the array's configuration. The placement of individual antennas is important as it determines the performance of the interferometric array which is associated with the recovered image quality. For a given interferometric imaging array, the spatial resolution achieved by a given array configuration is determined by the maximum baselines along all direction on the measurement plane considering the null-to-null bandwidth given by [48]

$$\Delta_{l,m} \approx \theta_{\text{NNBW}}^{(l,m)} \approx \frac{2}{\max\{D_{x_\lambda, y_\lambda}\}} \tag{2.4}$$

and the half-angle unambiguous field of view (FOV) across the two direction cosines is determined by the antenna spacing $(d_{x_\lambda, y_\lambda})$ such that

$$\text{FOV}_{\frac{l}{2}, \frac{m}{2}} = \frac{1}{2 \cdot d_{x_\lambda, y_\lambda}} \tag{2.5}$$

In addition to the imaging system's resolution and unambiguous coverage, redundancy of specific sampled uv-points can also be an important factor contributing to the recovered imagery quality. For a given two-dimensional interferometric array, the complete collection of all discretely sampled uv-points (i.e., spatial frequency information due to the array's configuration) can be formulated as

$$S_{\text{Total}}(u, v) = \sum_{n=1}^{N} \sum_{m=1}^{M} \delta(u - u_n)\delta(v - v_m) \tag{2.6}$$

where $\delta(\cdot)$ is the Dirac delta function and the product NM represents the total possible number of spatial frequency samples that the imaging array can acquire. Note that NM can be considered as the collection of redundant and unique spatial frequency samples

$$NM = (NM)_{\text{redundant}} + (NM)_{\text{unique}} \tag{2.7}$$

27

This is demonstrated in Figure 2.2 using a one-dimensional linear array with four antennas. Each color specifies the unique baseline associated with a given pair of antennas. Solid lines represent unique baselines and the dashed lines represent redundant baselines. For example, the pair of Antennas 1 and 2 and the pair Antennas 2 and 3 both yield the same electrical baseline and orientation (i.e., in the one-dimensional consideration), and hence will sample the same spatial Fourier sampling points. When multiple pairs of antennas within the array synthesize the exact sampled uv-points, a redundant sample is obtained and contributes to the term $(NM)_{\text{redundant}}$. Depending on the application, redundant samples may be useful, for example in calibration, but the typical design objective is to optimize $(NM)_{\text{unique}}$ using a fixed number of receiving elements. In general, when the number of receiving elements is small, the receiver numbers tend to have higher positive correlation to $(NM)_{\text{unique}}$. However, challenges arise when trying to implement additional elements, especially for arrays that are large, such as avoiding redundant antenna baselines.

The left-hand side of (2.1) can be treated as the measured visibility by the interferometric array. While (2.3) accounts for the location of the sampled spatial Fourier information in the uv-domain, it is necessary to understand the composition of the measured visibility from each pair of antennas within the array due to antenna orientation and polarization. One way to describe the output from a pair of antennas is to consider the Stokes visibilities, which assumes their correlating output to be modeled using an arbitrary polarized antenna considering two idealized dipoles in a cross configuration [32] as shown in Figure 2.3. The Stokes parameters are associated with the amplitudes of the two perpendicular electric field components that are both orthogonal to the direction of propagation [32]. Suppose that the electric field components take the following complex form,

$$E_x(t) = \mathcal{E}_x(t)e^{j[2\pi f t + \delta_x(t)]}$$
$$E_y(t) = \mathcal{E}_y(t)e^{j[2\pi f t + \delta_y(t)]}$$

(2.8)

where f is the considered frequency and the $\delta(t)$ terms describe an arbitrary phase of the associated field component.
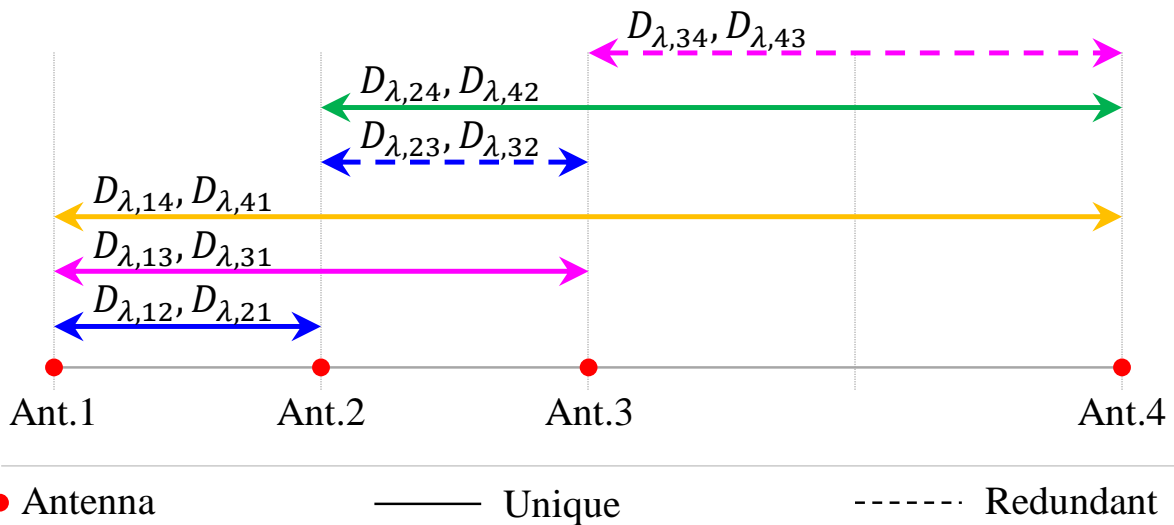
Figure 2.2 Example of a one-dimensional linear array consists of four antennas demonstrating the concept of unique and redundant sampling point due to the uniqueness of the baseline between two antennas that is determined by their electrical separation and orientation. Each color specifies the unique baseline associated for a given pair of antennas. Based on the ascending antenna numbering label, solid lines represent the considered unique baselines and the dash lines represent the redundant baselines. Originally submitted to *IEEE Access*, April 2024.
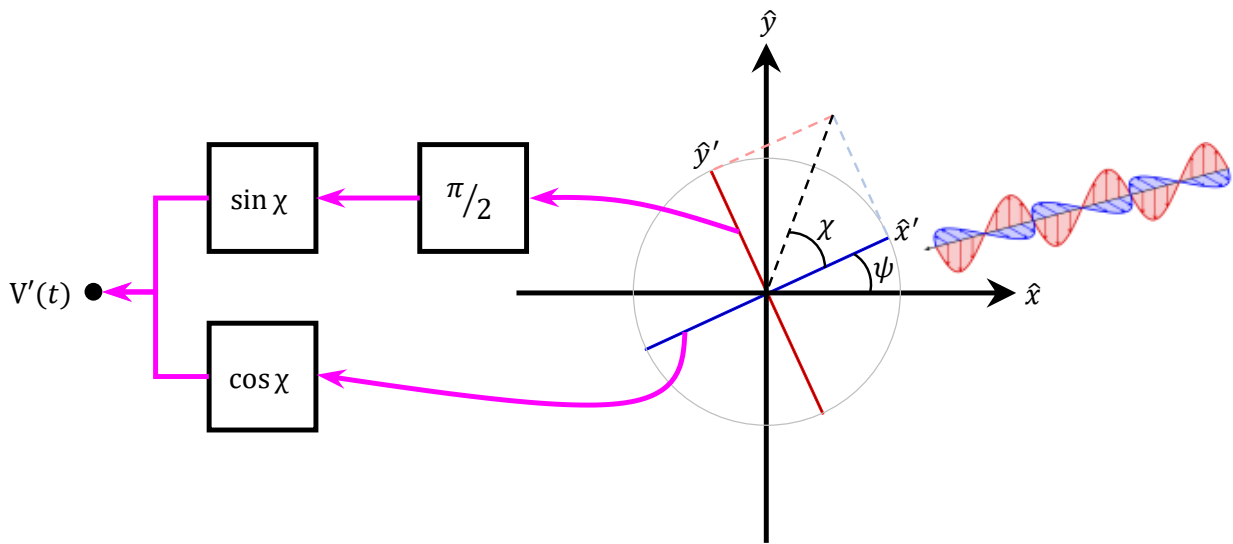
Figure 2.3 An antenna of arbitrary polarization can be described using two idealized dipoles that are physically orthogonal to each other [32]. The position angle ψ is between major axis of the polarization ellipse and the reference $\hat{x}$. The angle χ describes the axial ratio with a range within $\pm\pi/4$. The measured voltage response is the total response from each of the dipoles, and the measured x' and y' components each pass through networks with voltage response proportional to $\cos\chi$ and $\sin\chi$ with a $\pi/2$ phase lag, respectively. Note that the measured voltage response $V'(t)$ is not italicized to differentiate it from the visibility function $V(u, v)$. Originally submitted to *IEEE Transactions on Geoscience and Remote Sensing*, March 2024.

The Stokes parameter are defined as follows [32]:

$$I = \langle \mathcal{E}_x^2(t) \rangle + \langle \mathcal{E}_y^2(t) \rangle$$

$$Q = \langle \mathcal{E}_x^2(t) \rangle - \langle \mathcal{E}_y^2(t) \rangle$$

$$U = 2\langle \mathcal{E}_x(t)\mathcal{E}_y(t) \cos \left[\delta_x(t) - \delta_y(t) \right] \rangle$$

$$V = 2\langle \mathcal{E}_x(t)\mathcal{E}_y(t) \sin \left[\delta_x(t) - \delta_y(t) \right] \rangle$$

(2.9)

where the angle brackets represent the expectation (i.e., time averaging over a fast time integration of τ), and each of the Stokes parameters represents the total intensity (I), the two linearly polarized components (Q, U), and the circularly polarized component (V) of the wave. In Figure 2.3, the antenna model of arbitrary polarization makes an angle ψ between its major axis of polarization ellipse and the reference $\hat{x}$. Furthermore, the angle χ describes the axial ratio of the modeled antenna and is within a range of $\pm\pi/4$.

The measured voltage response as illustrated in Figure 2.3 can be expressed as

$$\text{V}'(t) = E_x'(t) \cos \chi - jE_y'(t) \sin \chi \qquad (2.10)$$

where the marks $'$ indicate measured responses, $\cos \chi$ and $\sin \chi$ represent the voltage response proportional to the associated network as indicated in Figure 2.3, and the factor $-j$ represents the $\pi/2$ lag applied to the measured component of y'. Note that the measured voltage response $\text{V}'(t)$ in (2.10) is not italicized to differentiate it from the visibility function $V(u, v)$. Furthermore, the components associated with the x' and y' in (2.10) can each be expressed by accounting for the position angle ψ and axial ratio χ as

$$E_{x'}(t) = \left[\mathcal{E}_x(t)e^{j\delta_x(t)} \cos \psi + \mathcal{E}_y(t)e^{j\delta_y(t)} \sin \psi \right] e^{j2\pi ft}$$

$$E_{y'}(t) = \left[-\mathcal{E}_x(t)e^{j\delta_x(t)} \sin \psi + \mathcal{E}_y(t)e^{j\delta_y(t)} \cos \psi \right] e^{j2\pi ft}$$

(2.11)

Therefore, the output response of a pair of correlating antennas can be expressed by considering a time averaging operation over a fast time integration of duration τ such that

$$R_{12} = G_{12}\langle \text{V}_1'(t)\text{V}_2'^*(t) \rangle \qquad (2.12)$$

31

where the subscripts 1 and 2 represent the two antennas, G_{12} is the instrumental gain factor. By considering the formulations from (2.9)–(2.11), (2.12) can be further expressed using the Stokes visibilities as [32]

$$
\begin{aligned}
R_{12} = G_{12}\{ & I_v \left[\cos(\chi_1 - \chi_2) \cos(\psi_1 - \psi_2) + j \sin(\chi_1 + \chi_2) \sin(\psi_1 - \psi_2) \right] \\
& +Q_v \left[\cos(\chi_1 + \chi_2) \cos(\psi_1 + \psi_2) + j \sin(\chi_1 - \chi_2) \sin(\psi_1 + \psi_2) \right] \\
& +U_v \left[\cos(\chi_1 + \chi_2) \sin(\psi_1 + \psi_2) - j \sin(\chi_1 - \chi_2) \cos(\psi_1 + \psi_2) \right] \\
& -V_v \left[\sin(\chi_1 + \chi_2) \cos(\psi_1 - \psi_2) + j \cos(\chi_1 - \chi_2) \sin(\psi_1 - \psi_2) \right] \}
\end{aligned}
\tag{2.13}
$$

where I_v, Q_v, U_v, and V_v are the Stokes visibilities with χ and ψ describing the axial ratio and the position angle off from the considered major axis of the measurement plane of an antenna, respectively. Details on the derivation of (2.13) are included in Appendix D. Composition of different Stokes visibilities can therefore be measured using different combinations of antenna polarization and/or position angles. The fast time integration duration τ is dependent on the sensitivity of the considered interferometric imaging array such that τ is inversely proportional to the signal-to-noise ratio (SNR) [54]. For systems with significant SNR yielding a very short duration of dwell time, this represents an opportunity to consider the scenario that array elements move across the measurement plane at a relatively slow time dimension, hence enabling the concept of dynamic antenna array.

2.1.2 The Integrated Sampling Function Through Array Trajectory

As observed from the above formulation, it is evident that array design for an interferometric imager is complex. For example, balancing the number of unique sampled uv-points and the redundancy at each of the sampled uv-point considering a small/fixed number of receiving antennas. Fortunately, in radio astronomy, the synthesized sampling function due to a fixed interferometric array configuration varies as the Earth rotates, which modifies the apparent baselines among array elements with respect to the observing celestial direction [32]. This represents an integrated sampling function throughout the array trajectory due to the Earth's rotation that is much more filled when compared to the synthesized sampling function at any given instance. However, the Earth's rotation is slow, uncontrollable, and inapplicable outside the use case of observing celestial objects. Nevertheless, this motivates the concept of using a dynamic distributed interferometric array for remote sensing application which is shown at the bottom of Figure 2.4 illustrating nine aerial platforms each with independent trajectory synthesizing specific Fourier domain sampling function at a given slow time instance due to array configuration. Over the duration of slow time, an integrated sampling function is obtained where an inverse Fourier transformation can be applied to the aggregated sampled visibility to obtain the reconstructed scene intensity assuming that the scene intensity remains quasi-static relative to the slow time duration T. As shown in the top right of Figure 2.4, the idea of integrating individual synthesized sampling functions over all synthesized sampling function during the array trajectory is analogous to the concept of a radar data cube considering the individual synthesized sampling function $S(u, v)$, the fast time t enabling sufficient duration of received signal to be measured, and slow time T for the integrated sampling function

$$S_T(u, v) = \int_0^T \mathcal{A}\left(x_\lambda(T), y_\lambda(T)\right) \star \star \, \mathcal{A}^*\left(x_\lambda(T), y_\lambda(T)\right) \; dT \qquad (2.14)$$
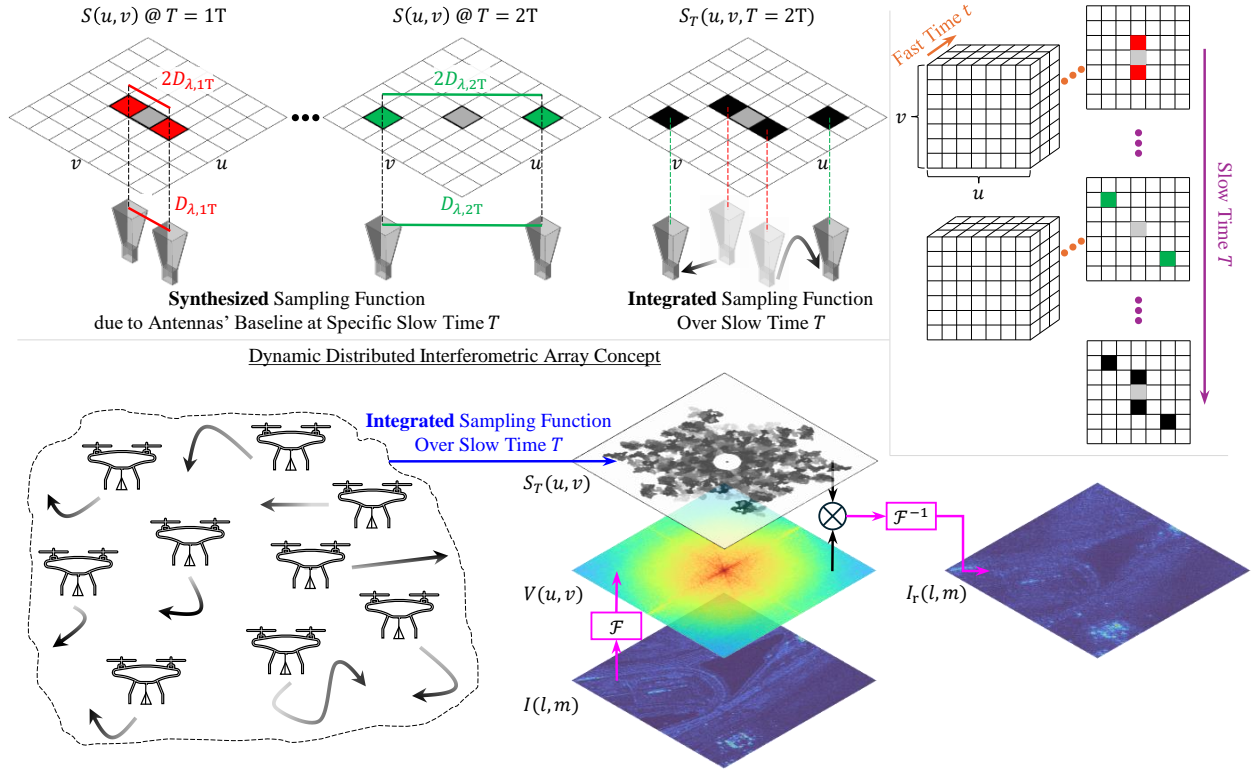
Figure 2.4 **Top left**: Illustration of the synthesized sampling function from a two-element correlation pair at different slow time instances. At $T = 1T$ or $T = 2T$, the uv-points sampled according to (2.3) are shown in red or green for the cross-correlation response and gray for the auto-correlation responses. Over a duration of $T = 2T$, the integrated sampling function includes the aggregated synthesized sampling function at various slow time instances. **Top right**: The integrated sampling function is analogous to the concept of a radar data cube considering the fast time t, slow time T, and the individual synthesized sampling function $S(u, v)$. **Bottom**: The dynamic distributed interferometric array concept illustrates nine aerial platforms each with independent trajectory synthesizing specific Fourier domain sampling function at a given slow time instance due to array configuration. Over the duration of slow time, an integrated sampling function is obtained where an inverse Fourier transformation can be applied to the aggregated sampled visibility to obtain the reconstructed scene intensity assuming that the scene intensity remains quasi-static relative to the slow time duration T. Originally submitted to *IEEE Transactions on Geoscience and Remote Sensing*, March 2024.

The $x_\lambda(T)$ and $y_\lambda(T)$ in (2.14) represent coordinates of all antennas within the dynamic distributed aperture at a given T.

$$x_\lambda(T) = \left\{ x_{\lambda,1}(T), x_{\lambda,2}(T), x_{\lambda,3}(T), \ldots x_{\lambda,N}(T) \right\}$$
$$y_\lambda(T) = \left\{ y_{\lambda,1}(T), y_{\lambda,2}(T), y_{\lambda,3}(T), \ldots y_{\lambda,N}(T) \right\}$$

(2.15)

where N is the number of antennas within the dynamic antenna array's aperture. Furthermore, the coordinates of the n-th antenna as function of slow time T can be described using a trajectory function

$$\overrightarrow{\mathrm{TRJ}}_n(T) = \hat{x} x_{\lambda,n}(T) + \hat{y} y_{\lambda,n}(T)$$
$$= \vec{p}_n(T) + \overrightarrow{\mathrm{trj}}_n(T)$$

(2.16)

where $\overrightarrow{\mathrm{TRJ}}_n(T)$ represent the global trajectory function with reference to the global origin of the considered plane where the dynamic distributed aperture resides, which can be further represented using the commutative vector addition property such that an offset vector $\vec{p}_n(T)$ relates the global origin to the local trajectory function $\overrightarrow{\mathrm{trj}}_n(T)$ that is referenced to a local origin. An illustration of (2.16) is shown in Figure 2.5 where the left demonstrates an arbitrary trajectory in purple with three slow time instances T_1, T_2, and T_3 colored in red, green, and blue, respectively. Furthermore, on the right of Figure 2.5 is an example of how an offset vector $\vec{p}_n(T)$ (shown in red) can be utilized to more efficiently relate a local trajectory function $\overrightarrow{\mathrm{trj}}_n(T)$ (shown in blue) to the global origin.

In terms of the Stokes visibility, it is expected that the position angle can vary as a result of individual antenna's movement, hence (2.13) should be modified to account for the individual antenna's position angle at slow time T

$$R_{nm} = G_{nm} \{ I_v \left[\cos(\chi_n - \chi_m) \cos(\psi_-(T)) + j \sin(\chi_n + \chi_m) \sin(\psi_-(T)) \right]$$
$$+ Q_v \left[\cos(\chi_n + \chi_m) \cos(\psi_+(T)) + j \sin(\chi_n - \chi_m) \sin(\psi_+(T)) \right]$$
$$+ U_v \left[\cos(\chi_n + \chi_m) \sin(\psi_+(T)) - j \sin(\chi_n - \chi_m) \cos(\psi_+(T)) \right]$$
$$- V_v \left[\sin(\chi_n + \chi_m) \cos(\psi_-(T)) + j \cos(\chi_n - \chi_m) \sin(\psi_-(T)) \right] \}$$

(2.17)

where the subscripts n and m represent any two given antennas of the dynamic antenna array, and $\psi_\pm(T) = \psi_n(T) \pm \psi_m(T)$.
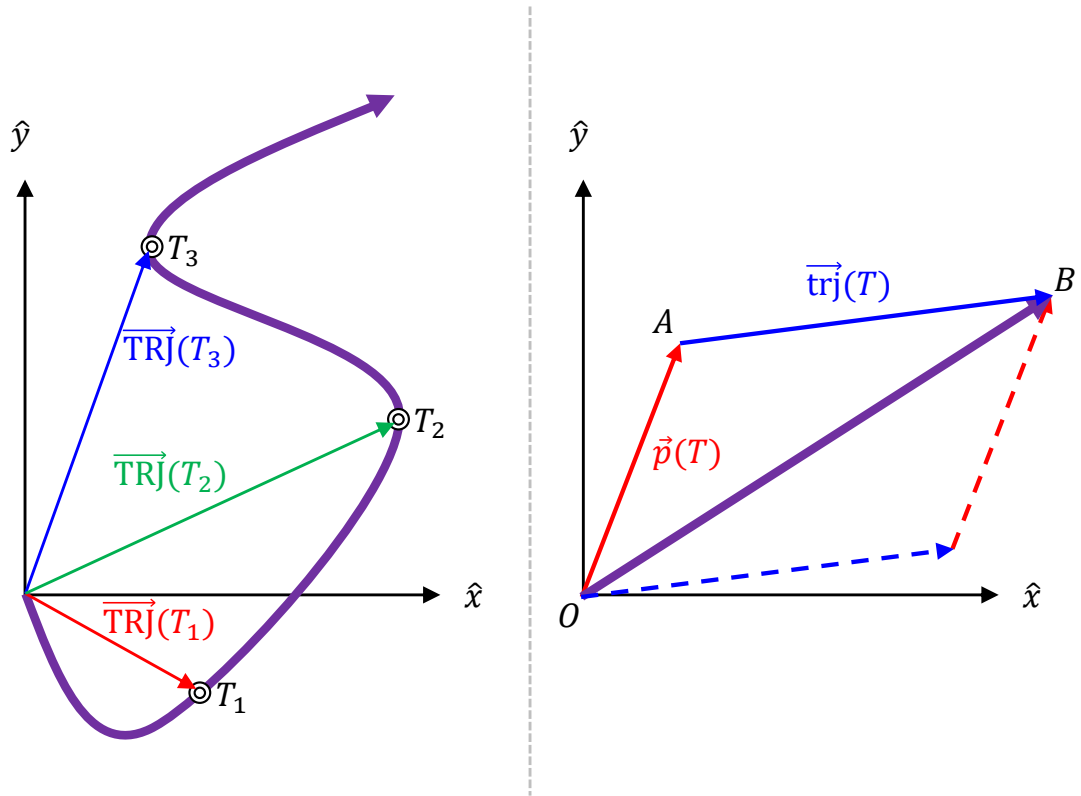
Figure 2.5 **Left**: Two-dimensional arbitrary trajectory shown in purple along with three slow time instances T_1, T_2, and T_3 colored in red, green, and blue, respectively. **Right**: Example of commutative vector addition property where an offset vector (shown in red) can be utilized to more efficiently relate a local trajectory function (shown in blue) to the global origin.

2.2 Remote Sensing Using a Dynamic Interferometric Array

2.2.1 Simulation Setup and Assumption

To demonstrate the potential of an interferometric array with controllable dynamics, a simulation based remote sensing scenario is investigated. A nine-platform dynamic distributed interferometric array operating at 10 GHz where each platform is assumed to be a DJI MATRICE 600 Pro with a full span of 1.668 m or $\approx 56\lambda$ as shown in the top of Figure 2.6. Each platform is assumed to have either a single antenna integrated at its centroid or a three-element sub-array as shown in the bottom of Figure 2.6. Each individual antenna is assumed to have equal beamwidth of $30°$ and gain for each of its principle plane, and is also dual polarized such that both linearly cross-polarized components can be measured simultaneously. Furthermore, we assume all antennas position angle remain unchanged during the movement such that they also remain co-polarized. Therefore, all Stokes visibilities as described by (2.17) can be measured and the expression can be further simplified with the assumptions on the antenna characteristics such that

$$R_{nm,vv} = G_{nm} \left[I_v - Q_v \right]$$

$$R_{nm,hh} = G_{nm} \left[I_v + Q_v \right]$$

$$R_{nm,vh} = G_{nm} \left[U_v - jV_v \right]$$

$$R_{nm,hv} = G_{nm} \left[U_v + jV_v \right]$$

(2.18)

where the additional subscripts v and h represent the vertically and horizontally polarized component that can be measured independently by each of the antennas. A scene intensity with a spatial extent of 1000 m×1000 m based on a ground scene radar image measured at 9.65 GHz from [60] is used as a reference to investigate the scene reconstruction quality of various array dynamics with and without the use of a sub-array. The reference scene intensity is shown in Figure 2.7 along with the associated visibility function assuming satisfying the van Cittert-Zernike theorem. Considering the beamwidth of the antenna and the spatial extent of the reference scene, the flying altitude of the platform is approximately 1866 m which is lower than the advertised flying ceiling for the considered platform between 2500–4500 m based on its propeller configuration.

Platform

1.668 m, $\approx 56\lambda$ @ 10 GHz

Three-element sub-array
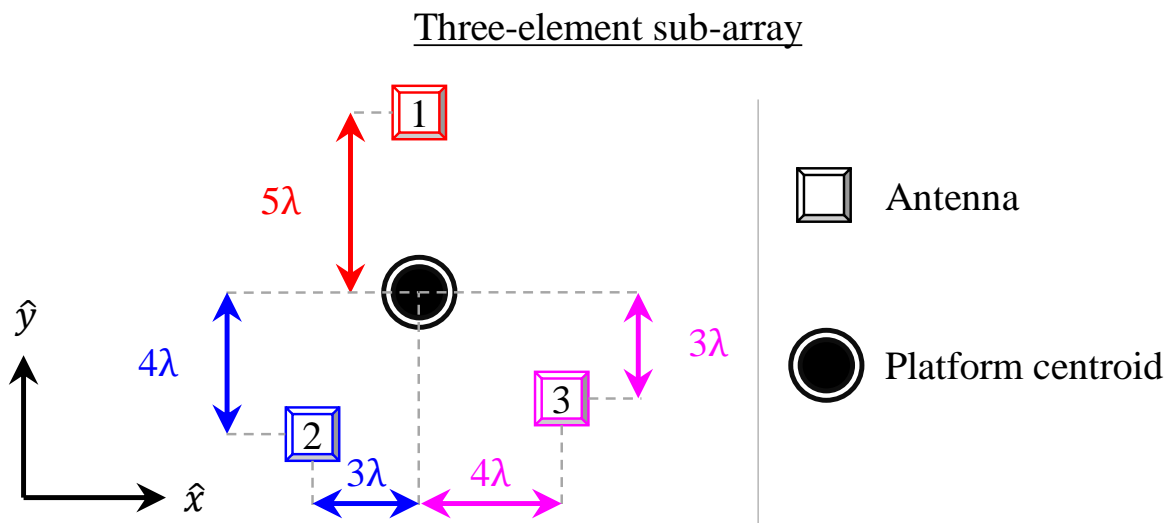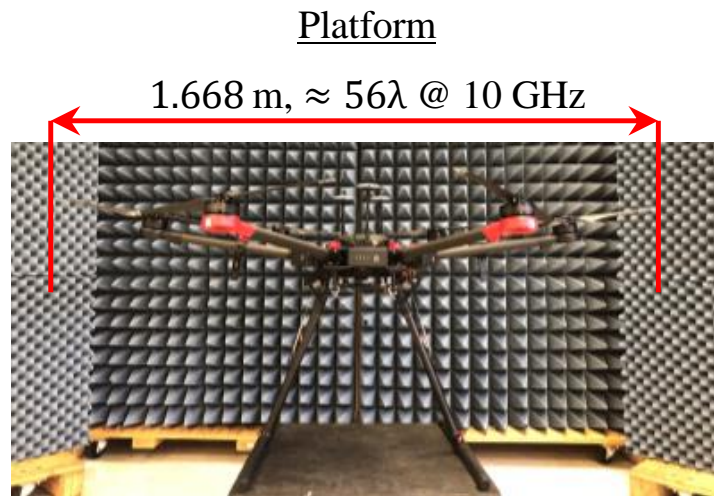
Figure 2.6 **Top**: Photo of the assumed platform, DJI MATRICE 600 Pro, with a full span of 1.668 m, or $\approx 56\lambda$ considering an operating frequency of 10 GHz. **Bottom**: Configuration of a three-element sub-array that is considered to be integrated with respect to the platform's centroid where each of the antenna is 5λ to the centroid of the platform. Originally submitted to *IEEE Transactions on Geoscience and Remote Sensing*, March 2024.
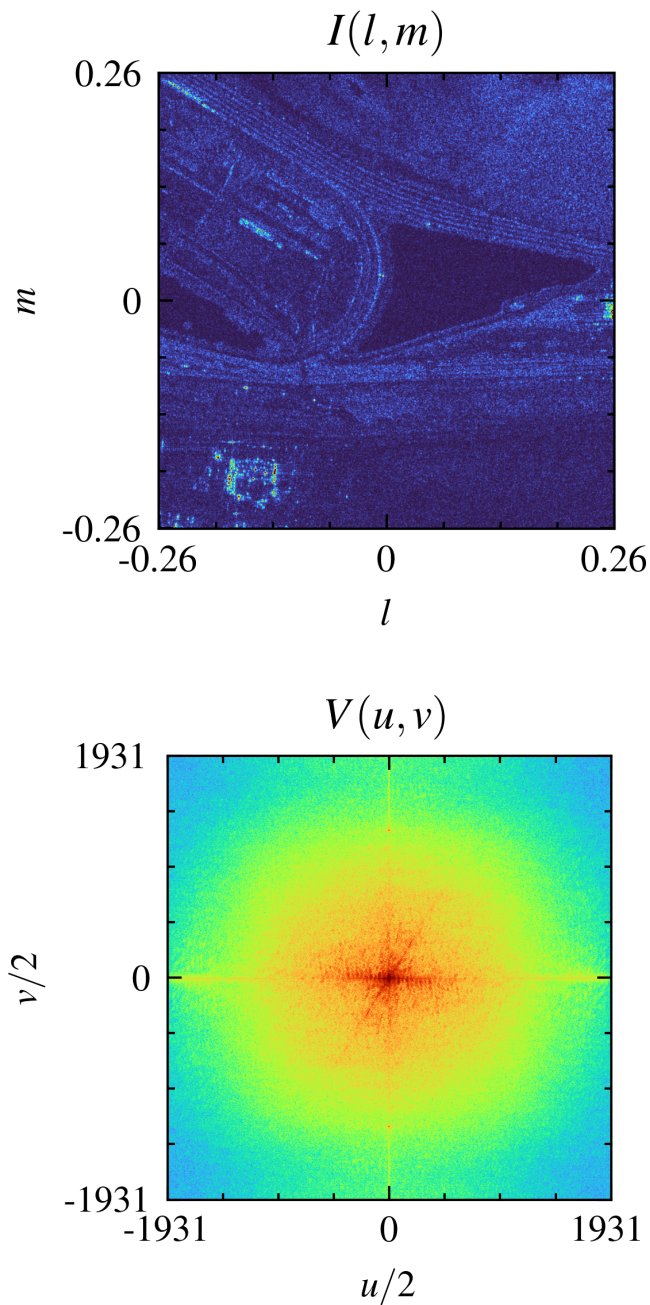
Figure 2.7 Top: The scene intensity function $I(l, m)$ with spatial extent of $1000\,\mathrm{m} \times 1000\,\mathrm{m}$. **Bottom**: The visibility function $V(u, v)$ which is the Fourier transform of the scene intensity function assuming that the van Cittert-Zernike theorem is fulfilled. Source of scene intensity data [60]. Both figures were reformatted for this dissertation and originally submitted to *IEEE Transactions on Geoscience and Remote Sensing*, March 2024.

2.2.2 Array Trajectory Approach and Integrated Sampling Function

Two approaches for designing array trajectory are investigated: coordinated and random. As shown in the top of Figure 2.8 and Figure 2.9, both approaches assume the nine-element distributed array with an initial configuration of a Y-array which is a common and efficient array configuration in radio astronomy [32]. The coordinated array trajectory (i.e., Array Trajectory 1) enforces the platform configuration to adhere to that of a Y-array while the random array trajectory (i.e., Array Trajectory 2) allows each platform to move in random manner. It is assumed that all platforms remain in the same altitude (i.e., measurement plane) throughout the 2D trajectories. Furthermore, both approaches require that none of the platform exits a measurement plane with dimension of $27\,\text{m}\times27\,\text{m}$ and a clearance requirement that each platform cannot get closer than 60λ which is slightly wider than a full span of the considered platform. Both array dynamics are assumed to elapse for a slow time duration of $T =1\text{T}$ with an additional scenario of the random array dynamics over a slow time period of $T =10\text{T}$. We also assume that there will be platforms not part of the receiving array near the perimeter of the measurement plane (but not inside) such that they perform active incoherent illumination [61] to ensure proper sampling in the spatial Fourier domain. Each antenna is assumed to dwell for a duration of $t = \tau$ for the fast time integration to obtain a synthesized sampling function at a given slow time T (i.e., $T \gg t, \tau$), and that the antenna locations fall on a 0.5λ spatial grid (in [62], a localization accuracy of 0.15λ was achieved). The slow time increment is uniformly at $T =0.01\text{T}$ representing an integrated sampling function consisting of 100 and 1000 synthesized sampling functions for the consideration of $T =1\text{T}$ and $T =10\text{T}$, respectively. Based on the considered platform, the value T is taken to be $2\,\text{s}$ so that no platform in the studied trajectories will move faster than the advertised maximum speed of $\approx17.88\,\text{m/s}$. This represents a slow time increment of $20\,\text{ms}$ which is reasonable considering the recent active incoherent approach achieving a fast time integration of as low as $\tau =64\,\upmu\text{s}$ per synthesized sampling function with sufficient signal-to-noise ratio (SNR) [54].

For the coordinated array trajectory (i.e., Array Trajectory 1), each platform's trajectory can be

expressed using (2.16) as

$$\overrightarrow{\text{TRJ}}_{1,n}(T) = \vec{p}_{1,n}(T) + \overrightarrow{\text{trj}}_{1,n}(T) \tag{2.19}$$

for the n-th platform and that

$$\vec{p}_{1,n}(T) = 0$$

$$\overrightarrow{\text{trj}}_{1,n}(T) = \overrightarrow{\text{TRJ}}_{1,n}(T) = \hat{x} D_{\lambda,n} \cos\left[\Theta_n(T)\right] \tag{2.20}$$

$$+ \hat{y} D_{\lambda,n} \sin\left[\Theta_n(T)\right]$$

where the quantity $D_{\lambda,n}$ and $\Theta_n(T)$ represent the magnitude (i.e., distance in wavelength) and the angle of a vector pointing from the global origin (i.e., origin of the assumed measurement plane) to the n-th platform. It is assumed that individual platforms with trajectories achieve a 120° rotation on the maintained Y-array over a period duration of $T =$1T and continuing the periodic array trajectory does not yield in additional uv-points covered by the integrated sampling function. This is shown in the top row of Fig. 2.8 where both the array trajectory and the integrated sampling function form concentric rings.

For the random array trajectory (i.e., Array Trajectory 2), each platform's trajectory can be expressed using (2.16) as

$$\overrightarrow{\text{TRJ}}_{2,n}(T) = \vec{p}_{2,n}(T) + \overrightarrow{\text{trj}}_{2,n}(T) \tag{2.21}$$

for the n-th platform and that

$$\vec{p}_{2,n}(T) = \vec{p}_{2,n}(T-1)$$

$$\overrightarrow{\text{trj}}_{n,2}(T) = \hat{x} d_{\lambda,n}(T) \cos\left[\theta_n(T)\right] \tag{2.22}$$

$$+ \hat{y} d_{\lambda,n}(T) \sin\left[\theta_n(T)\right]$$

where the quantity $d_{\lambda,n}(T)$ and $\theta_n(T)$ represent the magnitude (i.e., distance in wavelength) and the angle of a vector pointing from the local origin to the n-th platform; and that both $d_{\lambda,n}(T)$ and $\theta_n(T)$ follow a specific uniform distribution of $U(0\lambda, 10\lambda)$ and $U(0, 2\pi)$, respectively. Note that the upper- and lower-case of variable naming $D_{\lambda,n}$, $\Theta_n(T)$, $d_{\lambda,n}$, and $\theta_n(T)$, in (2.20) and

41

(2.22) represent referencing to the global and local coordinate in consistency with the notation of (2.16), respectively. This is shown in Figure 2.9 where the array trajectory still exhibits a Y-array configuration with varying inter-element spacing across array aperture and that the integrated sampling function takes the form of a star pattern which is the result of integrating over multiple synthesized sampling functions of similar star pattern. Unlike the coordinated trajectory that is periodic and has a maximum number of sampled uv-points by the integrated sampling function, the random trajectory approach is capable of acquiring additional spatial Fourier information such that each subsequent synthesized sampling function $S(u, v)$ can acquire new uv-points leading to an improved integrated sampling function $S_T(u, v)$ as T increases.

A third scenario considering the random trajectory approach is shown in Figure 2.10 which is a continuation from the random trajectory with T =1T in Figure 2.9 that elapses until T =10T. As expected, a much denser integrated sampling function is achieved due to the random trajectories of individual platforms within the array. We note the apparent un-sampled lower spatial frequency region in the integrated sampling function is a direct result of the clearance assumption that each of the platforms must adhere to. This means that for a dynamic distributed interferometric array, spatial Fourier information that resides in regions that commensurate to the clearance requirement can only be sampled by leveraging a well-designed sub-array mounted on each of the platforms. In the following analysis, each of the platforms is assumed to carry the same three-element sub-array as depicted in the bottom of Figure 2.6. However, we note that additional antennas within the sub-array can improve the number of uv-samples within the un-sampled region due to clearance, and that integrating different types of sub-array on each platform can further improve the sampling. For brevity, the integrated sampling functions considering the sub-array scenario in combination with the three aforementioned trajectories are not shown since the results will just appear wider due to additional uv-samples enabled by additional antenna elements within the dynamic antenna array aperture (i.e., 27 instead of 9) while exhibit similar form which is mainly to the trajectory.
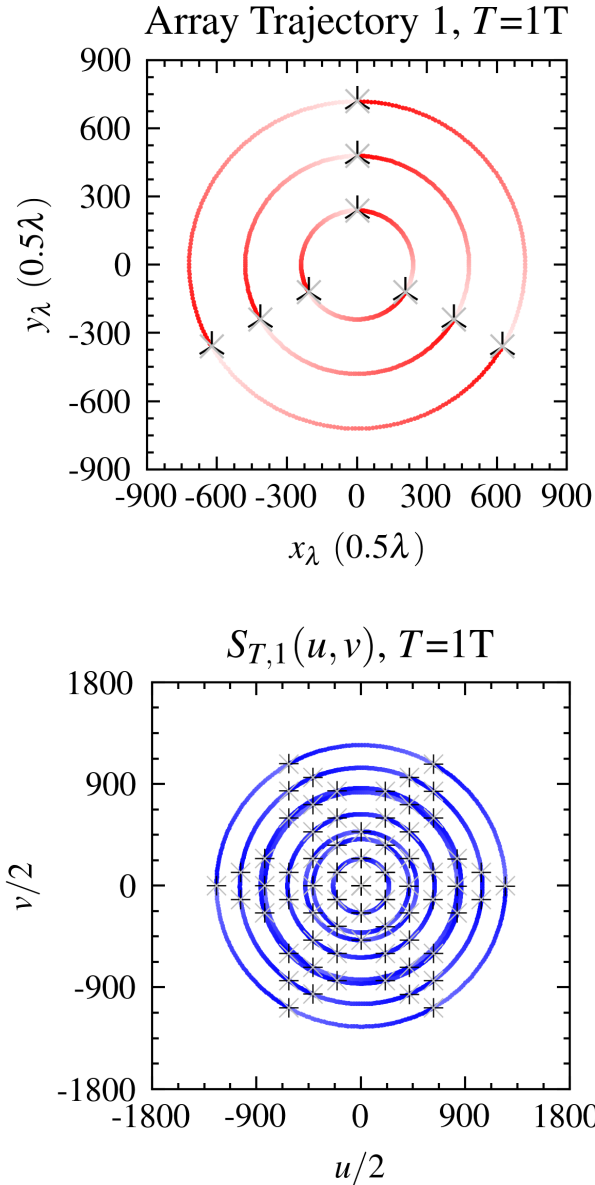
Figure 2.8 Top: A coordinated trajectory approach as described by (2.19) and (2.20) with nine platforms that maintain a Y-array configuration over a rotating trajectory that is periodic every 120° rotation and is assumed to account for a slow time duration of T =1T. **Bottom**: The integrated sampling function over the slow time duration of T =1T for the coordinated trajectory approach exhibiting a form of concentric rings. The gray cross markers represent either the initial position of the platforms or the initial synthesized sampling function; the black inverted-Y markers represent the final position of the platforms at the end of the slow time duration T; the black plus markers represent the final synthesized sampling function at the end of the slow time duration T; and transition of the color red and blue represent the elapsed trajectory and the integrated sampling function over the slow time duration T, respectively. Both figures were reformatted for this dissertation and originally submitted to *IEEE Transactions on Geoscience and Remote Sensing*, March 2024.

Array Trajectory 2, T=1T

$S_{T,2}(u,v)$, T=1T
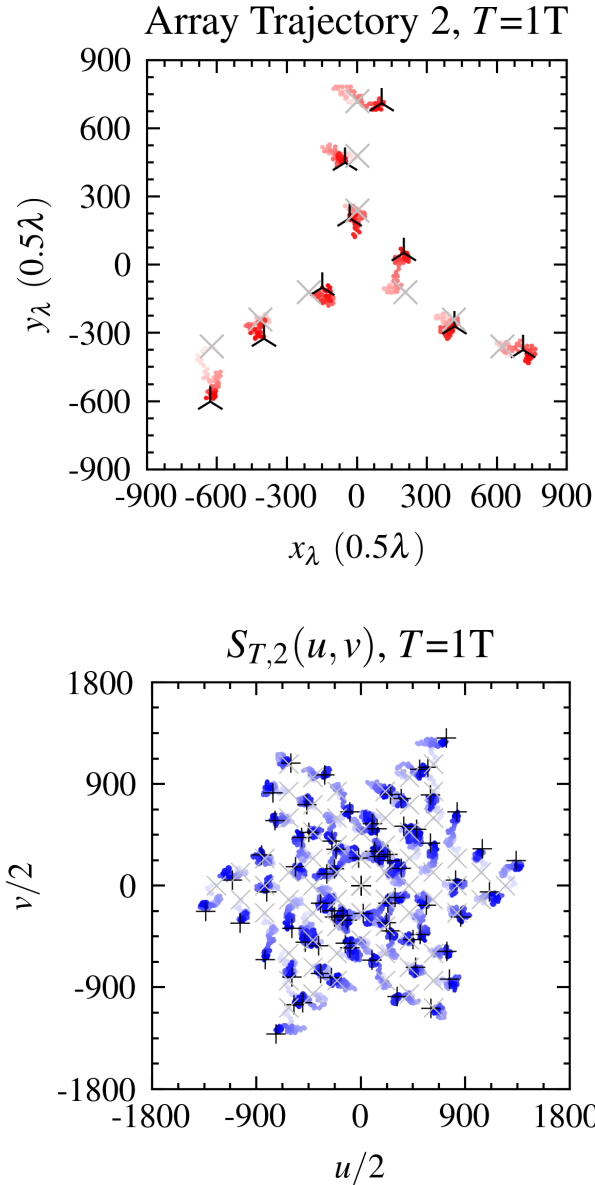
Figure 2.9 **Top**: A random trajectory approach as described by (2.21) and (2.22) with nine platforms that start with a Y-array configuration where an individual platform is assumed to randomly move across the measurement plane for a slow time duration of T =1T. **Bottom**: The integrated sampling function over the slow time duration of T =1T for the above random trajectory approach. The gray cross markers represent either the initial position of the platforms or the initial synthesized sampling function; the black inverted-Y markers represent the final position of the platforms at the end of the slow time duration T; the black plus markers represent the final synthesized sampling function at the end of the slow time duration T; and transition of the color red and blue represent the elapsed trajectory and the integrated sampling function over the slow time duration T, respectively. Both figures were reformatted for this dissertation and originally submitted to *IEEE Transactions on Geoscience and Remote Sensing*, March 2024.

Figure 2.10 Top: The same random trajectory approach over a longer slow time duration for T =10T. **Bottom**: The integrated sampling function over the slow time duration of T =10T for the above random trajectory approach. The gray cross markers represent either the initial position of the platforms or the initial synthesized sampling function; the black inverted-Y markers represent the final position of the platforms at the end of the slow time duration T; the black plus markers represent the final synthesized sampling function at the end of the slow time duration T; and transition of the color red and blue represent the elapsed trajectory and the integrated sampling function over the slow time duration T, respectively. Both figures were reformatted for this dissertation and originally submitted to *IEEE Transactions on Geoscience and Remote Sensing*, March 2024.

2.2.3 Performance Evaluation of Integrated Sampling Function Considering Scene Reconstruction

In Figure 2.11, Figure 2.13, and Figure 2.15, the point spread function (PSF) of the integrated sampling function and the scene intensity reconstruction of the reference scene intensity in Figure 2.7 are shown for the three trajectory scenarios with single antenna assumption as described in Figure 2.8, Figure 2.9, and Figure 2.10 above. For the scenarios with the sub-array consideration, the corresponding PSF and scene intensity reconstruction are shown in Figure 2.12, Figure 2.14, and Figure 2.16.

From the top of Figure 2.11 and Figure 2.12, it can be seen that the coordinated trajectory's PSFs (i.e., considering both single antenna and three-element sub-array per platform) exhibit the form of an 2D Airy function [63] which is a direct result of the concentric integrated sampling function as illustrated in Figure 2.8 for the single antenna scenario. As shown in the bottom of Figure 2.11 and Figure 2.12, the scene intensity reconstructions due to the coordinated trajectory recovered perceptible responses from the reference scene intensity (in the lower left and center right of the scene). Furthermore, the consideration of sub-array shows improvement over the single antenna scenario which is a direct result of sampling additional uv-points. From the top of Figure 2.13–Figure 2.16, the random trajectory's PSFs with and without the sub-array assumption both appear to be noise-like which is expected as the integrated sampling function is the aggregation of randomly sampled uv-points. Similar to the coordinated trajectory scenario, the sub-array enables more uv-points to be sampled, hence reducing the level of surrounding artifacts (i.e., improving the contrast of the point of the PSF). Unlike the coordinated trajectory scenario, the single antenna scenario considering the random trajectory did not recover perceptible information of the reference scene as shown in the bottom of Figure 2.13 when the slow time duration is $T =1$T. However, with the consideration of the sub-array, not only are the two responses in the bottom left and center right of the reference scene intensity (Figure 2.7) are recovered, but also the response from top left.

$PSF_{T,1}(l,m)$, $T{=}1\text{T}$

$I_{\text{r},1}(l,m)$, $T{=}1\text{T}$
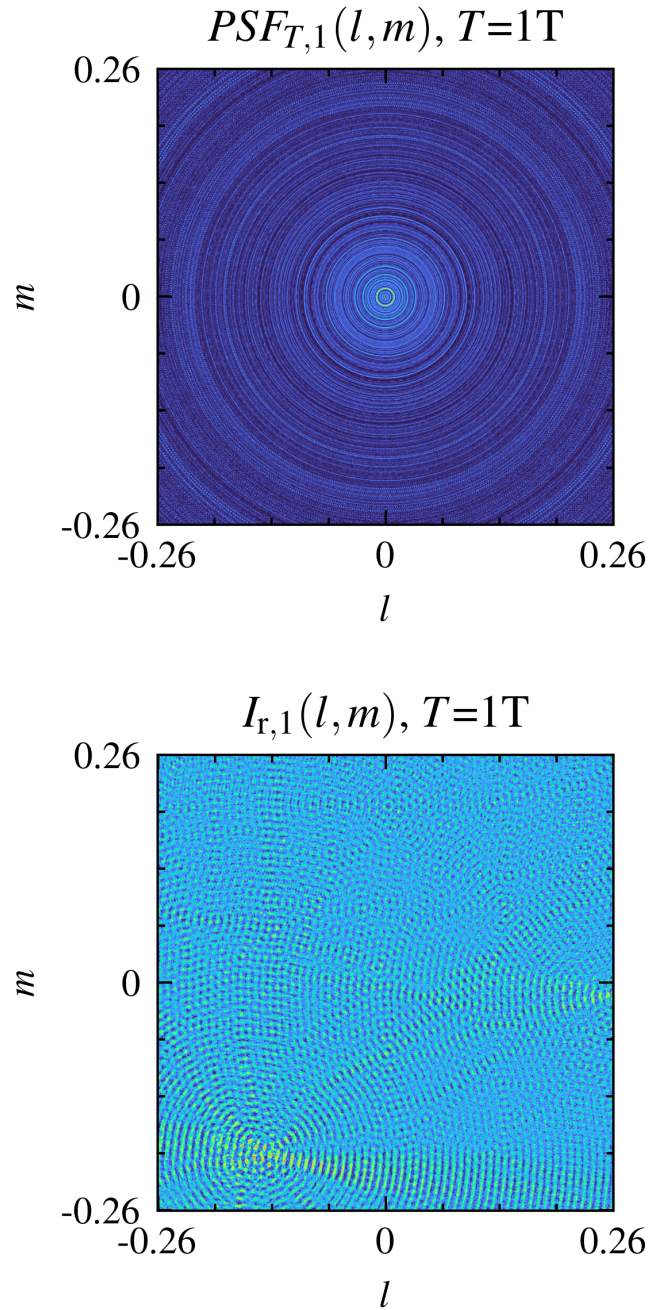
Figure 2.11 **Top**: The point spread function of the integrated sampling function due to the array trajectory shown in Figure 2.8 considering a single antenna at each of the nine platforms. **Bottom**: The scene intensity reconstruction of the reference scene intensity in Figure 2.7 using the integrated sampling function as a result of the coordinated trajectory with the consideration of a single antenna at each of the nine platforms. Both figures were reformatted for this dissertation and originally submitted to *IEEE Transactions on Geoscience and Remote Sensing*, March 2024.

$PSF_{T,1}(l,m)$ w/S.a., T=1T

$I_{r,1}(l,m)$ w/S.a., T=1T
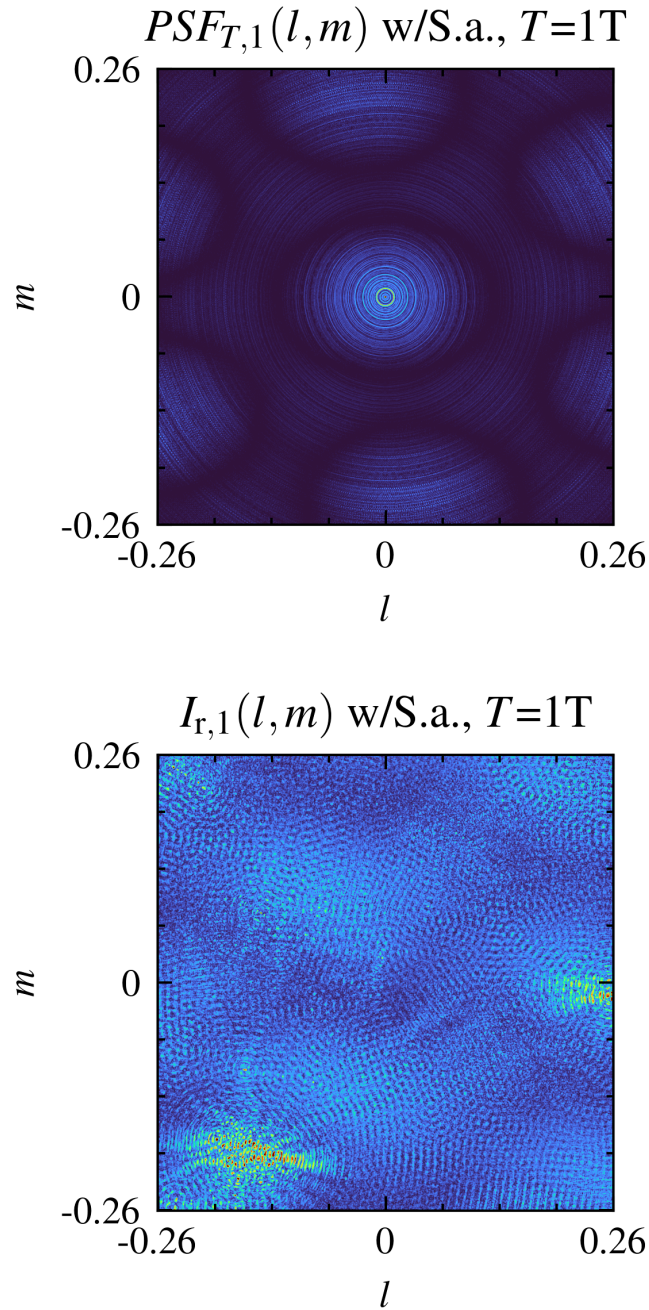
Figure 2.12 **Top**: The point spread function of the integrated sampling function due to the array trajectory shown in Figure 2.8 considering the three-element sub-array at each of the nine platforms. **Bottom**: The scene intensity reconstruction of the reference scene intensity in Figure 2.7 using the integrated sampling function as a result of the coordinated trajectory with the consideration of the three-element sub-array at each of the nine platforms. Both figures were reformatted for this dissertation and originally submitted to *IEEE Transactions on Geoscience and Remote Sensing*, March 2024.

$PSF_{T,2}(l,m)$, T=1T

$I_{r,2}(l,m)$, T=1T
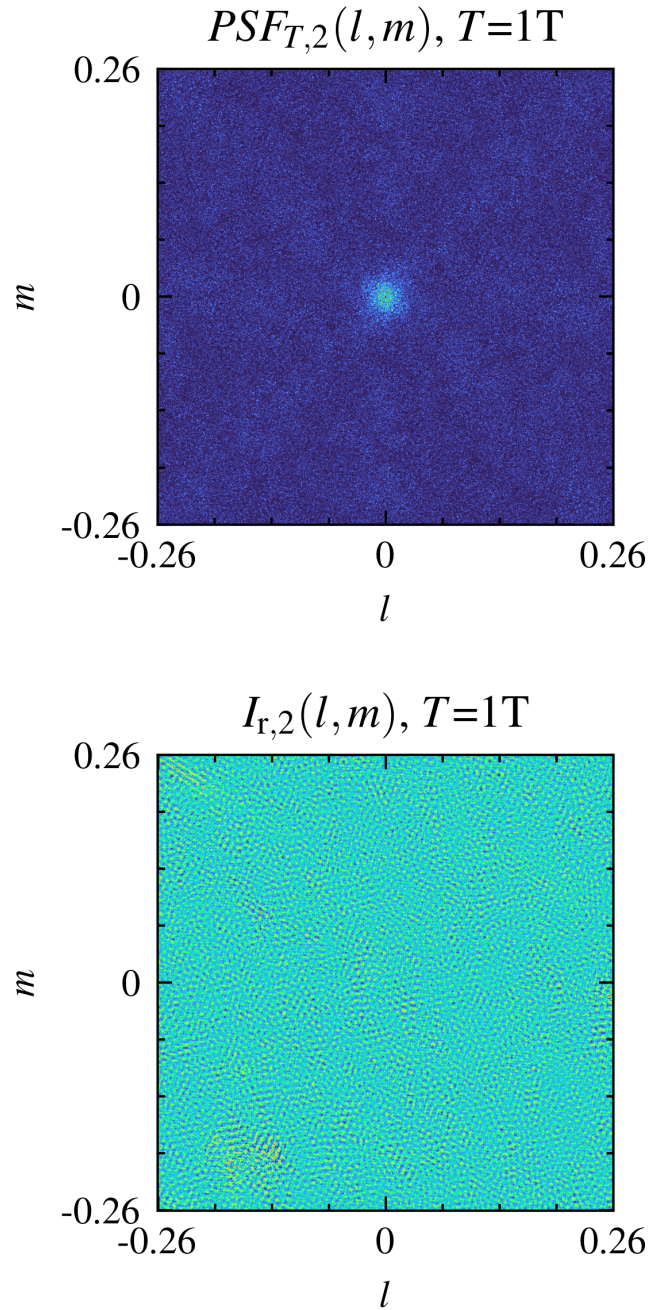
Figure 2.13 **Top**: The point spread function of the integrated sampling function due to the array trajectory shown in Figure 2.9 considering a single antenna at each of the nine platforms. **Bottom**: The scene intensity reconstruction of the reference scene intensity in Figure 2.7 using the integrated sampling function as a result of the coordinated trajectory with the consideration of a single antenna at each of the nine platforms. Both figures were reformatted for this dissertation and originally submitted to *IEEE Transactions on Geoscience and Remote Sensing*, March 2024.
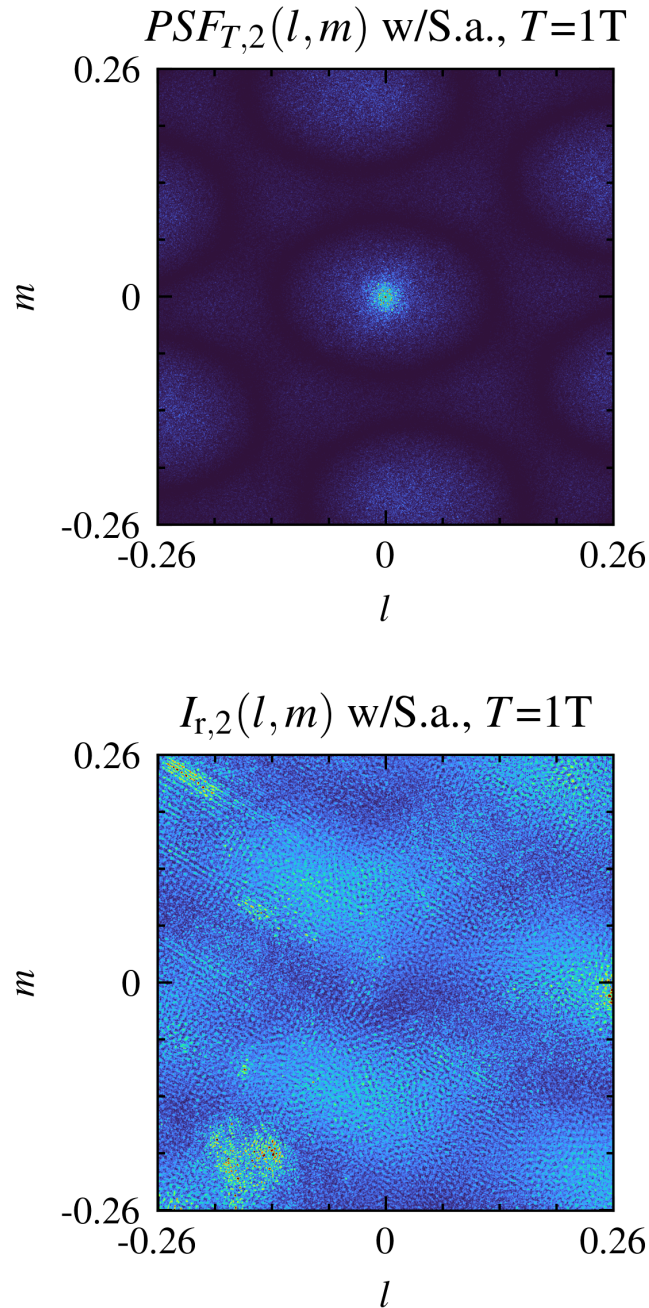
Figure 2.14 Top: The point spread function of the integrated sampling function due to the array trajectory shown in Figure 2.9 considering the three-element sub-array at each of the nine platforms. **Bottom**: The scene intensity reconstruction of the reference scene intensity in Figure 2.7 using the integrated sampling function as a result of the coordinated trajectory with the consideration of the three-element sub-array at each of the nine platforms. Both figures were reformatted for this dissertation and originally submitted to *IEEE Transactions on Geoscience and Remote Sensing*, March 2024.

$PSF_{T,2}(l,m)$, T=10T

$I_{r,2}(l,m)$, T=10T
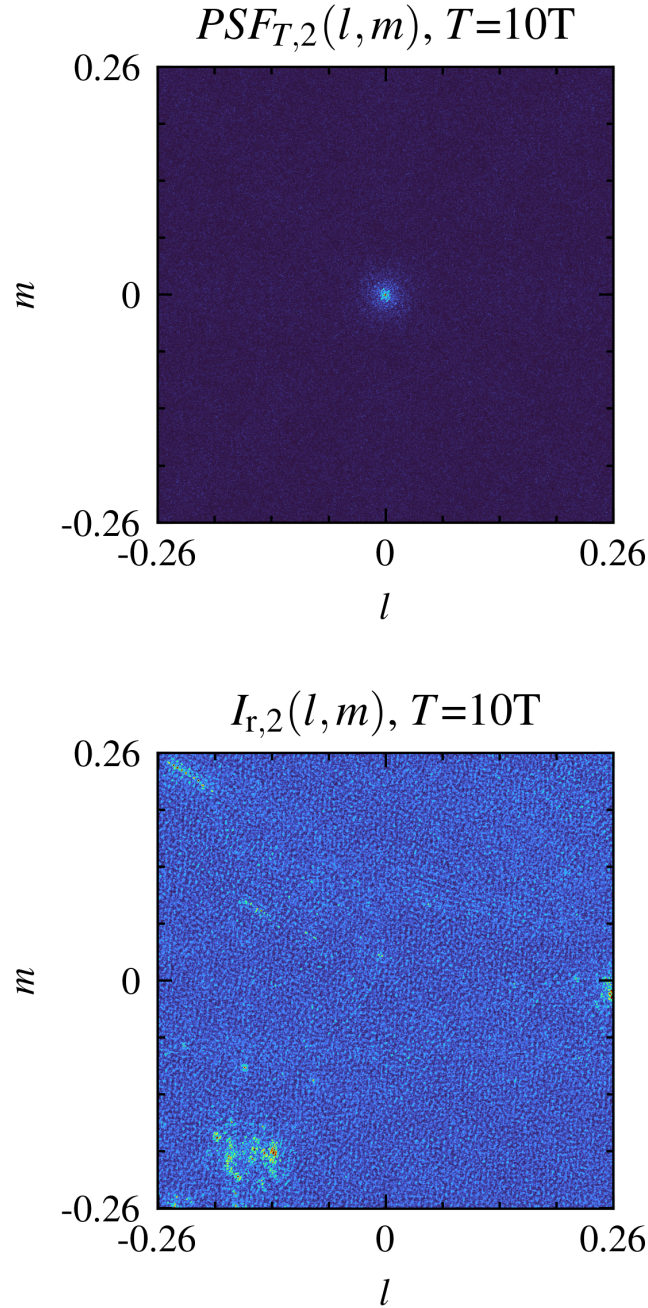
Figure 2.15 **Top**: The point spread function of the integrated sampling function due to the array trajectory shown in Figure 2.10 considering a single antenna at each of the nine platforms. **Bottom**: The scene intensity reconstruction of the reference scene intensity in Figure 2.7 using the integrated sampling function as a result of the coordinated trajectory with the consideration of a single antenna at each of the nine platforms. Both figures were reformatted for this dissertation and originally submitted to *IEEE Transactions on Geoscience and Remote Sensing*, March 2024.
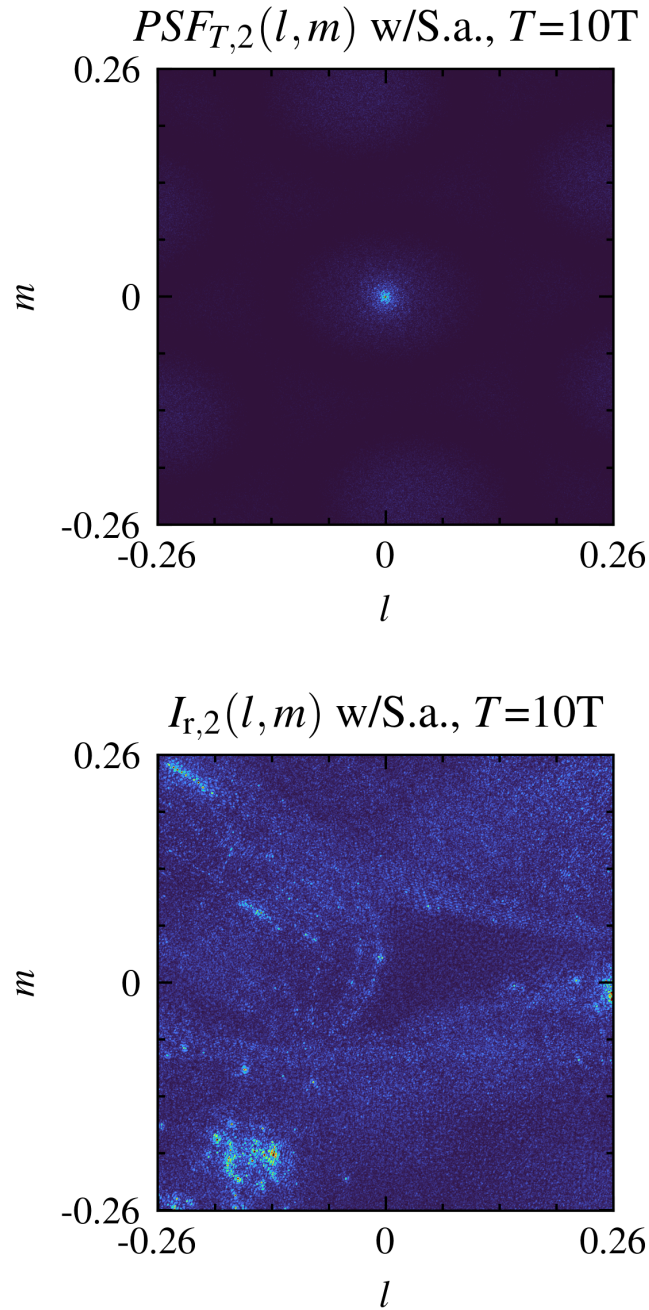
Figure 2.16 **Top**: The point spread function of the integrated sampling function due to the array tra-jectory shown in Figure 2.10 considering the three-element sub-array at each of the nine platforms. **Bottom**: The scene intensity reconstruction of the reference scene intensity in Figure 2.7 using the integrated sampling function as a result of the coordinated trajectory with the consideration of the three-element sub-array at each of the nine platforms. Both figures were reformatted for this dissertation and originally submitted to *IEEE Transactions on Geoscience and Remote Sensing*, March 2024.

As stated above, the coordinated trajectory will not yield additional sampling points due to its periodic nature and the random trajectory has the potential to improve scene intensity reconstruction by measuring potentially additional unique uv-points as the slow time duration increases. This is demonstrated in Figure 2.13–Figure 2.16 for the consideration with and without the sub-array. The PSFs are noise-like due to the random trajectory and that the level of surrounding artifacts is much lower when compared to the random trajectory scenarios considering T =1T. Furthermore, the scene intensity reconstruction is improved, and a perceptible recovery of almost the full reference scene is achieved when considering the random trajectory integrating over a duration of T =10T where each platform carries the assumed three-element sub-array. Regardless of the trajectory or slow time integration T, it is observed that when assuming a sub-array at each of the platforms, the additional sampled uv-points reduce the side-lobe artifacts of the PSF, hence improving the reconstruction scene intensity.

Aside from the perception-based evaluation of the scene reconstructions shown above, it is also necessary to quantitatively evaluate the performance of the various integrated sampling function scenarios considered above. Two metrics are used to compare the reconstruction quality against the reference scene intensity: the peak signal-to-noise ratio (PSNR) and the structural similarity index measure (SSIM).

PSNR is defined as the ratio between the maximum possible power of signal (i.e., reference image) and the mean squared error which can be due to imperfectly recovering of the original signal such as corrupting noise [64]. The PSNR has a unit of dB where an ideal recovery of the original signal has a PSNR of $+\infty$. The evaluated PSNR are reported in Table 2.1 for each of the reconstructed scene intensities in Figure 2.11–Figure 2.16 against the reference scene intensity in Figure 2.7 along with the improvement by comparing between the scenarios of a single antenna versus the three-element sub-array or the random trajectory for the two integrated sampling function duration of T =1T and T =10T. It can be seen that when the slow time integration is at T =1T, the coordinated trajectory performs better than the random trajectory with and without the sub-array consideration, and that implementing the sub-array achieves at least 13.7 dB improvement over

PSNR (dB)	Single	Sub-array	Improvement
Trj.1	12.7	26.4	13.7
Trj.2	10.5	25.1	***14.6***
Trj.2, $T =$10T	29.1	**35.9**	6.8
Trj.2 Improvement over $T =$10T	***18.6***	10.8	

Table 2.1 Peak signal-to-noise ratio (PSNR) comparison between the reference scene intensity in Figure 2.7 and each of the reconstructed scene intensity in Figure 2.11–Figure 2.16. Originally submitted to *IEEE Transactions on Geoscience and Remote Sensing*, March 2024.

the single antenna assumption for both trajectory approaches. Comparing the random trajectory approach with two slow time integration duration, we observe that the single antenna scenario achieved 18.6 dB improvement and the sub-array scenario achieved 10.8 dB improvement. Overall, the random trajectory approach with sub-array over a slow time duration $T=$10T achieved the best PSNR at 35.9 dB.

The SSIM is an image specific quality metric that considers the structural information, contrast, and luminance between the recover image and the reference image and has a range of $[-1, 1]$ where 1 represents identical recover and reference images, and 0 and -1 indicate no similarity and perfect anti-correlation, respectively [65]. Compared to PSNR, the SSIM enables further evaluation of how similar the scene reconstruction is to the reference image. We report the SSIM in Table 2.2 for each of the reconstructed scene intensity in Figure 2.11–Figure 2.16 against the reference scene intensity in Figure 2.7 along with the improvement by comparing between the scenarios of a single antenna versus the three-element sub-array or the random trajectory for the two integrated sampling function duration of $T =$1T and $T =$10T. Similar to the observation made in PSNR (Table 2.1), the coordinated trajectory approach demonstrated higher SSIM than the random trajectory regardless of the sub-array assumption. Furthermore, both sub-array scenarios at slow time duration $T =$1T demonstrated improvement above 0.44. Comparing the random trajectory approach with two slow time integration duration, we observe that the single antenna scenario achieved 0.60 improvement and the sub-array scenario achieved 0.44 improvement. Overall, the random trajectory approach with sub-array over a slow time duration $T =$10T achieved the best SSIM at 0.93.

SSIM	Single	Sub-array	Improvement
Trj.1	0.08	0.58	***0.50***
Trj.2	0.05	0.49	0.44
Trj.2, T =10T	0.65	**0.93**	0.28
Trj.2 Improvement over T =10T	***0.60***	0.44	

Table 2.2 Structural similarity index measure (SSIM) comparison between the reference scene intensity in Figure 2.7 and each of the reconstructed scene intensity in Figure 2.11–Figure 2.16. Originally submitted to *IEEE Transactions on Geoscience and Remote Sensing*, March 2024.

From both the reported PSNR and SSIM evaluation, it is evident that for the random trajectory approach, the improvement by allowing the single antenna assumption over a longer slow time duration outperforms the assumption of implementing the three-element sub-array with unchanged slow time duration (i.e., PSNR: 18.6 versus 14.6 and SSIM: 0.60 versus 0.44). Furthermore, we report progression of the PSNR, SSIM, and the number of unique uv-points sampled by the integrated sampling function at different time T in Figure 2.17. For the random trajectory with sub-array, it is observed that both PSNR and SSIM converge as T increases suggesting that slow time duration longer than T =10T is unlikely to achieve significant improvement. While it seems obvious that the random trajectory approach with sufficient slow time integration duration is better at reconstructing the measured scene intensity, coordinated trajectory approaches can be useful in certain use cases and provide a more cost-effective remote sensing approach. For example, the decision to reconstruct specific ground scene intensities might not be necessary unless detection of certain spatial attributes such as man-made artificial structures like buildings and roads where their sharp edges generate spatial frequency responses that extend over a broad spatial frequency bandwidth but confined to a narrow angular range are recognized, which can be captured by a set of concentric rings of integrated sampling function due to a coordinated array trajectory as will be discussed in the subsequent chapter.
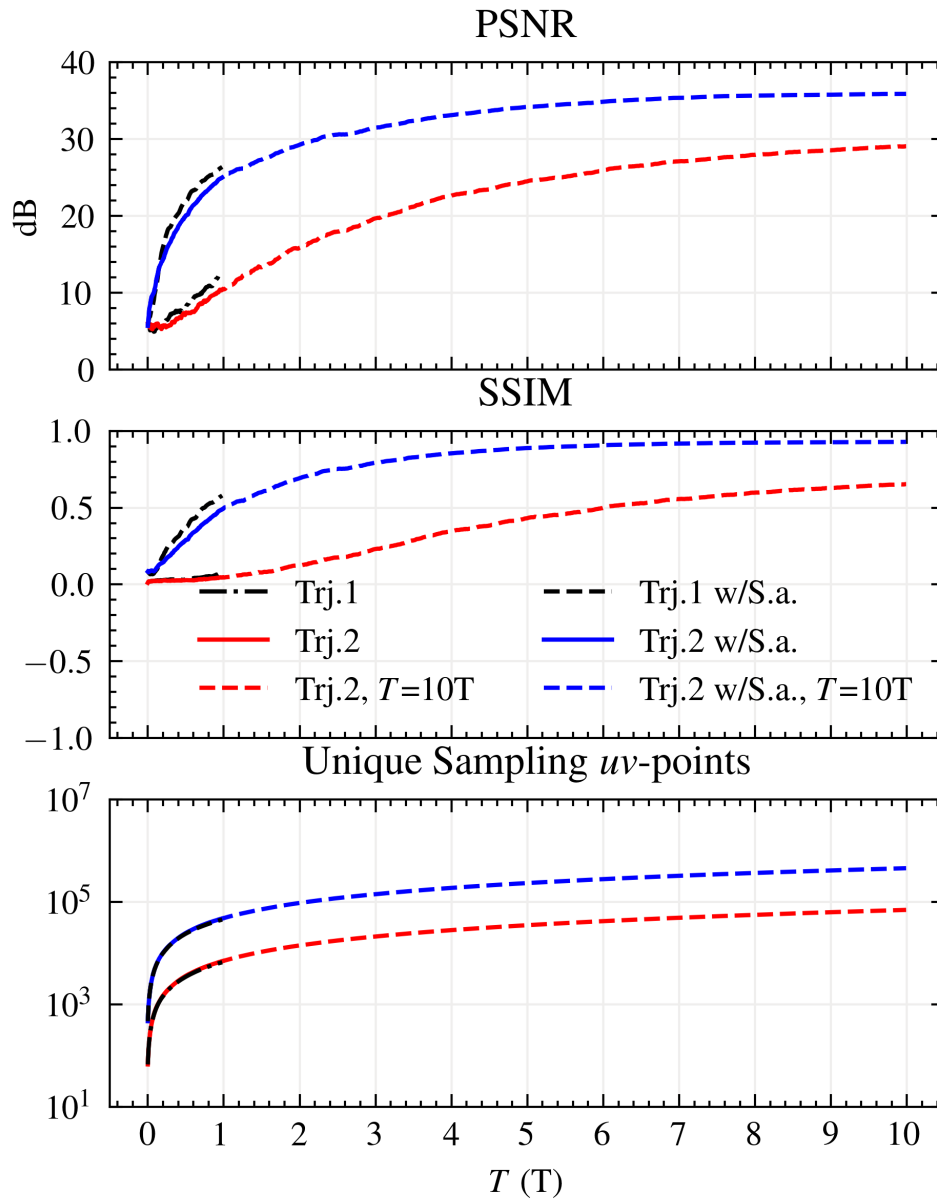
Figure 2.17 **Top**: Peak signal-to-noise ratio (PSNR) between the reference scene intensity in Figure 2.7 and the reconstructed scene intensity due to the integrated sampling function over the course of slow time duration T. **Center**: Structural similarity index measure (SSIM) between the reference scene intensity in Figure 2.7 and the reconstructed scene intensity due to the integrated sampling function over the course of slow time duration T. **Bottom**: Number of measured unique uv-points due to the integrated sampling function over the course of slow time duration T. Originally submitted to *IEEE Transactions on Geoscience and Remote Sensing*, March 2024.

CHAPTER 3

ENABLING IMAGELESS REMOTE SENSING USING ROTATIONAL DYNAMIC ANTENNA ARRAY

In this chapter, I discuss a specific use case where a correlation pair can be implemented in conjunction with rotational array dynamics such that it generates an integrated sampling function taking the form of a ring (i.e., ring filter) that covers the full two-dimensional (2D) spatial Fourier space. This approach enables an imageless remote sensing technique such that no image of the measured scene is recovered. I first present a remote sensing scenario where the ring-filtered spatial Fourier responses enable ground scene classification between scenes containing man-made structures such as road and bridges and scenes that exhibit naturally occurring characteristics like vegetation. Man-made, artificial structures such as buildings and roads are generally characterized by sharp edges, which generate spatial frequency responses that are confined to a narrow angular range but extend over a broad spatial frequency bandwidth. These artifacts can be detected by generating a ring-shaped filter in the Fourier domain, which can be obtained through the novel design of a linear antenna array with rotational dynamics. In addition, I present the design and implementation of an experimental setup of a two-element rotational dynamic antenna array and demonstrate the concept of capturing the sharp edge associated with spatial Fourier responses.

This chapter is, in part, a reprint or adaptation of materials with permission in "Analysis of Imageless Ground Scene Classification Using a Millimeter-Wave Dynamic Antenna Array" published in *IEEE Transactions on Geoscience and Remote Sensing* [66] © 2022 IEEE, "A 75-GHz Dynamic Antenna Array for Real-Time Imageless Object Detection via Fourier Domain Filtering" published in *2022 IEEE/MTT-S International Microwave Symposium* [67] © 2022 IEEE, "Imageless Contraband Detection Using a Millimeter-Wave Dynamic Antenna Array via Spatial Fourier Domain Sampling" submitted to the *IEEE Access*, April 2024, and "A Remote Sensing Approach Using Dynamic Distributed Interferometric Array" to be submitted to the *IEEE Transactions on Geoscience and Remote Sensing*, March 2024.

3.1 Techniques of Scene Information Classification

Classification of the scene information is important in a broad range of civilian and military remote sensing applications. Due to the abundance of information obtained from remote sensing systems, both from satellites and aerial platforms, methods of rapidly classifying scenes are of primary interest so that relevant information can be efficiently processed. Various sensing applications, from sensing the Earth surface via aerial platforms to distant security imaging of people, require the differentiation between naturally occurring and artificial structures/objects [68, 39, 69, 70, 40]. To effectively determine whether man-made structures/objects exist in the scene of interest, image-based classifiers are typically implemented where the classification performance is dependent on the measurement, signal processing, and the selected classifier in combination with the evaluated features. Each of the stages contribute to the overall cost in terms of hardware and the associated computational complexity. Interestingly, images often contain more than the required minimum information for effective classification results, which means unnecessary resources can be committed to the collection and processing of redundant data. Understanding this phenomenon, the designs associated with both the measurements (hardware and acquisition time) and the processing can be optimized to reduce system complexity and cost by eliminating resources that would have been designed for unnecessary tasks.

Typically, remote scene classification is approached separately from the data acquisition process. The remote sensing system acquires data and forms a set of images, which are then passed to a classification algorithm that operates on the image data. Many works have focused on classifying large numbers of images using image processing approaches. Various features can be obtained from images, such as target sizes, geometries, and/or edges of structures/objects, which can be leveraged individually or in combination to perform classification on the imaged scene [71]. Recently, machine-learning based techniques have been applied to this approach to address the sheer amount of data that must be processed [72, 73, 74, 75]. Such approaches, however, necessitate full image reconstruction for every scene of interest, which leads to a significant amount of data that must be acquired, transferred, and processed before classification takes place, which can strain resources in

hardware, communications, and computational processing.

In the subsequent sections, I investigate the use of a novel approach to obtain a small subset of the spatial frequency information in a scene using a rotationally dynamic millimeter-wave antenna array and demonstrate the ability to classify scenes containing man-made structures with only a small amount of data compared to a full imaging system. The approach only samples a ring of spatial frequencies in the Fourier transform domain of the scene spatial intensity, capturing the unique spatial frequency signatures of man-made objects. In contrast to other approaches, the presented technique does not sample sufficient information to reconstruct a full image; however, this leads to a significant reduction in the amount of information necessary for scene classification, and furthermore may be beneficial for privacy-preserving applications. A dynamic antenna array concept where a two-element interferometric antenna array was designed with rotational spatio-temporal dynamics to acquire filtered spatial frequency domain information [76, 77, 78] which focuses on features that are particular to man-made shapes in the scenes. The concept uses dynamic rotational motion of the array, which is far simpler than typical mechanically-steered imaging systems, and thus assumes that the scene is quasi-stationary during the measurement. I will also discuss the design of a millimeter-wave antenna array for obtaining filtered spatial frequency information from ground scenes and evaluate the classification capabilities using filtered spatial frequency data from a publicly available microwave remote sensing data set.

3.2   Artifacts in the Spatial Fourier Domain

Scene classification can operate on the reconstructed intensity $I_\mathrm{r}(l, m)$ via image processing technique as described in the previous chapters. The approach presented in this chapter, however, is to operate directly on the sampled visibility $V_\mathrm{s}(u, v)$ without reconstructing the image, and furthermore with extraordinarily little spatial frequency information. Imageless classification via the dynamic antenna array concept is based on capturing spatial Fourier features present in the scene. In particular, the objective is to distinguish remote sensing images of non-natural scenes (NNS) comprising man-made structures such as roadways and/or bridges from remote sensing images of natural scenes (NS) containing only natural landscapes. Man-made structures generally

have sharp edges, which are infrequent in natural scenes and that manifest strong spatial frequency signals that are localized to spatial frequency angles orthogonal to the edge direction in the spatial domain and extend radially outward over a broad spatial frequency bandwidth. Examples of NS and NNS radar images from [60] with a spatial field-of-view (FOV) of $1000\,\text{m}$ by $1000\,\text{m}$ and a resolution of $1\,\text{m/pixel}$ are shown in Figure 3.1. Furthermore, examples of the visibility for one NS and one NNS are shown in the top of Figure 3.2 along with their corresponding visibility in the bottom of Figure 3.2. Note that the visibility is not generally affected by topology since range information is not obtained. As observed in Figure 3.2, the visibility of the NS exhibits smoother spatial frequency content whereas the NNS visibility presents strong while discrete components that are orthogonal to the direction of the sharp edges.
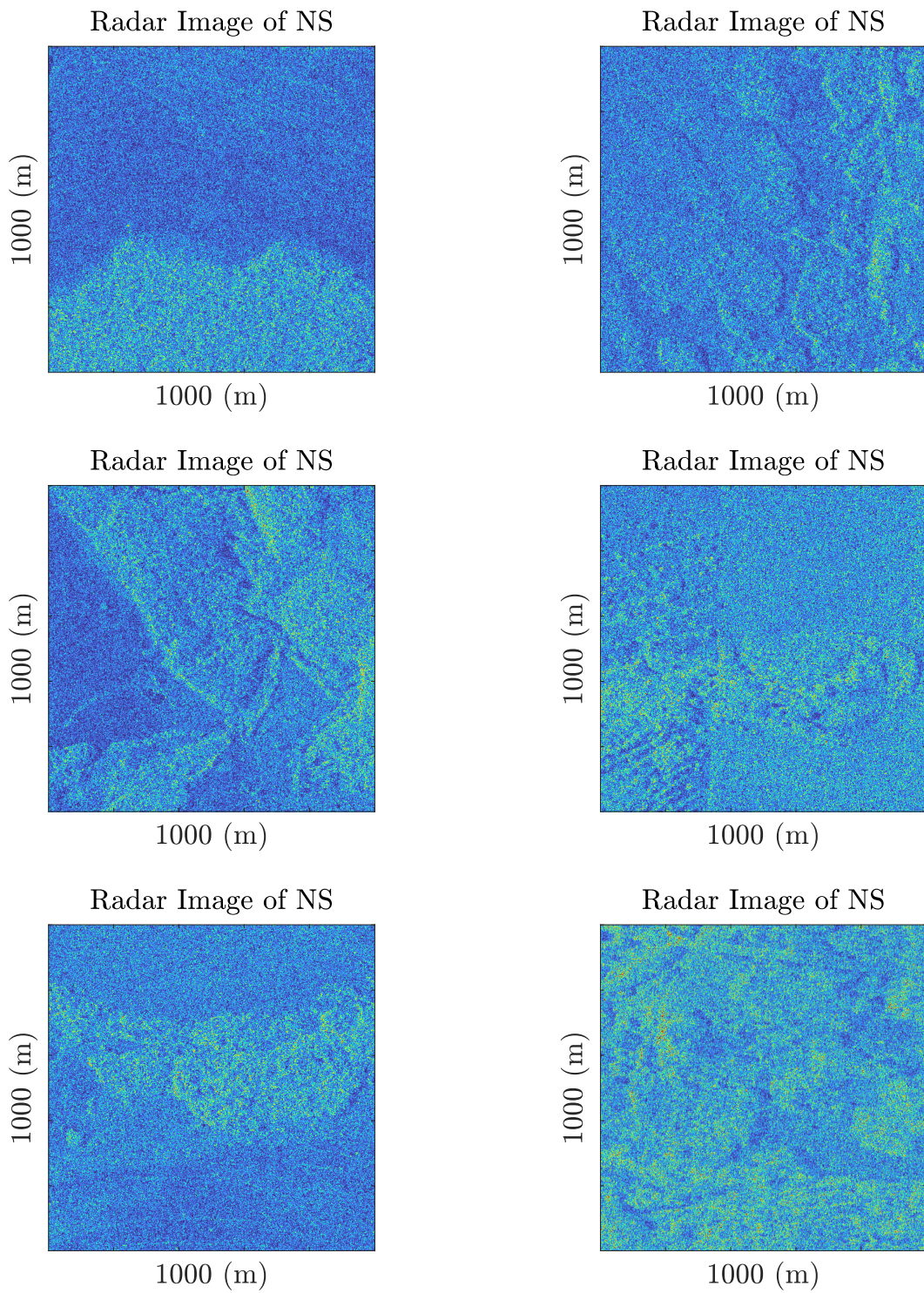
Figure 3.1 Processed radar images from [60] with a field-of-view of 1000 m by 1000 m and a resolution of 1 m/pixel. The top six figures represent examples of natural scenes (NS) and the bottom six figures represent examples of non-natural scenes (NNS). Image [66] © 2022 IEEE.

Figure 3.1 (cont'd)

Radar Image of NNS

1000 (m)

1000 (m)

Radar Image of NNS

1000 (m)

1000 (m)

Radar Image of NNS

1000 (m)

1000 (m)

Radar Image of NNS

1000 (m)

1000 (m)

Radar Image of NNS

1000 (m)

1000 (m)

Radar Image of NNS

1000 (m)

1000 (m)
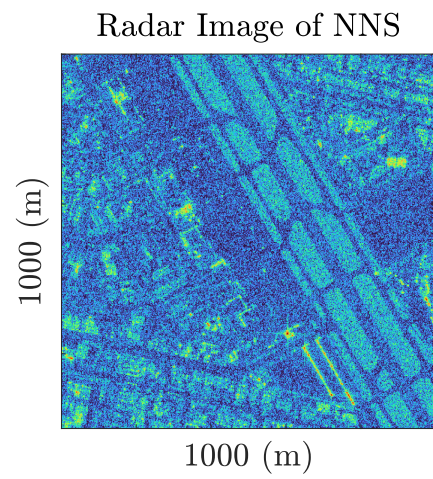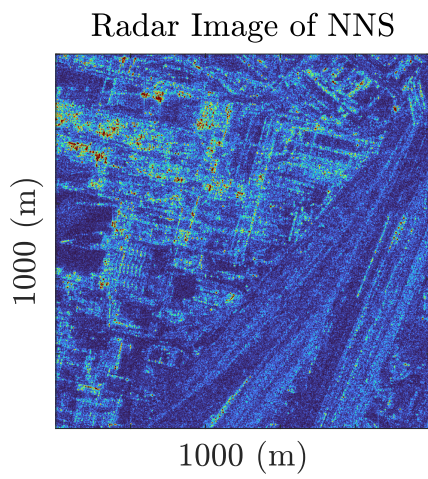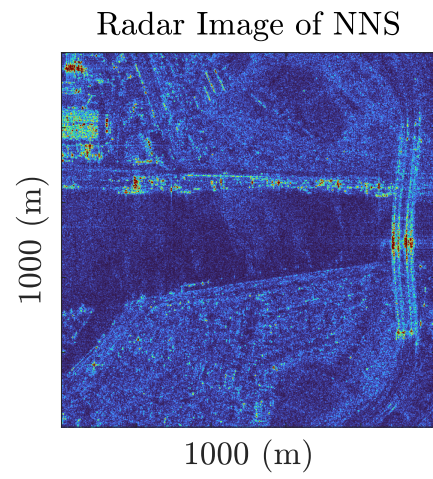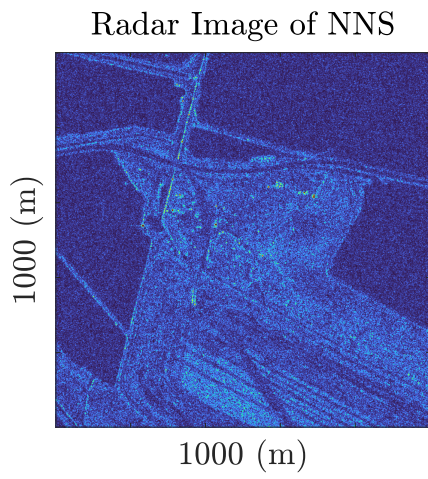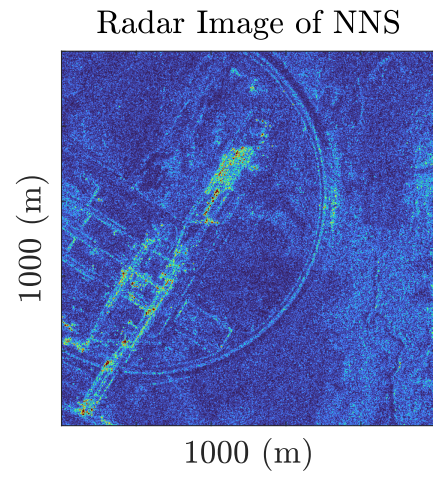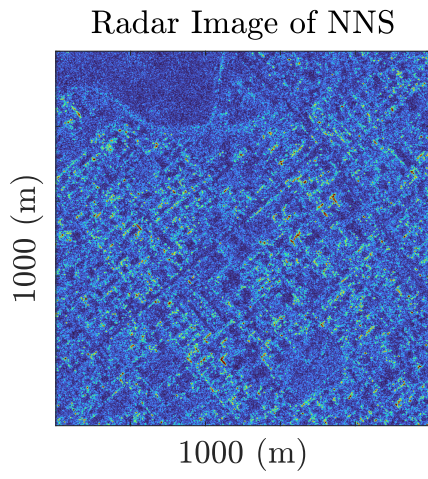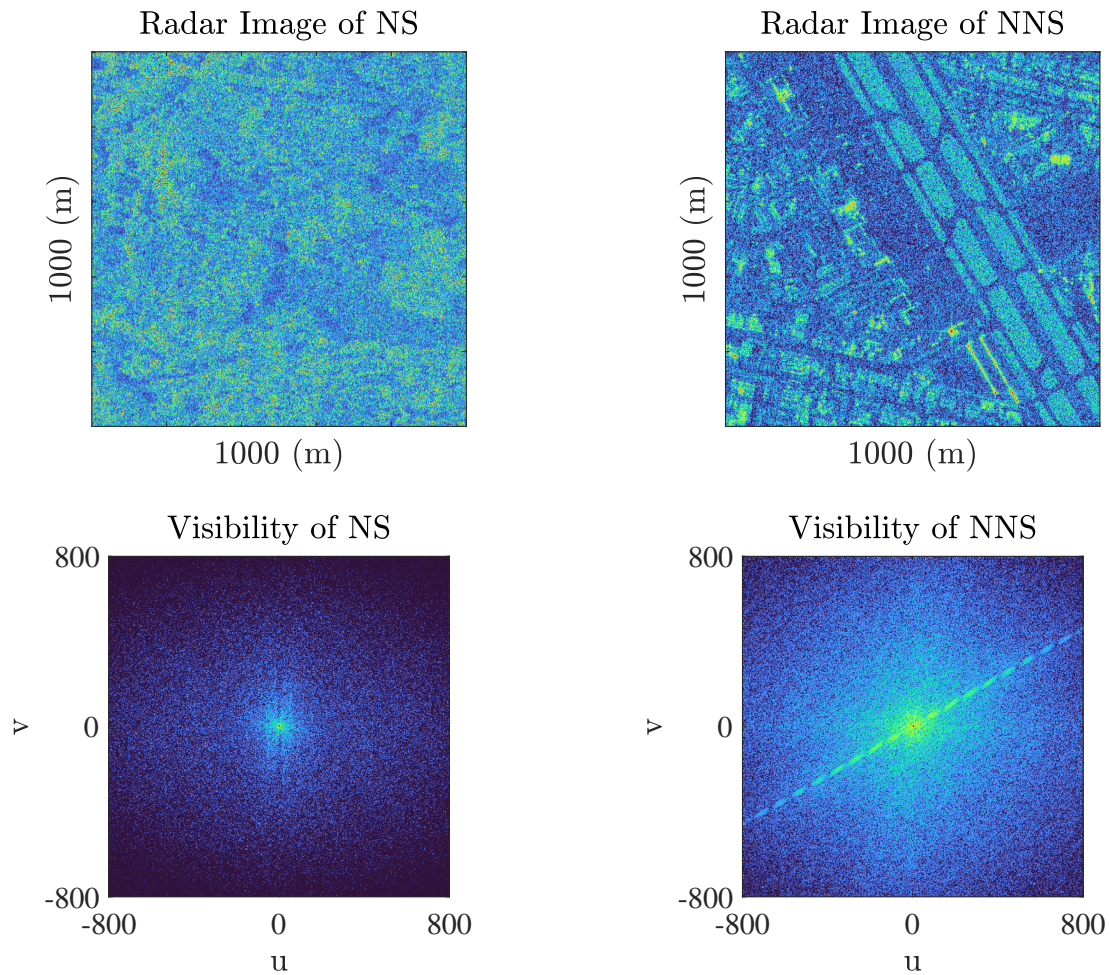
Figure 3.2 **Top**: Microwave radar images of a natural scene of a vegetation region of Cushing (left), Oklahoma and a non-natural scene of highway and building cluster from the region of Phoenix, Arizona (right). **Bottom**: The visibility of the corresponding scene above. Data from [60]. Image [66] © 2022 IEEE.

3.3 The Ring Filter

Since the spatial frequency features discussed above are largely discrete and directional, they enable detection with only a small subset of the available visibility information. One such way is to generate a ring-shaped sampling function in the spatial frequency domain [76], shown in Figure 3.3, where a two-element dynamic array is rotated regarding its centroid covering a spatial frequency bandwidth over the full 360° of the uv-plane. This ring-shaped spatial frequency sampling function integrated over the slow time duration T is referred to as the "ring filter". Since the ring filter covers the full angle of rotation, discrete spatial frequency features that extend radially outward can be captured. Note that this approach only requires the correlation pair to rotate 180° due to the Hermitian symmetric nature of the visibility given that the scene intensity function is of real value, and that the direction of rotation is arbitrary. As discussed in [76], a design may be implemented by rotating an array on an aerial vehicle's rotor blades where the two antennas always remain co-polarized enabling the dynamic array to operate either actively or passively as discussed earlier.

The ring filter concept based on the dynamic antenna array combines the interferometric technique and rotational array dynamics to sparsely sample spatial frequency information. Recall that interferometric imaging systems co-process the signals received at elements in a sparse array to generate high-resolution imagery with a fraction of the aperture area required in typical imaging systems. Pairwise cross-correlation of the received signals generates spatial frequency samples (Fourier-domain information) of the scene to be reconstructed [13, 32]. Intuitively, one can recognize that the smallest unit of a typical interferometric array is a two-element array (Figure 3.4, bottom left) where the spatial frequency being sampled corresponds to a far-field sinusoidal dependent on the baseline separation D_λ between the two antennas and the orientation formed between the baseline and the system's horizontal plane. A ring-shaped spatial frequency filter can be synthesized by dynamically rotating the array at a fixed baseline [76] as demonstrated in the bottom right of Figure 3.4 shown at three slow time instances. As shown in the upper right corner of Figure 3.4, boxed by solid orange and dash-dot magenta, sharp edges in the spatial domain manifest radially extending Fourier artifacts that are orthogonal to the edge direction. Such Fourier artifacts can be

easily sampled by utilizing array dynamics, assuming the measured scene is relatively static, where the achieved baseline $D_\lambda(T)$ depends on both the antenna placement and the array trajectory. The dynamic antenna array shown above is a correlation pair rotating with respect to their centroid, synthesizing a ring-shaped sampling function over a rotational trajectory of $180°$ that can effectively capture the radially extending Fourier artifacts in the uv-plane.

The array trajectory generating the ring filter can be considered as a coordinated trajectory approach as discussed in the previous chapter. Following the formulation of the coordinated trajectory function defined in (2.19) and (2.20), for a two-element linear interferometric pair (denoted by subscripts 1 and 2) residing on the measurement plane (xy-plane) co-rotating with respect to their centroid, the trajectory functions that enable the ring filter can be described by

$$\overrightarrow{\mathrm{TRJ}}_{\mathrm{ring},n}(T) = \vec{p}_{\mathrm{ring},n}(T) + \overrightarrow{\mathrm{trj}}_{\mathrm{ring},n}(T) \tag{3.1}$$

for the n-th antennas and that

$$
\begin{aligned}
\vec{p}_{\mathrm{ring},1}(T) &= 0 \\
\vec{p}_{\mathrm{ring},2}(T) &= 0 \\
\overrightarrow{\mathrm{trj}}_{\mathrm{ring},1}(T) = \overrightarrow{\mathrm{TRJ}}_{\mathrm{ring},1}(T) &= \hat{x}\tfrac{D_\lambda}{2}\cos\left[\Theta_n(T)\right] \\
&\quad + \hat{y}\tfrac{D_\lambda}{2}\sin\left[\Theta_n(T)\right] \\
\overrightarrow{\mathrm{trj}}_{\mathrm{ring},2}(T) = \overrightarrow{\mathrm{TRJ}}_{\mathrm{ring},2}(T) &= -\hat{x}\tfrac{D_\lambda}{2}\cos\left[\Theta_n(T)\right] \\
&\quad - \hat{y}\tfrac{D_\lambda}{2}\sin\left[\Theta_n(T)\right]
\end{aligned}
\tag{3.2}
$$

where D_λ is the separation between the two antennas and that the factor $\frac{1}{2}$ accounts for the definition that the two antennas co-rotate with respect to their centroid. Note that the quantity $D_\lambda(T)$ in Figure 3.4 is the electrical baseline (i.e., both separation and orientation) over the slow time dimension T and that the quantity D_λ in (3.1) only describes the separation between the two antennas in wavelength.

65

Dynamically Rotated Correlation Pair

y (λ)

x (λ)

D_λ

Physical separation

Generated Ring Filter

v (cycles/rad)

u (cycles/rad)

$2D_\lambda$

Center frequency

Antenna bandwidth
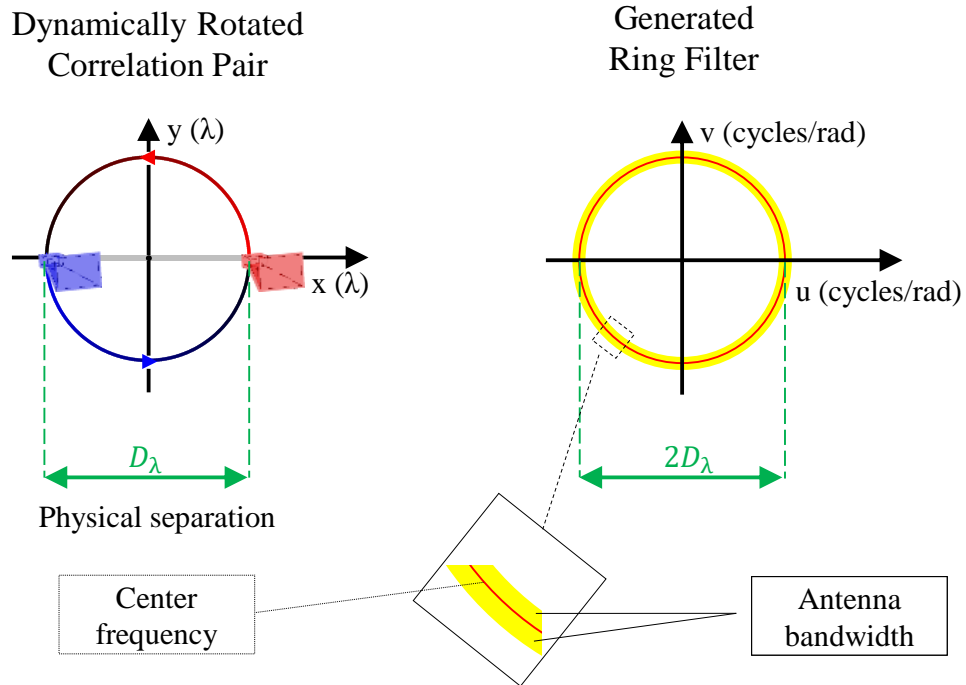
Figure 3.3 Example of utilizing a dynamically rotated correlation pair to synthesize a spatial frequency ring filter. A physical separation of D_λ will yield a ring filter with a radius of D_λ cycles/rad. The radius of the ring filter is also dependent on the center frequency (red circle) and the extending coverage of spatial frequency bandwidth is dependent on the antenna bandwidth (yellow). A 180° rotation from the correlation pair covers the full 360° span on the *uv*-plane indicating that no reset is required and that the continuing rotational dynamics will synthesize additional ring filters. Direction of rotation is a design choice. Image [66] © 2022 IEEE.
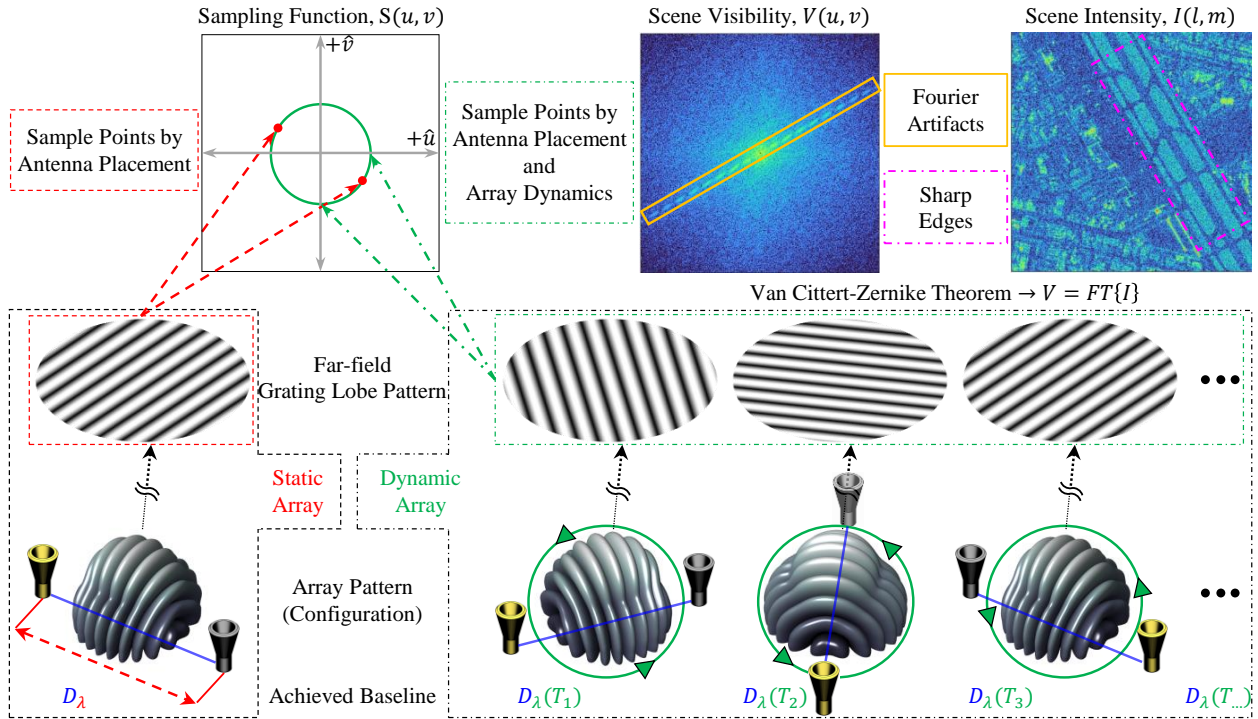
Figure 3.4 Overview of the interferometric technique and the comparison between static and dynamic antenna array. The smallest element of an interferometric array is a correlation pair which is shown by the yellow and gray conical horn antennas. Conventional interferometric arrays are considered static where the array pattern of a given correlation pair within the array is defined by antenna placement achieving a baseline, D_λ, and a far-field grating lobe pattern that corresponds to particular sampling points in the Fourier domain. The sampling Fourier-domain space is also known as the scene visibility, $V(u,v)$, which is the two-dimensional Fourier transformation of the scene intensity, $I(l,m)$, when satisfying the Van Cittert-Zernike theorem [79, 32] where the fields radiated from the measured scene is considered spatio-temporally incoherent. The visibility is the collection of all spatial frequency information of the measured scene which are related to particular spatial/physical features. As shown in the upper right corner, boxed by solid orange and dash-dot magenta, sharp edges in the spatial domain manifest radially extending Fourier artifacts that are orthogonal to the edge direction. Such Fourier artifacts can be easily sampled by utilizing array dynamics, assuming the measured scene is relatively static, where the achieved baseline $D_\lambda(T)$ depends on both the antenna placement and the array trajectory. The dynamic antenna array shown above is a correlation pair rotating with respect to their centroid, synthesizing a ring-shaped sampling function over a rotational trajectory of 180° that can effectively capture the radially extending Fourier artifacts in the uv-plane. Data source for Scene Intensity [60]. Originally submitted to *IEEE Access*, April 2024.

3.3.1 Direct Classification in the Spatial Fourier Domain

Previously in [76], a single ring filter of baseline 761λ was heuristically determined and subsequently fed to a decision-boundary-based classifier. The baseline decision not only considered the spatial-spectral signal length near 761 rad^{-1} but also considered a notional implementation of a 40 GHz system on a medium-sized unmanned aerial vehicle (UAV) [80] matching the altitude and physical separation requirement of the single correlation pair that is close to a typical rotor blade specification with an end-to-end length or wingspan of 5 m–10 m, amenable to implementation on industrial-grade UAV helicopters like the StarLite-2A [81]. In this work, a wider range of baselines are considered to investigate the influence of baseline on the ring filter's performance. With a maximum baseline of 761λ as considered in [76], seven additional ring filters varied in 100λ baseline difference are considered that are supported by an antenna separation in 50λ increment from their centroid to account for wider spatial frequency coverage. The baselines were 61λ, 161λ, 261λ, 361λ, 461λ, 561λ, 661λ, and 761λ. Note that at 40 GHz, these require physical separation is less than the rotor blade assumption above and that the occlusion from the UAV body is not considered here. Furthermore, an antenna beamwidth of 3% is assumed across all considered ring filters. For a 40 GHz (7.5 mm) system, the effective electrical baselines due to the beamwidth, 39.4 GHz–40.6 GHz (7.6 mm–7.4 mm), account for the spatial frequency bandwidth coverage as shown in Figure 3.3 and summarized in Table 3.1.

Physical Baseline	-1.5%	+1.5%
61λ	60λ	62λ
161λ	159λ	163λ
261λ	257λ	265λ
361λ	356λ	366λ
461λ	454λ	468λ
561λ	553λ	569λ
661λ	651λ	671λ
761λ	751λ	771λ

Table 3.1 Electrical baselines assuming 40 GHz and 3% antenna beamwidth. Table [66] © 2022 IEEE.

Microwave ground images from [60] were selected to facilitate the classification analyses. Data were selected to form a set containing 2076 ground scene radar images where 1038 were NS and 1038 were NNS. The data were processed to share a common resolution of 1 m/pixel. Furthermore, the assumed 40 GHz millimeter-wave frequency yields resolution commensurate with the data set. The data were then processed via two-dimensional (2D) Fourier transform of the radar images and subsequently filtered using the eight ring filters described above where it is assumed that the van Cittert-Zernike requirement is satisfied. Subsequently, the data were evaluated using a decision-boundary classifier operating on a single ring-filtered output. It is assumed that the measuring interval in the slow time dimension is uniform, hence, the sampled visibility based on the ring filter can also be considered as uniformly sampled over the rotated angle as covered by the generating trajectory as described in (3.1) and (3.2). By mapping the filtered visibility sample to the associated angle, a one-dimensional vector $S_s(\gamma)$ which is the averaged response (over the antenna bandwidth) spanning across the 360° of the uv-plane, where γ is the angle with respect to the positive u-axis, and is given by

$$S_s(\gamma) = \frac{\sum\limits_{r_{\text{ring}}=r_{\text{L}}}^{r_{\text{H}}} V_s(r_{\text{ring}} \cos(\gamma), r_{\text{ring}} \sin(\gamma))}{r_{\text{H}} - r_{\text{L}}} \tag{3.3}$$

where V_s is the ring-filtered visibility from the dynamic antenna array, r_{ring} is the radius of the ring filter that corresponds to the antenna pair's electrical baseline; and $r_{\text{H}} - r_{\text{L}}$ is the spatial frequency bandwidth due to antenna bandwidth as illustrated in Figure 3.3. Examples of the ring-filtered responses using (3.3) for a ring filter generated with a baseline of 161λ are shown in Figure 3.5 for the real data of Figure 3.2.
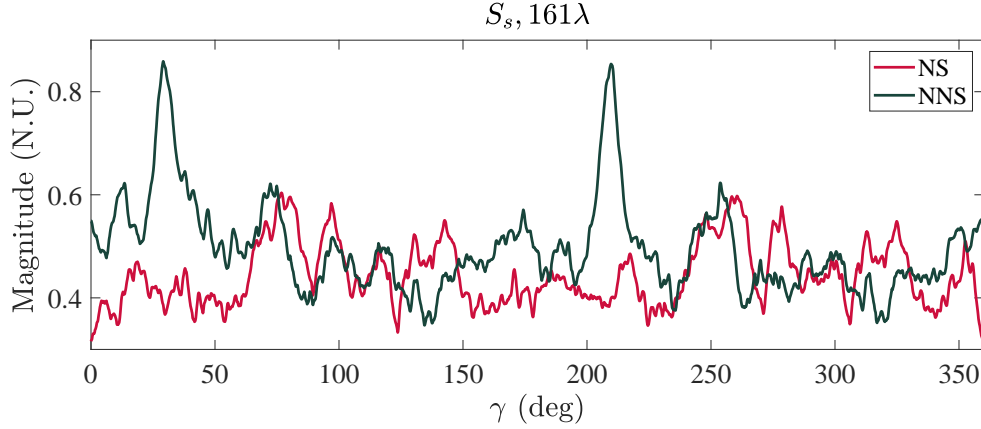
Figure 3.5 Example of ring-filtered responses, $S_s(\gamma)$ based on the example visibilities shown in Figure 3.2 using a baseline of 161λ over the entire $360°$ *uv*-plane. N.U.: Normalized Units. Image [66] © 2022 IEEE.

Subsequently, the vector $S_s(\gamma)$ is differentiated with respect to γ yielding

$$S'_s(\gamma) = \frac{d}{d\gamma} S_s(\gamma) \tag{3.4}$$

which yields the rate of change of the filtered data, which better captures the discrete spatial frequency components. Lastly, the mean of $S'_s(\gamma)$,

$$\mu S'_s = \text{mean}\{S'_s(\gamma)\} \tag{3.5}$$

is calculated to generate a specific pattern for each of the 2076 sets of data thus enabling a decision boundary to be defined to differentiate between NS and NNS. Furthermore, the distributions of the derived patterns for NS and NNS are shown in Figure 3.6 for all eight considered baselines/ring filters. It is observed that an apparent separation between NS (dark red) and NNS (dark green) exist which suggest that a threshold, or decision boundary, can be determined to differentiate the two classes of ring-filtered patterns.
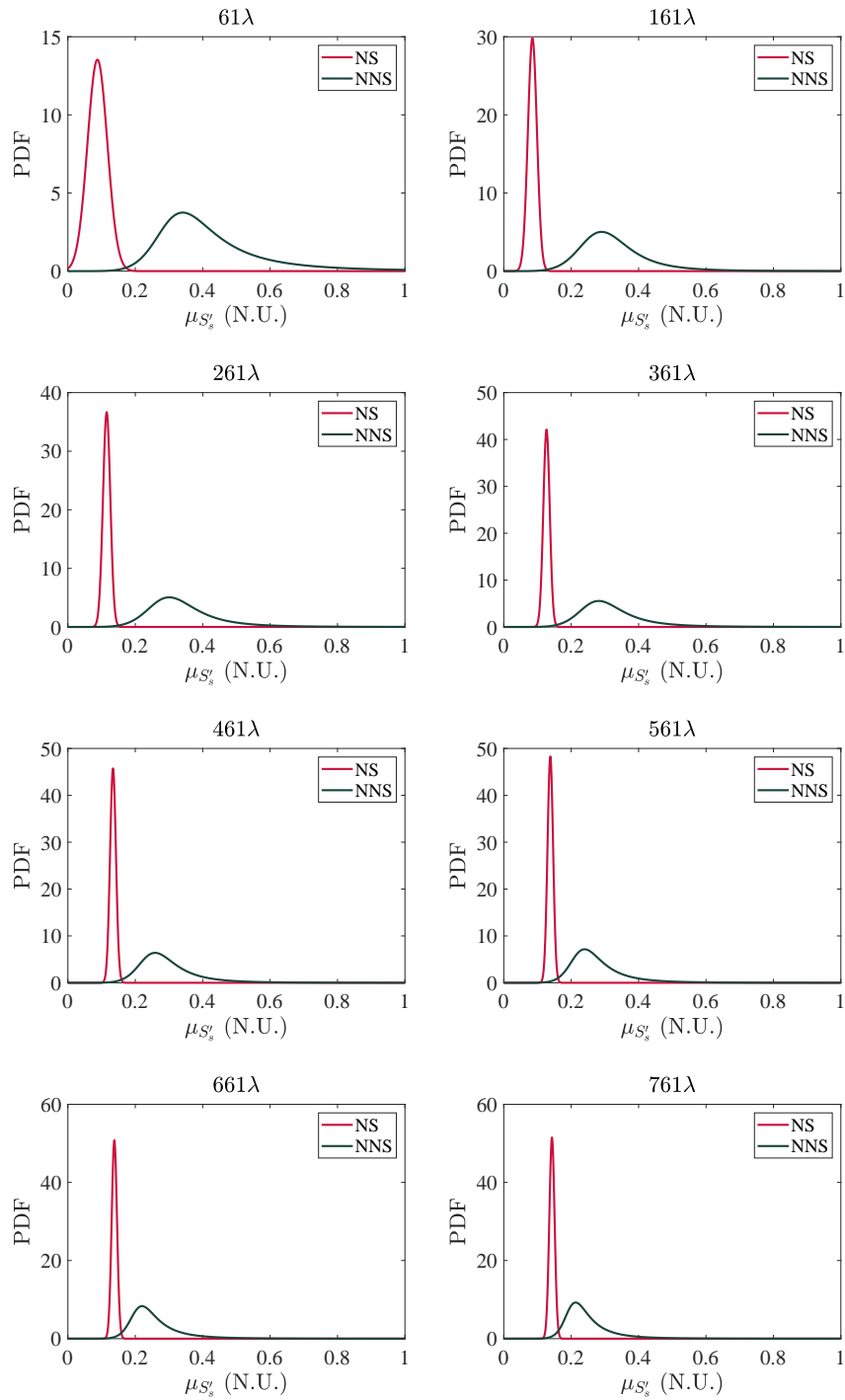
Figure 3.6 Distribution of (3.5), $\mu S'_s$, for the studied scenarios considering eight different spatial frequency ring filters generated by eight different antenna baselines. Image [66] © 2022 IEEE.

The decision boundary was calculated based on the midpoint between the two quantities $\max\{\mu S'_{s,\text{NS}}\}$ and $\min\{\mu S'_{s,\text{NNS}}\}$ where the former represents the NS pattern with the highest ring-filtered averaged responses and the latter corresponds to the NNS pattern with the lowest responses. From the total data set, approximately 70% of the images were used as the training set to determine the decision boundary and the remaining approximately 30% were used as the testing set to evaluate the performance of the classifier. To avoid biasing of evaluating specific combinations of the training and testing sets, a total of $1\,000\,000$ Monte Carlo simulations [82] were conducted where the data within the training and the testing sets were randomly reassigned between each iteration. To evaluate the performance of the classifier, the error rate and the F1 Score (F1) [83, 84] are reported in the top half portion of Table 3.2 representing the averaged metrics from the simulations. The error rate is defined as the sum of the false positives and false negatives divided by the total number of samples and gives a measure of the total number of errors. The F1 score is a measure of the accuracy of the classifier, and is the harmonic mean of precision and recall, where the former is the ratio of the true positives to the sum of all classified positives and the latter is the ratio between the true positives and the sum of the true positives and false negatives. As observed, a 161λ ring filter performed the best on average with an error rate of 1.4% and an F1 Score of 98.6%.

While the decision boundary provided reasonable classification performance, it only utilizes a single pattern from each scene type within the training set. For a two-class classification problem with a large training set of N patterns, $N-2$ patterns will be discarded which is not efficient utilization of the training patterns. However, using all available patterns is equally problematic as outliers can affected the outcomes for the decision boundary resulting in over-fitting, hence the K-nearest neighbor (KNN) classifier was selected as an alternative to improve the classification performance by evaluating multiple training patterns that are locally close to each of the incoming unknown pattern for classification. The KNN classifier determines the class of an unclassified sample by examining the class label of the K-nearest known patterns from the training set, where the final classification is based on the vote of the majority class among the K-nearest neighbors [85, 71].

In addition to the above discussed decision-boundary classification simulation, all eight ring filters were evaluated using a KNN classifier where the nearest K=37 patterns from the training set were used to determine the type of each pattern from the testing set. K was selected as an odd integer for $K = \sqrt{K_{\text{training}}}$ where K_{training} is the total number of patterns in the training set (i.e., 737 NS and 737 NNS). For each of the ring filter scenarios, 100 Monte Carlo iterations were also performed where the generation of training and testing sets were randomized between each iteration. The averaged KNN classifier results are shown in the lower half of Table 3.2 including the performance improvement for the F1 metric when compared to the aforementioned decision-boundary approach. It is evident that the KNN classifier outperforms the decision-boundary approach for all eight scenarios with an averaged F1 improvement of 1.2% and significantly lower error rate where the best performing single ring filter of 261λ had an average error rate of 0.6%. It is noted that the standard deviation of the evaluated metrics is lower when considering the KNN classifier which suggests that it is more robust over the discussed decision-boundary approach. The improvement by selecting the KNN classifier was expected as using more patterns in the training set should contribute to the performance of the classification process. Similar to the decision-boundary results, the performance differences among different baselines of ring filters are noted which may possibly be due to the difference of the number of structures manifesting spatial frequency responses that falls within the spatial frequency bandwidth of a single ring filter. Therefore, it is reasonable to assume that the classification results should be further improved by using a dynamic linear antenna array comprising multiple ring filters.

Scenario	Error$\pm\sigma$ (%)	F1$\pm\sigma$ (%)	Improvement (%)
Threshold (1 000 000 MC)			
61λ	1.9±0.7	98.1±0.7	-
161λ	**1.4±0.5**	**98.6±0.5**	-
261λ	1.5±0.5	98.5±0.5	-
361λ	2.0±0.8	98.0±0.7	-
461λ	3.2±1.2	96.9±1.2	-
561λ	3.2±0.7	96.9±0.7	-
661λ	2.4±1.2	97.6±1.2	-
761λ	2.9±0.9	97.1±0.8	-
KNN (100 MC)			
61λ	0.9±0.3	99.1±0.3	1
161λ	0.7±0.3	99.3±0.3	0.7
261λ	**0.6±0.3**	**99.4±0.3**	0.9
361λ	0.7±0.3	99.3±0.3	1.3
461λ	0.9±0.3	99.1±0.4	2.2
561λ	1.3±0.4	98.7±0.4	1.8
661λ	1.3±0.4	98.7±0.4	1.1
761λ	2.2±0.4	97.8±0.4	0.7

Table 3.2 Imageless classification results using different single ring filters. F1: F1-score. MC: Monte Carlo simulation. Table [66] © 2022 IEEE.

3.4 Design Consideration Using Multiple Ring Filters

In the previous section, the choice antenna baseline yielding specific ring filter design is determined heuristically. While this demonstrates the possible framework of imageless classification, it is also important to discuss the impact of spatial bandwidth of man-made objects and its spatial frequency bandwidth appearing in the visibility that can drive the choice of antenna baseline. Therefore, the design of the ring filter should consider the visibility of the objects of interest. Shown in Figure 3.7 are a set of simulated targets of common dimensions for man-made structures, simulated using exact FOV and resolution of the radar images of Figure 3.2, with their associated normalized visibility. As in one-dimensional Fourier transform where a rectangular function with pulse width T_{pulse} is related to a sinc function with its main lobe residing across the frequency range $2/T_{\text{pulse}}$, the same applies to two-dimensional structures and their visibilities. As observed in Figure 3.7, the effective spatial extent formed by the edges of a tennis court is much smaller than a football field which explains how the spatial frequency bandwidth of the edge related responses are wider and narrower, respectively. The inversely proportional relationship between spatial extent and spatial frequency bandwidth is also demonstrated where spatial extent in the vertical direction is significantly greater than the horizontal direction of a four-lane highway meaning that the associated orthogonal visibility responses extend wider in the u-direction and diminishes faster in the v-direction. Furthermore, as demonstrated in Figure 3.7, when multiple man-made structures appear in the same FOV, the radially extended outward spatial frequency features can diminish at spatial frequency region which can make the design of a single ring filter implementation challenging. Therefore, it is reasonable to consider utilizing multiple ring filters to improve the probability of observing these spatial frequency features by implementing a dynamically rotated linear antenna array. While individual object responses cannot generally be separated after filtering, the use of multiple ring filters has the potential to improve the likelihood of detecting responses from multiple different objects.
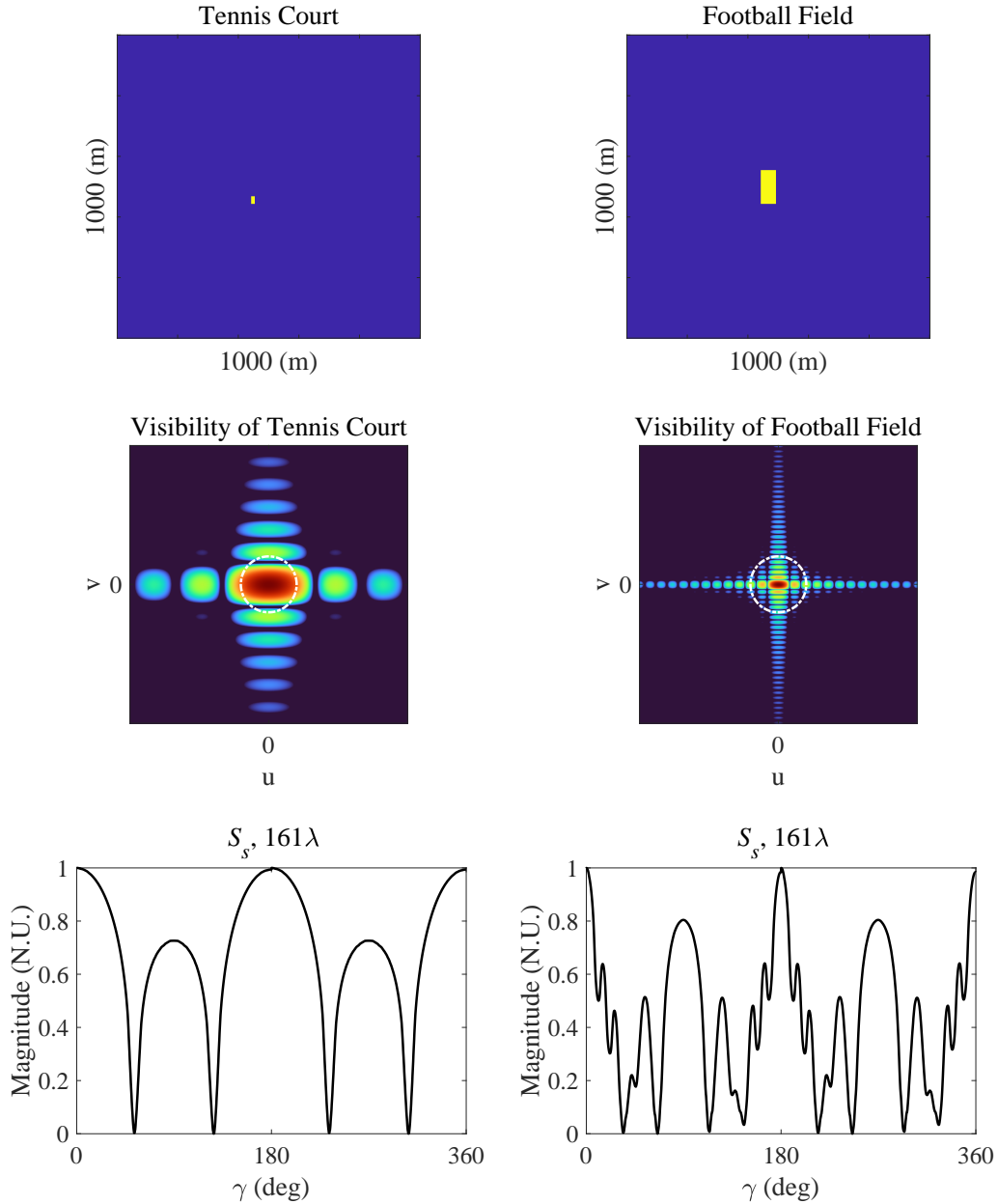
Figure 3.7 **First Row**: Simulated scene examples of size 1000 m by 1000 m demonstrating common dimensions of man-made structures. **Second Row**: Corresponding normalized visibilities. The spatial bandwidth as formed by the edges is inversely proportional to the spatial frequency bandwidth of the associated features. When multiple man-made structures of different dimension exist in the same scene, a single ring filter implementation might not detect spatial frequency features outside of the sampled bandwidth motivating the investigation of utilizing multiple ring filters. **Third Row**: Corresponding processed ring-filtered $S_s(\gamma)$ from (3.3), synthesized with a baseline of 161λ. N.U.: Normalized Units. Image [66] © 2022 IEEE.

Figure 3.7 (cont'd)

Highway

Structures

Visibility of Highway

Visibility of Structures

S_s, 161λ

S_s, 161λ
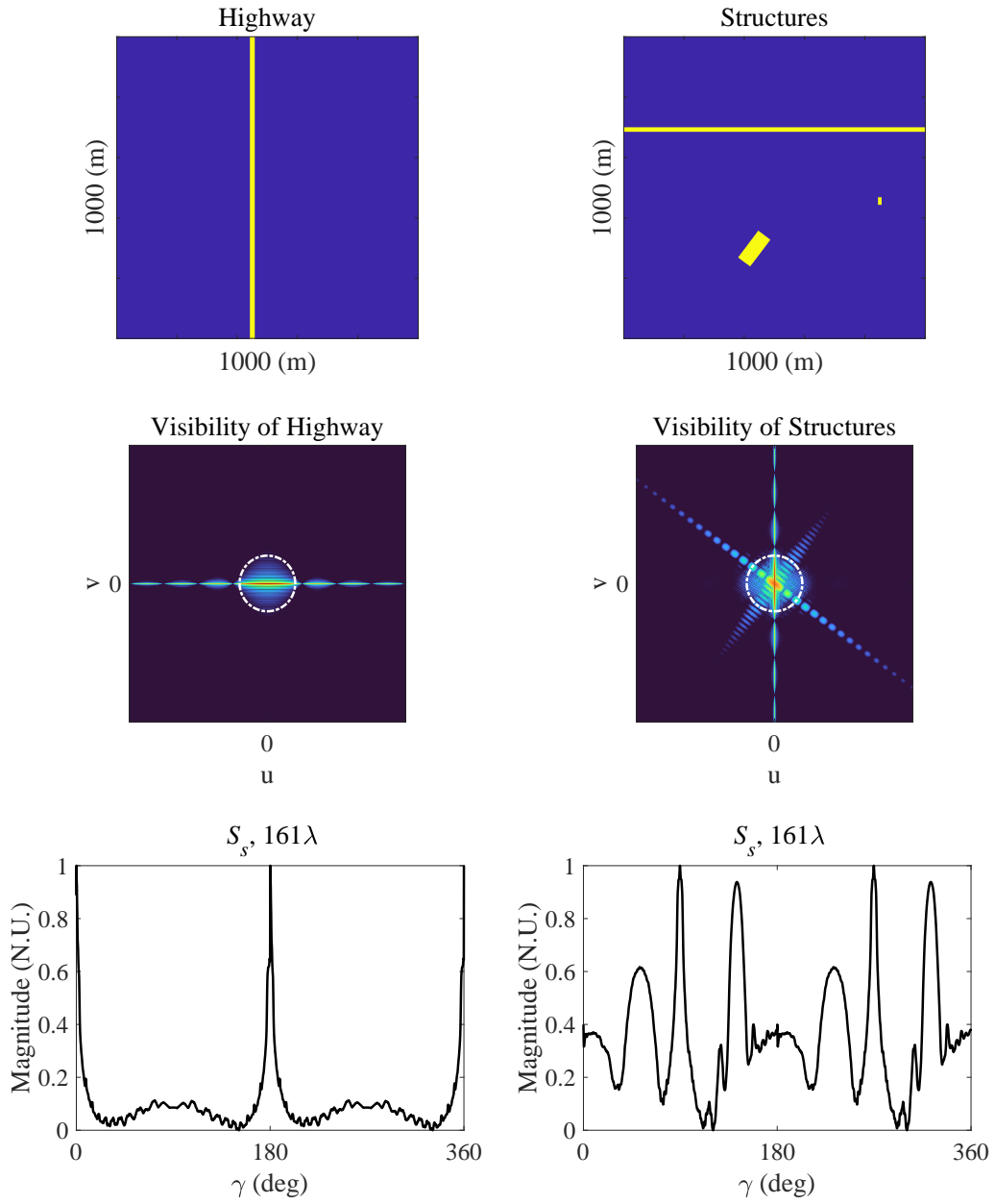
By implementing the dynamic spatio-temporal modulation on a simple linear antenna array (i.e., multiple pairs of co-rotating antennas generating multiple ring filters), additional spatial frequency filters can be obtained simultaneously, while far fewer elements are needed to achieve adequate scene classification compared to other millimeter-wave imaging approaches. The dynamic linear antenna array concept is shown in Figure 3.8 where eight interferometric correlation pairs are shown in different colors. Each pair forms a different baseline and can synthesize spatial frequency ring filters through rotational dynamics thus can capture a wider range of unique features in the spatial frequency spectrum. Note that the presented concept only requires cross-correlation of received signal at each of the ring filter pairs (same color as shown in Figure 3.8) which further reduces the amount of receivers' combination to be processed when compared to an interferometric array with the objective of recovering images. In fact, the approach uses an amount that is insufficient for full image reconstruction, thereby allowing privacy-preserving detection and classification. The dynamic array approach has the added benefit of reduced the hardware requirements compared to conventional imaging approaches; high-gain steered-beam systems use either a large, filled aperture (e.g., a reflector antenna) or an electronically steered phased array, which necessitates the use of many antenna elements along with their associated transceiver hardware. Conventional interferometric arrays already reduce hardware burdens by eliminating beam scanning to realize larger synthesized apertures using comparably fewer antennas as in traditional phased arrays and/or focal-plane arrays [32, 86, 57, 49, 87, 58, 88]. By implementing appropriate array dynamics, the number of antennas required can be further reduced as a larger physical array can be dynamically synthesized over time through antennas' movements.
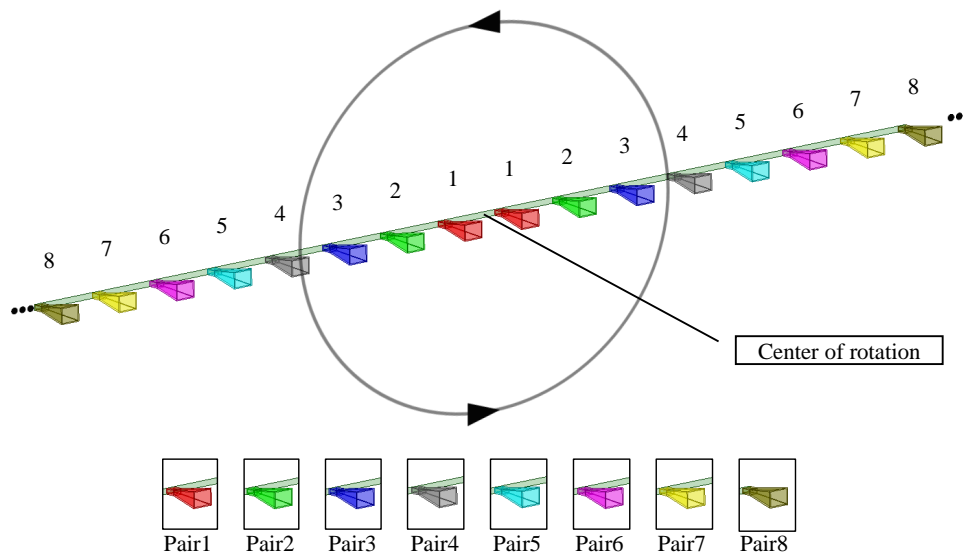
Figure 3.8 Concept diagram for the rotational dynamic linear antenna array. Each interferometric correlation pair(colored differently) forms a different baseline separation and represents a separate spatial frequency domain ring filter when considering a rotation regarding the antenna array's centroid. The black dots on each end of the dynamic linear antenna array denote the possibility to expand the number of antenna pairs. Image [66] © 2022 IEEE.

3.4.1 Rotational Dynamic Linear Antenna Array Design and Optimization

As previously discussed, it is reasonable to assume that the classification results should be further improved by using a dynamic linear antenna array comprising multiple ring filters when compared to the performance of a single ring filter. Here, I consider a postulated rotational dynamic linear antenna array capable of generating eight ring filters that was shown in Figure 3.8 where eight differently colored cross-correlation pairs (i.e., 16 antennas) rotate regarding a common centroid (i.e., each individual pair's centroid is the same as the full linear antenna array's centroid). The implementation can be further optimized by removing redundant antennas [89, 1] from the linear antenna array such that the total required antennas can be reduced. However, this will require the center of rotation to be properly designed to ensure that a set of circular spatial frequency sampling points can be synthesized. This design aspect is noted but not further expanded in this work. A summary of the discussed rotational dynamic linear antenna array concept and the associated antenna baselines are in Table 3.3.

Baseline D_λ	Antenna Pair
61λ	Pair 1
161λ	Pair 2
261λ	Pair 3
361λ	Pair 4
461λ	Pair 5
561λ	Pair 6
661λ	Pair 7
761λ	Pair 8
Number of Antennas	*16*

Table 3.3 Investigated baselines and the corresponding pairs from Figure 3.8. Table [66] © 2022 IEEE.

To understand the effect of whether using multiple ring filters improves the classification performance, two sequential selection algorithms were utilized to determine the best N ring filters combination where $N = 2, 3..., 7$. The selected sequential selection algorithms are the widely known sequential forward selection (SFS) and its reverse counterpart, the sequential backward selection (SBS) [90, 91]. Both SFS and SBS algorithms are sub-optimal but efficient methods compared to exhaustive search of optimal subset where the former obtains a subset of all the available features by adding locally the best feature during each iteration, and the latter seeks the same objective by removing locally the worst feature during each iteration. The two selected sequential selection algorithms were applied to the eight baselines in conjunction with the KNN classifier where the objective function was to optimize the F1 metric of the classifier. The following sequential selection scenarios are performed: finding the best 7, 6, 5, 4, 3 and 2 baselines (ring filters) using the SFS and the SBS methods. In Table 3.4 and 3.5, the 12 optimized dynamic linear antenna array designs are summarized with their corresponding ring filter combinations. The associated KNN classifier outcomes corresponding to the 12 scenarios covered in Table 3.4 and 3.5 are summarized in Table 3.6 where SFS.Best$N$ and SBS.Best$N$ represent the best N ring filters determined by the corresponding sequential selection algorithms.

It is evident that the performance outcomes of the KNN classifier considering multiple baselines are all better than the best case for the single baseline case (i.e., 261λ using KNN in Table 3.2). An array with two baselines using SFS optimization (SFS.Best2 with error rate of 0.3% and F1 of 99.7%) obtained the best performance, while adding additional baselines either did not improve the performance, or, when seven baselines were used, the performance began to degrade. This can be explained by the commonly known "curse of dimensionality" in classification analyses where increasing the number of features in a classifier leads to better performance, however the improvement at some point has diminishing returns, leading to minimal performance improvements for significant effort. Increasing the number of features can undermine the classifier performance when the dimension is too high (i.e., too many features) [71]. Therefore, it is desired to use only a subset of all available features while achieving reasonable classification performance. Furthermore,

in the present case, reducing the number of features also leads to a reduction in the number of antennas required, further minimizing the hardware burden. As a comparison, all eight ring filters were selected in conjunction with the KNN classifier where an error rate of 0.5% was obtained with an F1 of 99.5% as shown in Table 3.6. As observed, while this also provides better performance compared to the single ring filter scenario (0.6% for 261λ), the additional required hardware does not justify the small improvement when compared to the optimized scenarios as determined by the sequential selection algorithms. As shown in Figure 3.9, considering the original postulated 16 antenna rotational dynamic linear antenna array as shown in Figure 3.8, the optimized design requires only four antennas: two pairs to achieve 61λ and 261λ. The optimized array design achieved an averaged error rate of 0.3% (half of the best performing single ring filter at 0.6%) and an averaged F1 of 99.7% where the cost of implementing the two additional receiving antennas is a reasonable trade-off for performance.

	61λ	161λ	261λ	361λ	461λ	561λ	661λ	761λ
SFS.Best7	X	X	X	X	X	X	X	
SFS.Best6	X	X	X	X	X	X		
SFS.Best5	X	X	X	X	X			
SFS.Best4	X	X	X	X				
SFS.Best3	X	X	X					
SFS.Best2	X		X					

Table 3.4 Feature selection results using sequential forward selection (SFS). Table [66] © 2022 IEEE.

	61λ	161λ	261λ	361λ	461λ	561λ	661λ	761λ
SBS.Best7	X		X	X	X	X	X	X
SBS.Best6	X			X	X	X	X	X
SBS.Best5	X				X	X	X	X
SBS.Best4	X					X	X	X
SBS.Best3	X						X	X
SBS.Best2	X							X

Table 3.5 Feature selection results using sequential backward selection (SBS). Table [66] © 2022 IEEE.

Scenario	Error$\pm\sigma$ (%)	F1$\pm\sigma$ (%)
All8	0.5±0.2	99.5±0.2
SFS.Best7	0.4±0.2	99.6±0.2
SBS.Best7	0.4±0.2	99.6±0.2
SFS.Best6	0.3±0.2	99.7±0.2
SBS.Best6	0.3±0.2	99.7±0.2
SFS.Best5	0.3±0.2	99.7±0.2
SBS.Best5	0.3±0.2	99.7±0.2
SFS.Best4	0.3±0.2	99.7±0.2
SBS.Best4	0.3±0.2	99.7±0.2
SFS.Best3	0.3±0.2	99.7±0.2
SBS.Best3	0.4±0.2	99.6±0.2
SFS.Best2	**0.3±0.2**	**99.7±0.2**
SBS.Best2	0.4±0.2	99.6±0.2

Table 3.6 Imageless classification results from different multi-baseline dynamic linear antenna array designs with 100 Monte Carlo simulations. F1: F1-score. Table [66] © 2022 IEEE.
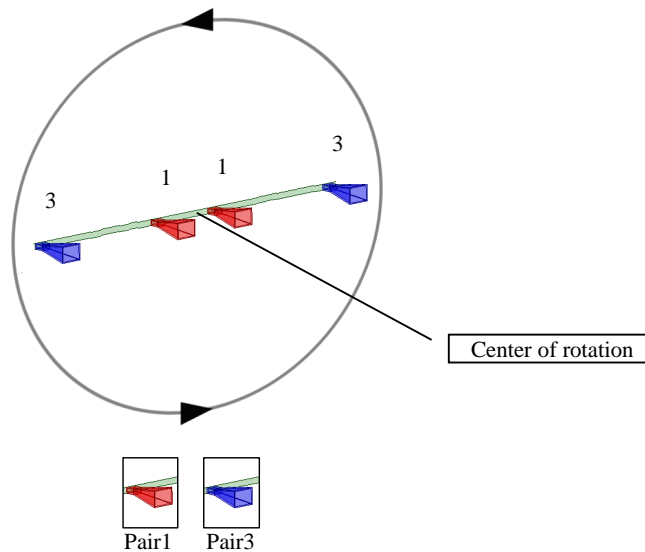
Figure 3.9 Final design of the rotational dynamic linear array using only four antennas to synthesize the two baselines that yield the best classification results (Table 3.6) as selected by the SFS (Table 3.4) when evaluated with the KNN classifier. Colors indicate different antenna pairs for the synthesization of specific spatial frequency ring filters. Image [66] © 2022 IEEE.

3.5   Design and Implementation of a Rotational Dynamic Antenna Array

As observed from the previous sections, a single ring filter can be effective at capturing spatial Fourier artifacts pertaining to sharp edges enabling direct classification using measured data without forming an image. Furthermore, it is shown that additional ring filters can improve the classification performance when balancing the associated cost and evaluation metrics. In this section, I discuss the design and implementation of a rotational dynamic antenna array capable of synthesizing the already discussed ring filter in the spatial Fourier domain.

The implemented rotational dynamic antenna array is shown in Figure 3.10 and can operate between 71 GHz–76 GHz (referred to as a 75 GHz system) consisting of two transmitters to satisfy the spatio-temporal incoherent radiation condition on the measured scene, and two receivers (i.e., correlation pair) [67]. As shown on the top right of Figure 3.10, from the source to the radiating antenna, the two transmitter sub-systems each contains a baseband noise source (RF-Gadgets XDM NSE15-1) with bandwidth of 10–1600 MHz; three cascaded baseband amplifiers (Mini-Circuits ZX50-V63+); a 180° coupler (Mini-Circuits ZFSCJ-2-232-S+); an upconverter (Analog Devices EVAL-ADMV7310) to enable the noise signals to be propagate through a linearly conical horn antenna (Eravant SAC-1533-12-S2) with a gain of 15 dBi at 75 GHz. From the receiving antenna to the baseband digitizer, each of the two receiving subsystems consists a linearly conical horn antenna (Eravant SAC-1533-12-S2) with a gain of 15 dBi; a downconverter (Analog Devices EVAL-ADMV7410); two pairs of 180° coupler each combines the differential baseband in-phase and quadrature signals which is subsequently acquired by a digitizer (AlazarTech ATS9416) supporting a sampling rate of 100 MS/s. A four-way splitter (Mini-Circuits ZN4PD1-183W-S+) is used to provide the local oscillator (LO) signals to each of the transmit and receiving sub-system and that the LO is generated using an Agilent PSG E8267D. Note that only the two receiving sub-systems require a common reference LO. Furthermore, note that both transmitters and both receivers are integrated on the same rotation platform to ensure co-polarization. The full schematics and additional photos of the rotational dynamic antenna array can be found in Appendix E. Furthermore, the MATLAB code operated from the host computer is included in Appendix F.

84
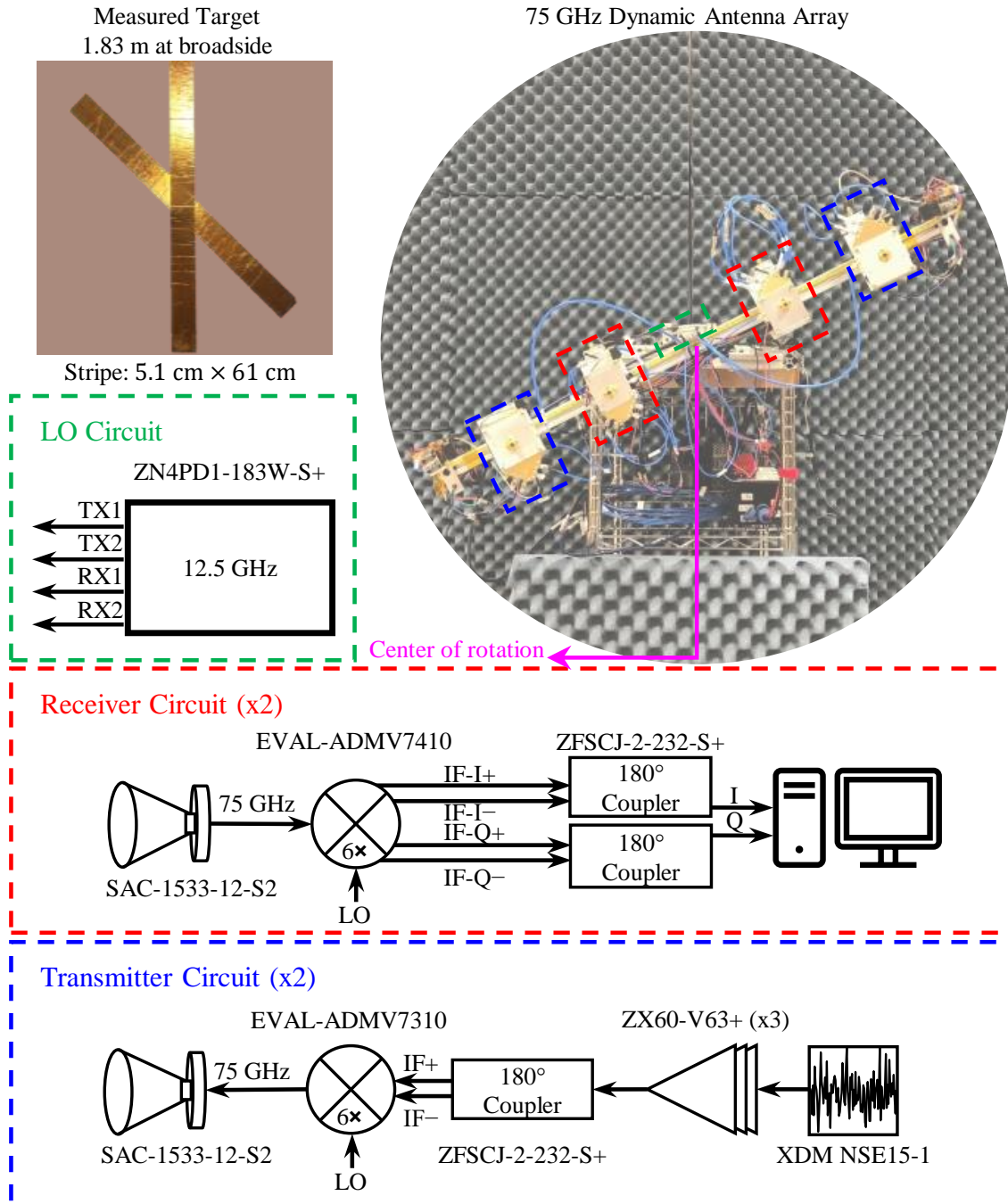
Figure 3.10 **Top left**: The measured target that is placed 1.83 m broadside to the rotational dynamic antenna array. The target is made from a foam board that is transparent at the considered frequency and uses two copper stripes to create sharp edges that make a 45° acute angle. Each of the stripes has a dimension of 61.0 cm×5.1 cm. **Top right**: Photo of the implemented 75 GHz rotational dynamic antenna array. **Bottom**: The radio frequency architecture includes the local oscillator circuit (green), receiver circuit (red), and the transmitter circuit (blue) of the rotational dynamic antenna array. Originally submitted to *IEEE Transactions on Geoscience and Remote Sensing*, March 2024.

The rotational dynamic antenna array system is capable of synthesizing a receiver baseline within the range of $[47\lambda, 127\lambda]$ at 75 GHz, and the two receivers can be linearly adjusted along the rotating structure. The two transmitters are fixed at locations forming a baseline that of 162λ at 75 GHz that is significantly wider than the widest possible receiver baseline to achieve the spatio-temporal illuminating condition at the measured scene when considered its combination with two independent wideband noise sources. Furthermore, the rotating structure of the dynamic antenna array is mechanically coupled to a motor encoder capable of 400 pulse-per-revolution (PPR) representing a rotating angular resolution of $0.9°$. Note that the array shown in Figure 3.10 supports a rotational span of $180°$ which is sufficient to achieve a $360°$ coverage in the spatial Fourier domain given that it is Hermitian symmetric. Therefore, the angle from $[0°, 180°)$ is the measured response and the angle from $[180°, 360°)$ is referred to as the inferred-measured response as at the rotated angle of $180°$ the two antennas effectively switched their location. The rotational dynamic antenna array is generally configured such that the fast time integration (dwell time) at each angle is 1.024 ms representing a slow time integration of 204.8 ms over $180°$ rotation achieving an integrated sampling function that is also referred to as the ring filter. The 75 GHz rotational dynamic antenna array is a real-time system and can be considered first of its kind to my best knowledge. In Table 3.7, I provided the summary of the 75 GHz rotational dynamic antenna array along with comparison to earlier implementation that was presented in my prior works [92, 93]. The main advancement of the 75 GHz rotational dynamic antenna array is its real-time capability where a comparable experimental setup (e.g., one ring filter measurement) is significantly shorter than the prior system.

	Prior Works [92, 93]	This Dissertation
Frequency (GHz)	37–40	71–76
Number of Transmitters	3	2
Number of Receivers	2	2
Receiver Baseline Range (λ)	50–106	47–127
Rotating Angle Resolution	$\geq 0.1°$	$0.9°$
Rotating Angle Determination	Manual[†]	Motor Encoder
Sampling Rate	2.5 GSamp/s	100 MSamp/s
Sampling Trigger	Manual[†]	Motor Encoder
Fast Time Integration (per angle)	0.1 ms	1.024 ms
Slow Time Integration for 200 angles (i.e., ring filter with 0.9° rotating resolution)	≈ 6.7 h[†]	≈ 205 ms
Slow Time Integration Improvement	n.a.	≈ 99.99 %[†]

Table 3.7 Comparison between the 75 GHz rotating dynamic antenna array systems and the previously implemented 38 GHz system [92, 93].[†] The 38 GHz system relies on a digital angle gauge to manually determine the rotated angle before manually triggering an oscilloscope for data acquisition. Therefore, although the fast time integration for an angle is short, it still takes about two minutes before a subsequent angle's measurement can be acquired.

3.5.1 Demonstration on the Measurement of Spatial Fourier Artifacts

As shown in the top left of Figure 3.10, a target which its spatial Fourier responses to be measured is constructed of a foam board that is transparent at the considered frequency. Two copper stripes are used to create sharp edges that make a 45° acute angle, and each of the stripes has a dimension of 61.0 cm×5.1 cm. The target is placed 1.83 m at broadside of the rotational dynamic antenna array and the measurement was conducted in a semi-enclosed anechoic environment where the target is backed by walls of radio frequency absorbing materials as illustrated in Figure 3.11.

A simulated binary scene intensity assuming strong reflection due to the copper tapes from the measured target and zeros elsewhere is shown in the top left of Figure 3.12 with its visibility shown on the top right where a transparent white ring is included to annotate the ring-filtering integrated sampling function due to the array trajectory described in (3.1). Note that the sharp edge induced spatial Fourier response is orthogonal to the sharp edge direction in the spatial domain. In the bottom of Figure 3.12, the measured (including the inferred) ring-filtered visibility is shown alongside the simulated response showing close agreement. The expected spatial Fourier artifacts that are induced by the physical edge of the target are expected to appear at rotated angles of {0°, 45°, 180°, 225°} where with respect to the positive u-axis of the uv-plane in the counter-clockwise direction. It is noted that specularity between the dynamic antenna array and the target can contribute to the difference between the measured and simulated response as the target plane and the measurement plane might not be exactly parallel. Nevertheless, the measurement successfully demonstrates the ability to recognize such spatial Fourier artifacts without requiring the inverse Fourier transformation to recover the measured scene intensity. This approach of using a coordinated array trajectory again can be used to efficiently determine a scene's significance before requiring the deployment of the random trajectory approach to recover a good quality scene intensity reconstruction.
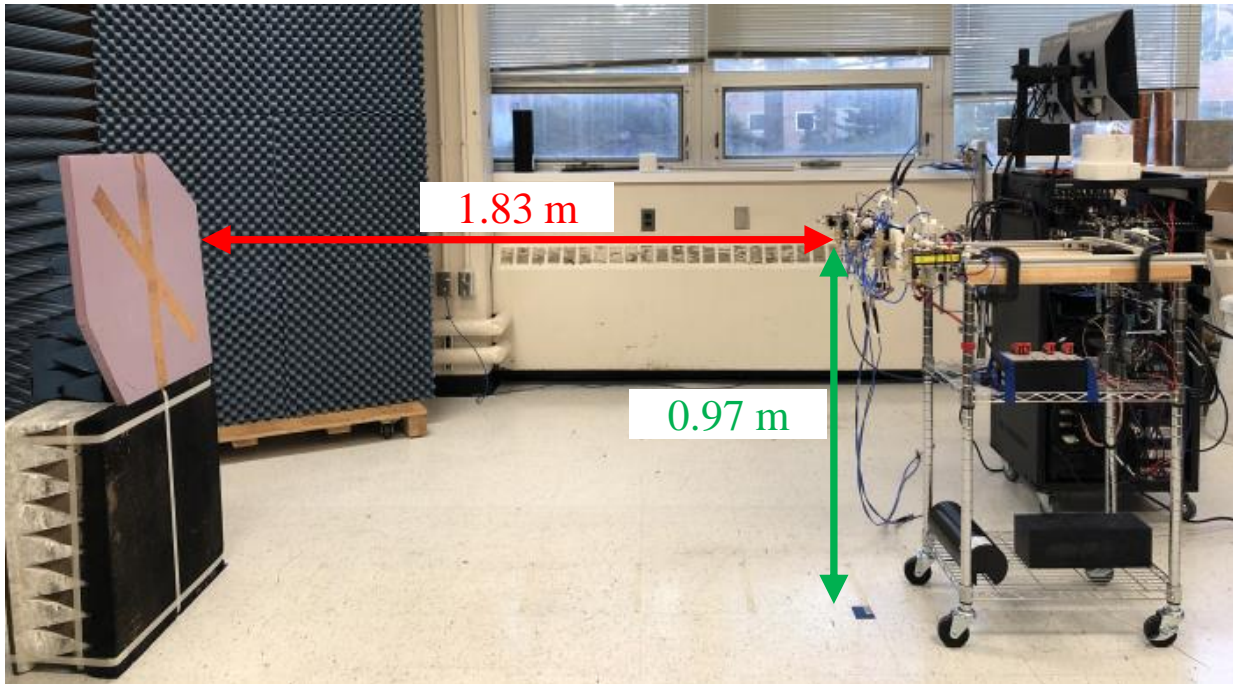
Figure 3.11 Measurement setup of the two-stripe target that is 1.83 m away from the broadside of the 75 GHz dynamic antenna array with height of 0.97 m measured from its center of rotation to the floor. Image [67] © 2022 IEEE.

Simulated Target

Simulated Visibility

Ring-filtered Visibility Response at $D_\lambda = 73.5\lambda$
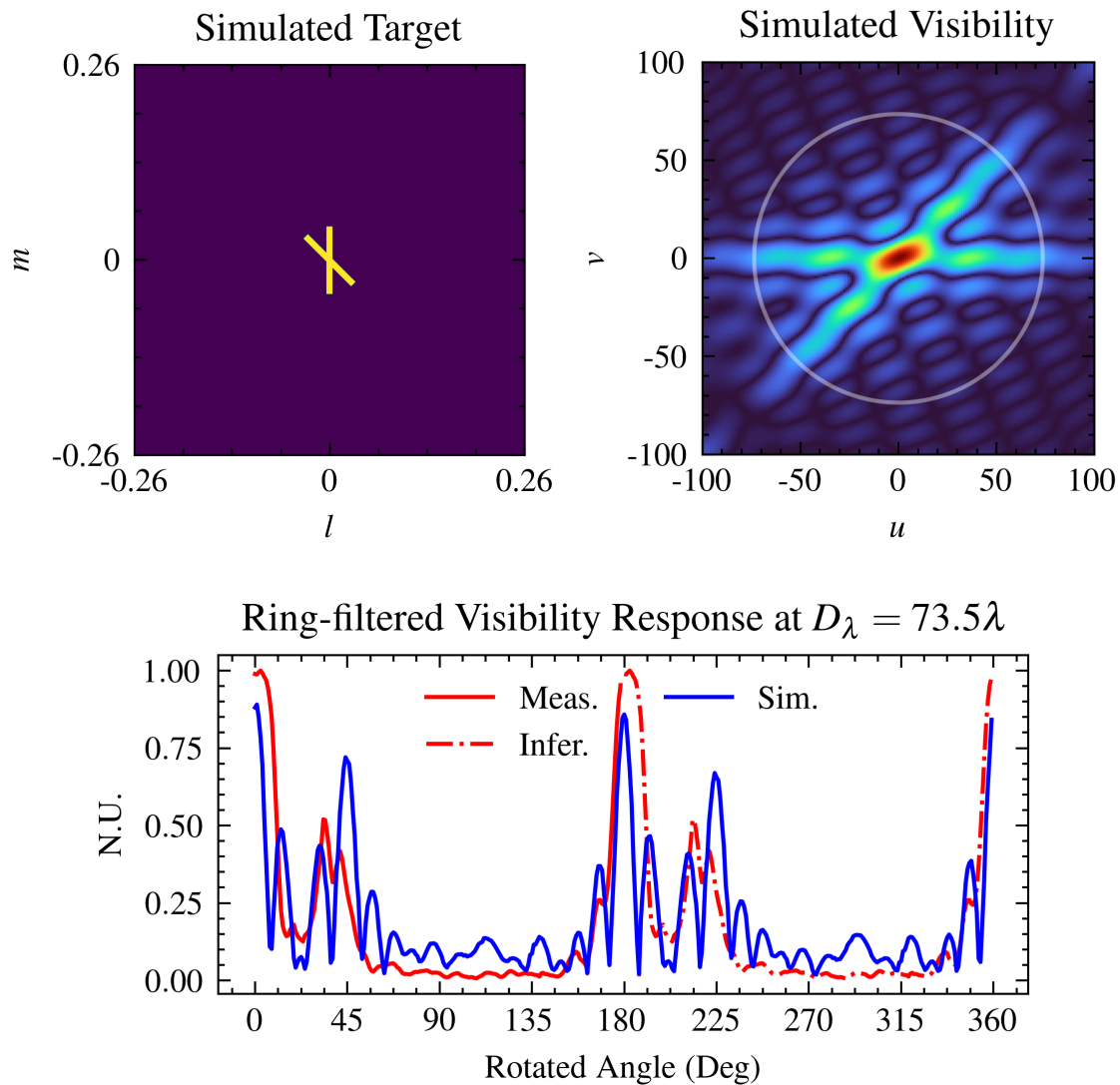
Figure 3.12 **Top left**: Simulated measured target as shown in Figure 3.10. **Top right**: Simulated visibility of the measured target with a white ring annotating the ring-filter (i.e., integrated sampling function) due to the two-element dynamic antenna array with a baseline separation of 73.5λ. **Bottom**: Comparison of the measured and simulated ring-filtered visibility response as a function of the rotated angle due to array trajectory. The array supports a rotation of $180°$ which is sufficient to achieve a $360°$ coverage in the spatial Fourier domain given that it is Hermitian symmetric. Therefore, the angle from $[0°, 180°)$ is the measured response and the angle from $[180°, 360°)$ is referred to as the inferred-measured response. N.U.: Normalized Unit. Originally submitted to *IEEE Transactions on Geoscience and Remote Sensing*, March 2024.

CHAPTER 4

A PRIVACY PRESERVING APPROACH FOR IMAGELESS
SECURITY SCREENING APPLICATION

In this chapter, I present an imageless approach to concealed contraband detection enabled by the direct measured spatial Fourier samples collected by the ring filter that is generated by the 75 GHz rotational dynamic antenna array. Concealed contraband detection via imagery typically relies on rigorous classification processes to identify objects [68]. However, such an approach relies on fully reconstructed imagery, which can be expensive to obtain due to the need for additional hardware, such as many receiving antennas, and extensive computational resources. As demonstrated in the previous chapter, objects with sharp edges manifest identifiable artifacts in the Fourier domain and represent the opportunity for direct object detection and classification without relying on imagery, with the potential for significant reductions in cost of the overall sensing system [67]. Furthermore, the collected spatial Fourier information is not sufficient to form imagery of the screened scene, thus ensuring privacy when the potential application involves humans. Using the 75 GHz rotational dynamic antenna array, a fiberglass mannequin, and a metallic gun-shaped object, I demonstrated the separability of spatial Fourier responses when the gun-shaped object is concealed beneath a clothed mannequin and when the gun-shaped object is not present. Subsequently, I investigated the applicability of the imageless concealed contraband approach where the mannequin is replaced by a real person meaning that the aforementioned quasi-static scene condition is not necessarily fulfilled when considering the array dynamics.

This chapter is, in part, a reprint or adaptation of materials with permission in "Privacy Preserving Contraband Detection Using a Millimeter-Wave Dynamic Antenna Array" published in *IEEE Microwave and Wireless Technology Letters* [94] © 2023 IEEE and "Imageless Contraband Detection Using a Millimeter-Wave Dynamic Antenna Array via Spatial Fourier Domain Sampling" submitted to the *IEEE Access*, April 2024.

4.1 Separability in the Spatial Fourier Domain

Based on the principle of improving unique uv sampling points through array dynamics and the demonstration on the captures of sharp edge induced spatial Fourier artifacts (in Chapter 3), the 75 GHz rotational dynamic antenna array can be suitable for security screening involving potential contraband concealed under clothing. The concept is shown in Figure 4.1 where the implemented 75 GHz rotational dynamic antenna array is used to collect spatial Fourier responses using the generated ring filter. Subsequently, direct classification is carried out using the ring-filtered information that is processed and evaluated using a classifier to determine the condition of the measured scene (i.e., contraband present or not). Furthermore, as discussed previously, it is expected that the information captured by the ring filter is insufficient for scene reconstruction representing an opportunity to preserve the privacy of the screened person using this imageless security screening technique. Due to the implemented design of the 75 GHz rotational dynamic antenna array, the ring-filtering integrated sampling function (2.14) becomes a function of the sampled angles k rather than T because of uniform angular sampling interval across the rotating trajectory due to the implemented motor encoder. For a dwell time of $t_{\text{single}} = \tau$ at each measured given angle, the total integrated slow time required to synthesize a complete ring filter is $T = t_{\text{ring}} = 200\tau$ assuming constant rotational speed. Therefore, the speed at which the dynamic antenna rotates will be $\gamma_{\text{ring}} = \frac{0.5}{200\tau}$ where a half rotation (i.e., $180°$) accounts for 200τ duration. To ensure that the uniform sampling interval assumption is valid, $\gamma_r \leq \gamma_{\text{ring}}$. When $\gamma_r > \gamma_{\text{ring}}$, certain angles will be skipped making the ring filter incomplete and nonuniform. When all possible spatial frequency samples at all angles are measured, the collection of the cross-correlating outputs can be represented as

$$\mathbb{S} = S_T(u_k, v_k), \quad \forall k = [0, K - 1] \tag{4.1}$$

where u_k and v_k are the uv-samples defined by the two-element array dimension normalized to the wavelength D_λ and the K discrete rotational angles $\gamma(k)$ over $180°$ as $u_k = D_\lambda \sin \gamma(k)$ and $v_k = D_\lambda \cos \gamma(k)$, respectively.
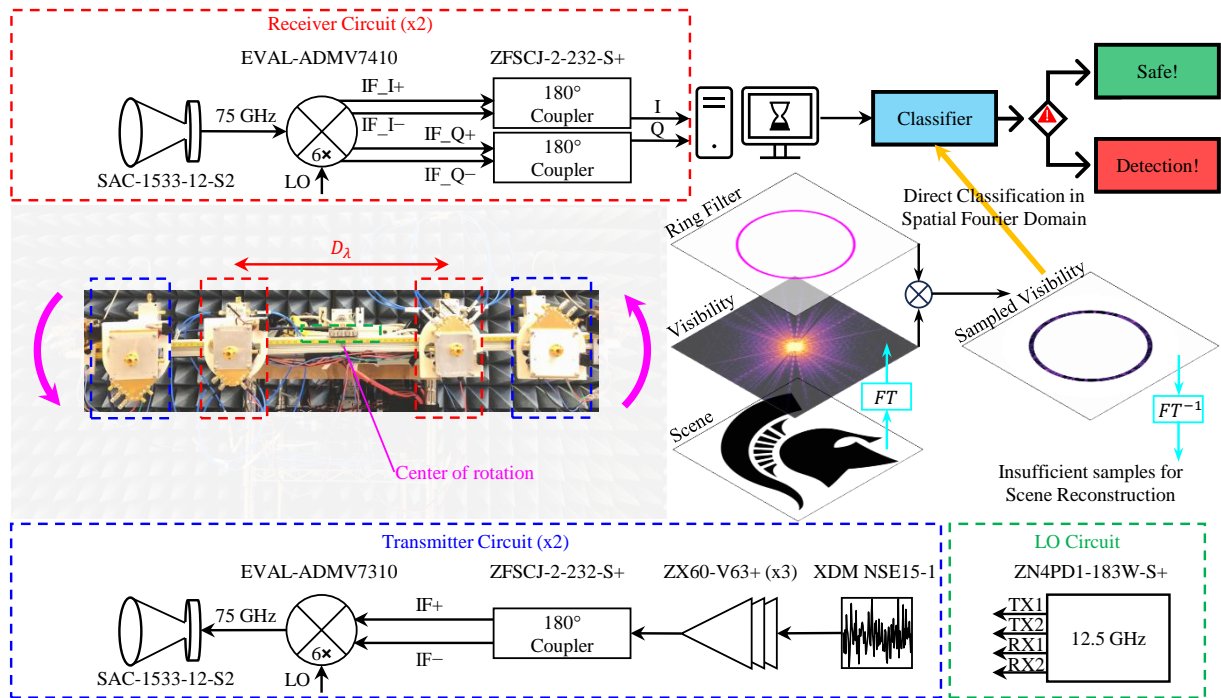
Figure 4.1 Concept diagram and system architecture of the experimental 75 GHz dynamic antenna array. The system includes two transmitters (blue dashed box), two receivers (red dashed box), and local oscillator (LO) (green dashed box). The noise transmitters satisfy the spatio-temporal incoherence condition which enables Fourier-domain sampling. The two received signals at any given sampled angle are cross-correlated to obtain visibility samples defined by the antenna baseline D_λ. As the dynamic antenna array rotates, the corresponding Fourier-domain sample also rotates, hence achieving a ring filter where additional Fourier-domain information can be obtained. The signals are sent to a classifier to determine whether a specific contraband, e.g., a handgun, is concealed by the screened subject. LO: local oscillator. IF: intermediate frequency. TX: transmitter. RX: receiver. Originally submitted to *IEEE Access*, April 2024.

4.1.1 Experiment Setup

For the remainder of this chapter, the term *subject* refers to the primary background (e.g., a mannequin or person) carrying an *object* which refers to items (e.g., a handgun), that can be concealed under clothing. Experiments were conducted to determine the separability of the spatial Fourier-domain responses of different scenarios with and without an object present in the measurement. The experiment consisted of 160 independent measurements equally grouped into two general classes as shown in Figure 4.2: a clothed fiberglass mannequin facing towards the dynamic antenna array with and without a gun-shaped target of dimension $164\,\text{mm}\times235\,\text{mm}$ concealed underneath the clothing. Between each successive measurement, the mannequin was removed and replaced to mimic the uncertainties of a practical test subject's relative orientation to the dynamic antenna array due to breathing and/or torso movements. Similarly, the gun-shaped target was randomly placed beneath the clothing with its barrel pointing at varying directions. The mannequin with and without the gun-shaped target was approximately $1.83\,\text{m}$ from the dynamic antenna array and was backed by walls of radio-frequency absorbers. The two receivers of the array were 77λ apart at $75\,\text{GHz}$ and rotated over a $180°$ rotational span at every $0.9°$ (equivalent to the motor encoder resolution) for all measurements.

Figure 4.2 From left to right: Front of a clothed mannequin (t-shirt shown transparent to show mannequin); front of a clothed mannequin with a concealed gun-shaped target; the gun-shaped target of dimension $164\,\text{mm}\times235\,\text{mm}$. Image [94] © 2023 IEEE.

4.1.2 Spatial Fourier Responses and Features Extraction

The two received signals at all 200 angles, tracing out a ring-shape sampling function, each with dwelling time of τ=1.024 ms, were then cross-correlated to recover the Fourier information to form the ring-filtered response $\mathbb{S}$ of (4.1). Examples of ring-filtered responses are shown in Figure 4.3 where the black and blue dashed lines represent the responses of an empty scene and a scene with only the absorbing staging materials, and the green/red pair in dash and dash-dot lines are two sets of data from scene with and without the gun shape, respectively. It is clear that the two classes are difficult to differentiate based solely on the sampled output in the Fourier domain from the dynamic antenna array.

To overcome this challenge, a multi-feature classification approach using 11 heuristically defined features is investigated, each of which was a different algorithmic process on the ring-filtered spatial Fourier-domain data $\mathbb{S}$. The 11 features were: mean, median, maximum, difference between maximum and mean, difference between maximum and median, difference between maximum and minimum, difference between mean and minimum, difference between median and minimum, difference between median and mean, standard deviation, and variance which are shown in Figure 4.4. The magnitude of the 11-feature space vector was computed for each measurement and normalized to all measurements. As seen in the bottom right of Figure 4.4, the two distributions display significant differences despite the similarities between the two classes of $\mathbb{S}$ seen in Figure 4.3. The responses with no target are concentrated below a normalized feature vector magnitude of 0.2, while the responses with a target spread over a wider range. This difference in the distribution points to a threshold value of the normalized feature vector magnitude of approximately 0.2. The multicollinearity among the 11 features via principal component analysis (PCA) and determined that the first five principal components contribute 89.1%, 8.6%, 1.7%, 0.4%, and 0.1% of the variance between the two classes, respectively, and all 11 features are highly correlated to the first principal component. It is noted that more complex processing techniques may be used to efficiently extract features and/or implemented to improve and/or enable other classification approaches.
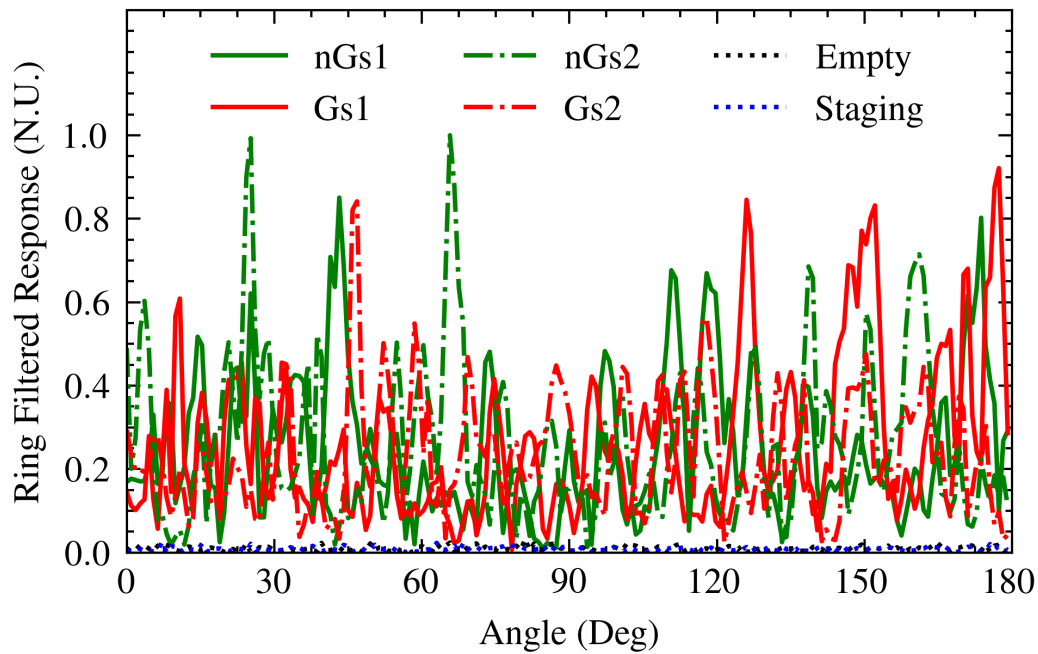
Figure 4.3 Six examples of the ring-filtered responses (4.1) using the 75 GHz rotational dynamic antenna array at $D_\lambda = 77\lambda$. The black and blue dash lines are the responses of empty scenes and absorbing staging materials, respectively. The solid green/red and dash-dot green/red lines show how varying mannequin placements and/or gun-shaped target can affect the measured responses. Gs: Gun-shape. nGs: non-Gun-shape. N.U.: Normalized Unit. Image [94] © 2023 IEEE.
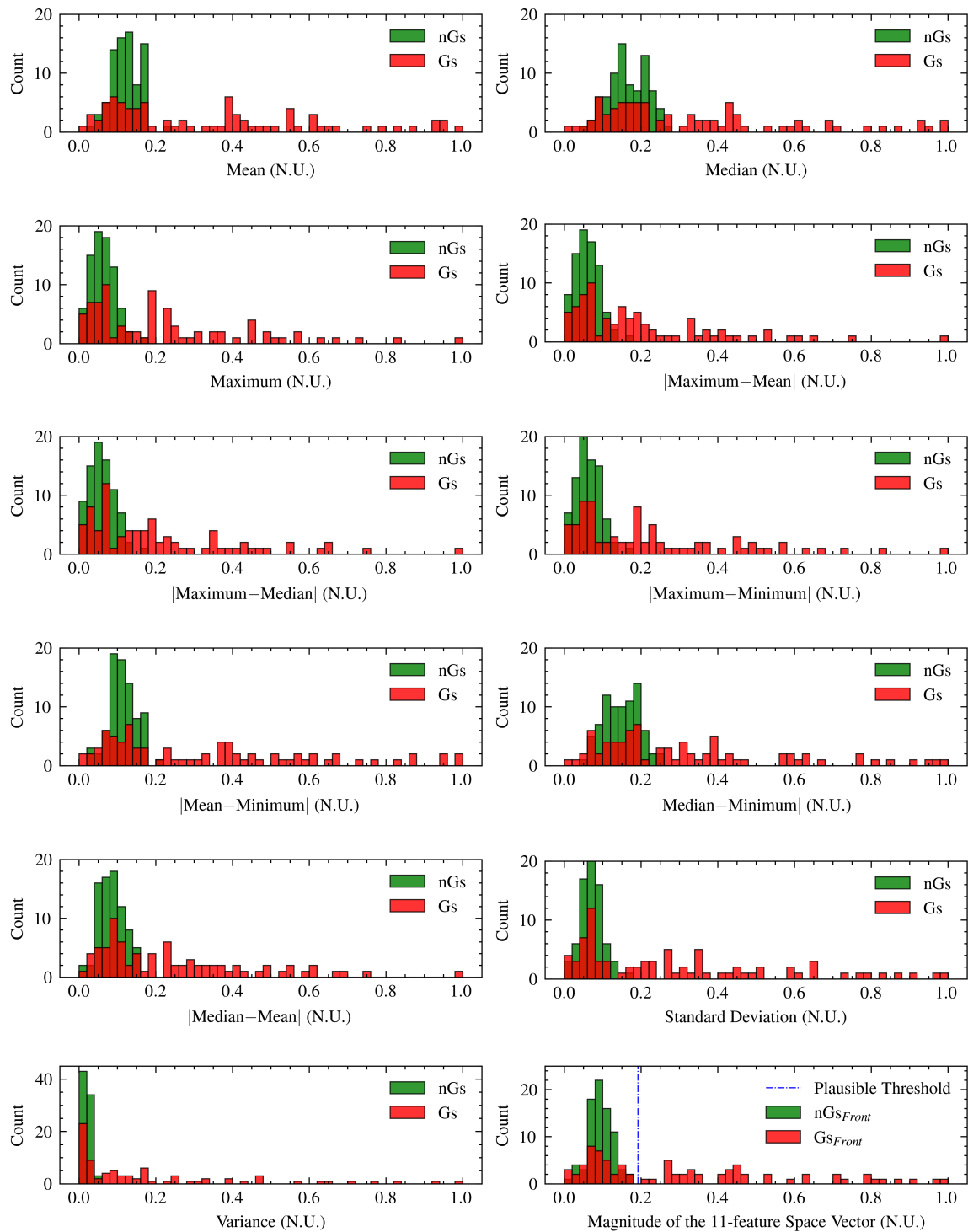
Figure 4.4 11 heuristically defined statistical features extracted from the ring-filtered spatial Fourier-domain data $\mathbb{S}$. **Bottom Right**: Distribution based on the magnitude of the 11-feature space vector for the two classes Gs (red) and nGs (green) based on measurements pertaining to varying conditions of when the mannequin is facing towards the DAA. A plausible threshold value of approximately 0.2 N.U. for the magnitude of the 11-feature space vector is observed and shown in dash-dot blue that can separate the two classes. Gs: Gun-shape. nGs: non-Gun-shape. N.U.: Normalized Units.

4.1.3 Performance of Different Classifiers

Given that the number of available measurements is not sufficiently large (i.e., 80 for each of the two investigated classes), a Monte Carlo analysis [82] of 10 000 iterations using the simple threshold method based on the heuristically defined features. Each iteration used a randomly selected 70% of the data set for training and the remaining 30% for testing. The 70% training data are used to determine a threshold value maximizing the accuracy of the simple threshold classifier within the training set. Under the assumption that individual measurements are independent of each other, the performed classification is based on N consecutive measurements of the same scene type for $N = [1, 7]$ where $N = 1$ and $N = 7$ represent classifying a single response and seven consecutive responses, respectively.

To evaluate the performance of a classifier, the following four metrics are used [83, 84]

- True positive rate (TPR) which represents the probability of detection, or successfully identifying an object concealed under the subject's clothing;

- False positive rate (FPR) which represents the probability of false detection when only the subject is measured;

- Accuracy (ACC) which represents the ratio of all correctly classified data over all data with emphasis on the true positives (i.e., correctly classified subjects with concealed object) and true negatives (i.e., correctly classified subjects without concealed object); and

- F1-score (F1) which is a metric similar to ACC but with emphasis on the false negatives (i.e., incorrectly classified subjects with concealed object) and false positives (i.e., incorrectly classified subjects without concealed object);

where

$$TPR = \frac{TP}{TP + FN}$$
$$FPR = \frac{FP}{FP + TN}$$
$$ACC = \frac{TP + TN}{TP + FN + FP + TN} \quad (4.2)$$
$$F1 = \frac{2TP}{2TP + FN + FP}$$

where TP is the number of true positives (correctly identified as contraband), FP is the number of false positives (incorrectly identified as contraband), TN is the number of true negatives (correctly identified as non-contraband), and FN is the number of false negatives (incorrectly identified as non-contraband). The averaged classification metrics from the Monte Carlo simulations are shown in Figure 4.5. It can be seen that the true positive rate (TPR) improves as N increases but at the cost of increasing false positive rate (FPR). Furthermore, it is noted that the accuracy (ACC) and F1-score (F1) peak when $N = 4$ at 0.908 and 0.916, respectively.
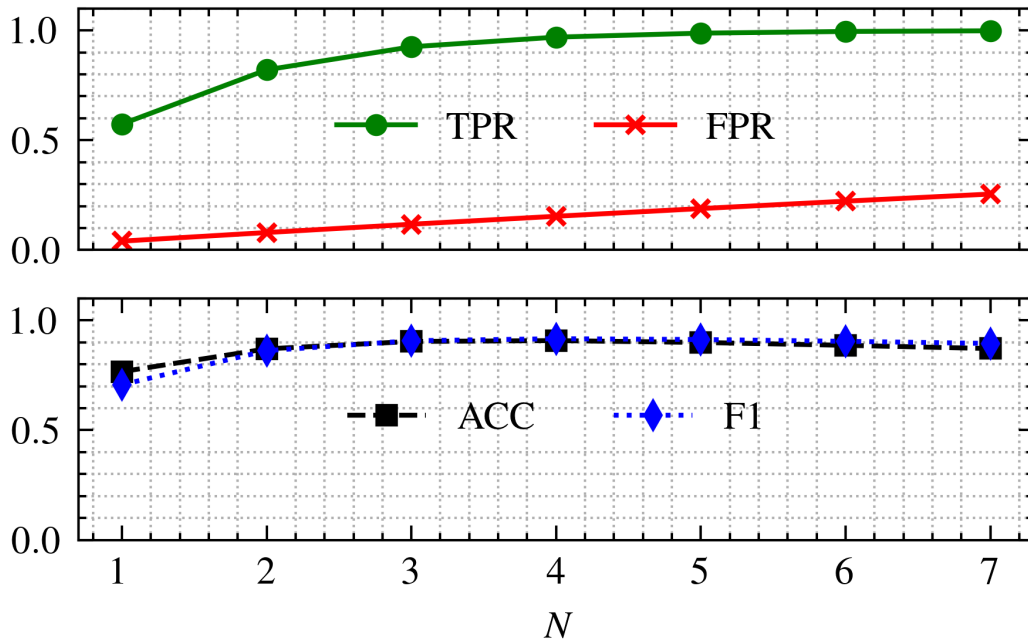
Figure 4.5 Classification results using N consecutive independent ring filtered responses of the same scene type. TPR: True Positive Rate. FPR: False Positive Rate. ACC: Accuracy. F1: F1-score. Image [94] © 2023 IEEE.

While the above results indicate that the simple threshold classifier performs well, one inevitable challenge with this approach to classification is the contribution of outliers in the training data set causing the exact value of the threshold to be significantly shifted, therefore degrading the classification. Another potential issue is when the two considered classes are not linearly separable in the training feature space. This could be due to an extremely complex decision boundary being required or the boundary might not exist. In addition, while classifying N consecutive responses provides opportunity to improve the overall performance, this approach only works when a classifier's performance on a single response is robust; and classifying on multiple consecutive responses can lead to longer screening time which can be undesirable. Therefore, two new classifiers were considered as potential alternatives to address the above concerns and to complement the investigation of the privacy preserving contraband detection technique.

The first classifier considered is the K-nearest neighbor (KNN) classifier [85, 71]. For an incoming unknown data point, the KNN classifier operates by considering K-nearest data points in the training feature space that are local to the unknown point where the classification outcome is based on the majority class type among the K-nearest neighboring points in the training data set. It is noted that while KNN can be more robust to potential outliers in the training data set as it benefits from the clustering effect of the data points rather than drawing specific decision boundary, it has an inherent drawback of higher computational expense due to the process of evaluating the nearest neighboring points as well as additional computational cost with increasing K values.

The second considered classifier is the support vector machine (SVM) using radial basis function (RBF) [95, 96, 97]. SVM is a technique that seeks to find the best hyperplane (i.e., decision boundary) that maximizes the distance between the training points of the classes. When the two considered classes are not linearly separable in the original feature space, a kernel function is typically applied to transform the original feature space into a higher-dimensional feature space where the points between the two classes become linearly separable. One such kernel function is the RBF that is also commonly known as the Gaussian radial basis kernel. During the classifier training stage, the SVM-RBF determines the proper regularization parameters such that the width of the

100

kernel function (i.e., RBF) is neither too wide nor too narrow which controls how much influence the training points have on the overall classifier. Once an RBF is determined, the SVM algorithm identifies the best hyperplane in the higher-dimensional feature space. During the classification stage, an incoming unknown data is transformed to the higher-dimensional feature space by the trained RBF and classified against the trained hyperplane/decision boundary.

The same Monte Carlo simulation configuration (i.e., number of iterations and training-testing data split) was applied to both the KNN and SVM-RBF classifiers. For the KNN classifier, five values of $K = [7, 9, 11, 13, 15]$ were considered. For the SVM-RBF classifier, the regularization parameters controlling the RBF are determined per iteration using a logarithmic grid search approach to maximize the accuracy of the classifier based on the training data set. The corresponding results are shown in Figure 4.6 and summarized in Table 4.1 and Table 4.2. Figure 4.6 is commonly known as the receiver operating characteristic (ROC) curve [84] that can be used to complement the evaluation of a classifier's performance. The ROC curve has two dimensions both ranging from 0 to 1 where the FPR and TPR are associated with the horizontal and vertical dimension, respectively. An ideal classifier will reside exactly at the upper left corner of an ROC curve (FPR = 0, TPR = 1) suggesting that a classifier's performance can be determined by how close its ROC is to the ideal classifier. On the contrary, the lower right corner of an ROC curve (FPR = 1, TPR = 0) represents the worst classifier. The diagonal line (magenta-dashed) in Figure 4.6 connecting (FPR = 0, TPR = 0) and (FPR = 1, TPR = 1) is also important as an ROC value residing on this line is equivalent to a classifier that is based on a random guess process, hence, a good classifier should always be above and away from this line. As discussed earlier for the threshold classifier, it can be seen that TPR improves as N increases but at the cost of increasing FPR. This is also illustrated in Figure 4.6 where the ROC of the threshold classifier approaches the ideal classifier as N increases until around $N = 4$ where it starts moving away as N continues to increase. Furthermore, at $N = 4$, it is noted that the ACC and F1 peak at 0.908 and 0.916, respectively. For the KNN classifier, it can be seen that FPR improves (i.e., decreasing) as the number of considered K neighbors increases but at the cost of decreasing TPR. Nevertheless, the KNN classifier's performance with $K = 15$ is

similar to that of the threshold classifier with $N = 1$ where the FPR improves by -0.017 (approximately $+41.5\%$) at the cost of a lower TPR by -0.027 (approximately -4.7%). For the SVM-RBF classifier, when compared to the threshold classifier with $N = 1$, the TPR improves by $+0.047$ (approximately $+8.2\%$) but with significant higher FPR by $+0.077$ which is at least one order of magnitude worse than the threshold classifier of $N = 1$.

Scenario	TPR	FPR	ACC	F1
THR (N=1)	0.574	0.041	0.766	0.707
THR (N=2)	0.820	0.080	0.870	0.862
THR (N=3)	0.925	0.118	0.904	0.907
THR (N=4)	0.969	0.154	0.908	0.916
THR (N=5)	0.987	0.189	0.899	0.913
THR (N=6)	0.995	0.223	0.886	0.905
THR (N=7)	0.998	0.255	0.872	0.895
KNN (K=7)	0.616	0.133	0.741	0.702
KNN (K=9)	0.598	0.101	0.749	0.702
KNN (K=11)	0.580	0.069	0.756	0.701
KNN (K=13)	0.562	0.042	0.760	0.698
KNN (K=15)	**0.547**	**0.024**	**0.762**	**0.694**
SVM-RBF	0.621	0.118	0.752	0.714

Table 4.1 Averaged classifier metrics based on the reported 10 000 Monte Carlo simulations shown in Figure 4.6. Bold represents the best performing classification scenario based on a single response. THR: Threshold.
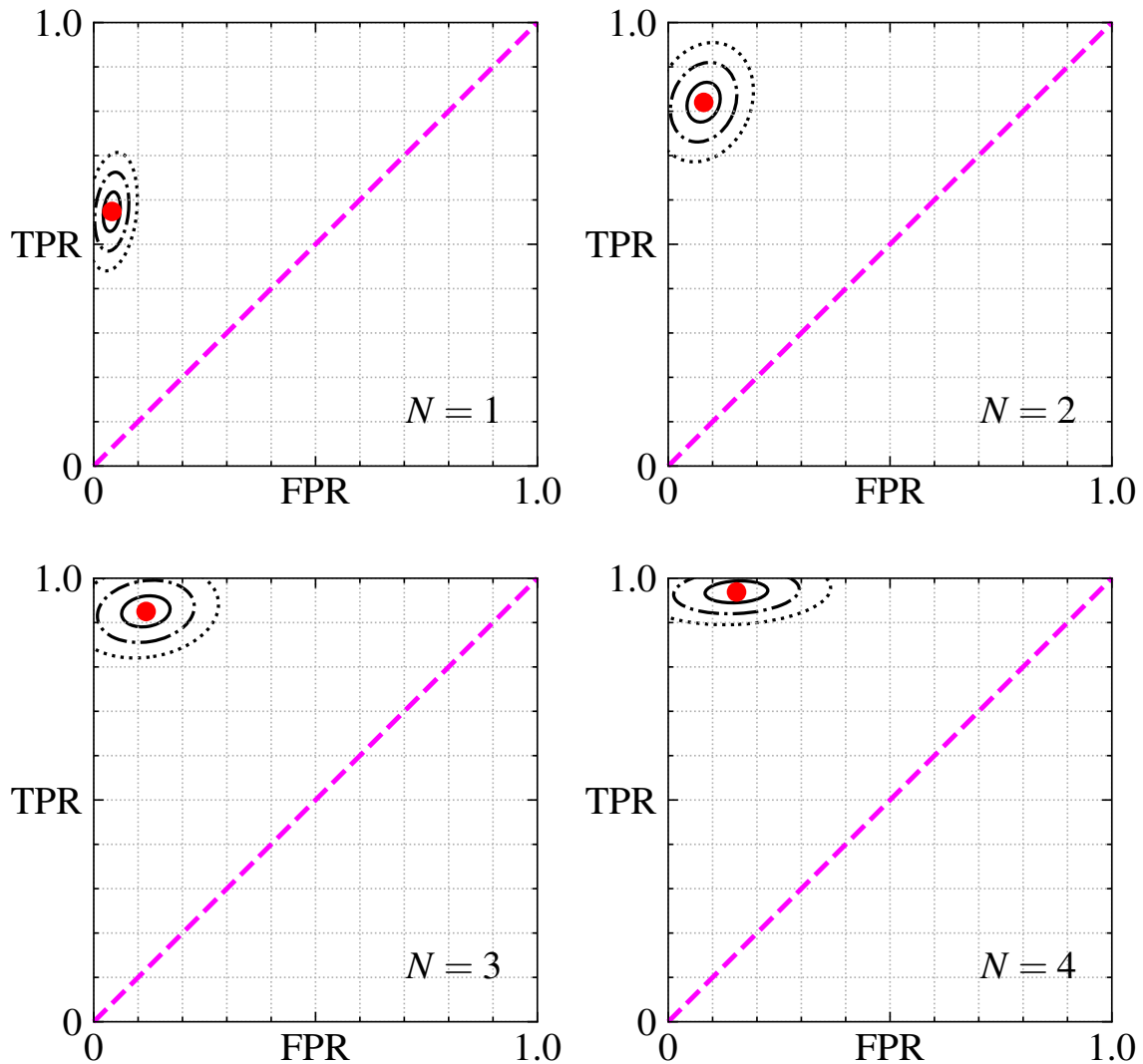
Figure 4.6 Receiving operating characteristic (ROC) curves of the 10 000-iteration Monte Carlo analysis on the experiment described in Figure 4.2 using the threshold classifiers (red circle markers), K-nearest neighbor (KNN) classifiers (blue triangle markers), and support vector machine (SVM) using radial basis function (RBF) (green diamond marker). A magenta dashed line is shown to demonstrate the random guess process. The solid black, dash-dot black, and dotted black lines represent the one, two, and three standard deviation (σ) contours for a particular classifier.

Figure 4.6 (cont'd)
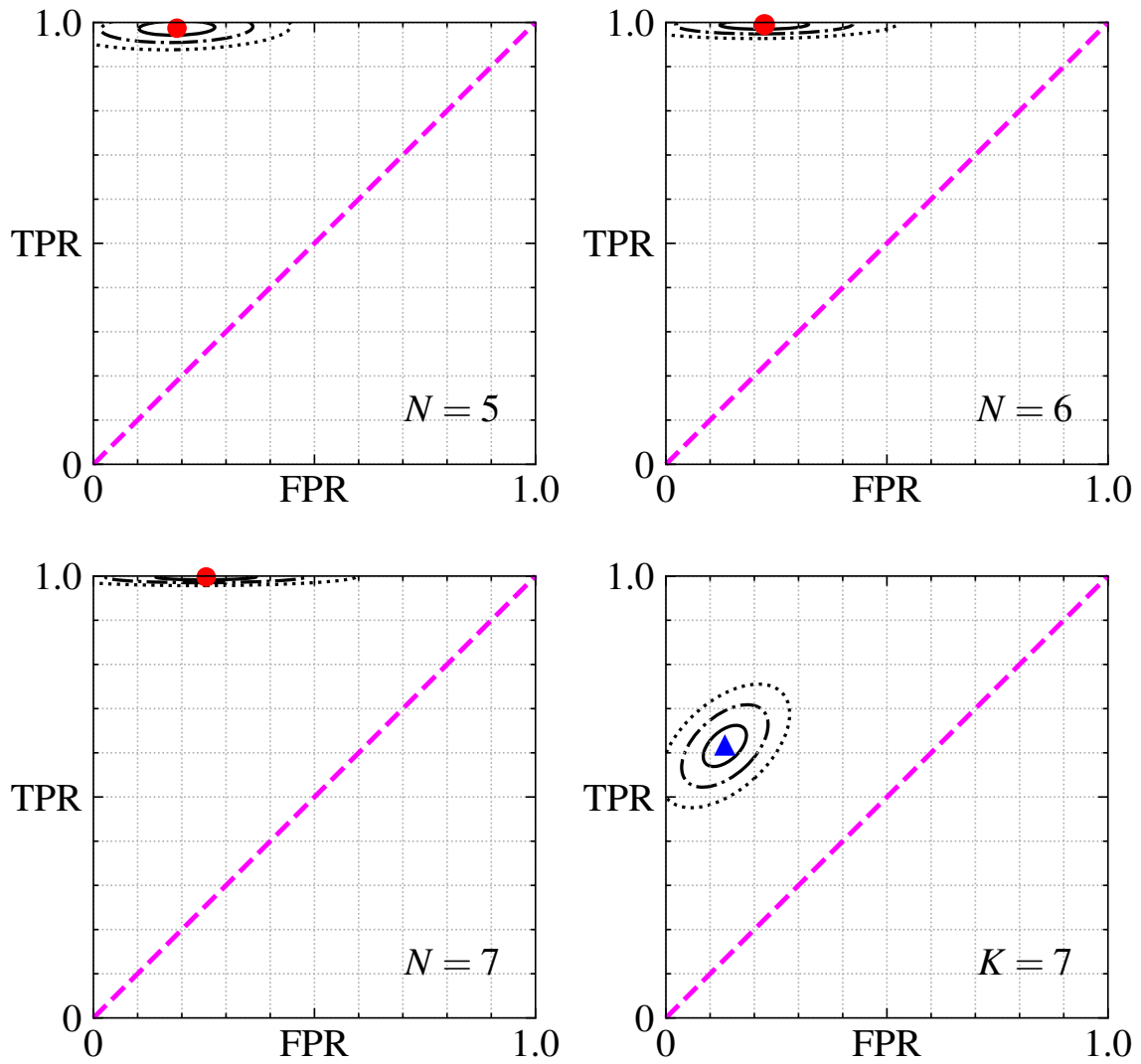
Figure 4.6 (cont'd)
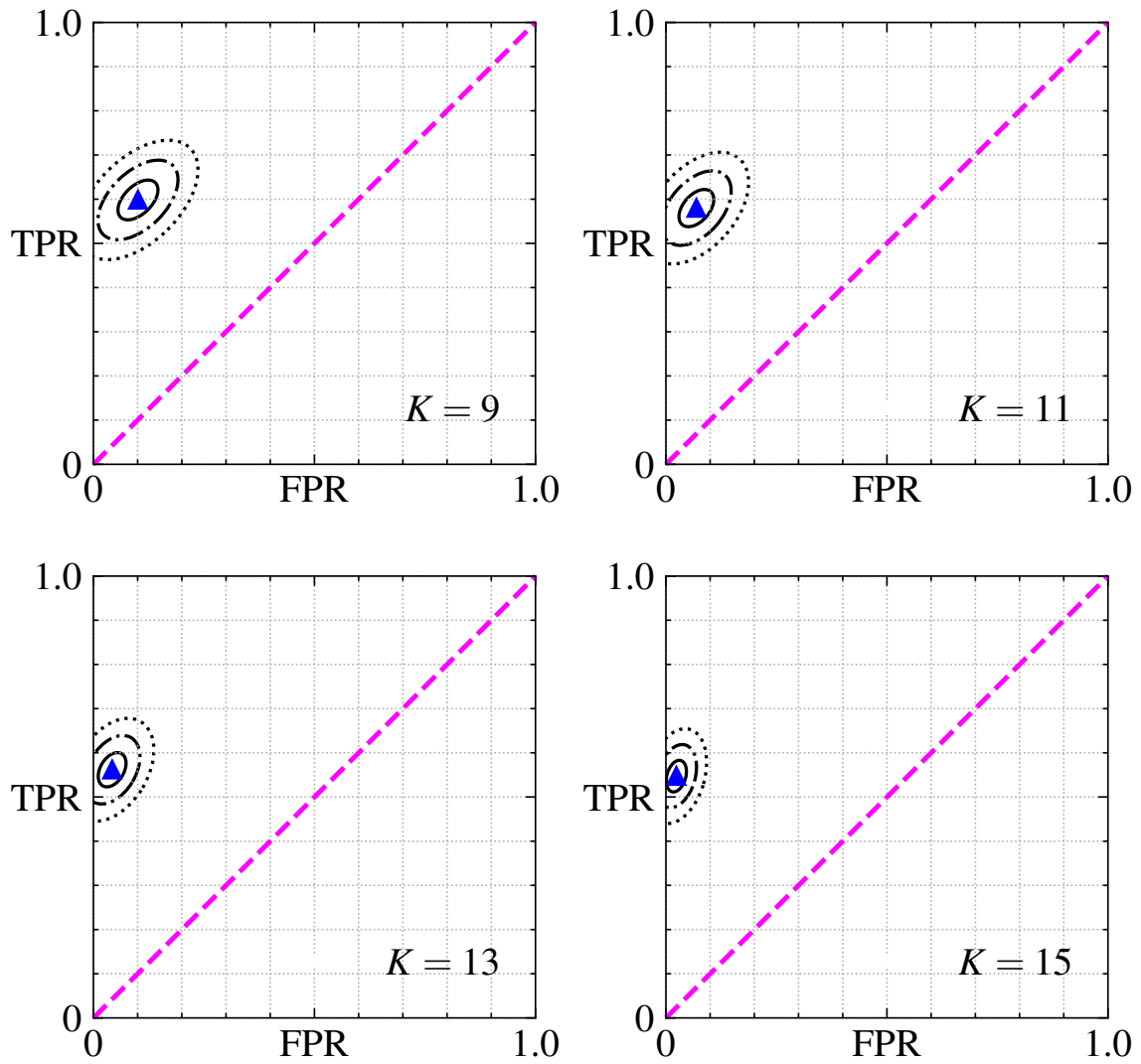
Figure 4.6 (cont'd)
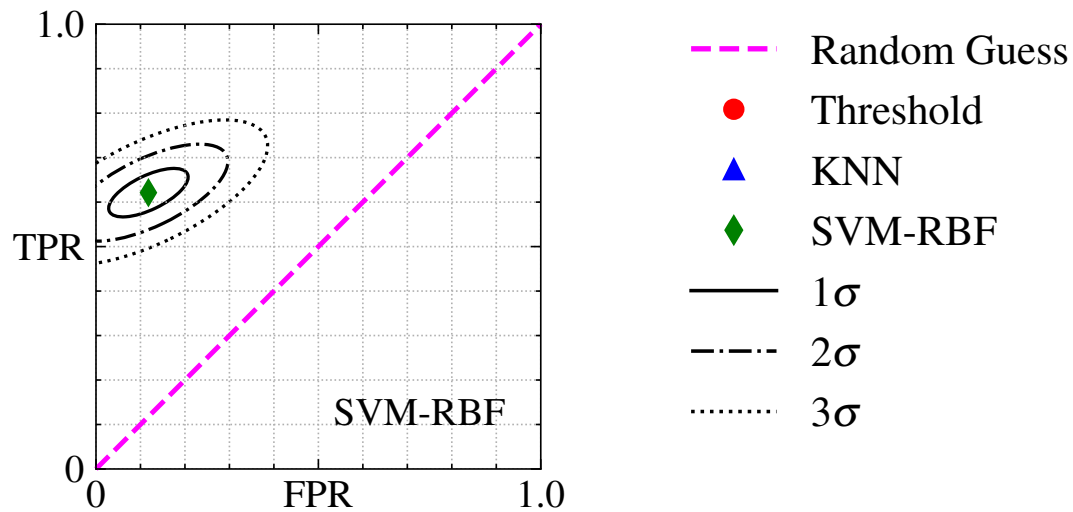
Scenario	σ_{TPR}	σ_{FPR}	σ_{ACC}	σ_{F1}
THR (N=1)	0.037	0.089	0.045	0.070
THR (N=2)	0.071	0.093	0.053	0.059
THR (N=3)	0.069	0.110	0.060	0.057
THR (N=4)	0.049	0.142	0.072	0.062
THR (N=5)	0.033	0.172	0.086	0.071
THR (N=6)	0.021	0.201	0.100	0.080
THR (N=7)	0.013	0.227	0.113	0.088
KNN (K=7)	0.066	0.118	0.047	0.059
KNN (K=9)	0.063	0.111	0.045	0.059
KNN (K=11)	0.060	0.099	0.042	0.059
KNN (K=13)	0.053	0.084	0.040	0.058
KNN (K=15)	**0.043**	**0.073**	**0.036**	**0.057**
SVM-RBF	0.077	0.195	0.068	0.064

Table 4.2 Standard deviations on the classifier metrics on the reported 10 000 Monte Carlo simulations shown in Figure 4.6. Bold represents the best performing classification scenario based on a single response. THR: Threshold.

4.1.4 Robustness of Different Classifiers

In the above analysis, I investigated the performance of three common classifiers focusing on the two classes where the subject and object were kept the same while their orientation and placement were varied between subsequent measurements as a means to introduce uncertainties in the measured scene. In this part, I investigate the robustness of the aforementioned classifiers that are trained based on the full experiment described in Figure 4.2 and that the incoming unknown measurements are based on different subjects and/or objects.

The additional subject and objects considered for this analysis are illustrated in Figure 4.7. The additional subject, Subject 2, is the same clothed fiberglass mannequin but with its back toward the dynamic antenna array. The consideration of a different subject is to investigate the changing scattered responses due to different surface profiles of the measured primary background which can be expected as a security screening system is likely to encounter various subject profiles. Furthermore, the two additional considered objects are all metallic. Object 2 is an object with a similar vertical dimension as Object 1 at 45 mm×202 mm; and Object 3 has similar dimensions as Object 1 at 193 mm×253 mm. Note that Object 1 is the considered gun-shaped object with a dimension of 164 mm×235 mm in Figure 4.2. While this work focuses on gun-sized metal objects for a proof-of-concept, the approach is applicable to the detection of smaller objects and dielectric objects providing sufficient SNR. Previously, our research group demonstrated the ability to image dielectric objects using active incoherent millimeter-wave imaging, which is based on the same concept as the work in this paper [98, 99], thus detection of such objects with the imageless system, described herein should also be feasible.

Figure 4.7 **Top**: Subjects considered. Subject 1: clothed fiberglass mannequin with its front toward the dynamic antenna array. Subject 2: clothed fiberglass mannequin with its back toward the dynamic antenna array. **Center**: Metallic objects considered for the experiments. Object 1: a gun-shaped object with a dimension of 164 mm×235 mm. Object 2: an object with a similar vertical dimension as Object 1 at 45 mm×202 mm. Object 3: an object with similar dimensions as Object 1 at 193 mm×253 mm. **Bottom**: Examples of the measured subject and object combination. From left to right: Subject 2 with no object underneath clothing; Subject 2 with Object 2 underneath clothing; and Subject 2 with Object 3 underneath clothing. Note that the optically opaque clothing for the figures are shown transparent to demonstrate the presence and/or the types of concealed object underneath clothing.

The following scenarios, each will be referred to as a numbered experiment, were investigated where the training data set is the full measurements described in Figure 4.2 and the incoming unknown data set for the implemented classifiers are from

1. Experiment 2: 80 measurements of only Subject 2 as the non-contraband class and 80 measurements of Subject 2 and Object 1 as the contraband class;

2. Experiment 3: 80 measurements of only Subject 2 as the non-contraband class and 80 measurements of Subject 2 and Object 2 as the contraband class; and

3. Experiment 4: 80 measurements of only Subject 2 as the non-contraband class and 80 measurements of Subject 2 and Object 3 as the contraband class.

Note that given the independent investigation among the three described experiments above, the 80 measurements of only Subject 2 is common. Furthermore, similar practices are conducted where the mannequin was removed and replaced to mimic the uncertainties of a practical scenario where the test subject's relative orientation to the dynamic antenna array, the object was randomly placed beneath the clothing at varying directions. The mannequin with and without the object was approximately 1.83 m from the dynamic antenna array and was backed by walls of radio-frequency absorbers. Lastly, the two receivers of the array were kept the same at 77λ apart at 75 GHz.

In Experiment 2, the consideration explores the robustness of the three classifiers (i.e., simple threshold, KNN, and SVM-RBF) when the measured subject has a different scattering profile (i.e., front versus back of the fiberglass mannequin) while keeping the same considered concealed object (i.e., gun-shaped object). The results are shown in Figure 4.8 and summarized in Table 4.3. From Figure 4.8, it is observed that the ROC for all considered classifiers operating on a single response are above the random guess process where the best performing classifier is the KNN classifier with $K = 11$ with an ACC = 0.725 and F1 = 0.662 considering its ROC of FPR = 0.088 and TPR = 0.538. For the threshold classifier, it is verified that when the single response classifier ($N = 1$) is associated with undesirable ROC (i.e., FPR = 0.438, TPR = 0.638), operating the classifier on N consecutive measured responses will only degrade the classifier performance as the

ROC begins to shift away from the ideal classifier's ROC as N increases. One possible explanation for the threshold classifier's undesirable performance is because the distribution based on the magnitude of the 11-feature space vector for the two classes in the training set is slightly different than that of the testing set. This is shown in the top and bottom of Figure 4.9 for the class where the subject conceals the gun-shaped object (red and cyan) and the class with only the subject (green and magenta), respectively. The general distribution is similar when Object 1 (gun-shape) is concealed by Subject 1 (red) and Subject 2 (cyan). However, when the concealed object is not presented, it is evident that Subject 2 (magenta) has a slightly higher response than that of Subject 1 (green). This means that the threshold value determined by training against measurements from Experiment 1 will be undesirably low when classified against measurements from Experiment 2, hence, explains the increase in the FPR of the single response threshold classifier. Furthermore, it is also evident from Figure 4.9 that the general clustering of the two classes are similar between measurements from Experiment 1 and Experiment 2, hence, explains why the KNN classifier has comparably lower FPR. Similar as observed in the previous analysis (i.e., Figure 4.6), for the KNN classifier, FPR improves (i.e., decreasing) as the number of considered K neighbors increases but at the cost of decreasing TPR. Of all KNN classifiers, the setup where $K = 11$ has the best performance with a TPR = 0.538, FPR = 0.088 resulting in an accuracy and F1-score of 0.725 and 0.662, respectively. The SVM-RBF classifier also outperforms the threshold method with a TPR = 0.625, FPR = 0.225 resulting in an accuracy and F1-score of 0.700 and 0.676, respectively. In this analysis, it is observed that even when the same concealed object is considered, the difference between the primary backgrounds, Subject 1 and Subject 2, can introduce shifts in the distribution of the Fourier-domain features extracted from the dynamic antenna array's captured responses. Such shifts in the feature space can potentially post challenges to a classifier's performance (i.e., threshold approach [94]). Therefore, the choice of the implemented classifier, e.g., KNN, shall also be considered as a way to alleviate the possible challenges.

110
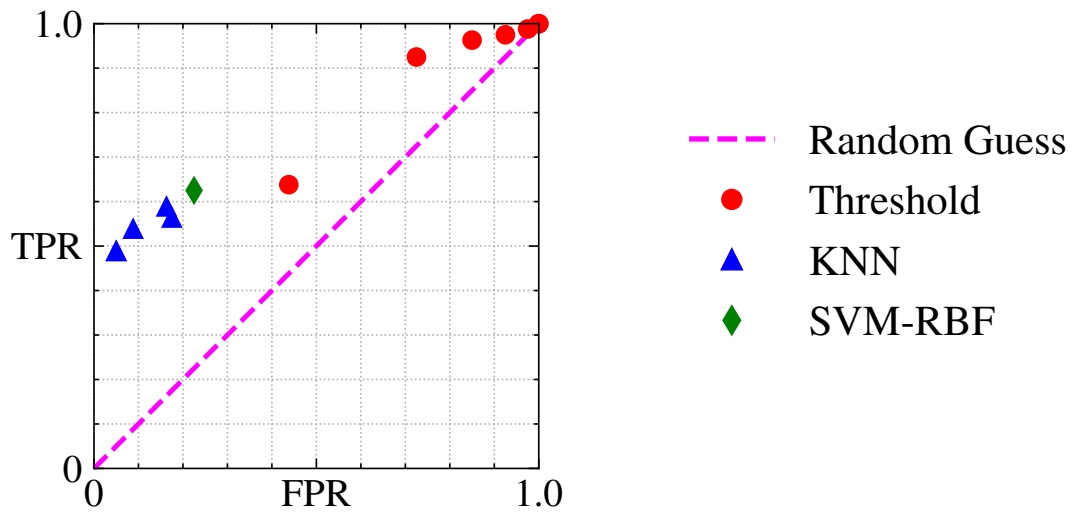
Figure 4.8 ROC curves of the classifier performance using measurements from Figure 4.2 for training and measurements from Experiment 2 for testing. TPR: true positive rate. FPR: false positive rate. KNN: K-nearest neighbor. SVM-RBF: support vector machine using radial basis function.

Scenario	TPR	FPR	ACC	F1
THR (N=1)	0.638	0.438	0.600	0.615
THR (N=2)	0.925	0.725	0.600	0.698
THR (N=3)	0.963	0.850	0.556	0.684
THR (N=4)	0.975	0.925	0.525	0.672
THR (N=5)	0.988	0.975	0.506	0.667
THR (N=6)	1.000	1.000	0.500	0.667
THR (N=7)	1.000	1.000	0.500	0.667
KNN (K=7)	0.588	0.163	0.713	0.671
KNN (K=9)	0.563	0.175	0.694	0.648
KNN (K=11)	**0.538**	**0.088**	**0.725**	**0.662**
KNN (K=13)	0.488	0.050	0.719	0.634
KNN (K=15)	0.488	0.050	0.719	0.634
SVM-RBF	0.625	0.225	0.700	0.676

Table 4.3 Summary of Figure 4.8. Bold represents the best performing classification scenario based on a single response. THR: Threshold.
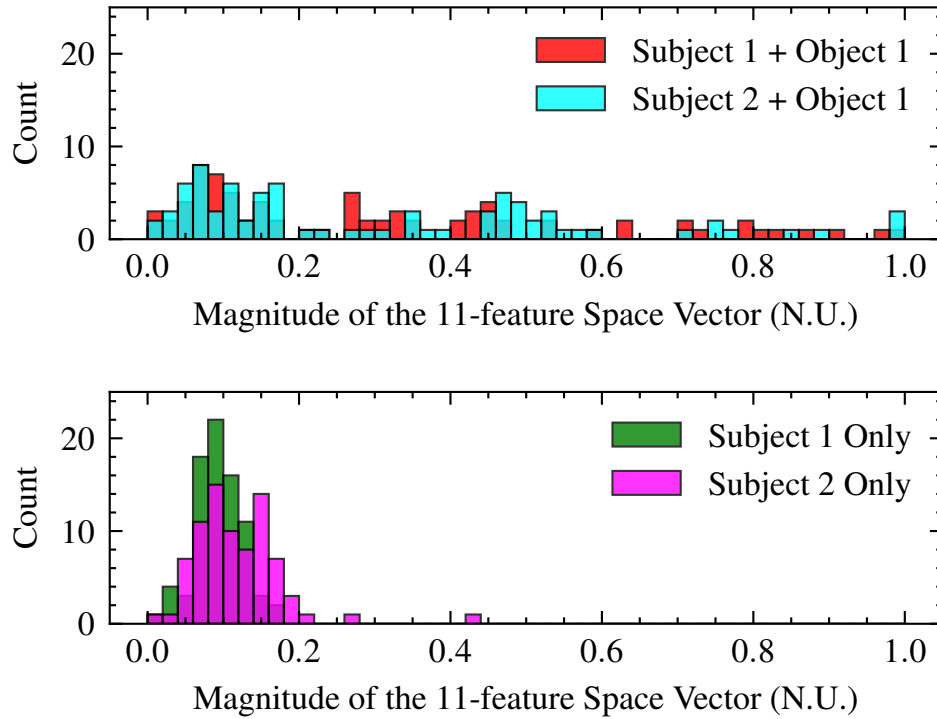
Figure 4.9 Comparison on the magnitude of the 11-feature space vector between measurements from Figure 4.2 and Experiment 2. **Top**: distribution comparison of Object 1 concealed by either Subject 1 (red) or Subject 2 (cyan) showing similar distribution. **Bottom**: distribution comparison of Subject 1 (green) and Subject 2 (magenta) with no object being concealed showing that distribution of only Subject 2 being presented is slightly shifted from Subject 1 only, hence, a possible reason to the degradation on the classifier performance using the threshold method (Figure 4.8 and Table 4.3). N.U.: Normalized Units.

In Experiment 3 and Experiment 4, both considerations explore the robustness of the three classifiers when both the measured subject and object have a different scattering profile (i.e., front versus back of the fiberglass mannequin while considering different concealed objects) that contribute to the overall varying scattering responses measured by the dynamic antenna array.

For Experiment 3, the results are shown in Figure 4.10 and summarized in Table 4.4. From Figure 4.10, it is observed that the ROC for all considered classifiers operating on a single response are above the random guess process where the best performing classifier is the KNN classifier with K = 15 with an ACC = 0.813 and F1 = 0.833 considering its ROC of FPR = 0.313 and TPR = 0.938.

For Experiment 4, the results are shown in Figure 4.11 and summarized in Table 4.5. From Figure 4.11, it is observed that the ROC for all considered classifiers operating on a single response are above the random guess process where the best performing classifier is the KNN classifier with K = 15 with an ACC = 0.856 and F1 = 0.841 considering its ROC of FPR = 0.050 and TPR = 0.763.

In both analyses, for the KNN classifier, the relationship between increasing K and decreasing TPR, and increasing K and decreasing FPR are again observed similar to that discussed in previous sections. It is noted that the SVM-RBF classifier yields the worst performance in the Experiment 3. In Experiment 4, the outcomes between the SVM-RBF classifier and the threshold classifier with N = 1 are similar. From the above analyses, it is observed that even when the training data are completely different from the incoming unknown data (i.e., both the screened subject and object), the choice of a robust classifier is important. Furthermore, they also demonstrate that the proposed privacy-preserving imageless contraband detection technique has the ability to accommodate for wider screened subject and object combination which is important for practical implementation.
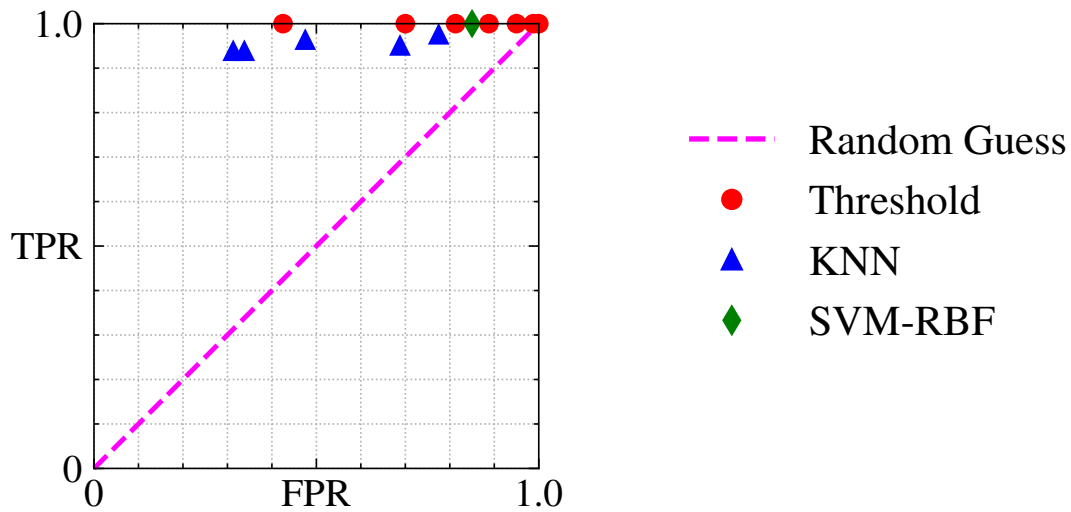
Figure 4.10 ROC curves of the classifier performance using measurements from Figure 4.2 for training and measurements from Experiment 3 for testing. TPR: true positive rate. FPR: false positive rate. KNN: K-nearest neighbor. SVM-RBF: support vector machine using radial basis function.

Scenario	TPR	FPR	ACC	F1
THR (N=1)	1.000	0.425	0.788	0.825
THR (N=2)	1.000	0.700	0.650	0.741
THR (N=3)	1.000	0.813	0.594	0.711
THR (N=4)	1.000	0.888	0.556	0.693
THR (N=5)	1.000	0.950	0.525	0.678
THR (N=6)	1.000	0.988	0.506	0.670
THR (N=7)	1.000	1.000	0.500	0.667
KNN (K=7)	0.975	0.775	0.600	0.709
KNN (K=9)	0.963	0.475	0.744	0.790
KNN (K=11)	0.950	0.688	0.631	0.720
KNN (K=13)	0.938	0.338	0.800	0.824
KNN (K=15)	**0.938**	**0.313**	**0.813**	**0.833**
SVM-RBF	1.000	0.850	0.575	0.702

Table 4.4 Summary of Figure 4.10. Bold represents the best performing classification scenario based on a single response. THR: Threshold.
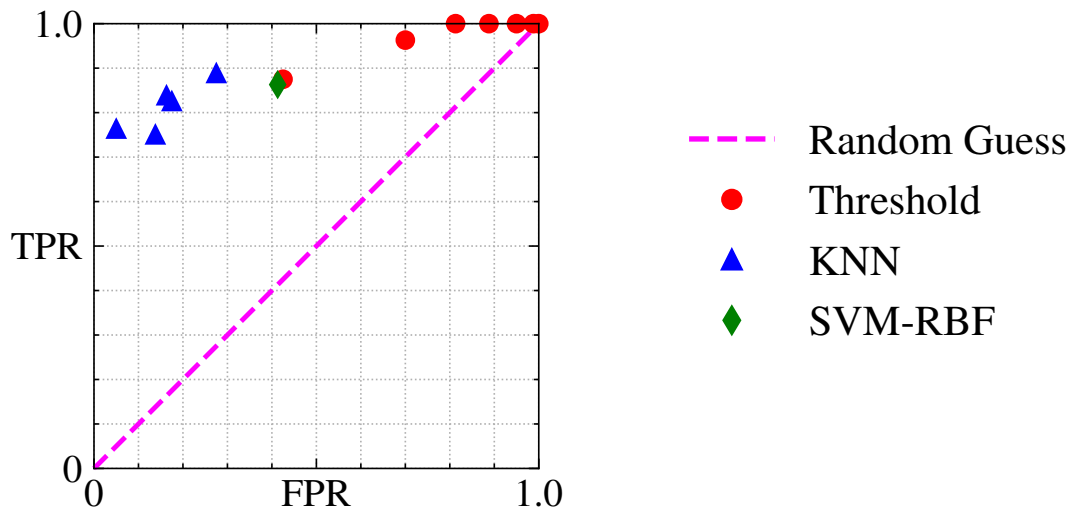
Figure 4.11 ROC curves of the classifier performance using measurements from Figure 4.2 for training and measurements from Experiment 3 for testing. TPR: true positive rate. FPR: false positive rate. KNN: K-nearest neighbor. SVM-RBF: support vector machine using radial basis function.

Scenario	TPR	FPR	ACC	F1
THR (N=1)	0.875	0.425	0.725	0.761
THR (N=2)	0.963	0.700	0.631	0.723
THR (N=3)	1.000	0.813	0.594	0.711
THR (N=4)	1.000	0.888	0.556	0.693
THR (N=5)	1.000	0.950	0.525	0.678
THR (N=6)	1.000	0.988	0.506	0.670
THR (N=7)	1.000	1.000	0.500	0.667
KNN (K=7)	0.888	0.275	0.806	0.821
KNN (K=9)	0.825	0.175	0.825	0.825
KNN (K=11)	0.838	0.163	0.838	0.838
KNN (K=13)	0.750	0.138	0.806	0.795
KNN (K=15)	**0.763**	**0.050**	**0.856**	**0.841**
SVM-RBF	0.863	0.413	0.725	0.758

Table 4.5 Summary of Figure 4.11. Bold represents the best performing classification scenario based on a single response. THR: Threshold.

4.2 Applicability Involving a Real Person

Up to this point in this dissertation, all investigations involving the dynamic antenna array assume that the quasi-static scene condition is maintained. However, this assumption is unlikely to be satisfied regardless of how fast the implemented array dynamics is when the measured scene involves a real person, which is a more practical scenario involved in security screening application as breathing and/or torso movements can happen at any instance even during the fast array dynamics screening process. In this part, I investigate the validity of the imageless contraband detection approach where the involved screening subject is a real person and the considered contraband gun-shaped object is metallic by exploring various classification algorithms applied to the extracted arithmetic features.

4.2.1 Experiment Setup

In this experiment, as shown in Figure 4.12, the considered subject is a real person and the considered object is the same metallic gun-shaped object used in the previous analyses. The person with and without the object was approximately 1.83 m from the dynamic antenna array and was backed by walls of radio-frequency absorbers. Furthermore, the generated ring filter for each measurement is based on the two receivers of the rotational dynamic antenna array with a separation of 77λ at 75 GHz. The two classes considered are the non-contraband class involving only the person and the contraband class where the metallic gun-shape is concealed beneath clothing by the person. In total, 80 measurements for each class were taken. Between each successive measurement, the object was randomly placed beneath the clothing at varying directions.

Figure 4.12 **Left**: The subject for the imageless contraband detection experiment which is a real person. **Right**: The object for the imageless contraband detection experiment which is a metallic gun-shape with a dimension of 164 mm×235 mm. Originally submitted to *IEEE Access*, April 2024.

4.2.2 Performance and Robustness of Different Classifiers

The results of the threshold classifiers are shown in Figure 4.13 comprising the receiver operating characteristic (ROC) curve [84] that are used to complement the evaluation of a classifier's performance. As observed, the threshold classifier failed to differentiate between the two measured classes regardless of the consideration of N consecutive measurements and that the outcome is similar to a random guess process as shown in Figure 4.13, and summarized in Table 4.6 and Table 4.7. It is noted the degradation of the threshold classifier can be related with motion of the person during the measurements. While in the analyses involving the mannequin, considerations were given by varying position and orientation of the measured subject and object, the scattering profile remains constant for any given measurement. This is no longer valid when the measured subject is a real person as a single measurement can capture various scattering profiles due to the person's movements. In Figure 4.14, the distribution of the heuristically determined 11 features are shown. In contrast to Figure 4.4, no apparent threshold value can be computed as a high level of overlapping between the two classes is observed. Unlike the threshold-based method, both the KNN classifier (for all considered K) and the SVM-RBF classifiers achieved comparably better performance. The SVM-RBF method is the best performing classifier with an ACC = 0.986 and F1 = 0.986 considering its ROC of FPR = 0.017 and TPR = 0.989. Furthermore, it is also noted that the SVM-RBF classifier exhibits the smallest standard deviation across the Monte Carlo simulation followed by the KNN classifier then the randomly guessing threshold classifier.
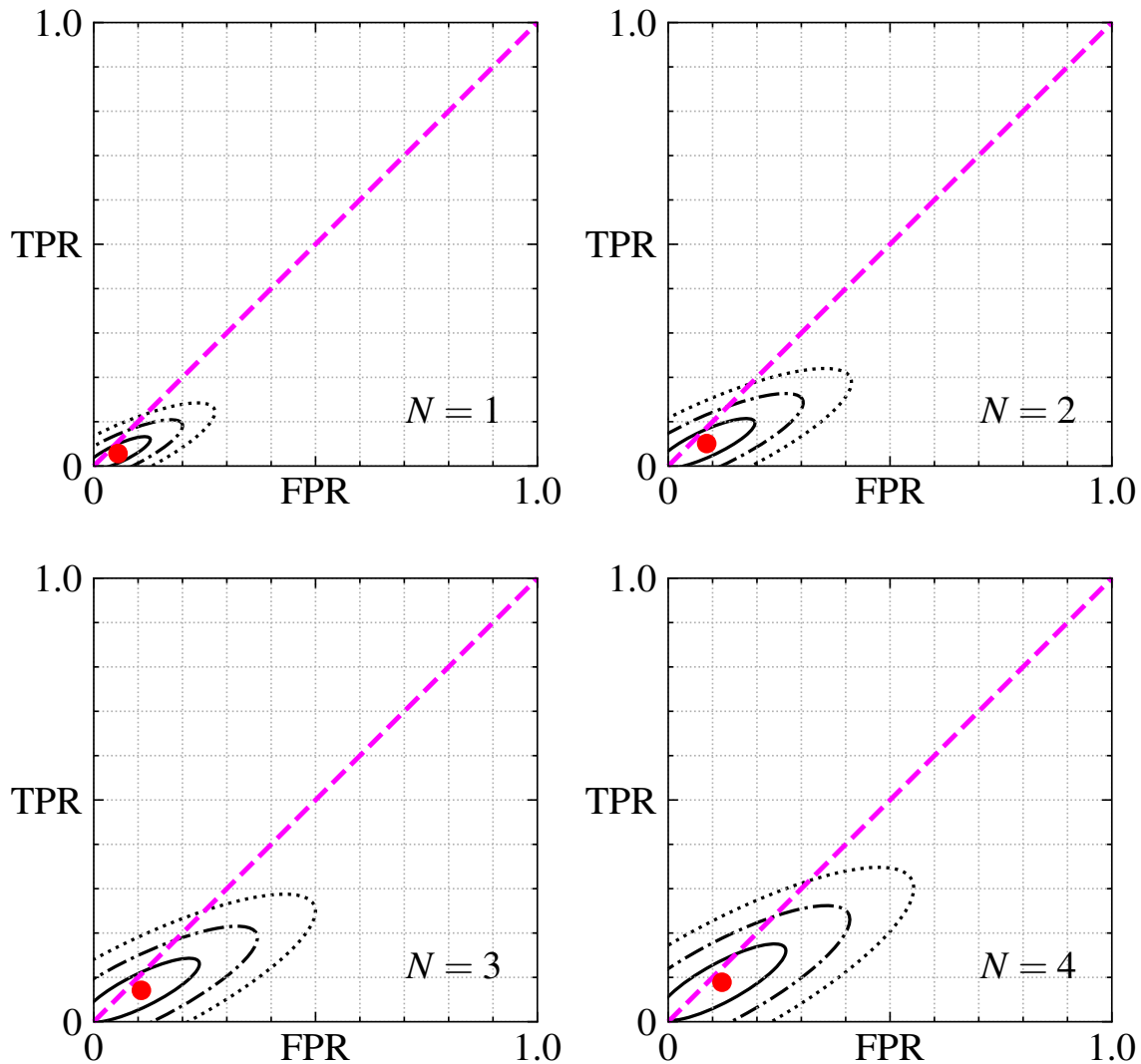
Figure 4.13 Receiving operating characteristic (ROC) curves of the 10 000-iteration Monte Carlo analysis on the experiment described in Figure 4.12 using the threshold classifiers (red circle markers), K-nearest neighbor (KNN) classifiers (blue triangle markers), and support vector machine (SVM) using radial basis function (RBF) (green diamond marker). A magenta dashed line is shown to demonstrate the random guess process. The solid black, dash-dot black, and dotted black lines represent the one, two, and three standard deviation (σ) contours for a particular classifier. Originally submitted to *IEEE Access*, April 2024.

Figure 4.13 (cont'd)
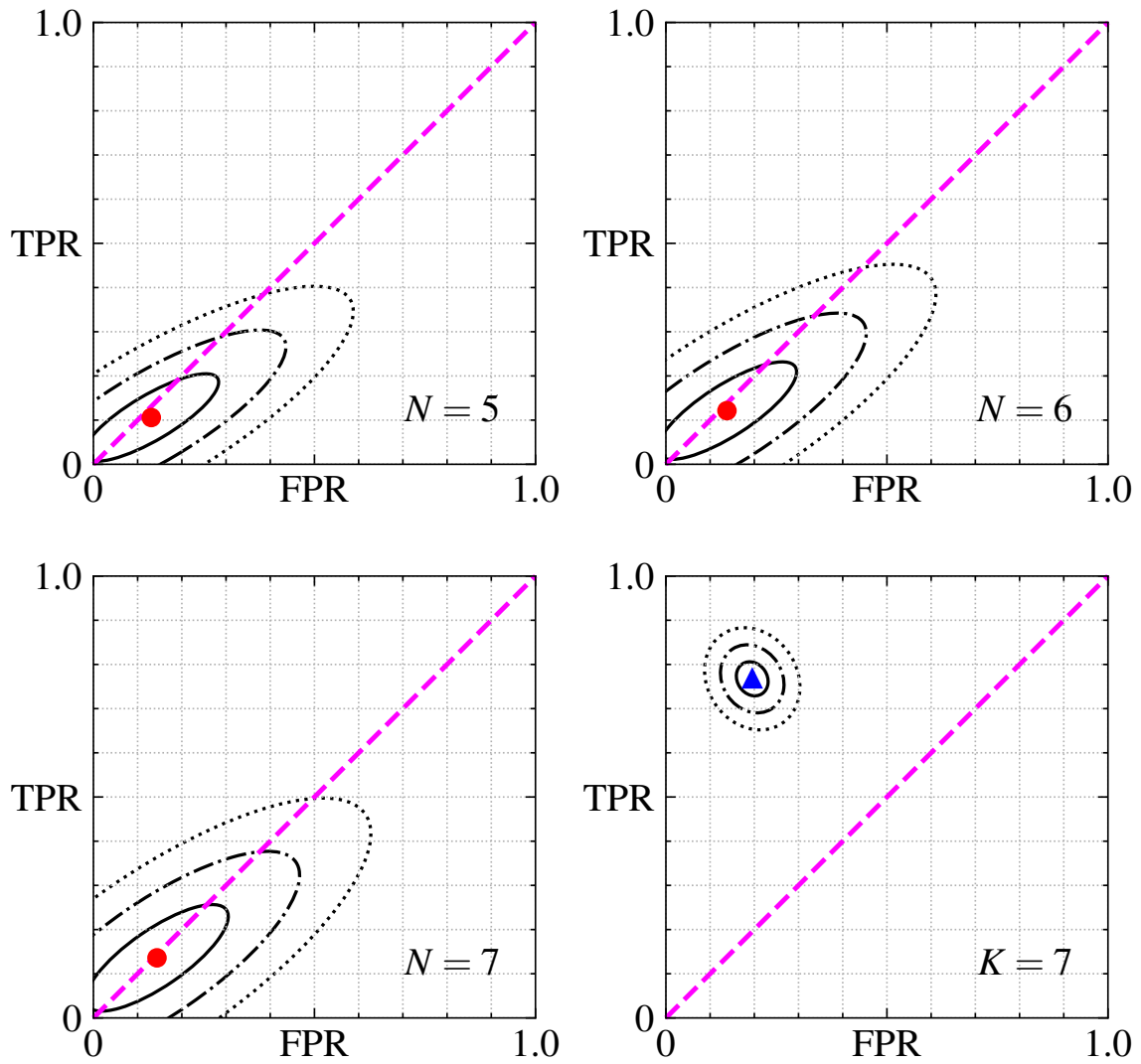
Figure 4.13 (cont'd)
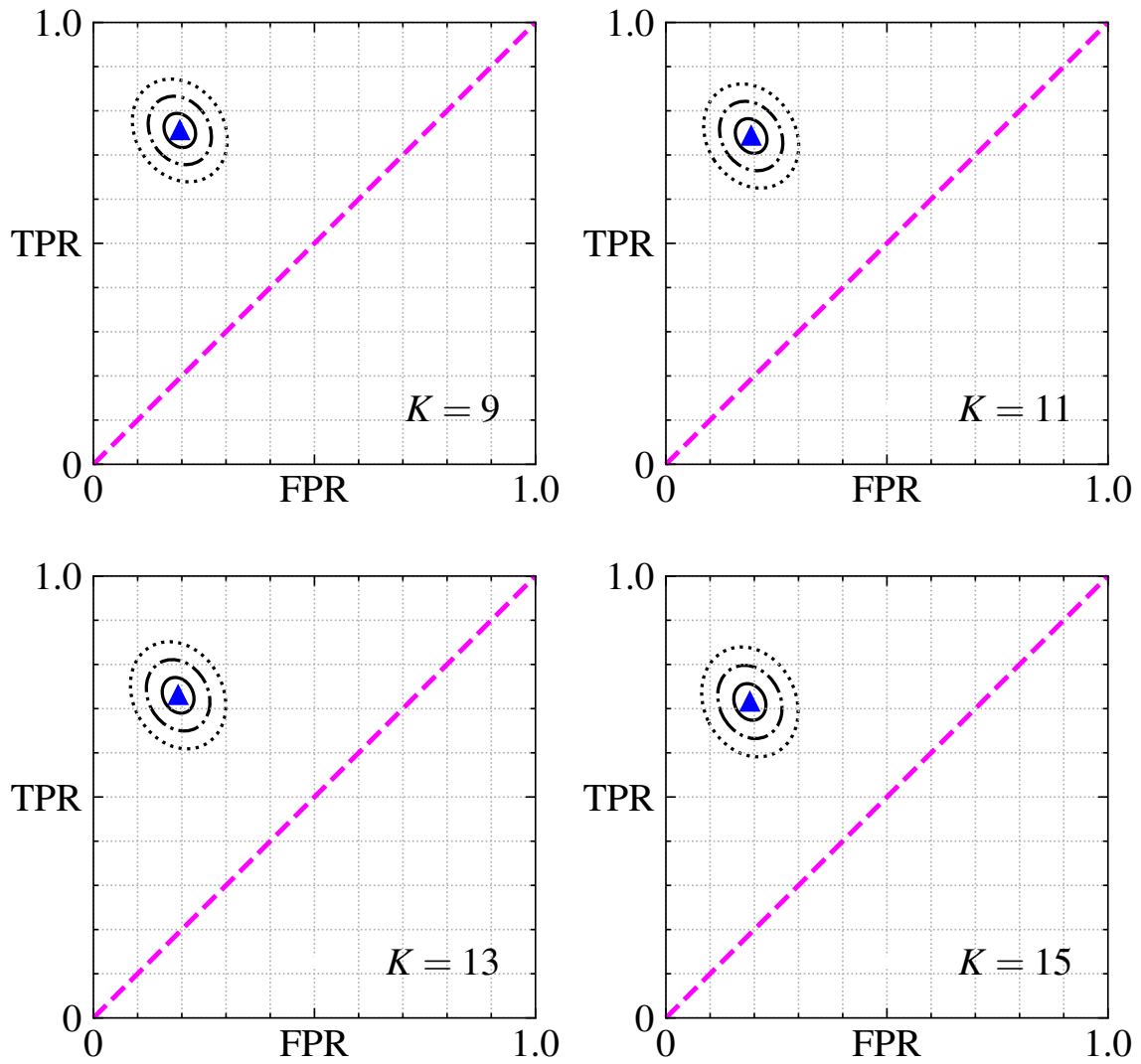
Figure 4.13 (cont'd)
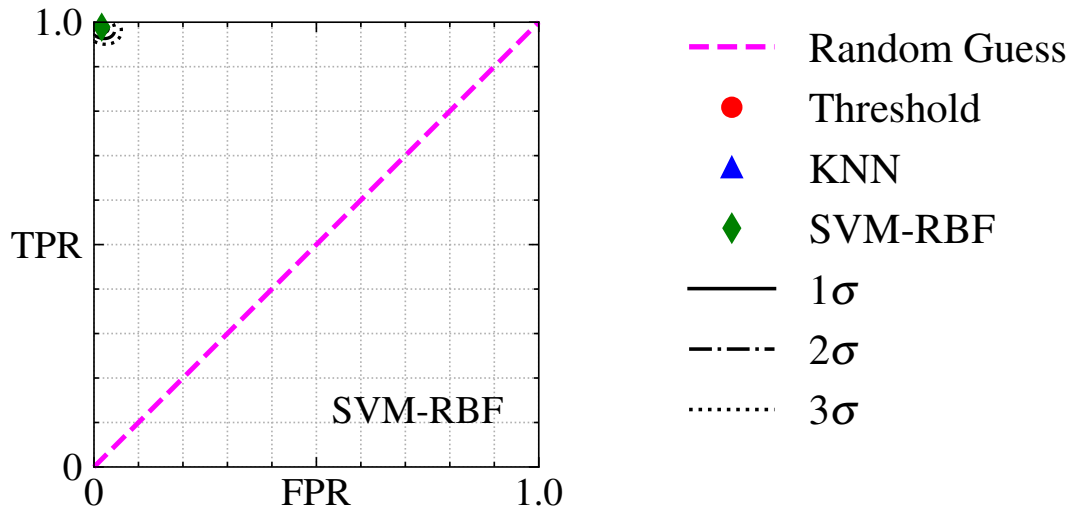
Scenario	TPR	FPR	ACC	F1
THR (N=1)	0.028	0.055	0.487	0.039
THR (N=2)	0.051	0.087	0.482	0.063
THR (N=3)	0.071	0.107	0.482	0.083
THR (N=4)	0.089	0.121	0.484	0.101
THR (N=5)	0.106	0.131	0.488	0.117
THR (N=6)	0.121	0.138	0.492	0.131
THR (N=7)	0.136	0.144	0.496	0.144
KNN (K=7)	0.767	0.195	0.786	0.781
KNN (K=9)	0.756	0.195	0.780	0.774
KNN (K=11)	0.743	0.193	0.775	0.767
KNN (K=13)	0.730	0.192	0.769	0.759
KNN (K=15)	0.715	0.190	0.763	0.750
SVM-RBF	**0.989**	**0.017**	**0.986**	**0.986**

Table 4.6 Averaged classifier metrics based on the reported 10 000 Monte Carlo simulations shown in Figure 4.13. Bold represents the best performing classification scenario based on a single response. THR: Threshold. Originally submitted to *IEEE Access*, April 2024.

Scenario	σ_{TPR}	σ_{FPR}	σ_{ACC}	σ_{F1}
THR (N=1)	0.040	0.159	0.047	0.076
THR (N=2)	0.060	0.238	0.071	0.110
THR (N=3)	0.074	0.290	0.082	0.137
THR (N=4)	0.088	0.324	0.089	0.161
THR (N=5)	0.102	0.349	0.093	0.183
THR (N=6)	0.115	0.367	0.097	0.203
THR (N=7)	0.128	0.382	0.102	0.221
KNN (K=7)	0.068	0.081	0.057	0.060
KNN (K=9)	0.066	0.082	0.058	0.061
KNN (K=11)	0.067	0.083	0.058	0.063
KNN (K=13)	0.068	0.085	0.059	0.065
KNN (K=15)	0.069	0.086	0.060	0.066
SVM-RBF	**0.024**	**0.031**	**0.021**	**0.021**

Table 4.7 Standard deviations on the classifier metrics on the reported 10 000 Monte Carlo simulations shown in Figure 4.13. Bold represents the best performing classification scenario based on a single response. THR: Threshold. Originally submitted to *IEEE Access*, April 2024.
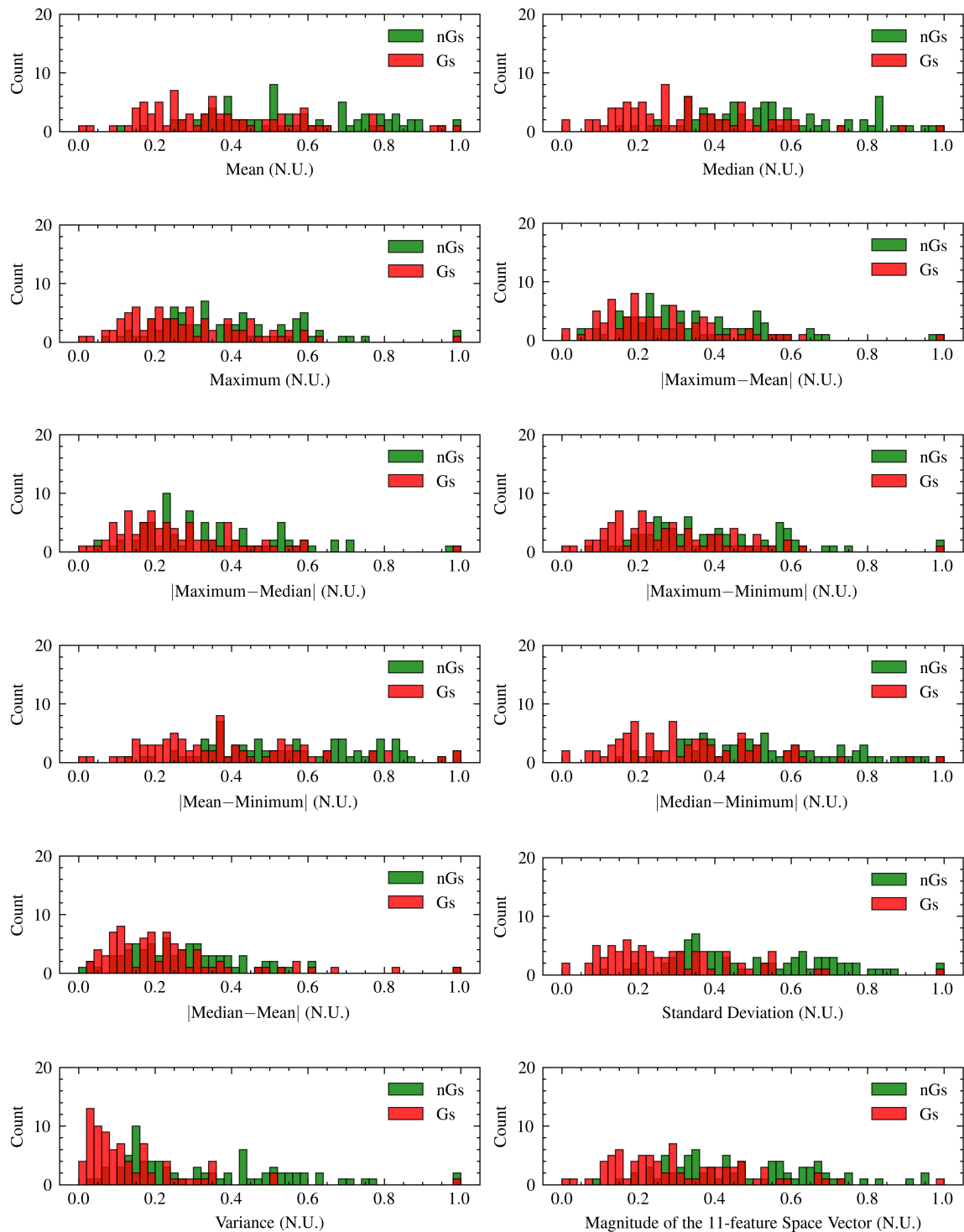
Figure 4.14 11 heuristically defined statistical features extracted from the ring-filtered spatial Fourier-domain data $\mathbb{S}$ when the screened subject is a real person. **Bottom Right**: Distribution based on the magnitude of the 11-feature space vector for the two classes Gs (red) and nGs (green) based on measurements pertaining to varying conditions of when the person's back is facing towards the DAA. Unlike the experiment with mannequin, a plausible threshold value for magnitude of the 11-feature space vector is not apparent to separate the two classes. Gs: Gun-shape. nGs: non-Gun-shape. N.U.: Normalized Units.

124

4.2.3 Processing Cost Analysis

The ability for real-time operation is one important consideration for a screening system to be used for real world application. The imageless detection system processing can be generalized to four separate processes (in sequence): data acquisition, visibility generation, feature extraction, and classification (i.e., inference). Averaged values of the computational time of each process are shown in Table 4.8; the processor of the host machine was an Intel® Core™ i9-9820X. The data acquisition time was 200 ms and accounts for the majority of the duration from measurement to inference. It is noted that the resolution of the angle rotation, the dwell time per angle, and the integration time, among other factors, contribute to the data acquisition time required to complete a single screening measurement. The visibility generation time was 8.53 ms for a single screening measurement with 200 angles. The feature extraction time to obtain the 11 features was 0.03 ms. The time to infer an incoming unknown sample ranged from 0.22 ms–2.01 ms depending on the classifier. The threshold method (for a single event) required the least amount of time followed by SVM-RBF, and followed by KNN in increasing K values which is expected for KNN classifiers where the choice of K affects the number of neighboring data that will be compared to. Based on Table 4.8, the longest duration from measurements to inference was approximately 211 ms considering the KNN (K=15) scenario. As discussed in [100], a measurement time of a few hundred milliseconds is sufficient for screening people that are standing or sitting still. Note that the above assumes a serial configuration for the four processes and that the training and evaluation for the classifier is done offline. Furthermore, the demonstrated technique can continue to operate for screening without reset due to the benefit of the rotational array dynamics. In Table 4.9, comparison is shown for the demonstrated imageless contraband detection technique and other image-based techniques that are also intended for contraband detection application [101, 102, 100]. Nevertheless, it is worth noting that the presented imageless technique accounts for the full screening process from measurements to inference in under 211 ms which is feasible for real-time applications, considering that some techniques consume more time simply for image formation [101, 102]. Furthermore, current airport security screening systems can take up to 1.5 s to complete scanning and up to 6 s to complete both

scanning and detection [59, 103]. Finally, it is evident that the presented imageless contraband detection approach enables significant hardware reduction (i.e., number of antennas).

Process	Time (ms)
Data Acquisition	200
Visibility Generation	8.53
Feature Extraction	0.03
Classification (Inference)	
THR (N=1)	0.22
KNN (K=7)	1.98
KNN (K=9)	1.99
KNN (K=11)	2.00
KNN (K=13)	2.00
KNN (K=15)	2.01
SVM-RBF	1.32

Table 4.8 Averaged elapsed time for individual processes of the demonstrated imageless contraband detection technique. THR: Threshold. Originally submitted to *IEEE Access*, April 2024.

Work	Frequency (GHz)	Number of Antennas	Image Formation	Detection Demonstration	Number of Detected Classes	Processing Time
[101]	20–26	40	Yes	No	n.a.	15 s
[102]	20–30	256	Yes	No (Visual)	n.a.	1.5 s
[100]	72–80	1472 (736 TX + 736 RX)	Yes	No (Visual)	n.a.	157 ms
[104]	32	220	Yes	No (Visual)	n.a.	2.07 s
[105]	12	2 (1 TX + 1 RX)	Yes	Yes (Best ACC: 0.930)	Four	3.8 ms
This Work	75	4 (2 TX + 2 RX)	No	Yes (Best ACC: 0.986)	Two	211 ms

Table 4.9 Comparison of techniques intended for contraband detection application. TX: Transmitter. RX: Receiver. ACC: Accuracy. Originally submitted to *IEEE Access*, April 2024.

4.2.4 Privacy Preservation via Unrecoverable Image Reconstruction

In applications of concealed contraband detection where the primary background is a person, the ability to identify potential prohibited objects without compromising personal privacy can be beneficial. With recent advancements of automatic recognition techniques, it is possible to extract sensitive information from a wide range of biometric modalities [106]; for example, an individual's age and gender can be determined from gait patterns [107, 108, 109]. Imagery from security screenings of people falls in the category of biometric data that potentially contains personal information that may be used for malicious purposes. Approaches addressing the concern are therefore of interest. Recent research has sought to address the challenges related to privacy issues with such sensing techniques. As discussed in [106], there are multiple points of opportunities where privacy enhancing techniques can be applied, ranging from designing imaging sensors with embedded privacy protection features [110], using template protection techniques [111], deidentifying sensitive information within the data [112, 113], using cancelable biometrics [114], sharing data using privacy-preserving schemes [112], and applying adversarial approaches for automatic recognition techniques [115], among others. In general, these approaches can be categorized into three levels [106]: image level, representation level, and inference level. Regardless of where a privacy enhancing technique is applied, there generally exists a trade space between privacy enhancement and biometric utility of the measured data. This means that complete privacy protection can eliminate the utility of biometric data while a complete biometric utility offers no protection on privacy. One possible solution to this problem is to shift away from using modalities that require imaged-based data.

In the remainder of this part, I demonstrate the inherent privacy preservation attribute of the demonstrated imageless technique. As shown in the top row of Figure 4.15, I simulated a reference scene and its visibility using the metallic gun-shaped object described in the above experiment. To illustrate the privacy-preserving aspect, I first conducted a simulation using a similar rotational Fourier-domain system, however one that includes far more samples and that is intended to reconstruct images; I demonstrated such a system in [93]. In the bottom of Figure 4.15,

the reconstructed gun-shaped object shown on the left is obtained from a far denser sampling function shown on the right. In the top row of Figure 4.16, the simulated point spread function (PSF), its two-dimensional Fourier transform pair, and the ring filter (i.e., sampling function) are shown. A semi-transparent magenta annotation is included in the ring filter plot to illustrate spatial Fourier regions that the ring filter samples. In the bottom left of Figure 4.16, the simulated scene intensity reconstruction is shown which is processed based on the interferometric imaging technique as described in Chapter 1. As observed, the reconstructed scene intensity can be considered to be unrecoverable since no perceptible spatial information is represented in the reconstructed image. To demonstrate the fact that the recovered "image" does not represent useful data from which biometrics may be obtained when sensing a person, I also computed the structural similarity index measured (SSIM) between the simulated reference and the reconstruction. The reconstructed image yielded a SSIM with a value of 0.070, meaning that there is essentially no correlation between the information in the reconstructed image and that in the original image. This demonstrates that the sensing technique does not provide sufficient information from which biometric data may be obtained when sensing a person. In the bottom right of Figure 4.16, I present a measured unrecoverable scene intensity of the metallic gun-shaped object using the same systems setup as in the imageless contraband detection measurements where the object is horizontally and vertically aligned to the array's center of rotation with similar orientation as the simulated reference scene (top left of Figure 4.15). Similar to the simulated reconstruction, the measured reconstruction yielded no useful spatial information demonstrating the capability for privacy preservation. In addition, I include two unrecoverable reconstruction examples for each of the two classes from the imageless classification measurements on a person in Figure 4.17. Evidently, the recovered measured scenes exhibit no spatial information of the screened person nor the gun-shaped object. It is evident that the proposed approach, using far fewer spatial frequency samples, does not collect sufficient information to form images, and is thus inherently privacy-preserving.
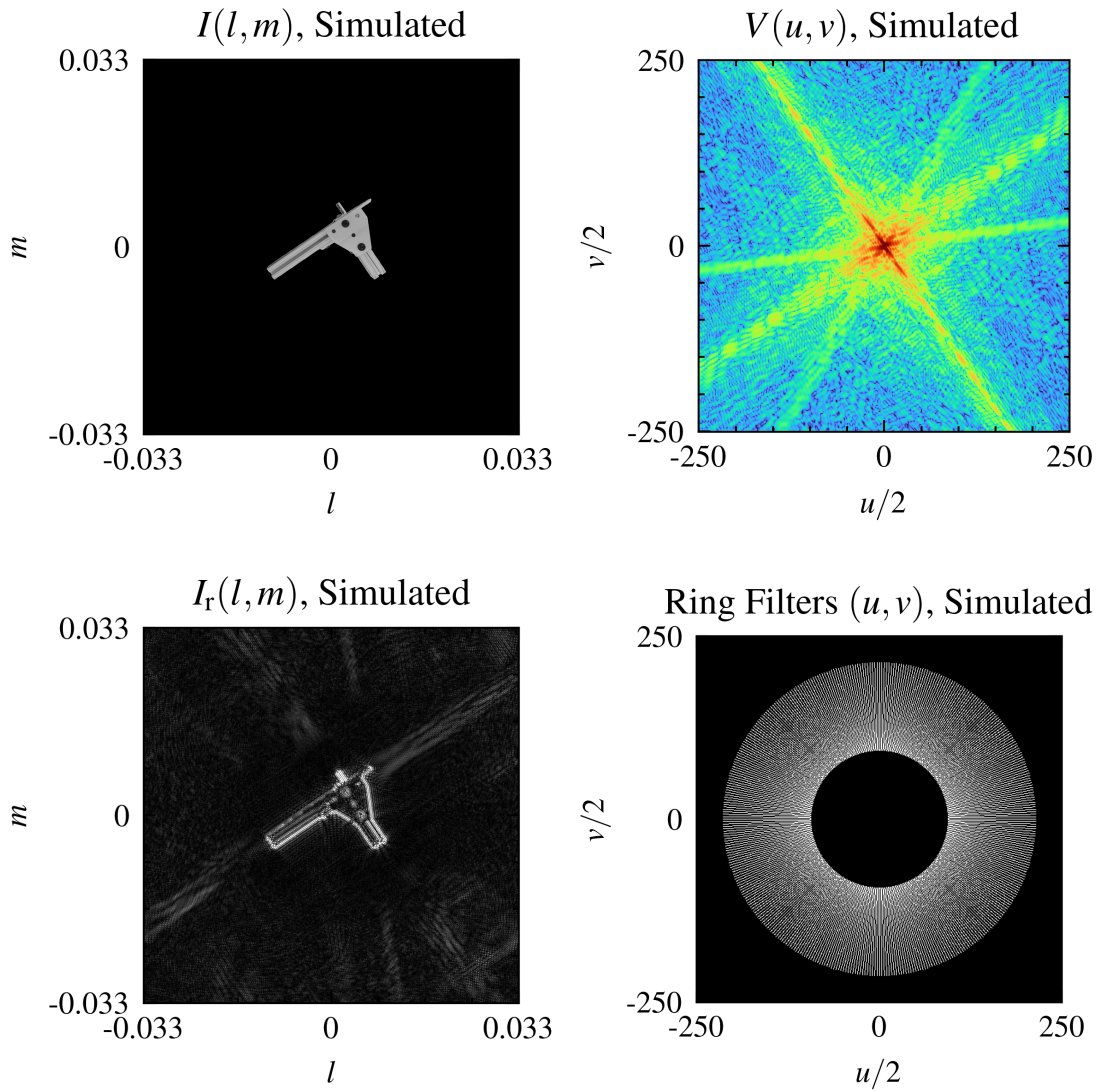
Figure 4.15 Top Row: Simulated scene intensity using the metallic gun-shaped object in the imageless contraband detection measurements (left), and the simulated visibility (right). **Bottom Row**: Simulated examples showing that the rotational dynamic antenna array can recover useful spatial information when sufficient spatial Fourier information is measured, such as using the technique demonstrated in [93]. Originally submitted to *IEEE Access*, April 2024.
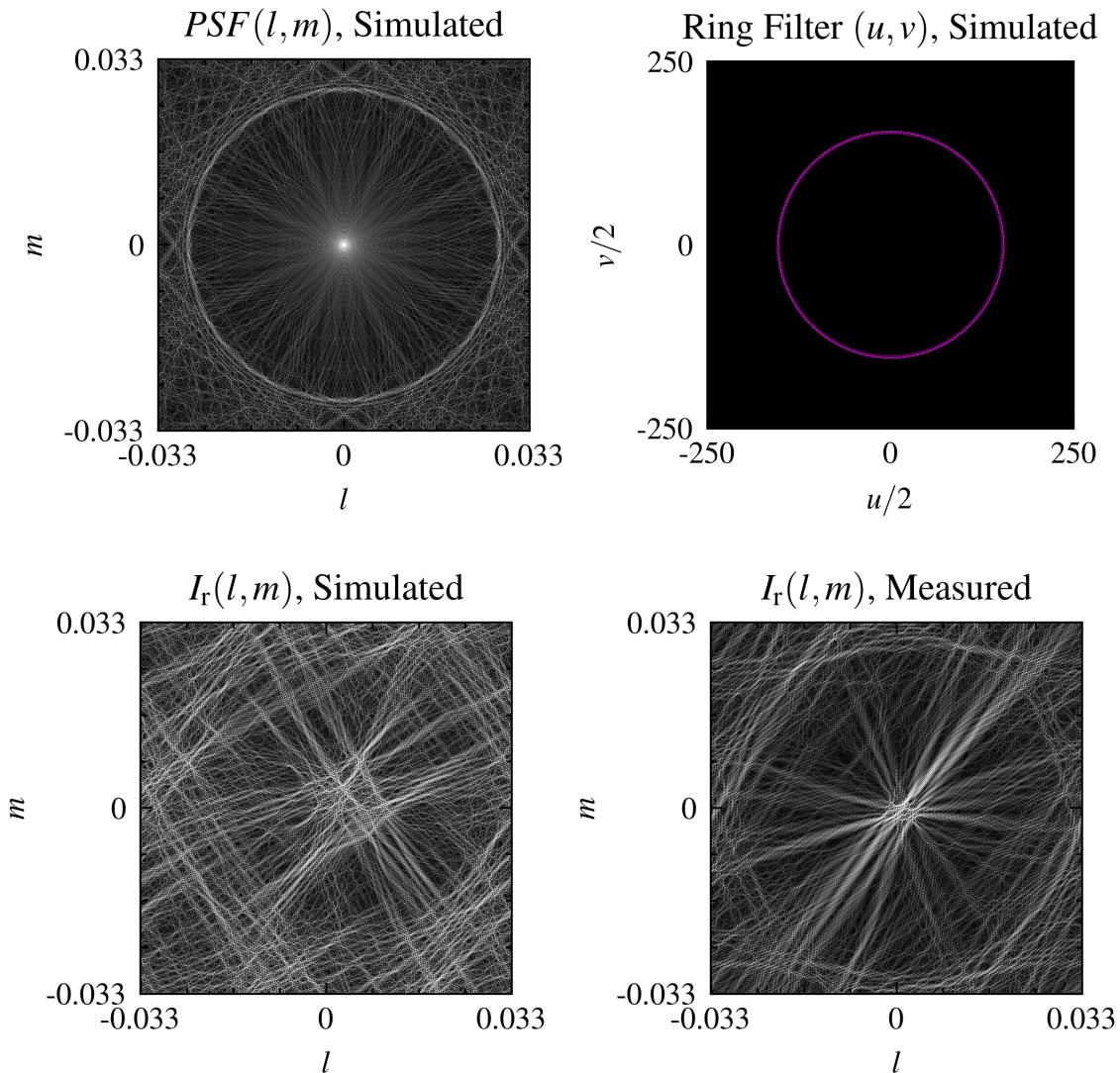
Figure 4.16 **Top Row**: Simulated point spread function (PSF) of the ring filter (i.e., sampling function) based on the receivers' configuration of the rotational dynamic antenna array used in the imageless contraband detection measurement. Note that a semi-transparent magenta annotation is included in the ring filter plot to illustrate spatial Fourier regions that the ring filter samples. **Bottom Row**: The simulated unrecoverable scene intensity based on the simulated ring filtered visibility (i.e., product between the simulated ring filter and simulated visibility) of the metallic gun-shaped object (left). The measured unrecoverable scene intensity of the metallic gun-shaped object using the same systems setup as in the imageless contraband detection measurements where the object is horizontally and vertically aligned to the array's center of rotation (right). Originally submitted to *IEEE Access*, April 2024.
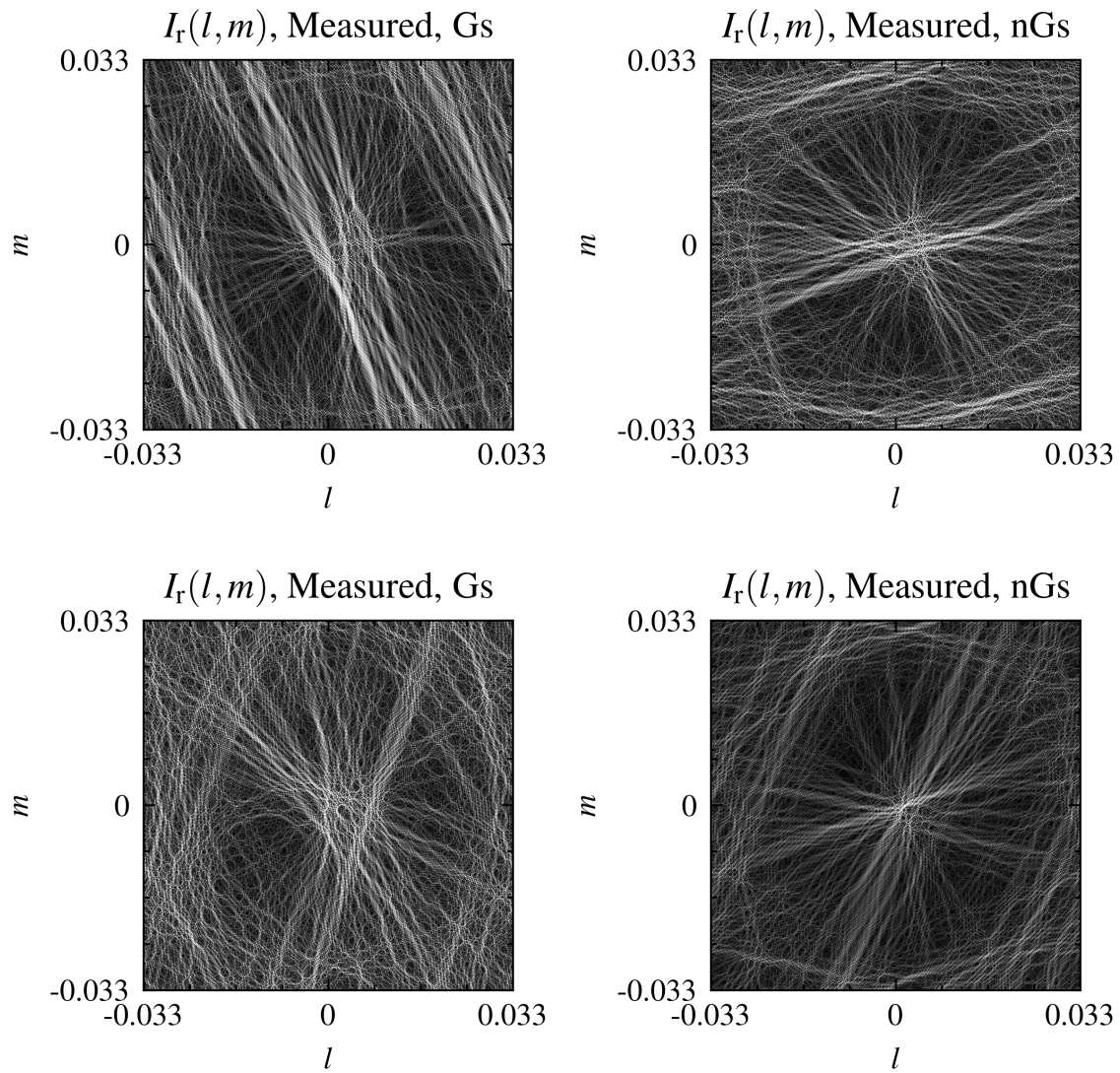
Figure 4.17 Examples demonstrating unrecoverable image reconstruction based on the ring-filtered visibilities for the imageless concealed contraband detection of a real person with (left column) and without the metallic gun-shape (right column). Gs: Gun-shape (with real person). nGs: No gun-shape (real person only). Originally submitted to *IEEE Access*, April 2024.

CHAPTER 5

CONCLUSION

Remote sensing using micro- or millimeter-wave radars is an emerging field that presents opportunities for obtaining new knowledge and/or developing new techniques enabling more efficient sensing technologies. This dissertation investigated a new way to design micro- and millimeter-wave antenna arrays where individual receiving antennas within the array are allowed to move across the measurement plane, hence, achieving a dynamic antenna array with a dynamic aperture by assuming the measured scenes remain quasi static to the array dynamics. Challenges of designing micro- and millimeter-wave remote sensing arrays are already abundant with a diverse trade space including but not limited to system resolution, hardware cost, sensitivity, and computational complexity, etc. This dissertation addressed a possible trade to leverage array dynamics with reasonably longer total measurement time to reduce the system cost due to the large number of antennas needed when compared to conventional array design approaches.

I investigated the dynamic antenna array design by first exploring a specific remote sensing approach based off of the interferometric antenna array commonly found in radio astronomy application as well as the recently introduced active incoherent millimeter-wave technique developed in my research group. By satisfying the van Cittert-Zernike theorem, cross-correlation between any two antennas within the array represent a sample in the spatial Fourier domain. With the implementation of array dynamics, a small number of antennas can generate sampling functions associated with array trajectory such that much more spatial Fourier information can be recovered, hence, improving the quality of the scene reconstruction. I compared two types of array trajectory where a coordinated strategy tries to maintain certain array configurations throughout the trajectory, and a random strategy where elements within the dynamic antenna array are allowed to move randomly on the measurement plane as long as avoiding physical collision with others. After investigation by comparing the generated sampling function of the two trajectory strategies, it is demonstrated in this dissertation that the random trajectory strategy has the potential to collect much more unique spatial Fourier information given longer observation time.

133

While the random trajectory strategy is better for remote sensing systems intended for scene recovery, the coordinated trajectory strategy is also useful for specific use cases. Interestingly, the generate sampling function can efficiently cover the full two-dimensional spatial Fourier domain at specific spatial frequency bandwidth by designing a dynamic antenna array using as few as two receivers that co-rotates with respect to their centroid which is referred to as the ring filter. As discussed, spatial features such as sharp edges in the measured scene manifest radially extending responses in the spatial Fourier domain that are orthogonal to the edges' direction. By using a ring filter, it was demonstrated that only a subset of samples on the spatial Fourier domain can potentially enable the inference on specific spatial features of the measured scene. I investigated a remote sensing scenario where ring filters generated by correlating pairs integrated on the rotor blades of an aerial vehicle can differentiate scenes that contain man-made structures such as roadway and bridges with accuracy above 90%. Furthermore, I discussed in detail the design consideration of single ring filter design as well as possible improvement to achieve wider spatial frequency coverage by generating multiple ring filters using multiple correlating pairs. Based on this concept of using a ring filter to measure specific spatial Fourier domain artifacts, a real-time 75 GHz rotational dynamic antenna array was designed and implemented capable of capturing the sharp edge induced responses.

One possible use case of the ring filter generating rotational dynamic antenna array is concealed contraband detection for security screening. I investigated the separability of spatial Fourier responses captured by the ring filter between cases when a fiberglass mannequin concealed a metallic gun-shape beneath clothing and when the gun-shape object is not presented. With a simple threshold classifier and the consideration of classifying on consecutive measurements, an accuracy of 90.8% was achieved. Subsequently, I investigated the performance of multiple classifiers as well as their robustness when the unknown incoming data captured by the ring filter do not share similar primary background (i.e., mannequin profile) and/or object (i.e., contraband) as the training data while maintaining an accuracy above 72.5% among different considered scenarios. In addition, I further relax the assumption on the scene's quasi-static condition by considering a more practical

security screening scenario where the primary background is a real person. The investigation demonstrated that while a non-static scene condition due to a person's breathing and/or torso movements can significantly degrade the performance of some classifier, specific classifiers can still differentiate between the contraband and non-contraband measurements achieving an accuracy as high as 98.6%.

In summary, this dissertation provides a framework for remote sensing applications that do not necessarily require the recovery of images. By using an antenna array with controllable array dynamics, the number of antennas along with the associated chains of hardware and processing can be further reduced when compared to the non-dynamic counterparts. Finally, by investigating the particular spatial Fourier location of interest where antennas within a dynamic antenna array can easily move across the measurement plane to recover spatial Fourier artifacts enabling direct inference of the measured scene. The work presented in this dissertation can prove useful for advanced remote sensing modalities with simplified/reduced hardware requirements by enabling individual antennas with controllable trajectories.

BIBLIOGRAPHY

[1] J. A. Nanzer. *Microwave and Millimeter-Wave Remote Sensing for Security Applications*. Artech House, 2012.

[2] C. Sherman and J. Butler. *Transducers and Arrays for Underwater Sound*. The Underwater Acoustics Series. Springer New York, 2007.

[3] Shripad P. Mahulikar, Hemant R. Sonawane, and G. Arvind Rao. Infrared signature studies of aerospace vehicles. *Progress in Aerospace Sciences*, 43(7):218–245, 2007.

[4] J.P. Dakin and R. Brown. *Handbook of Optoelectronics: Concepts, Devices, and Techniques (Volume One)*. Series in Optics and Optoelectronics. CRC Press, 2017.

[5] Christiaan Huygens. *Traité de la lumière*. Chez Pierre vander Aa, marchand libraire, 1690.

[6] A treatise on electricity and magnetism. *Nature*, 7(182):478–480, Apr 1873.

[7] H. Hertz. Ueber die ausbreitungsgeschwindigkeit der electrodynamischen wirkungen. *Annalen der Physik und Chemie*, 270(7):551–569, 1888.

[8] Radio detection and ranging. *Nature*, 152(3857):391–392, Oct 1943.

[9] F. Zidane, J. Lanteri, J. Marot, L. Brochier, N. Joachimowicz, H. Roussel, and C. Migliaccio. Nondestructive control of fruit quality via millimeter waves and classification techniques: Investigations in the automated health monitoring of fruits. *IEEE Antennas and Propagation Magazine*, 62(5):43–54, 2020.

[10] E. J. Bond, Xu Li, S. C. Hagness, and B. D. Van Veen. Microwave imaging via space-time beamforming for early detection of breast cancer. *IEEE Transactions on Antennas and Propagation*, 51(8):1690–1705, Aug 2003.

[11] M. Bassi, M. Caruso, M. S. Khan, A. Bevilacqua, A. D. Capobianco, and A. Neviani. An integrated microwave imaging radar with planar antennas for breast cancer detection. *IEEE Transactions on Microwave Theory and Techniques*, 61(5):2108–2118, May 2013.

[12] L. C. Graham. Synthetic interferometer radar for topographic mapping. *Proceedings of the IEEE*, 62(6):763–768, 1974.

[13] C. S. Ruf, C. T. Swift, A. B. Tanner, and D. M. Le Vine. Interferometric synthetic aperture microwave radiometry for the remote sensing of the Earth. *IEEE Trans. Geosci. Remote Sens.*, 26(5):597–611, Sep. 1988.

[14] D. Moller, S. Hensley, G. A. Sadowy, C. D. Fisher, T. Michel, M. Zawadzki, and E. Rignot. The Glacier and Land Ice Surface Topography Interferometer: An Airborne Proof-of-Concept Demonstration of High-Precision Ka-Band Single-Pass Elevation Mapping. *IEEE Trans. Geosci. Remote Sens.*, 49(2):827–842, 2011.

[15] D. M. Sheen, D. L. McMakin, and T. E. Hall. Three-dimensional millimeter-wave imaging for concealed weapon detection. *IEEE Trans. Microw. Theory Techn.*, 49(9):1581–1592, 2001.

[16] R. Appleby and H. B. Wallace. Standoff detection of weapons and contraband in the 100 ghz to 1 thz region. *IEEE Transactions on Antennas and Propagation*, 55(11):2944–2956, Nov 2007.

[17] Amala Sonny, Abhinav Kumar, and Linga Reddy Cenkeramaddi. Carry object detection utilizing mmwave radar sensors and ensemble-based extra tree classifiers on the edge computing systems. *IEEE Sensors Journal*, 23(17):20137–20149, 2023.

[18] N.C. Currie and C.E. Brown. *Principles and Applications of Millimeter-Wave Radar*. Artech House, 1987.

[19] Mohammad Abdul Alim, Ali A. Rezazadeh, and Christophe Gaquiere. Temperature effect on dc and equivalent circuit parameters of 0.15- μm gate length gan/sic hemt for microwave applications. *IEEE Transactions on Microwave Theory and Techniques*, 64(11):3483–3491, 2016.

[20] Ting Zhang, Jia Du, and Y. Jay Guo. High-tc superconducting microwave and millimeter devices and circuits—an overview. *IEEE Journal of Microwaves*, 2(3):374–388, 2022.

[21] Merrill I Skolnik. *Radar Handbook*. McGraw-Hill, New York, NY, June 1970.

[22] R. S. Grisetti, M. M. Santa, and G. M. Kirkpatrick. Effect of internal fluctuations and scanning on clutter attenuation in mti radar. *IRE Transactions on Aeronautical and Navigational Electronics*, ANE-2(1):37–41, 1955.

[23] Xinkai Zhou, Pengbo Wang, Hongcheng Zeng, and Jie Chen. Moving target detection using gnss-based passive bistatic radar. *IEEE Transactions on Geoscience and Remote Sensing*, 60:1–15, 2022.

[24] Peyton Z. Peebles. Signal processors and accuracy of three-beam monopulse tracking radar. *IEEE Transactions on Aerospace and Electronic Systems*, AES-5(1):52–57, 1969.

[25] Zhen Wang, Jiaqi Liu, Xinru Yuan, Chang Chen, Jun Liu, and Weidong Chen. A dynamic model-based doppler-adaptive correlation filter for maritime radar target tracking. *IEEE Transactions on Geoscience and Remote Sensing*, 62:1–15, 2024.

[26] T.N. Anderson. Double-ridge waveguide for commercial airlines weather radar installation. *IRE Transactions on Microwave Theory and Techniques*, 3(4):2–9, 1955.

[27] Tworit Dash, Hans Driessen, Oleg A. Krasnov, and Alexander Yarovoy. Doppler spectrum parameter estimation for weather radar echoes using a parametric semianalytical model. *IEEE Transactions on Geoscience and Remote Sensing*, 62:1–18, 2024.

[28] C. W. Sherwin, J. P. Ruina, and R. D. Rawcliffe. Some early developments in synthetic aperture radar systems. *IRE Transactions on Military Electronics*, MIL-6(2):111–115, 1962.

[29] S.R. Cloude and E. Pottier. An entropy based classification scheme for land applications of polarimetric sar. *IEEE Transactions on Geoscience and Remote Sensing*, 35(1):68–78, 1997.

[30] Nanbo Jin and Yahya Rahmat-Samii. Analysis and particle swarm optimization of correlator antenna arrays for radio astronomy applications. *IEEE Transactions on Antennas and Propagation*, 56(5):1269–1279, 2008.

[31] J.J. Condon and S.M. Ransom. *Essential Radio Astronomy*. Princeton Series in Modern Observational Astronomy. Princeton University Press, 2016.

[32] A Richard Thompson, James M Moran, and George W Swenson. *Interferometry and Synthesis in Radio Astronomy*. Astronomy and astrophysics library. Springer International Publishing, Cham, Switzerland, 3 edition, March 2017.

[33] E.F. Belohoubek. Radar control for automotive collision mitigation and headway spacing. *IEEE Transactions on Vehicular Technology*, 31(2):89–99, 1982.

[34] Kwo Wei Chang, Huei Wang, G. Shreve, J.G. Harrison, M. Core, A. Paxton, M. Yu, C.H. Chen, and G.S. Dow. Forward-looking automotive radar using a w-band single-chip transceiver. *IEEE Transactions on Microwave Theory and Techniques*, 43(7):1659–1668, 1995.

[35] Xiao Wang, Linhai Xu, Hongbin Sun, Jingmin Xin, and Nanning Zheng. On-road vehicle detection and tracking using mmw radar and monovision fusion. *IEEE Transactions on Intelligent Transportation Systems*, 17(7):2075–2084, 2016.

[36] Ann-Kathrin Seifert, Moeness G. Amin, and Abdelhak M. Zoubir. Toward unobtrusive in-home gait analysis based on radar micro-doppler signatures. *IEEE Transactions on Biomedical Engineering*, 66(9):2629–2640, 2019.

[37] Ann-Kathrin Seifert, Martin Grimmer, and Abdelhak M. Zoubir. Doppler radar for the extraction of biomechanical parameters in gait analysis. *IEEE Journal of Biomedical and Health Informatics*, 25(2):547–558, 2021.

[38] Cory Hilton and Jeffrey A. Nanzer. Narrowband passive rf tags for frequency-selective harmonic doppler radar tracking. *IEEE Transactions on Antennas and Propagation*, 71(2):1216–1222, 2023.

[39] J. P. P. Gomes, J. F. B. Brancalion, and D. Fernandes. Automatic Target Recognition in Synthetic Aperture Radar image using multiresolution analysis and classifiers combination. In *2008 IEEE Radar Conference*, pages 1–5, 2008.

[40] U. Srinivas, V. Monga, and R. G. Raj. SAR Automatic Target Recognition Using Discriminative Graphical Models. *IEEE Trans. Aerosp. Electron. Syst.*, 50(1):591–606, Jan. 2014.

[41] Ushemadzoro Chipengo. Full physics simulation study of guardrail radar-returns for 77 ghz automotive radar systems. *IEEE Access*, 6:70053–70060, 2018.

[42] Robert C Hansen. *Phased Array Antennas*. Wiley Series in Microwave and Optical Engineering. Wiley-Blackwell, Hoboken, NJ, 2 edition, November 2009.

[43] Robert J Mailloux. *Phased array antenna handbook*. Artech House antennas and electromagnetics analysis library. Artech House, Norwood, MA, 3 edition, December 2017.

[44] W N Christiansen and J A Hogbom. *Cambridge Monographs on Physics: Radiotelescopes*. Cambridge University Press, Cambridge, England, 2 edition, December 1987.

[45] R Wohlleben, H Mattes, and Th Krichbaum. *Interferometry in Radioastronomy and Radar Techniques*. Springer, Dordrecht, Netherlands, 1991 edition, December 1990.

[46] S. Vakalis and J. A. Nanzer. Microwave Imaging Using Noise Signals. *IEEE Trans. Microw. Theory Techn.*, 66(12):5842–5851, Dec. 2018.

[47] S. Vakalis, L. Gong, and J. A. Nanzer. Imaging With WiFi. *IEEE Access*, 7:28616–28624, 2019.

[48] Stavros Vakalis, Liang Gong, Yuxiao He, John Papapolymerou, and Jeffrey A. Nanzer. Experimental Demonstration and Calibration of a 16-Element Active Incoherent Millimeter-Wave Imaging Array. *IEEE Trans. Microw. Theory Techn.*, 68(9):3804–3813, Sep. 2020.

[49] J. A. Nanzer. Millimeter-wave interferometric imaging sensors. In *SENSORS, 2013 IEEE*, pages 1–4, Nov 2013.

[50] Jeffrey A. Nanzer. Millimeter-wave interferometric angular velocity detection. *IEEE Transactions on Microwave Theory and Techniques*, 58(12):4128–4136, 2010.

[51] P. Hvan Cittert. Die Wahrscheinliche Schwingungsverteilung in Einer von Einer Lichtquelle Direkt Oder Mittels Einer Linse Beleuchteten Ebene. *Physica*, 1(1-6):201–210, 1934.

[52] F. Zernike. The concept of degree of coherence and its application to optical problems. *Physica*, 5(8):785–795, 1938.

[53] Gerrit L Verschuur and Kenneth I Kellermann, editors. *Galactic and extragalactic radio astronomy*. Astronomy and Astrophysics Library. Springer, New York, NY, 2 edition, December 2012.

[54] Stavros Vakalis, Daniel Chen, and Jeffrey A. Nanzer. Millimeter-Wave Imaging at 652 Frames per Second. *IEEE Journal of Microwaves*, pages 1–9, 2021.

[55] Jorge R. Colon-Berrios, Daniel Chen, Derek Luzano, and Jeffrey A. Nanzer. A comparison of image reconstruction versus array layout in a 24-element 38-ghz active incoherent millimeter-wave imaging system. In *2023 IEEE International Symposium on Antennas and Propagation and USNC-URSI Radio Science Meeting (USNC-URSI)*, pages 339–340, 2023.

[56] Max Born, Emil Wolf, A. B. Bhatia, P. C. Clemmow, D. Gabor, A. R. Stokes, A. M. Taylor, P. A. Wayman, and W. L. Wilcock. *Principles of Optics: Electromagnetic Theory of Propagation, Interference and Diffraction of Light*. Cambridge University Press, 7 edition, 1999.

[57] K. Schulz, D. Brunner, and M. Boldt. Comparison of CoVAmCoh and ILU image products for interferometric very high resolution SAR image pairs. In *2011 IEEE International Geoscience and Remote Sensing Symposium*, pages 313–315, 2011.

[58] D. Soncco, C. Barbanson, M. Nikolova, A. Almansa, and Y. Ferrec. Fast and Accurate Multiplicative Decomposition for Fringe Removal in Interferometric Images. *IEEE Trans. Comput. Imaging*, 3(2):187–201, Jun. 2017.

[59] https://www.leidos.com/markets/aviation/security-detection/aviation-checkpoint/people-screening, 2023 (accessed September 11, 2023).

[60] https://www.iceye.com/downloads/datasets, 2019 (accessed March 17, 2020).

[61] Stavros Vakalis, Daniel Chen, and Jeffrey A. Nanzer. Toward space–time incoherent transmitter design for millimeter-wave imaging. *IEEE Antennas and Wireless Propagation Letters*, 19(9):1471–1475, 2020.

[62] Ahona Bhattacharyya, Jason M. Merlo, and Jeffrey A. Nanzer. A dual-carrier linear-frequency modulated waveform for high-accuracy localization in distributed antenna arrays. In *2023 20th European Radar Conference (EuRAD)*, pages 331–334, 2023.

[63] George Biddell Airy. On the intensity of light in the neighbourhood of a caustic. *Transactions of the Cambridge Philosophical Society*, VI, Part. III:379–402, 1938.

[64] Hemanth D Jude, Deepak Gupta, and Valentina Emilia Balas. *Intelligent Data Analysis for Biomedical Applications: Challenges and solutions*. Academic Press, San Diego, CA, March 2019.

[65] Zhou Wang, A.C. Bovik, H.R. Sheikh, and E.P. Simoncelli. Image quality assessment: from error visibility to structural similarity. *IEEE Transactions on Image Processing*, 13(4):600–612, 2004.

[66] Daniel Chen and Jeffrey A. Nanzer. Analysis of imageless ground scene classification using a millimeter-wave dynamic antenna array. *IEEE Transactions on Geoscience and Remote Sensing*, 60:1–10, 2022.

[67] Daniel Chen, Stavros Vakalis, and Jeffrey A. Nanzer. A 75-ghz dynamic antenna array for real-time imageless object detection via fourier domain filtering. In *2022 IEEE/MTT-S International Microwave Symposium - IMS 2022*, pages 727–730, 2022.

[68] S. Stanko, D. Notel, A. Wahlen, J. Huck, F. Kloppel, R. Sommer, M. Hagelen, and H. Essen. Active and passive mm-wave imaging for concealed weapon detection and surveillance. In *2008 33rd International Conference on Infrared, Millimeter and Terahertz Waves*, pages 1–2, 2008.

[69] F. Gumbmann and L. Schmidt. Millimeter-Wave Imaging With Optimized Sparse Periodic Array for Short-Range Applications. *IEEE Trans. Geosci. Remote Sens.*, 49(10):3629–3638, 2011.

[70] Cheng Zheng, Xianxun Yao, Anyong Hu, and Jungang Miao. Initial Results Of A Passive Millimeter-Wave Imager Used For Concealed Weapon Detection Bhu-2D-U. *Progress In Electromagnetics Research C*, 43:151–163, 2013.

[71] Richard O. Duda, Peter E. Hart, and David G. Stork. *Pattern Classification*. Wiley, New York, 2 edition, 2001.

[72] Qin Zou, Lihao Ni, Tong Zhang, and Qian Wang. Deep learning based feature selection for remote sensing scene classification. *IEEE Geoscience and Remote Sensing Letters*, 12(11):2321–2325, 2015.

[73] Xiaoqiang Lu, Xiangtao Zheng, and Yuan Yuan. Remote sensing scene classification by unsupervised representation learning. *IEEE Transactions on Geoscience and Remote Sensing*, 55(9):5148–5157, 2017.

[74] Erzhu Li, Junshi Xia, Peijun Du, Cong Lin, and Alim Samat. Integrating multilayer features of convolutional neural networks for remote sensing scene classification. *IEEE Transactions on Geoscience and Remote Sensing*, 55(10):5653–5665, 2017.

[75] Jie Xie, Nanjun He, Leyuan Fang, and Antonio Plaza. Scale-free convolutional neural network for remote sensing scene classification. *IEEE Transactions on Geoscience and Remote Sensing*, 57(9):6916–6928, 2019.

[76] Daniel Chen, Stavros Vakalis, and Jeffrey A. Nanzer. Dynamic Antenna Array Design for Scene Classification Through Fourier-Domain Filtering. *IEEE Trans. Antennas Propag.*, 69(9):5953–5962, Sep. 2021.

[77] D. Chen, S. Vakalis, V. Holmes, and J. A. Nanzer. Spatial Frequency Filter Design for Interferometric Image Classification Without Image Reconstruction. In *2020 IEEE USNC-CNC-URSI North American Radio Science Meeting (Joint with AP-S Symposium)*, pages 23–24, 2020.

[78] Daniel Chen, Stavros Vakalis, and Jeffrey A. Nanzer. A Millimeter-Wave Dynamic Antenna Array for Classifying Objects Via Sparse Fourier Domain Sampling. In *2021 IEEE MTT-S International Microwave Symposium (IMS)*, pages 748–751, 2021.

[79] Max Born and Emil Wolf. *Principles of optics*. Cambridge Univ. Pr., 1999.

[80] Paul Gerin. Fahlstrom and Thomas J. Gleason. *Introduction to UAV systems*. Wiley, 2012.

[81] http://fettersaerospace.com/uav-helicopters.html, 2017 (accessed June 16, 2020).

[82] Nicholas Metropolis and S. Ulam. The Monte Carlo Method. *Journal of the American Statistical Association*, 44(247):335–341, 1949.

[83] Douglas G Altman and J Martin Bland. Statistics Notes: Diagnostic tests 2: predictive values. *BMJ*, 309(6947):102, 1994.

[84] Tom Fawcett. An introduction to ROC analysis. *Pattern Recognition Letters*, 27(8):861 – 874, 2006. ROC Analysis in Pattern Recognition.

[85] T. Cover and P. Hart. Nearest neighbor pattern classification. *IEEE Transactions on Information Theory*, 13(1):21–27, 1967.

[86] A. Ferretti, C. Prati, and F. Rocca. Permanent scatterers in SAR interferometry. *IEEE Trans. Geosci. Remote Sens.*, 39(1):8–20, 2001.

[87] Y. Álvarez, Y. Rodriguez-Vaqueiro, B. Gonzalez-Valdes, F. Las-Heras, and A. García-Pino. Fourier-Based Imaging for Subsampled Multistatic Arrays. *IEEE Trans. Antennas Propag.*, 64(6):2557–2562, Jun. 2016.

[88] E. Kpré, C. Decroze, M. Mouhamadou, and T. Fromenteze. Computational Imaging for Compressive Synthetic Aperture Interferometric Radiometer. *IEEE Trans. Antennas Propag.*, 66(10):5546–5557, Oct. 2018.

[89] A. Moffet. Minimum-redundancy linear arrays. *IEEE Trans. Antennas Propag.*, 16(2):172–175, 1968.

[90] F.J. Ferri, P. Pudil, M. Hatef, and J. Kittler. Comparative study of techniques for large-scale feature selection. In Edzard S. GELSEMA and Laveen S. KANAL, editors, *Pattern Recognition in Practice IV*, volume 16 of *Machine Intelligence and Pattern Recognition*, pages 403–413. North-Holland, 1994.

[91] David W. Aha and Richard L. Bankert. A Comparative Evaluation of Sequential Feature Selection Algorithms. In *In Proceedings of the Fifth International Workshop on Artificial Intelligence and Statistics*, pages 1–7. Springer-Verlag, 1995.

[92] Daniel Chen, Stavros Vakalis, and Jeffrey A. Nanzer. Imageless shape detection using a millimeter-wave dynamic antenna array and noise illumination. *IEEE Transactions on Microwave Theory and Techniques*, 70(1):758–765, 2022.

[93] Daniel Chen, Stavros Vakalis, and Jeffrey A. Nanzer. Millimeter-wave imaging using a rotating dynamic antenna array and noise illumination. *IEEE Transactions on Antennas and Propagation*, 70(11):10965–10973, 2022.

[94] Daniel Chen and Jeffrey A. Nanzer. Privacy preserving contraband detection using a millimeter-wave dynamic antenna array. *IEEE Microwave and Wireless Technology Letters*, 33(6):915–918, 2023.

[95] Corinna Cortes and Vladimir Vapnik. Support-vector networks. *Machine Learning*, 20(3):273–297, Sep 1995.

[96] B. Scholkopf, Kah-Kay Sung, C.J.C. Burges, F. Girosi, P. Niyogi, T. Poggio, and V. Vapnik. Comparing support vector machines with gaussian kernels to radial basis function classifiers. *IEEE Transactions on Signal Processing*, 45(11):2758–2765, 1997.

[97] Alex M. Andrew. An introduction to support vector machines and other kernel-based learning methods by nello christianini and john shawe-taylor, cambridge university press, cambridge, 2000, xiii 189 pp., isbn 0-521-78019-5 (hbk, £27.50). *Robotica*, 18(6):687–689, 2000.

[98] Stavros Vakalis, Liang Gong, John Papapolymerou, and Jeffrey A. Nanzer. Active incoherent millimeter-wave imaging of dielectric objects. In *2020 IEEE International Symposium on Antennas and Propagation and North American Radio Science Meeting*, pages 1123–1124, 2020.

[99] Jorge R. Colon-Berrios, Daniel Chen, Stavros Vakalis, and Jeffrey A. Nanzer. Multiplicative frequency diverse active incoherent millimeter-wave imaging. *IEEE Antennas and Wireless Propagation Letters*, pages 1–5, 2023.

[100] Sherif Sayed Ahmed, Andreas Schiessl, and Lorenz-Peter Schmidt. A novel fully electronic active real-time imager based on a planar multistatic sparse array. *IEEE Transactions on Microwave Theory and Techniques*, 59(12):3567–3576, 2011.

[101] Yolanda Rodríguez-Vaqueiro, Yuri Álvarez López, Borja González-Valdes, José Ángel Martínez, Fernando Las-Heras, and Carey M. Rappaport. On the use of compressed sensing techniques for improving multistatic millimeter-wave portal-based personnel screening. *IEEE Transactions on Antennas and Propagation*, 62(1):494–499, 2014.

[102] Jaime Laviada, Mohammad Tayeb Ghasr, Miguel López-Portugués, Fernando Las-Heras, and Reza Zoughi. Real-time multiview sar imaging using a portable microwave camera with arbitrary movement. *IEEE Transactions on Antennas and Propagation*, 66(12):7305–7314, 2018.

[103] Sherif S. Ahmed. Microwave imaging in security — two decades of innovation. *IEEE Journal of Microwaves*, 1(1):191–201, 2021.

[104] Luning Tang, Shuoguang Wang, and Shiyong Li. Improved ray tracing based augmentations for concealed object detection in activate millimeter wave imaging. In *2021 IEEE International Conference on Signal Processing, Communications and Computing (ICSPCC)*, pages 1–5, 2021.

[105] Rahul Sharma, Raphael Hussung, Andreas Keil, Fabian Friederich, Thomas Fromenteze, Mohsen Khalily, Bhabesh Deka, Vincent Fusco, and Okan Yurduseven. Coded-aperture computational millimeter-wave image classifier using convolutional neural network. *IEEE Access*, 9:119830–119844, 2021.

[106] Blaž Meden, Peter Rot, Philipp Terhörst, Naser Damer, Arjan Kuijper, Walter J. Scheirer, Arun Ross, Peter Peer, and Vitomir Štruc. Privacy–enhancing face biometrics: A comprehensive survey. *IEEE Transactions on Information Forensics and Security*, 16:4147–4183, 2021.

[107] Chi Xu, Yasushi Makihara, Ruochen Liao, Hirotaka Niitsuma, Xiang Li, Yasushi Yagi, and Jianfeng Lu. Real-time gait-based age estimation and gender classification from a single image. In *2021 IEEE Winter Conference on Applications of Computer Vision (WACV)*, pages 3459–3469, 2021.

[108] Shaoxiong Zhang, Yunhong Wang, and Annan Li. Gait energy image-based human attribute recognition using two-branch deep convolutional neural network. *IEEE Transactions on Biometrics, Behavior, and Identity Science*, 5(1):53–63, 2023.

[109] Cheng-En Sung and Nada Attar. Gender classification accuracy via two-dimensional body joints using convolutional neural networks. In *2023 IEEE International Conference on Big Data (BigData)*, pages 2229–2233, 2023.

[110] Ankur Chattopadhyay and T.E. Boult. Privacycam: a privacy preserving camera using uclinux on the blackfin dsp. In *2007 IEEE Conference on Computer Vision and Pattern Recognition*, pages 1–8, 2007.

[111] Karthik Nandakumar and Anil K. Jain. Biometric template protection: Bridging the performance gap between theory and practice. *IEEE Signal Processing Magazine*, 32(5):88–100, 2015.

[112] E.M. Newton, L. Sweeney, and B. Malin. Preserving privacy by de-identifying face images. *IEEE Transactions on Knowledge and Data Engineering*, 17(2):232–243, 2005.

[113] Slobodan Ribaric and Nikola Pavesic. An overview of face de-identification in still images and videos. In *2015 11th IEEE International Conference and Workshops on Automatic Face and Gesture Recognition (FG)*, volume 04, pages 1–6, 2015.

[114] Vishal M. Patel, Nalini K. Ratha, and Rama Chellappa. Cancelable biometrics: A review. *IEEE Signal Processing Magazine*, 32(5):54–65, 2015.

[115] Vahid Mirjalili, Sebastian Raschka, and Arun Ross. Flowsan: Privacy-enhancing semi-adversarial networks to confound arbitrary face-based gender classifiers. *IEEE Access*, 7:99735–99745, 2019.

APPENDIX A

ACTIVE INCOHERENT MILLIMETER-WAVE (AIM) IMAGING RADAR
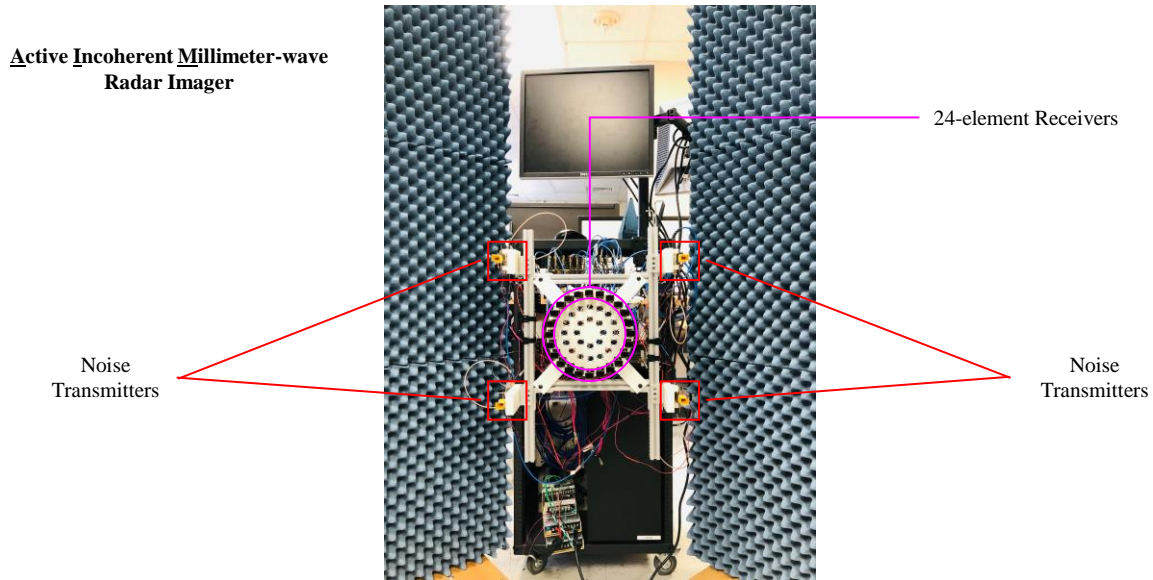
Figure A.1 Photo of the active incoherent millimeter-wave (AIM) radar imager developed by the Distributed Electromagnetics Theory and Applications research group at Michigan State University. The active interferometric radar imaging system uses four independent noise transmitters (annotated with red) to achieve the spatio-temporal radiation condition at the measured scene required by the van Cittert-Zernike theorem. The 24-element receiving array (annotated with magenta) has a circular array configuration.

APPENDIX B

DERIVATION OF (1.3)

Begin with

$$r(\theta) = \langle \cos(2\pi ft) \cos[2\pi f(t - \tau_g)] \rangle$$

Expand the second cosine term and apply the identity $\cos(A - B) = \cos A \cos B + \sin A \sin B$,

$$r(\theta) = \langle \cos(2\pi ft) \cos(2\pi ft - 2\pi f\tau_g) \rangle$$

$$r(\theta) = \langle \cos(2\pi ft)[\cos(2\pi ft) \cos(2\pi f\tau_g) + \sin(2\pi ft) \sin(2\pi f\tau_g)] \rangle$$

$$r(\theta) = \langle \cos^2(2\pi ft) \cos(2\pi f\tau_g) + \cos(2\pi ft) \sin(2\pi ft) \sin(2\pi f\tau_g) \rangle$$

Add $0 = \frac{1}{2}\cos(2\pi f\tau_g) - \frac{1}{2}\cos(2\pi f\tau_g)$ within the angle brackets,

$$r(\theta)$$
$$= \langle \cos^2(2\pi ft) \cos(2\pi f\tau_g) - \frac{1}{2}\cos(2\pi f\tau_g) + \cos(2\pi ft) \sin(2\pi ft) \sin(2\pi f\tau_g) + \frac{1}{2}\cos(2\pi f\tau_g) \rangle$$

Factor out $\frac{1}{2}\cos(2\pi f\tau_g)$ among the first two terms and apply the identity $\cos 2\theta = 2\cos^2 \theta - 1$,

$$r(\theta) = \langle \frac{1}{2}\cos(2\pi f\tau_g)[2\cos^2(2\pi ft) - 1] + \cos(2\pi ft) \sin(2\pi ft) \sin(2\pi f\tau_g) + \frac{1}{2}\cos(2\pi f\tau_g) \rangle$$

$$r(\theta) = \langle \frac{1}{2}\cos(2\pi f\tau_g) \cos(4\pi ft) + \cos(2\pi ft) \sin(2\pi ft) \sin(2\pi f\tau_g) + \frac{1}{2}\cos(2\pi f\tau_g) \rangle$$

Similarly, apply the identity $\sin 2\theta = 2\sin \theta \cos \theta$ to the second term,

$$r(\theta) = \langle \frac{1}{2}\cos(4\pi ft) \cos(2\pi f\tau_g) + \frac{1}{2}\sin(4\pi ft) \sin(2\pi f\tau_g) + \frac{1}{2}\cos(2\pi f\tau_g) \rangle$$

Apply the identity $\cos(A - B) = \cos A \cos B + \sin A \sin B$ to the first two term,

$$r(\theta) = \langle \frac{1}{2}\cos(4\pi ft - 2\pi f\tau_g) + \frac{1}{2}\cos(2\pi f\tau_g) \rangle$$

$$r(\theta) = \langle \frac{1}{2}\cos[2\pi f(2t - \tau_g)] + \frac{1}{2}\cos(2\pi f\tau_g) \rangle$$

APPENDIX C

DERIVATION OF (1.9)

Begin with

$$\langle E_1(l,m,n,t)E_2^*(l,m,n,t)\rangle$$

Substitute with the right-hand side expressions from (1.7),

$$\langle E_1(l,m,n,t)E_2^*(l,m,n,t)\rangle$$
$$= \left\langle \mathcal{E}\left(l,m,n,t-\tfrac{R_1}{c}\right)\frac{e^{-j\omega(t-R_1/c)}}{R_1}\mathcal{E}^*\left(l,m,n,t-\tfrac{R_2}{c}\right)\frac{e^{j\omega(t-R_2/c)}}{R_2}\right\rangle$$

Group the exponential terms, apply the product rule of exponents and simplify,

$$\langle E_1(l,m,n,t)E_2^*(l,m,n,t)\rangle$$
$$= \left\langle \mathcal{E}\left(l,m,n,t-\tfrac{R_1}{c}\right)\mathcal{E}^*\left(l,m,n,t-\tfrac{R_2}{c}\right)\left(\frac{e^{-j\omega(t-R_1/c)}}{R_1}\frac{e^{j\omega(t-R_2/c)}}{R_2}\right)\right\rangle$$
$$= \left\langle \mathcal{E}\left(l,m,n,t-\tfrac{R_1}{c}\right)\mathcal{E}^*\left(l,m,n,t-\tfrac{R_2}{c}\right)\left(\frac{e^{-j\omega(t-R_1/c)+j\omega(t-R_2/c)}}{R_1 R_2}\right)\right\rangle$$
$$= \left\langle \mathcal{E}\left(l,m,n,t-\tfrac{R_1}{c}\right)\mathcal{E}^*\left(l,m,n,t-\tfrac{R_2}{c}\right)\left(\frac{e^{-j\omega(R_2-R_1)/c}}{R_1 R_2}\right)\right\rangle$$

Move the fraction containing the exponential term out of the time averaging angle bracket as it is no longer dependent on t,

$$\langle E_1(l,m,n,t)E_2^*(l,m,n,t)\rangle$$
$$= \left\langle \mathcal{E}\left(l,m,n,t-\tfrac{R_1}{c}\right)\mathcal{E}^*\left(l,m,n,t-\tfrac{R_2}{c}\right)\right\rangle \cdot \left(\frac{e^{-j\omega(R_2-R_1)/c}}{R_1 R_2}\right)$$

Shift the referenced time by $+\tfrac{R_1}{c}$ for both the electric fields,

$$\langle E_1(l,m,n,t)E_2^*(l,m,n,t)\rangle$$
$$= \left\langle \mathcal{E}\left(l,m,n,t\right)\mathcal{E}^*\left(l,m,n,t+\tfrac{R_1}{c}-\tfrac{R_2}{c}\right)\right\rangle \cdot \left(\frac{e^{-j\omega(R_2-R_1)/c}}{R_1 R_2}\right)$$
$$= \left\langle \mathcal{E}\left(l,m,n,t\right)\mathcal{E}^*\left(l,m,n,t-\left(\tfrac{R_2-R_1}{c}\right)\right)\right\rangle \cdot \left(\frac{e^{-j\omega(R_2-R_1)/c}}{R_1 R_2}\right)$$

APPENDIX D

DERIVATION OF (2.13)

Let 1 and 2 specify the two antennas of a two-element interferometer, the correlator output will be based on each of the two antenna that has specific components of the field in its arbitrary directions (i.e., $(\hat{x}'_1, \hat{y}'_1)$ and $(\hat{x}'_2, \hat{y}'_2)$). With such consideration, the components of the field at the two antennas are

$$E_{x'1}(t) = \left[\mathcal{E}_x(t)e^{j\delta_x(t)} \cos\psi_1 + \mathcal{E}_y(t)e^{j\delta_y(t)} \sin\psi_1 \right] e^{j2\pi ft}$$

$$E_{y'1}(t) = \left[-\mathcal{E}_x(t)e^{j\delta_x(t)} \sin\psi_1 + \mathcal{E}_y(t)e^{j\delta_y(t)} \cos\psi_1 \right] e^{j2\pi ft}$$

for Antenna 1 and

$$E_{x'2}(t) = \left[\mathcal{E}_x(t)e^{j\delta_x(t)} \cos\psi_2 + \mathcal{E}_y(t)e^{j\delta_y(t)} \sin\psi_2 \right] e^{j2\pi ft}$$

$$E_{y'2}(t) = \left[-\mathcal{E}_x(t)e^{j\delta_x(t)} \sin\psi_2 + \mathcal{E}_y(t)e^{j\delta_y(t)} \cos\psi_2 \right] e^{j2\pi ft}$$

for Antenna 2.

The measured voltage response (2.10) for the two antennas are therefore

$$V'_1(t) = E_{x'1}(t) \cos\chi_1 - jE_{y'1}(t) \sin\chi_1$$

$$V'_2(t) = E_{x'2}(t) \cos\chi_2 - jE_{y'2}(t) \sin\chi_2$$

Substitute the individual voltage response of the two antennas to find the correlator output response

$$
\begin{aligned}
R_{12} &= G_{12}\langle V'_1(t)V'^{*}_2(t)\rangle \\
&= G_{12}\langle \left(E_{x'1}(t) \cos\chi_1 - jE_{y'1}(t) \sin\chi_1 \right) \left(E_{x'2}(t) \cos\chi_2 - jE_{y'2}(t) \sin\chi_2 \right)^{*}\rangle \\
&= G_{12}\langle \left(E_{x'1}(t) \cos\chi_1 - jE_{y'1}(t) \sin\chi_1 \right) \left(E^{*}_{x'2}(t) \cos\chi_2 + jE^{*}_{y'2}(t) \sin\chi_2 \right)\rangle \\
&= G_{12}\langle E_{x'_1}(t)E^{*}_{x'_2}(t) \cos\chi_1 \cos\chi_2 + jE_{x'_1}(t)E^{*}_{y'_2}(t) \cos\chi_1 \sin\chi_2 \\
&\qquad - jE_{y'_1}(t)E^{*}_{x'_2}(t) \sin\chi_1 \cos\chi_2 + E_{y'_1}(t)E^{*}_{y'_2}(t) \sin\chi_1 \sin\chi_2\rangle
\end{aligned}
$$

Substitute the field components for the two antennas

$$\frac{R_{12}}{G_{12}} = \Big\langle$$

$$\cos \chi_1 \cos \chi_2$$

$$\left[\mathcal{E}_x(t) e^{j\delta_x(t)} \cos \psi_1 + \mathcal{E}_y(t) e^{j\delta_y(t)} \sin \psi_1 \right] e^{j2\pi ft}$$

$$\left[\mathcal{E}_x(t) e^{-j\delta_x(t)} \cos \psi_2 + \mathcal{E}_y(t) e^{-j\delta_y(t)} \sin \psi_2 \right] e^{-j2\pi ft}$$

$$+ j \cos \chi_1 \sin \chi_2$$

$$\left[\mathcal{E}_x(t) e^{j\delta_x(t)} \cos \psi_1 + \mathcal{E}_y(t) e^{j\delta_y(t)} \sin \psi_1 \right] e^{j2\pi ft}$$

$$\left[-\mathcal{E}_x(t) e^{-j\delta_x(t)} \sin \psi_2 + \mathcal{E}_y(t) e^{-j\delta_y(t)} \cos \psi_2 \right] e^{-j2\pi ft}$$

$$- j \sin \chi_1 \cos \chi_2$$

$$\left[-\mathcal{E}_x(t) e^{j\delta_x(t)} \sin \psi_1 + \mathcal{E}_y(t) e^{j\delta_y(t)} \cos \psi_1 \right] e^{j2\pi ft}$$

$$\left[\mathcal{E}_x(t) e^{-j\delta_x(t)} \cos \psi_2 + \mathcal{E}_y(t) e^{-j\delta_y(t)} \sin \psi_2 \right] e^{-j2\pi ft}$$

$$+ \sin \chi_1 \sin \chi_2$$

$$\left[-\mathcal{E}_x(t) e^{j\delta_x(t)} \sin \psi_1 + \mathcal{E}_y(t) e^{j\delta_y(t)} \cos \psi_1 \right] e^{j2\pi ft}$$

$$\left[-\mathcal{E}_x(t) e^{-j\delta_x(t)} \sin \psi_2 + \mathcal{E}_y(t) e^{-j\delta_y(t)} \cos \psi_2 \right] e^{-j2\pi ft}$$

$$\Big\rangle$$

Cancel out the common term $e^{j2\pi ft}e^{-j2\pi ft} = 1$,

$$\frac{R_{12}}{G_{12}} = \Big\langle$$

$$\cos \chi_1 \cos \chi_2$$

$$\left[\mathcal{E}_x(t)e^{j\delta_x(t)} \cos \psi_1 + \mathcal{E}_y(t)e^{j\delta_y(t)} \sin \psi_1\right]$$

$$\left[\mathcal{E}_x(t)e^{-j\delta_x(t)} \cos \psi_2 + \mathcal{E}_y(t)e^{-j\delta_y(t)} \sin \psi_2\right]$$

$$+ j \cos \chi_1 \sin \chi_2$$

$$\left[\mathcal{E}_x(t)e^{j\delta_x(t)} \cos \psi_1 + \mathcal{E}_y(t)e^{j\delta_y(t)} \sin \psi_1\right]$$

$$\left[-\mathcal{E}_x(t)e^{-j\delta_x(t)} \sin \psi_2 + \mathcal{E}_y(t)e^{-j\delta_y(t)} \cos \psi_2\right]$$

$$- j \sin \chi_1 \cos \chi_2$$

$$\left[-\mathcal{E}_x(t)e^{j\delta_x(t)} \sin \psi_1 + \mathcal{E}_y(t)e^{j\delta_y(t)} \cos \psi_1\right]$$

$$\left[\mathcal{E}_x(t)e^{-j\delta_x(t)} \cos \psi_2 + \mathcal{E}_y(t)e^{-j\delta_y(t)} \sin \psi_2\right]$$

$$+ \sin \chi_1 \sin \chi_2$$

$$\left[-\mathcal{E}_x(t)e^{j\delta_x(t)} \sin \psi_1 + \mathcal{E}_y(t)e^{j\delta_y(t)} \cos \psi_1\right]$$

$$\left[-\mathcal{E}_x(t)e^{-j\delta_x(t)} \sin \psi_2 + \mathcal{E}_y(t)e^{-j\delta_y(t)} \cos \psi_2\right]$$

$$\Big\rangle$$

Rewrite the above expression by introducing four terms A, B, C, and D to represent the expressions in the square brackets

$$\frac{R_{12}}{G_{12}} = \langle \cos\chi_1 \cos\chi_2 \{A\} + j\cos\chi_1 \sin\chi_2 \{B\} - j\sin\chi_1 \cos\chi_2 \{C\} + \sin\chi_1 \sin\chi_2 \{D\}\rangle$$

where

$$A = + \mathcal{E}_x(t)e^{j\delta_x(t)}\cos\psi_1 \mathcal{E}_x(t)e^{-j\delta_x(t)}\cos\psi_2 + \mathcal{E}_x(t)e^{j\delta_x(t)}\cos\psi_1 \mathcal{E}_y(t)e^{-j\delta_y(t)}\sin\psi_2$$

$$+ \mathcal{E}_y(t)e^{j\delta_y(t)}\sin\psi_1 \mathcal{E}_x(t)e^{-j\delta_x(t)}\cos\psi_2 + \mathcal{E}_y(t)e^{j\delta_y(t)}\sin\psi_1 \mathcal{E}_y(t)e^{-j\delta_y(t)}\sin\psi_2$$

$$B = - \mathcal{E}_x(t)e^{j\delta_x(t)}\cos\psi_1 \mathcal{E}_x(t)e^{-j\delta_x(t)}\sin\psi_2 + \mathcal{E}_x(t)e^{j\delta_x(t)}\cos\psi_1 \mathcal{E}_y(t)e^{-j\delta_y(t)}\cos\psi_2$$

$$- \mathcal{E}_y(t)e^{j\delta_y(t)}\sin\psi_1 \mathcal{E}_x(t)e^{-j\delta_x(t)}\sin\psi_2 + \mathcal{E}_y(t)e^{j\delta_y(t)}\sin\psi_1 \mathcal{E}_y(t)e^{-j\delta_y(t)}\cos\psi_2$$

$$C = - \mathcal{E}_x(t)e^{j\delta_x(t)}\sin\psi_1 \mathcal{E}_x(t)e^{-j\delta_x(t)}\cos\psi_2 - \mathcal{E}_x(t)e^{j\delta_x(t)}\sin\psi_1 \mathcal{E}_y(t)e^{-j\delta_y(t)}\sin\psi_2$$

$$+ \mathcal{E}_y(t)e^{j\delta_y(t)}\cos\psi_1 \mathcal{E}_x(t)e^{-j\delta_x(t)}\cos\psi_2 + \mathcal{E}_y(t)e^{j\delta_y(t)}\cos\psi_1 \mathcal{E}_y(t)e^{-j\delta_y(t)}\sin\psi_2$$

$$D = + \mathcal{E}_x(t)e^{j\delta_x(t)}\sin\psi_1 \mathcal{E}_x(t)e^{-j\delta_x(t)}\sin\psi_2 - \mathcal{E}_x(t)e^{j\delta_x(t)}\sin\psi_1 \mathcal{E}_y(t)e^{-j\delta_y(t)}\cos\psi_2$$

$$- \mathcal{E}_y(t)e^{j\delta_y(t)}\cos\psi_1 \mathcal{E}_x(t)e^{-j\delta_x(t)}\sin\psi_2 + \mathcal{E}_y(t)e^{j\delta_y(t)}\cos\psi_1 \mathcal{E}_y(t)e^{-j\delta_y(t)}\cos\psi_2$$

Examine the terms A, B, C, and D and simplify

$$A = + \mathcal{E}_x(t)\cos\psi_1 \mathcal{E}_x(t)\cos\psi_2 + \mathcal{E}_x(t)e^{j\delta_x(t)}\cos\psi_1 \mathcal{E}_y(t)e^{-j\delta_y(t)}\sin\psi_2$$

$$+ \mathcal{E}_y(t)e^{j\delta_y(t)}\sin\psi_1 \mathcal{E}_x(t)e^{-j\delta_x(t)}\cos\psi_2 + \mathcal{E}_y(t)\sin\psi_1 \mathcal{E}_y(t)\sin\psi_2$$

$$B = - \mathcal{E}_x(t)\cos\psi_1 \mathcal{E}_x(t)\sin\psi_2 + \mathcal{E}_x(t)e^{j\delta_x(t)}\cos\psi_1 \mathcal{E}_y(t)e^{-j\delta_y(t)}\cos\psi_2$$

$$- \mathcal{E}_y(t)e^{j\delta_y(t)}\sin\psi_1 \mathcal{E}_x(t)e^{-j\delta_x(t)}\sin\psi_2 + \mathcal{E}_y(t)\sin\psi_1 \mathcal{E}_y(t)\cos\psi_2$$

$$C = - \mathcal{E}_x(t)\sin\psi_1 \mathcal{E}_x(t)\cos\psi_2 - \mathcal{E}_x(t)e^{j\delta_x(t)}\sin\psi_1 \mathcal{E}_y(t)e^{-j\delta_y(t)}\sin\psi_2$$

$$+ \mathcal{E}_y(t)e^{j\delta_y(t)}\cos\psi_1 \mathcal{E}_x(t)e^{-j\delta_x(t)}\cos\psi_2 + \mathcal{E}_y(t)\cos\psi_1 \mathcal{E}_y(t)\sin\psi_2$$

$$D = + \mathcal{E}_x(t)\sin\psi_1 \mathcal{E}_x(t)\sin\psi_2 - \mathcal{E}_x(t)e^{j\delta_x(t)}\sin\psi_1 \mathcal{E}_y(t)e^{-j\delta_y(t)}\cos\psi_2$$

$$- \mathcal{E}_y(t)e^{j\delta_y(t)}\cos\psi_1 \mathcal{E}_x(t)e^{-j\delta_x(t)}\sin\psi_2 + \mathcal{E}_y(t)\cos\psi_1 \mathcal{E}_y(t)\cos\psi_2$$

Group the like terms and further simplify the A, B, C, and D terms

$$A = + \mathcal{E}_x^2(t) \cos \psi_1 \cos \psi_2 + \mathcal{E}_x(t) \mathcal{E}_y(t) e^{j(\delta_x(t) - \delta_y(t))} \cos \psi_1 \sin \psi_2$$
$$+ \mathcal{E}_x(t) \mathcal{E}_y(t) e^{-j(\delta_x(t) - \delta_y(t))} \sin \psi_1 \cos \psi_2 + \mathcal{E}_y^2(t) \sin \psi_1 \sin \psi_2$$

$$B = - \mathcal{E}_x^2(t) \cos \psi_1 \sin \psi_2 + \mathcal{E}_x(t) \mathcal{E}_y(t) e^{j(\delta_x(t) - \delta_y(t))} \cos \psi_1 \cos \psi_2$$
$$- \mathcal{E}_x(t) \mathcal{E}_y(t) e^{-j(\delta_x(t) - \delta_y(t))} \sin \psi_1 \sin \psi_2 + \mathcal{E}_y^2(t) \sin \psi_1 \cos \psi_2$$

$$C = - \mathcal{E}_x^2(t) \sin \psi_1 \cos \psi_2 - \mathcal{E}_x(t) \mathcal{E}_y(t) e^{j(\delta_x(t) - \delta_y(t))} \sin \psi_1 \sin \psi_2$$
$$+ \mathcal{E}_x(t) \mathcal{E}_y(t) e^{-j(\delta_x(t) - \delta_y(t))} \cos \psi_1 \cos \psi_2 + \mathcal{E}_y^2(t) \cos \psi_1 \sin \psi_2$$

$$D = + \mathcal{E}_x^2(t) \sin \psi_1 \sin \psi_2 - \mathcal{E}_x(t) \mathcal{E}_y(t) e^{j(\delta_x(t) - \delta_y(t))} \sin \psi_1 \cos \psi_2$$
$$- \mathcal{E}_x(t) \mathcal{E}_y(t) e^{-j(\delta_x(t) - \delta_y(t))} \cos \psi_1 \sin \psi_2 + \mathcal{E}_y^2(t) \cos \psi_1 \cos \psi_2$$

Rewrite the correlator output using the simplified A, B, C, and D terms

$$\frac{R_{12}}{G_{12}} =$$

$$\langle \cos \chi_1 \cos \chi_2$$

$$\{\mathcal{E}_x^2(t) \cos \psi_1 \cos \psi_2 + \mathcal{E}_x(t) \mathcal{E}_y(t) e^{j(\delta_x(t) - \delta_y(t))} \cos \psi_1 \sin \psi_2$$

$$+ \mathcal{E}_x(t) \mathcal{E}_y(t) e^{-j(\delta_x(t) - \delta_y(t))} \sin \psi_1 \cos \psi_2 + \mathcal{E}_y^2(t) \sin \psi_1 \sin \psi_2\}$$

$$+ j \cos \chi_1 \sin \chi_2$$

$$\{-\mathcal{E}_x^2(t) \cos \psi_1 \sin \psi_2 + \mathcal{E}_x(t) \mathcal{E}_y(t) e^{j(\delta_x(t) - \delta_y(t))} \cos \psi_1 \cos \psi_2$$

$$-\mathcal{E}_x(t) \mathcal{E}_y(t) e^{-j(\delta_x(t) - \delta_y(t))} \sin \psi_1 \sin \psi_2 + \mathcal{E}_y^2(t) \sin \psi_1 \cos \psi_2\}$$

$$- j \sin \chi_1 \cos \chi_2$$

$$\{-\mathcal{E}_x^2(t) \sin \psi_1 \cos \psi_2 - \mathcal{E}_x(t) \mathcal{E}_y(t) e^{j(\delta_x(t) - \delta_y(t))} \sin \psi_1 \sin \psi_2$$

$$+\mathcal{E}_x(t) \mathcal{E}_y(t) e^{-j(\delta_x(t) - \delta_y(t))} \cos \psi_1 \cos \psi_2 + \mathcal{E}_y^2(t) \cos \psi_1 \sin \psi_2\}$$

$$+ \sin \chi_1 \sin \chi_2$$

$$\{+\mathcal{E}_x^2(t) \sin \psi_1 \sin \psi_2 - \mathcal{E}_x(t) \mathcal{E}_y(t) e^{j(\delta_x(t) - \delta_y(t))} \sin \psi_1 \cos \psi_2$$

$$-\mathcal{E}_x(t) \mathcal{E}_y(t) e^{-j(\delta_x(t) - \delta_y(t))} \cos \psi_1 \sin \psi_2 + \mathcal{E}_y^2(t) \cos \psi_1 \cos \psi_2\} \rangle$$

Expand the expression inside the angle bracket $\langle \cdot \rangle$

$$\frac{R_{12}}{G_{12}} =$$

$\langle \cos\chi_1 \cos\chi_2 \mathcal{E}_x^2(t) \cos\psi_1 \cos\psi_2$

$+ \cos\chi_1 \cos\chi_2 \mathcal{E}_x(t)\mathcal{E}_y(t)e^{j(\delta_x(t)-\delta_y(t))} \cos\psi_1 \sin\psi_2$

$+ \cos\chi_1 \cos\chi_2 \mathcal{E}_x(t)\mathcal{E}_y(t)e^{-j(\delta_x(t)-\delta_y(t))} \sin\psi_1 \cos\psi_2$

$+ \cos\chi_1 \cos\chi_2 \mathcal{E}_y^2(t) \sin\psi_1 \sin\psi_2$

$- j\cos\chi_1 \sin\chi_2 \mathcal{E}_x^2(t) \cos\psi_1 \sin\psi_2$

$+ j\cos\chi_1 \sin\chi_2 \mathcal{E}_x(t)\mathcal{E}_y(t)e^{j(\delta_x(t)-\delta_y(t))} \cos\psi_1 \cos\psi_2$

$- j\cos\chi_1 \sin\chi_2 \mathcal{E}_x(t)\mathcal{E}_y(t)e^{-j(\delta_x(t)-\delta_y(t))} \sin\psi_1 \sin\psi_2$

$+ j\cos\chi_1 \sin\chi_2 \mathcal{E}_y^2(t) \sin\psi_1 \cos\psi_2$

$+ j\sin\chi_1 \cos\chi_2 \mathcal{E}_x^2(t) \sin\psi_1 \cos\psi_2$

$+ j\sin\chi_1 \cos\chi_2 \mathcal{E}_x(t)\mathcal{E}_y(t)e^{j(\delta_x(t)-\delta_y(t))} \sin\psi_1 \sin\psi_2$

$- j\sin\chi_1 \cos\chi_2 \mathcal{E}_x(t)\mathcal{E}_y(t)e^{-j(\delta_x(t)-\delta_y(t))} \cos\psi_1 \cos\psi_2$

$- j\sin\chi_1 \cos\chi_2 \mathcal{E}_y^2(t) \cos\psi_1 \sin\psi_2$

$+ \sin\chi_1 \sin\chi_2 \mathcal{E}_x^2(t) \sin\psi_1 \sin\psi_2$

$- \sin\chi_1 \sin\chi_2 \mathcal{E}_x(t)\mathcal{E}_y(t)e^{j(\delta_x(t)-\delta_y(t))} \sin\psi_1 \cos\psi_2$

$- \sin\chi_1 \sin\chi_2 \mathcal{E}_x(t)\mathcal{E}_y(t)e^{-j(\delta_x(t)-\delta_y(t))} \cos\psi_1 \sin\psi_2$

$+ \sin\chi_1 \sin\chi_2 \mathcal{E}_y^2(t) \cos\psi_1 \cos\psi_2 \rangle$

Rewrite the time-averaging expression by considering individual contribution from the combination of field components

$$\frac{R_{12}}{G_{12}} =$$

$$\langle \cos \chi_1 \cos \chi_2 \mathcal{E}_x^2(t) \cos \psi_1 \cos \psi_2 \rangle$$

$$+ \langle \cos \chi_1 \cos \chi_2 \mathcal{E}_x(t) \mathcal{E}_y(t) e^{j(\delta_x(t) - \delta_y(t))} \cos \psi_1 \sin \psi_2 \rangle$$

$$+ \langle \cos \chi_1 \cos \chi_2 \mathcal{E}_x(t) \mathcal{E}_y(t) e^{-j(\delta_x(t) - \delta_y(t))} \sin \psi_1 \cos \psi_2 \rangle$$

$$+ \langle \cos \chi_1 \cos \chi_2 \mathcal{E}_y^2(t) \sin \psi_1 \sin \psi_2 \rangle$$

$$- j \langle \cos \chi_1 \sin \chi_2 \mathcal{E}_x^2(t) \cos \psi_1 \sin \psi_2 \rangle$$

$$+ j \langle \cos \chi_1 \sin \chi_2 \mathcal{E}_x(t) \mathcal{E}_y(t) e^{j(\delta_x(t) - \delta_y(t))} \cos \psi_1 \cos \psi_2 \rangle$$

$$- j \langle \cos \chi_1 \sin \chi_2 \mathcal{E}_x(t) \mathcal{E}_y(t) e^{-j(\delta_x(t) - \delta_y(t))} \sin \psi_1 \sin \psi_2 \rangle$$

$$+ j \langle \cos \chi_1 \sin \chi_2 \mathcal{E}_y^2(t) \sin \psi_1 \cos \psi_2 \rangle$$

$$+ j \langle \sin \chi_1 \cos \chi_2 \mathcal{E}_x^2(t) \sin \psi_1 \cos \psi_2 \rangle$$

$$+ j \langle \sin \chi_1 \cos \chi_2 \mathcal{E}_x(t) \mathcal{E}_y(t) e^{j(\delta_x(t) - \delta_y(t))} \sin \psi_1 \sin \psi_2 \rangle$$

$$- j \langle \sin \chi_1 \cos \chi_2 \mathcal{E}_x(t) \mathcal{E}_y(t) e^{-j(\delta_x(t) - \delta_y(t))} \cos \psi_1 \cos \psi_2 \rangle$$

$$- j \langle \sin \chi_1 \cos \chi_2 \mathcal{E}_y^2(t) \cos \psi_1 \sin \psi_2 \rangle$$

$$+ \langle \sin \chi_1 \sin \chi_2 \mathcal{E}_x^2(t) \sin \psi_1 \sin \psi_2 \rangle$$

$$- \langle \sin \chi_1 \sin \chi_2 \mathcal{E}_x(t) \mathcal{E}_y(t) e^{j(\delta_x(t) - \delta_y(t))} \sin \psi_1 \cos \psi_2 \rangle$$

$$- \langle \sin \chi_1 \sin \chi_2 \mathcal{E}_x(t) \mathcal{E}_y(t) e^{-j(\delta_x(t) - \delta_y(t))} \cos \psi_1 \sin \psi_2 \rangle$$

$$+ \langle \sin \chi_1 \sin \chi_2 \mathcal{E}_y^2(t) \cos \psi_1 \cos \psi_2 \rangle$$

Terms that are not time-dependent can be moved out of the time-averaging operators

$$\frac{R_{12}}{G_{12}} =$$

$$\cos\chi_1 \cos\chi_2 \cos\psi_1 \cos\psi_2 \langle \mathcal{E}_x^2(t) \rangle$$

$$+ \cos\chi_1 \cos\chi_2 \cos\psi_1 \sin\psi_2 \langle \mathcal{E}_x(t)\mathcal{E}_y(t) e^{j(\delta_x(t)-\delta_y(t))} \rangle$$

$$+ \cos\chi_1 \cos\chi_2 \sin\psi_1 \cos\psi_2 \langle \mathcal{E}_x(t)\mathcal{E}_y(t) e^{-j(\delta_x(t)-\delta_y(t))} \rangle$$

$$+ \cos\chi_1 \cos\chi_2 \sin\psi_1 \sin\psi_2 \langle \mathcal{E}_y^2(t) \rangle$$

$$- j\cos\chi_1 \sin\chi_2 \cos\psi_1 \sin\psi_2 \langle \mathcal{E}_x^2(t) \rangle$$

$$+ j\cos\chi_1 \sin\chi_2 \cos\psi_1 \cos\psi_2 \langle \mathcal{E}_x(t)\mathcal{E}_y(t) e^{j(\delta_x(t)-\delta_y(t))} \rangle$$

$$- j\cos\chi_1 \sin\chi_2 \sin\psi_1 \sin\psi_2 \langle \mathcal{E}_x(t)\mathcal{E}_y(t) e^{-j(\delta_x(t)-\delta_y(t))} \rangle$$

$$+ j\cos\chi_1 \sin\chi_2 \sin\psi_1 \cos\psi_2 \langle \mathcal{E}_y^2(t) \rangle$$

$$+ j\sin\chi_1 \cos\chi_2 \sin\psi_1 \cos\psi_2 \langle \mathcal{E}_x^2(t) \rangle$$

$$+ j\sin\chi_1 \cos\chi_2 \sin\psi_1 \sin\psi_2 \langle \mathcal{E}_x(t)\mathcal{E}_y(t) e^{j(\delta_x(t)-\delta_y(t))} \rangle$$

$$- j\sin\chi_1 \cos\chi_2 \cos\psi_1 \cos\psi_2 \langle \mathcal{E}_x(t)\mathcal{E}_y(t) e^{-j(\delta_x(t)-\delta_y(t))} \rangle$$

$$- j\sin\chi_1 \cos\chi_2 \cos\psi_1 \sin\psi_2 \langle \mathcal{E}_y^2(t) \rangle$$

$$+ \sin\chi_1 \sin\chi_2 \sin\psi_1 \sin\psi_2 \langle \mathcal{E}_x^2(t) \rangle$$

$$- \sin\chi_1 \sin\chi_2 \sin\psi_1 \cos\psi_2 \langle \mathcal{E}_x(t)\mathcal{E}_y(t) e^{j(\delta_x(t)-\delta_y(t))} \rangle$$

$$- \sin\chi_1 \sin\chi_2 \cos\psi_1 \sin\psi_2 \langle \mathcal{E}_x(t)\mathcal{E}_y(t) e^{-j(\delta_x(t)-\delta_y(t))} \rangle$$

$$+ \sin\chi_1 \sin\chi_2 \cos\psi_1 \cos\psi_2 \langle \mathcal{E}_y^2(t) \rangle$$

The terms within the time-averaging operators can be replaced with the Stokes parameters using the following expressions

$$\langle \mathcal{E}_x^2(t) \rangle = \frac{1}{2}(I + Q)$$

$$\langle \mathcal{E}_y^2(t) \rangle = \frac{1}{2}(I - Q)$$

$$\langle \mathcal{E}_x(t)\mathcal{E}_y(t) e^{j(\delta_x(t)-\delta_y(t))} \rangle = \frac{1}{2}(U + jV)$$

$$\langle \mathcal{E}_x(t)\mathcal{E}_y(t) e^{-j(\delta_x(t)-\delta_y(t))} \rangle = \frac{1}{2}(U - jV)$$

156

Multiply both side by a factor of 2 (i.e., common $\frac{1}{2}$ term)

$$\frac{2R_{12}}{G_{12}} =$$

$\cos\chi_1 \cos\chi_2 \cos\psi_1 \cos\psi_2 (I + Q)$

$+ \cos\chi_1 \cos\chi_2 \cos\psi_1 \sin\psi_2 (U + jV)$

$+ \cos\chi_1 \cos\chi_2 \sin\psi_1 \cos\psi_2 (U - jV)$

$+ \cos\chi_1 \cos\chi_2 \sin\psi_1 \sin\psi_2 (I - Q)$

$- j\cos\chi_1 \sin\chi_2 \cos\psi_1 \sin\psi_2 (I + Q)$

$+ j\cos\chi_1 \sin\chi_2 \cos\psi_1 \cos\psi_2 (U + jV)$

$- j\cos\chi_1 \sin\chi_2 \sin\psi_1 \sin\psi_2 (U - jV)$

$+ j\cos\chi_1 \sin\chi_2 \sin\psi_1 \cos\psi_2 (I - Q)$

$+ j\sin\chi_1 \cos\chi_2 \sin\psi_1 \cos\psi_2 (I + Q)$

$+ j\sin\chi_1 \cos\chi_2 \sin\psi_1 \sin\psi_2 (U + jV)$

$- j\sin\chi_1 \cos\chi_2 \cos\psi_1 \cos\psi_2 (U - jV)$

$- j\sin\chi_1 \cos\chi_2 \cos\psi_1 \sin\psi_2 (I - Q)$

$+ \sin\chi_1 \sin\chi_2 \sin\psi_1 \sin\psi_2 (I + Q)$

$- \sin\chi_1 \sin\chi_2 \sin\psi_1 \cos\psi_2 (U + jV)$

$- \sin\chi_1 \sin\chi_2 \cos\psi_1 \sin\psi_2 (U - jV)$

$+ \sin\chi_1 \sin\chi_2 \cos\psi_1 \cos\psi_2 (I - Q)$

Group the same parenthesized Stokes parameters together,

$$\frac{2R_{12}}{G_{12}} =$$

$$\cos\chi_1 \cos\chi_2 \cos\psi_1 \cos\psi_2 (I+Q)$$

$$- j \cos\chi_1 \sin\chi_2 \cos\psi_1 \sin\psi_2 (I+Q)$$

$$+ j \sin\chi_1 \cos\chi_2 \sin\psi_1 \cos\psi_2 (I+Q)$$

$$+ \sin\chi_1 \sin\chi_2 \sin\psi_1 \sin\psi_2 (I+Q)$$

$$+ \cos\chi_1 \cos\chi_2 \sin\psi_1 \sin\psi_2 (I-Q)$$

$$+ j \cos\chi_1 \sin\chi_2 \sin\psi_1 \cos\psi_2 (I-Q)$$

$$- j \sin\chi_1 \cos\chi_2 \cos\psi_1 \sin\psi_2 (I-Q)$$

$$+ \sin\chi_1 \sin\chi_2 \cos\psi_1 \cos\psi_2 (I-Q)$$

$$+ \cos\chi_1 \cos\chi_2 \cos\psi_1 \sin\psi_2 (U+jV)$$

$$+ j \cos\chi_1 \sin\chi_2 \cos\psi_1 \cos\psi_2 (U+jV)$$

$$+ j \sin\chi_1 \cos\chi_2 \sin\psi_1 \sin\psi_2 (U+jV)$$

$$- \sin\chi_1 \sin\chi_2 \sin\psi_1 \cos\psi_2 (U+jV)$$

$$+ \cos\chi_1 \cos\chi_2 \sin\psi_1 \cos\psi_2 (U-jV)$$

$$- j \cos\chi_1 \sin\chi_2 \sin\psi_1 \sin\psi_2 (U-jV)$$

$$- j \sin\chi_1 \cos\chi_2 \cos\psi_1 \cos\psi_2 (U-jV)$$

$$- \sin\chi_1 \sin\chi_2 \cos\psi_1 \sin\psi_2 (U-jV)$$

Expand the expression

$$\frac{2R_{12}}{G_{12}} =$$

$I \cos \chi_1 \cos \chi_2 \cos \psi_1 \cos \psi_2 + Q \cos \chi_1 \cos \chi_2 \cos \psi_1 \cos \psi_2$

$- jI \cos \chi_1 \sin \chi_2 \cos \psi_1 \sin \psi_2 - jQ \cos \chi_1 \sin \chi_2 \cos \psi_1 \sin \psi_2$

$+ jI \sin \chi_1 \cos \chi_2 \sin \psi_1 \cos \psi_2 + jQ \sin \chi_1 \cos \chi_2 \sin \psi_1 \cos \psi_2$

$+ I \sin \chi_1 \sin \chi_2 \sin \psi_1 \sin \psi_2 + Q \sin \chi_1 \sin \chi_2 \sin \psi_1 \sin \psi_2$

$+ I \cos \chi_1 \cos \chi_2 \sin \psi_1 \sin \psi_2 - Q \cos \chi_1 \cos \chi_2 \sin \psi_1 \sin \psi_2$

$+ jI \cos \chi_1 \sin \chi_2 \sin \psi_1 \cos \psi_2 - jQ \cos \chi_1 \sin \chi_2 \sin \psi_1 \cos \psi_2$

$- jI \sin \chi_1 \cos \chi_2 \cos \psi_1 \sin \psi_2 + jQ \sin \chi_1 \cos \chi_2 \cos \psi_1 \sin \psi_2$

$+ I \sin \chi_1 \sin \chi_2 \cos \psi_1 \cos \psi_2 - Q \sin \chi_1 \sin \chi_2 \cos \psi_1 \cos \psi_2$

$+ U \cos \chi_1 \cos \chi_2 \cos \psi_1 \sin \psi_2 + jV \cos \chi_1 \cos \chi_2 \cos \psi_1 \sin \psi_2$

$+ jU \cos \chi_1 \sin \chi_2 \cos \psi_1 \cos \psi_2 - V \cos \chi_1 \sin \chi_2 \cos \psi_1 \cos \psi_2$

$+ jU \sin \chi_1 \cos \chi_2 \sin \psi_1 \sin \psi_2 - V \sin \chi_1 \cos \chi_2 \sin \psi_1 \sin \psi_2$

$- U \sin \chi_1 \sin \chi_2 \sin \psi_1 \cos \psi_2 - jV \sin \chi_1 \sin \chi_2 \sin \psi_1 \cos \psi_2$

$+ U \cos \chi_1 \cos \chi_2 \sin \psi_1 \cos \psi_2 - jV \cos \chi_1 \cos \chi_2 \sin \psi_1 \cos \psi_2$

$- jU \cos \chi_1 \sin \chi_2 \sin \psi_1 \sin \psi_2 - V \cos \chi_1 \sin \chi_2 \sin \psi_1 \sin \psi_2$

$- jU \sin \chi_1 \cos \chi_2 \cos \psi_1 \cos \psi_2 - V \sin \chi_1 \cos \chi_2 \cos \psi_1 \cos \psi_2$

$- U \sin \chi_1 \sin \chi_2 \cos \psi_1 \sin \psi_2 + jV \sin \chi_1 \sin \chi_2 \cos \psi_1 \sin \psi_2$

Group and real and imaginary part then factor out the common Stokes parameters (and j when applicable),

$$\frac{2R_{12}}{G_{12}} =$$

$I[\cos\chi_1\cos\chi_2\cos\psi_1\cos\psi_2 + \sin\chi_1\sin\chi_2\cos\psi_1\cos\psi_2$

$+ \sin\chi_1\sin\chi_2\sin\psi_1\sin\psi_2 + \cos\chi_1\cos\chi_2\sin\psi_1\sin\psi_2]$

$- jI[\cos\chi_1\sin\chi_2\cos\psi_1\sin\psi_2 + \sin\chi_1\cos\chi_2\cos\psi_1\sin\psi_2$

$- \sin\chi_1\cos\chi_2\sin\psi_1\cos\psi_2 - \cos\chi_1\sin\chi_2\sin\psi_1\cos\psi_2]$

$+ Q[\cos\chi_1\cos\chi_2\cos\psi_1\cos\psi_2 - \sin\chi_1\sin\chi_2\cos\psi_1\cos\psi_2$

$+ \sin\chi_1\sin\chi_2\sin\psi_1\sin\psi_2 - \cos\chi_1\cos\chi_2\sin\psi_1\sin\psi_2]$

$- jQ[\cos\chi_1\sin\chi_2\cos\psi_1\sin\psi_2 - \sin\chi_1\cos\chi_2\cos\psi_1\sin\psi_2$

$- \sin\chi_1\cos\chi_2\sin\psi_1\cos\psi_2 + \cos\chi_1\sin\chi_2\sin\psi_1\cos\psi_2]$

$+ jU[\cos\chi_1\sin\chi_2\cos\psi_1\cos\psi_2 - \sin\chi_1\cos\chi_2\cos\psi_1\cos\psi_2$

$+ \sin\chi_1\cos\chi_2\sin\psi_1\sin\psi_2 - \cos\chi_1\sin\chi_2\sin\psi_1\sin\psi_2]$

$+ U[\cos\chi_1\cos\chi_2\cos\psi_1\sin\psi_2 - \sin\chi_1\sin\chi_2\cos\psi_1\sin\psi_2$

$- \sin\chi_1\sin\chi_2\sin\psi_1\cos\psi_2 + \cos\chi_1\cos\chi_2\sin\psi_1\cos\psi_2]$

$- V[\cos\chi_1\sin\chi_2\cos\psi_1\cos\psi_2 + \sin\chi_1\cos\chi_2\cos\psi_1\cos\psi_2$

$+ \sin\chi_1\cos\chi_2\sin\psi_1\sin\psi_2 + \cos\chi_1\sin\chi_2\sin\psi_1\sin\psi_2]$

$+ jV[\cos\chi_1\cos\chi_2\cos\psi_1\sin\psi_2 + \sin\chi_1\sin\chi_2\cos\psi_1\sin\psi_2$

$- \sin\chi_1\sin\chi_2\sin\psi_1\cos\psi_2 - \cos\chi_1\cos\chi_2\sin\psi_1\cos\psi_2]$

Factor out the sines and cosines of ψ, then simplify the sines and cosines of χ using the compound angle properties,

$$\frac{2R_{12}}{G_{12}} =$$

$I[\cos\psi_1\cos\psi_2(\cos\chi_1\cos\chi_2 + \sin\chi_1\sin\chi_2) + \sin\psi_1\sin\psi_2(\sin\chi_1\sin\chi_2 + \cos\chi_1\cos\chi_2)]$

$- jI[\cos\psi_1\sin\psi_2(\cos\chi_1\sin\chi_2 + \sin\chi_1\cos\chi_2) - \sin\psi_1\cos\psi_2(\sin\chi_1\cos\chi_2 + \cos\chi_1\sin\chi_2)]$

$+ Q[\cos\psi_1\cos\psi_2(\cos\chi_1\cos\chi_2 - \sin\chi_1\sin\chi_2) + \sin\psi_1\sin\psi_2(\sin\chi_1\sin\chi_2 - \cos\chi_1\cos\chi_2)]$

$- jQ[\cos\psi_1\sin\psi_2(\cos\chi_1\sin\chi_2 - \sin\chi_1\cos\chi_2) - \sin\psi_1\cos\psi_2(\sin\chi_1\cos\chi_2 - \cos\chi_1\sin\chi_2)]$

$+ jU[\cos\psi_1\cos\psi_2(\cos\chi_1\sin\chi_2 - \sin\chi_1\cos\chi_2) + \sin\psi_1\sin\psi_2(\sin\chi_1\cos\chi_2 - \cos\chi_1\sin\chi_2)]$

$+ U[\cos\psi_1\sin\psi_2(\cos\chi_1\cos\chi_2 - \sin\chi_1\sin\chi_2) - \sin\psi_1\cos\psi_2(\sin\chi_1\sin\chi_2 - \cos\chi_1\cos\chi_2)]$

$- V[\cos\psi_1\cos\psi_2(\cos\chi_1\sin\chi_2 + \sin\chi_1\cos\chi_2) + \sin\psi_1\sin\psi_2(\sin\chi_1\cos\chi_2 + \cos\chi_1\sin\chi_2)]$

$+ jV[\cos\psi_1\sin\psi_2(\cos\chi_1\cos\chi_2 + \sin\chi_1\sin\chi_2) - \sin\psi_1\cos\psi_2(\sin\chi_1\sin\chi_2 + \cos\chi_1\cos\chi_2)]$

$$\begin{aligned}
\frac{2R_{12}}{G_{12}} = \ & I[\cos\psi_1\cos\psi_2\cos(\chi_1 - \chi_2) + \sin\psi_1\sin\psi_2\cos(\chi_1 - \chi_2)] \\
& - jI[\cos\psi_1\sin\psi_2\sin(\chi_1 + \chi_2) - \sin\psi_1\cos\psi_2\sin(\chi_1 + \chi_2)] \\
& + Q[\cos\psi_1\cos\psi_2\cos(\chi_1 + \chi_2) + \sin\psi_1\sin\psi_2(-\cos(\chi_1 + \chi_2))] \\
& - jQ[\cos\psi_1\sin\psi_2(-\sin(\chi_1 - \chi_2)) - \sin\psi_1\cos\psi_2\sin(\chi_1 - \chi_2)] \\
& + jU[\cos\psi_1\cos\psi_2(-\sin(\chi_1 - \chi_2)) + \sin\psi_1\sin\psi_2\sin(\chi_1 - \chi_2)] \\
& + U[\cos\psi_1\sin\psi_2\cos(\chi_1 + \chi_2) - \sin\psi_1\cos\psi_2(-\cos(\chi_1 + \chi_2))] \\
& - V[\cos\psi_1\cos\psi_2\sin(\chi_1 + \chi_2) + \sin\psi_1\sin\psi_2\sin(\chi_1 + \chi_2)] \\
& + jV[\cos\psi_1\sin\psi_2\cos(\chi_1 - \chi_2) - \sin\psi_1\cos\psi_2\cos(\chi_1 - \chi_2)]
\end{aligned}$$

Factor out the sines and cosines of χ, then simplify the sines and cosines of ψ using the compound angle properties,

$$\frac{2R_{12}}{G_{12}} = I[\cos(\chi_1 - \chi_2)(\cos\psi_1\cos\psi_2 + \sin\psi_1\sin\psi_2]$$

$$- jI[\sin(\chi_1 + \chi_2)(\cos\psi_1\sin\psi_2 - \sin\psi_1\cos\psi_2)]$$

$$+ Q[\cos(\chi_1 + \chi_2)(\cos\psi_1\cos\psi_2 - \sin\psi_1\sin\psi_2)]$$

$$+ jQ[\sin(\chi_1 - \chi_2)(\cos\psi_1\sin\psi_2 + \sin\psi_1\cos\psi_2)]$$

$$- jU[\sin(\chi_1 - \chi_2)(\cos\psi_1\cos\psi_2 - \sin\psi_1\sin\psi_2)]$$

$$+ U[\cos(\chi_1 + \chi_2)(\cos\psi_1\sin\psi_2 + \sin\psi_1\cos\psi_2)]$$

$$- V[\sin(\chi_1 + \chi_2)(\cos\psi_1\cos\psi_2 + \sin\psi_1\sin\psi_2)]$$

$$+ jV[\cos(\chi_1 - \chi_2)(\cos\psi_1\sin\psi_2 - \sin\psi_1\cos\psi_2)]$$

$$\frac{2R_{12}}{G_{12}} = I\cos(\chi_1 - \chi_2)\cos(\psi_1 - \psi_2)$$

$$+ jI\sin(\chi_1 + \chi_2)\sin(\psi_1 - \psi_2)$$

$$+ Q\cos(\chi_1 + \chi_2)\cos(\psi_1 + \psi_2)$$

$$+ jQ\sin(\chi_1 - \chi_2)\sin(\psi_1 + \psi_2)$$

$$- jU\sin(\chi_1 - \chi_2)\cos(\psi_1 + \psi_2)$$

$$+ U\cos(\chi_1 + \chi_2)\sin(\psi_1 + \psi_2)$$

$$- V\sin(\chi_1 + \chi_2)\cos(\psi_1 - \psi_2)$$

$$- jV\cos(\chi_1 - \chi_2)\sin(\psi_1 - \psi_2)$$

With further simplification, the Stokes visibilities expression in (2.13) can be obtained as follow

$$R_{12} = \tfrac{1}{2}G_{12}\{I\left[\cos(\chi_1 - \chi_2)\cos(\psi_1 - \psi_2) + j\sin(\chi_1 + \chi_2)\sin(\psi_1 - \psi_2)\right]$$

$$+Q\left[\cos(\chi_1 + \chi_2)\cos(\psi_1 + \psi_2) + j\sin(\chi_1 - \chi_2)\sin(\psi_1 + \psi_2)\right]$$

$$+U\left[\cos(\chi_1 + \chi_2)\sin(\psi_1 + \psi_2) - j\sin(\chi_1 - \chi_2)\cos(\psi_1 + \psi_2)\right]$$

$$-V\left[\sin(\chi_1 + \chi_2)\cos(\psi_1 - \psi_2) + j\cos(\chi_1 - \chi_2)\sin(\psi_1 - \psi_2)\right]\}$$

Note that the difference of $\tfrac{1}{2}$ when compared to (2.13) assumes that this factor is subsumed into the instrumental gain term G_{12}.

PARTS, FULL SCHEMATIC, AND ADDITIONAL PHOTOS OF THE 75 GHZ DYNAMIC ANTENNA ARRAY

Parts

Label(s)	Manufacturer	Part Number
P24V0	MEAN WELL USA Inc.	RS-15-24
P5V0	XP Power	VCS100US05
N5V0	MEAN WELL USA Inc.	RS-25-5
SW1, SW2, SW3, SW4	Nilight	90014E
CALO	Mini-Circuits	FLC-6FT-SMSM+
1:4	Mini-Circuits	ZN4PD1-183W-S+
CALO_**x**	Mini-Circuits	141-18SMRSM+
NS_**x**	RF-GADGETS	XDM NSE15-1
DCBN_**x**	Mini-Circuits	BLK-89-S+
CAN_**x**	Mini-Circuits	086-2SM+
A1_**x**, A2_**x**, A3_**x**	Mini-Circuits	ZX60-V63+
ADP1_**x**, ADP2_**x**	Linx Technologies Inc.	ADP-SMAM-SMAM
CAN1_**x**	Mini-Circuits	FL086-9SM+
HT_**x**	Mini-Circuits	ZFSCJ-2-232-S+
CANP_**x**, CANN_**x**	Mini-Circuits	FL086-9SM+
UC_**x**	Analog Devices	ADMV7310-EVALZ
T50-1_**x**, T50-2_**x**	Mini-Circuits	ANNE-50+
TxAnt_**x**, RxAnt_**x**	Eravant	SAC-1533-12-S2
DC_**x**	Analog Devices	ADMV7410-EVALZ
CAIP_**x**, CAIN_**x**	Mini-Circuits	FL086-9SM+
CAQP_**x**, CAQN_**x**	Mini-Circuits	FL086-9SM+
HI_**x**, HQ_**x**	Mini-Circuits	ZFSCJ-2-232-S+
DCBI_**x**, DCBQ_**x**	Mini-Circuits	BLK-89-S+
CAI_**x**, CAQ_**x**	Mini-Circuits	ULC-6FT-SMSM+

Table E.1 Labels and the associated manufacturer and part number for the subsequent schematics. Bold '**x**'s indicate common parts that are used in either transmit, receive, or all channels. Standard insulated (i.e., stranded/solid) electrical wires for power supply related connections are not listed.

Full Schematic (1/2)
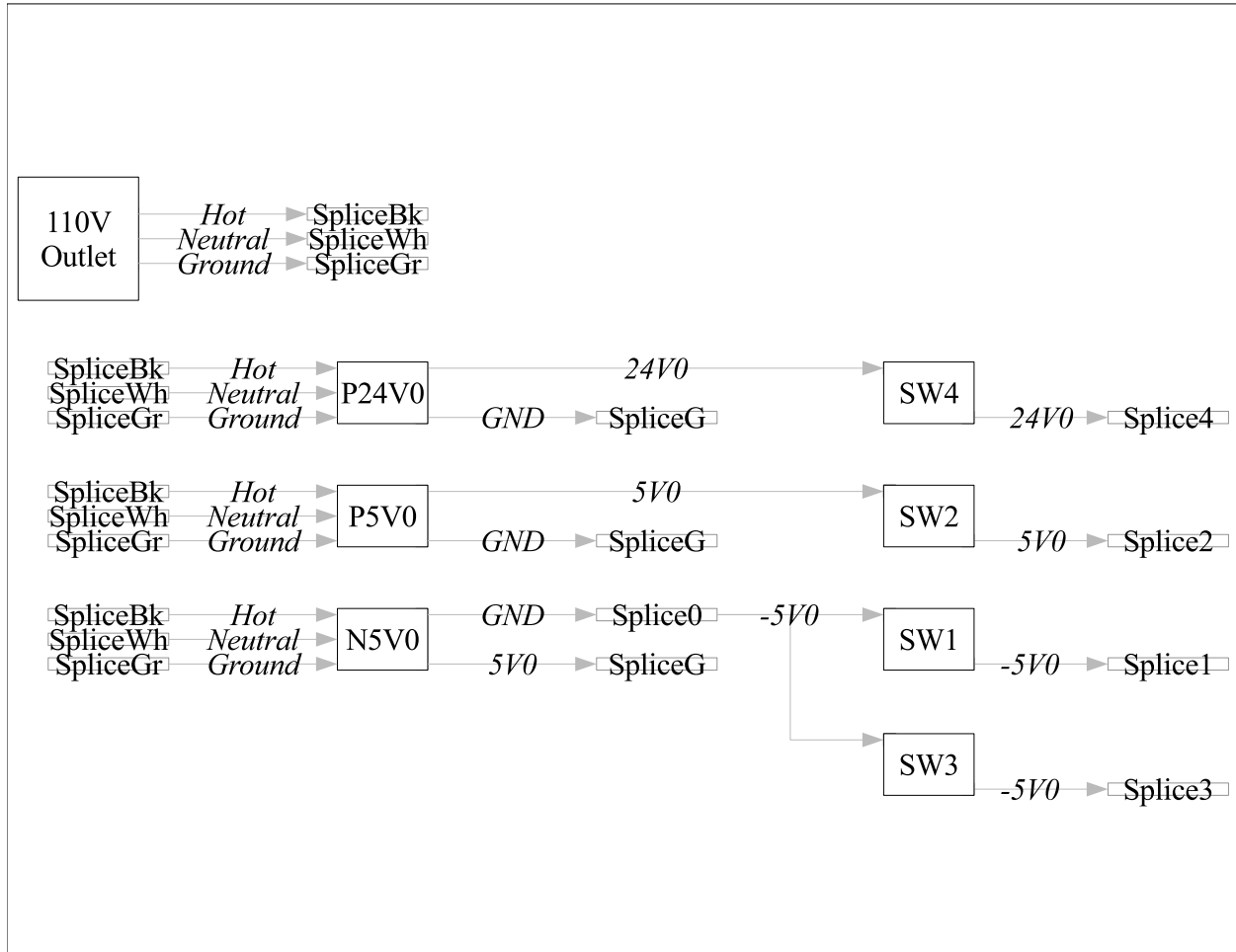
Figure E.1 Schematic of the power supply subsystem for the dynamic antenna array.

Full Schematic (2/2)
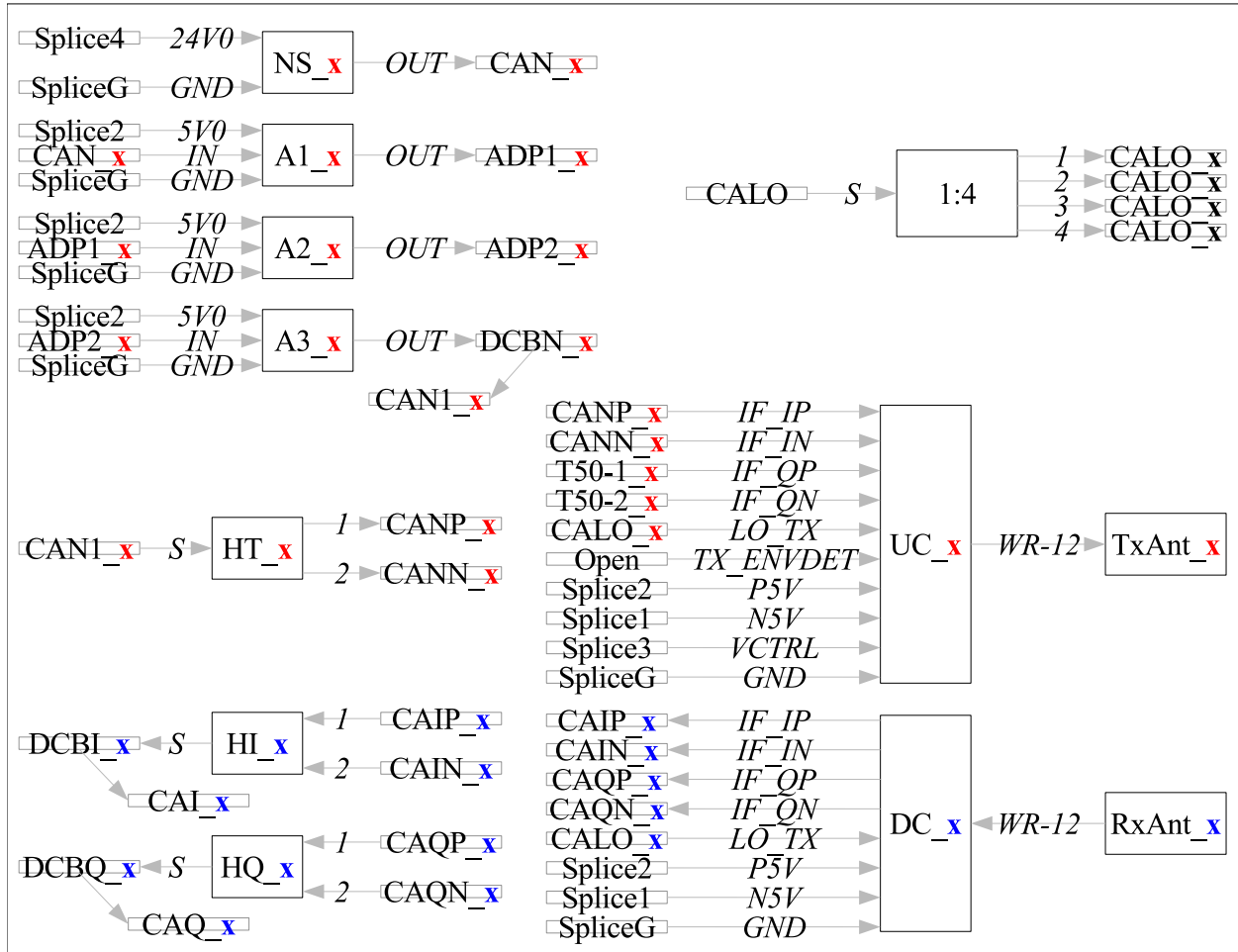
Figure E.2 Schematic of the radio frequency subsystem for the dynamic antenna array. The red 'x's indicate the two transmitting channels (i.e., 1 and 2). The blue 'x's indicate the two receiving channels (i.e., 1 and 2).

Photo
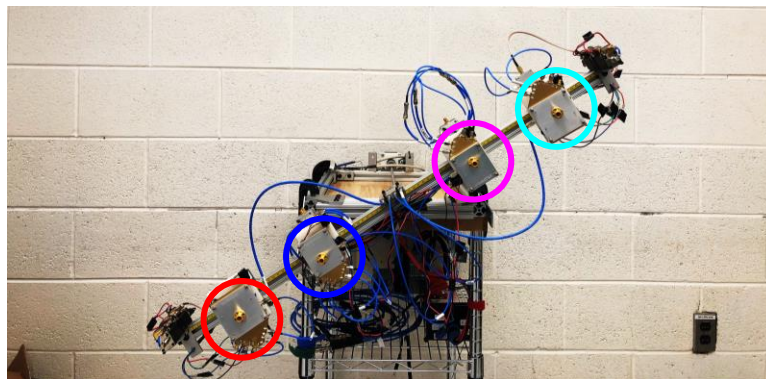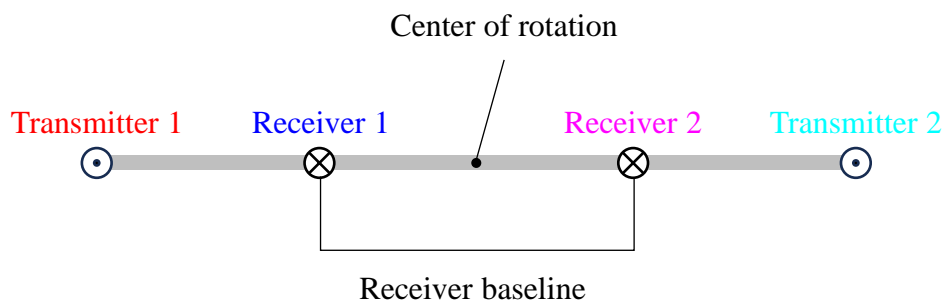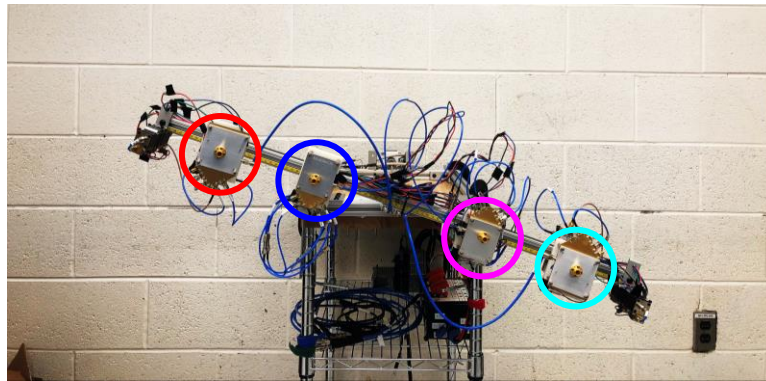
Figure E.3 Additional photos of the 75 GHz dynamic antenna array implementation demonstrating the rotational dynamics.

APPENDIX F

DATA ACQUISITION SCRIPT FOR ROTATIONAL DYNAMIC ANTENNA ARRAY (MATLAB)

```matlab
%%%%%%%%%%%%%%%%%%%%%%%%%%%%%%%%%
%%        Daniel S. Chen       %%
%% Michigan State University %%
%%%%%%%%%%%%%%%%%%%%%%%%%%%%%%%%%


%$$$$$$$$$$$$$$$$$$$$$$$$$$$$$$$$$$$$$$$$$$$$$$$$$$$$$$$$$$$$$$$$$$$$$$$$$$$$$$$$$$$$$$$$$$$$%
%$$$$$$$$$$$$$$$$$$$$$$$$$$$$$$$$$$$$$$$$$$$$$$$$$$$$$$$$$$$$$$$$$$$$$$$$$$$$$$$$$$$$$$$$$$$$$%
%$$$$$$$$$$$$$$$$$$$$$$$$$$$$$$$$$$$$$$$$$$$$$$$$$$$$$$$$$$$$$$$$$$$$$$$$$$$$$$$$$$$$$$$$$$$$$%


%%%%%%%%%%%%%%%%%%%%%%%%%%
%% Pre-configuration %%
%%%%%%%%%%%%%%%%%%%%%%%%%%


close all;
clear
clc
% Add path to AlazarTech mfiles
addpath('..\Include')


%$$$$$$$$$$$$$$$$$$$$$$$$$$$$$$$$$$$$$$$$$$$$$$$$$$$$$$$$$$$$$$$$$$$$$$$$$$$$$$$$$$$$$$$$$$$$$%
%$$$$$$$$$$$$$$$$$$$$$$$$$$$$$$$$$$$$$$$$$$$$$$$$$$$$$$$$$$$$$$$$$$$$$$$$$$$$$$$$$$$$$$$$$$$$$%
%$$$$$$$$$$$$$$$$$$$$$$$$$$$$$$$$$$$$$$$$$$$$$$$$$$$$$$$$$$$$$$$$$$$$$$$$$$$$$$$$$$$$$$$$$$$$$%


%%%%%%%%%%%%%%%%%%%%%
%% Main function%%
%%%%%%%%%%%%%%%%%%%%%


instrreset
disp('Check Available Serial Port and find Arduino:')
```

```matlab
seriallist("available")
disp('====================================================================')
disp('Connnect to Arduino')
arduinoObj = serial("COM4")
disp('====================================================================')
PPR = 400;
angle = linspace(0,360-360/PPR,PPR);


% Call mfile with library definitions
AlazarDefs


% Load driver library
if ~alazarLoadLibrary()
    fprintf('Error: ATSApi.dll not loaded\n');
    return
end


% Select a board
systemId = int32(1);
boardId = int32(1);


% Get a handle to the board
boardHandle = AlazarGetBoardBySystemID(systemId, boardId);
setdatatype(boardHandle, 'voidPtr', 1, 1);
if boardHandle.Value == 0
    fprintf('Error: Unable to open board system ID %u board ID %u\n',...
        systemId, boardId);
    return
end


% Configure the board's sample rate, input, and trigger settings
if ~configureBoard(boardHandle)
    fprintf('Error: Board configuration failed\n');
```

```matlab
        return
    end


    a_all_data(length(angle)) = struct();
    fopen(arduinoObj);
    while(1)
        % Get current angle from Arduino
        curr_angle = str2double(fgets(arduinoObj));


        % Display the current angle
        disp(curr_angle)


        if curr_angle == 201
            break
        elseif curr_angle >=1
            % Acquire data
            raw_data=double(acquireData(boardHandle));


            a_all_data(curr_angle).angle = angle(curr_angle);
            a_all_data(curr_angle).rawIQs = raw_data;
        end
    end
    plot(0,0); set(gca, 'color', [0 1 0]); drawnow;


    save('temp.mat', 'a_all_data')
    cd ..


    aaa_ringFilt_responses = [angle; zeros(3, length(angle))];


    n=1;
    while(n<201)
        matrix_double=double(a_all_data(n).rawIQs);
        % Combine the in-phase and qudrature data per receiver channel
```

```matlab
    b=((matrix_double(:,1:2:3))-nanmean(matrix_double(:,1:2:3)))+...
        1i*(matrix_double(:,2:2:4)-nanmean(matrix_double(:,2:2:4)));


    % Compute the visibility
    visM = transpose(b)*conj(b);
    aaa_ringFilt_responses(2,n) = abs(visM(1,1));
    aaa_ringFilt_responses(3,n) = abs(visM(2,2));
    aaa_ringFilt_responses(4,n) = abs(visM(1,2));


    n=n+1;
end


figure
subplot(311)
plot(aaa_ringFilt_responses(1,:),aaa_ringFilt_responses(2,:),'r');
xlim([min(angle) max(angle)/2]);
xlabel('Deg'); ylabel('Rx1. Response');
subplot(312)
plot(aaa_ringFilt_responses(1,:),aaa_ringFilt_responses(3,:),'r');
xlim([min(angle) max(angle)/2]);
xlabel('Deg'); ylabel('Rx2. Response');
subplot(313)
plot(aaa_ringFilt_responses(1,:),aaa_ringFilt_responses(4,:),'r');
xlim([min(angle) max(angle)/2]);
xlabel('Deg'); ylabel('xCorr. Response');


%$$$$$$$$$$$$$$$$$$$$$$$$$$$$$$$$$$$$$$$$$$$$$$$$$$$$$$$$$$$$$$$$$$$$$$$$$$$$$$$$$$$$$$$$$$$$$$$$%
%$$$$$$$$$$$$$$$$$$$$$$$$$$$$$$$$$$$$$$$$$$$$$$$$$$$$$$$$$$$$$$$$$$$$$$$$$$$$$$$$$$$$$$$$$$$$$$$$%
%$$$$$$$$$$$$$$$$$$$$$$$$$$$$$$$$$$$$$$$$$$$$$$$$$$$$$$$$$$$$$$$$$$$$$$$$$$$$$$$$$$$$$$$$$$$$$$$$%


%%%%%%%%%%%%%%%%%%%%%%%%%%%%%%%%
%% Configure board function %%
%%%%%%%%%%%%%%%%%%%%%%%%%%%%%%%%
```

```matlab
function [ result ] = configureBoard ( boardHandle )
% Configure sample rate, input, and trigger settings

% Call mfile with library definitions
AlazarDefs

% set default return code to indicate failure
result = false;

% global variable used in acquireData.m
global samplesPerSec;

samplesPerSec = 100000000.0;

retCode = ...
    AlazarSetCaptureClock(   ...
    boardHandle,            ... % HANDLE -- board handle
    INTERNAL_CLOCK,         ... % U32 -- clock source id
    SAMPLE_RATE_100MSPS,    ... % U32 -- sample rate id
    CLOCK_EDGE_RISING,      ... % U32 -- clock edge id
    0                       ... % U32 -- clock decimation
    );
if retCode ~= ApiSuccess
    fprintf( 'Error: AlazarSetCaptureClock failed -- %s\n' ,...
        errorToText(retCode));
    return
end
% Select channel A input parameters as required.
retCode = ...
    AlazarInputControlEx(             ...
    boardHandle,                      ... % HANDLE -- board handle
    CHANNEL_A,       ... % U32 -- input channel
```

```matlab
        DC_COUPLING,        ... % U32 — input coupling id
        INPUT_RANGE_PM_1_V, ... % U32 — input range id
        IMPEDANCE_50_OHM        ... % U32 — input impedance id
        );
if retCode ~= ApiSuccess
    fprintf('Error: AlazarInputControlEx failed — %s\n',...
        errorToText(retCode));
    return
end
% Select channel B input parameters as required.
retCode = ...
    AlazarInputControlEx(               ...
    boardHandle,                        ... % HANDLE — board handle
    CHANNEL_B,          ... % U32 — input channel
    DC_COUPLING,        ... % U32 — input coupling id
    INPUT_RANGE_PM_1_V, ... % U32 — input range id
    IMPEDANCE_50_OHM        ... % U32 — input impedance id
    );
if retCode ~= ApiSuccess
    fprintf('Error: AlazarInputControlEx failed — %s\n',...
        errorToText(retCode));
    return
end
% Select channel C input parameters as required.
retCode = ...
    AlazarInputControlEx(           ...
    boardHandle,                    ... % HANDLE — board handle
    CHANNEL_C,          ... % U32 — input channel
    DC_COUPLING,        ... % U32 — input coupling id
    INPUT_RANGE_PM_1_V, ... % U32 — input range id
    IMPEDANCE_50_OHM        ... % U32 — input impedance id
    );
if retCode ~= ApiSuccess
```

```matlab
        fprintf('Error: AlazarInputControlEx failed -- %s\n',...
            errorToText(retCode));
        return
    end

% Select channel D input parameters as required.

retCode = ...
    AlazarInputControlEx(                  ...
    boardHandle,                      ... % HANDLE -- board handle
    CHANNEL_D,         ... % U32 -- input channel
    DC_COUPLING,       ... % U32 -- input coupling id
    INPUT_RANGE_PM_1_V,  ... % U32 -- input range id
    IMPEDANCE_50_OHM       ... % U32 -- input impedance id
    );

if retCode ~= ApiSuccess
    fprintf('Error: AlazarInputControlEx failed -- %s\n',...
        errorToText(retCode));
    return
end


% Select trigger inputs and levels as required

retCode = ...
    AlazarSetTriggerOperation( ...
    boardHandle,... % HANDLE -- board handle
    TRIG_ENGINE_OP_J,... % U32 -- trigger operation
    TRIG_ENGINE_J,... % U32 -- trigger engine id
    TRIG_EXTERNAL,... % U32 -- trigger source id
    TRIGGER_SLOPE_POSITIVE,... % U32 -- trigger slope id
    150,... % U32 -- trigger level from 0 (-range) to 255 (+range)
    TRIG_ENGINE_K,... % U32 -- trigger engine id
    TRIG_DISABLE,... % U32 -- trigger source id for engine K
    TRIGGER_SLOPE_POSITIVE,... % U32 -- trigger slope id
    128 ... % U32 -- trigger level from 0 (-range) to 255 (+range)
    );
```

```matlab
if retCode ~= ApiSuccess
    fprintf('Error: AlazarSetTriggerOperation failed -- %s\n',...
        errorToText(retCode));
    return
end


% Select external trigger parameters as required
% retCode = ...
%     AlazarSetExternalTrigger( ...
%         boardHandle,            ... % HANDLE -- board handle
%         DC_COUPLING,            ... % U32 -- external trigger coupling id
%         ETR_TTL                 ... % U32 -- external trigger range id
%         );
% if retCode ~= ApiSuccess
%     fprintf('Error: AlazarSetExternalTrigger failed -- %s\n',...
%         errorToText(retCode));
%     return
% end


% Set trigger delay as required.
triggerDelay_sec = 0;
triggerDelay_samples = uint32(floor(triggerDelay_sec * samplesPerSec + 0.5));
retCode = AlazarSetTriggerDelay(boardHandle, triggerDelay_samples);
if retCode ~= ApiSuccess
    fprintf('Error: AlazarSetTriggerDelay failed -- %s\n',...
        errorToText(retCode));
    return;
end


% Set trigger timeout as required.
triggerTimeout_sec = 0;
triggerTimeout_clocks = uint32(floor(triggerTimeout_sec / 10.e-6 + 0.5));
retCode = ...
```

```matlab
    AlazarSetTriggerTimeOut ( ...
    boardHandle , ... % HANDLE — board handle
    triggerTimeout_clocks ... % U32 — timeout_sec / 10.e-6 (0 == wait forever)
    );
if retCode ~= ApiSuccess
    fprintf ( 'Error: AlazarSetTriggerTimeOut failed — %s \n' , ...
        errorToText ( retCode ));
    return
end


% Configure AUX I/O connector as required
retCode = ...
    AlazarConfigureAuxIO ( ...
    boardHandle , ... % HANDLE — board handle
    AUX_OUT_TRIGGER , ... % U32 — mode
    0 ... % U32 — parameter
    );
if retCode ~= ApiSuccess
    fprintf ( 'Error: AlazarConfigureAuxIO failed — %s \n' , ...
        errorToText ( retCode ));
    return
end


% set return code to indicate success
result = true ;
end


%$$$$$$$$$$$$$$$$$$$$$$$$$$$$$$$$$$$$$$$$$$$$$$$$$$$$$$$$$$$$$$$$$$$$$$$$$$$$$$$$$$$$$$$$%
%$$$$$$$$$$$$$$$$$$$$$$$$$$$$$$$$$$$$$$$$$$$$$$$$$$$$$$$$$$$$$$$$$$$$$$$$$$$$$$$$$$$$$$$$$%
%$$$$$$$$$$$$$$$$$$$$$$$$$$$$$$$$$$$$$$$$$$$$$$$$$$$$$$$$$$$$$$$$$$$$$$$$$$$$$$$$$$$$$$$$$%


%%%%%%%%%%%%%%%%%%%%%%%%%%%%%
%% Acquire data function %%
```

```matlab
%%%%%%%%%%%%%%%%%%%%%%%%%%%%%%%%%

function [dataMatrix] = acquireData(boardHandle)
% Make an AutoDMA acquisition from dual-ported memory.


% global variable set in configureBoard.m
global samplesPerSec;


% call mfile with library definitions
AlazarDefs
% There are no pre-trigger samples in NPT mode
preTriggerSamples = 0;


% Select the number of post-trigger samples per record
postTriggerSamples = 400*256;


% Specify the number of records per channel per DMA buffer
recordsPerBuffer = 1;


% Specifiy the total number of buffers to capture
buffersPerAcquisition = 1;


% Select which channels to capture (A, B, or both)
channelMask = CHANNEL_A + CHANNEL_B + CHANNEL_C + CHANNEL_D;


% Calculate the number of enabled channels from the channel mask
channelCount = 0;
channelsPerBoard = 16;
for channel = 0:channelsPerBoard - 1
    channelId = 2^channel;
    if bitand(channelId, channelMask)
        channelCount = channelCount + 1;
    end
```

```matlab
end

fprintf ('Number of enabled channels: %d\n' ,...
    channelCount );

if (channelCount < 1) || (channelCount > channelsPerBoard )
    fprintf ('Error: Invalid channel mask %08X\n' , channelMask );
    return
end


% Get the sample and memory size
[retCode , boardHandle , maxSamplesPerRecord , bitsPerSample ] =...
    AlazarGetChannelInfo (boardHandle , 0, 0);
if retCode ~= ApiSuccess
    fprintf ('Error: AlazarGetChannelInfo failed —— %s\n' ,...
        errorToText (retCode ));
    return
end


% Calculate the size of each buffer in bytes
bytesPerSample = floor (( double (bitsPerSample ) + 7) / double (8));
samplesPerRecord = preTriggerSamples + postTriggerSamples ;
samplesPerBuffer = samplesPerRecord * recordsPerBuffer * channelCount ;
bytesPerBuffer = bytesPerSample * samplesPerBuffer ;

% Select the number of DMA buffers to allocate .
bufferCount = uint32 (4);

% Create an array of DMA buffers
buffers = cell (1, bufferCount );
for j = 1 : bufferCount
    pbuffer = AlazarAllocBuffer (boardHandle , bytesPerBuffer );
    if pbuffer == 0
```

178

```matlab
            fprintf('Error:_AlazarAllocBuffer_%u_samples_failed\n',...
                samplesPerBuffer);
            return
        end
        buffers(1, j) = { pbuffer };
    end


% Set the record size
retCode = AlazarSetRecordSize(...
    boardHandle, preTriggerSamples, postTriggerSamples);
if retCode ~= ApiSuccess
    fprintf('Error:_AlazarSetRecordSize_failed_—_%s\n',...
        errorToText(retCode));
    return
end


% Select AutoDMA flags as required
admaFlags = ADMA_EXTERNAL_STARTCAPTURE + ADMA_NPT + ADMA_FIFO_ONLY_STREAMING;


% Configure the board to make an AutoDMA acquisition
recordsPerAcquisition = recordsPerBuffer * buffersPerAcquisition;
retCode = AlazarBeforeAsyncRead(...
    boardHandle, channelMask, -int32(preTriggerSamples),...
    samplesPerRecord, recordsPerBuffer, recordsPerAcquisition, admaFlags);
if retCode ~= ApiSuccess
    fprintf('Error:_AlazarBeforeAsyncRead_failed_—_%s\n',...
        errorToText(retCode));
    return
end


% Post the buffers to the board
for bufferIndex = 1 : bufferCount
    pbuffer = buffers{1, bufferIndex};
```

```matlab
        retCode = AlazarPostAsyncBuffer(boardHandle, pbuffer, bytesPerBuffer);
        if retCode ~= ApiSuccess
            fprintf('Error: AlazarPostAsyncBuffer failed -- %s\n',...
                errorToText(retCode));
            return
        end
    end


    % Arm the board system to wait for triggers
    retCode = AlazarStartCapture(boardHandle);
    if retCode ~= ApiSuccess
        fprintf('Error: AlazarStartCapture failed -- %s\n', errorToText(retCode));
        return
    end


    % Wait for sufficient data to arrive to fill a buffer, process the buffer,
    % and repeat until the acquisition is complete
    startTickCount = tic;
    updateTickCount = tic;
    updateInterval_sec = 0.1;
    buffersCompleted = 0;
    captureDone = false;
    success = false;


    while ~captureDone

        dataMatrix =[];

        bufferIndex = mod(buffersCompleted, bufferCount) + 1;
        pbuffer = buffers{1, bufferIndex};

        % Wait for the first available buffer to be filled by the board
        [retCode, boardHandle, bufferOut] = ...
```

```matlab
        AlazarWaitAsyncBufferComplete(boardHandle, pbuffer, 5000);
if retCode == ApiSuccess
    % This buffer is full
    bufferFull = true;
    captureDone = false;
elseif retCode == ApiWaitTimeout
    % The wait timeout expired before this buffer was filled.
    % The board may not be triggering, or the timeout period
    % may be too short.
    fprintf(...
        'Error:_AlazarWaitAsyncBufferComplete_timeout_—_Verify!\n');
    bufferFull = false;
    captureDone = true;
else
    % The acquisition failed
    fprintf('Error:_AlazarWaitAsyncBufferComplete_failed_—_%s\n',...
        errorToText(retCode));
    bufferFull = false;
    captureDone = true;
end


if bufferFull
    % Process sample data in this buffer.

    if bytesPerSample == 1
        setdatatype(bufferOut, 'uint8Ptr', 1, samplesPerBuffer);
    else
        setdatatype(bufferOut, 'uint16Ptr', 1, samplesPerBuffer);
    end

    datatemp=bufferOut.Value;
    for ich=1:channelCount
        dataMatrix=[dataMatrix datatemp(ich:channelCount:end)'];
```

```matlab
        end


        % Make the buffer available to be filled again by the board
        retCode = AlazarPostAsyncBuffer(boardHandle, pbuffer, bytesPerBuffer);
        if retCode ~= ApiSuccess
            fprintf('Error: AlazarPostAsyncBuffer failed -- %s\n', ...
                errorToText(retCode));
            captureDone = true;
        end


        % Update progress
        buffersCompleted = buffersCompleted + 1;
        if buffersCompleted >= buffersPerAcquisition
            captureDone = true;
            success = true;
        elseif toc(updateTickCount) > updateInterval_sec
            updateTickCount = tic;


            % Update waitbar progress
            waitbar(double(buffersCompleted) / ...
                double(buffersPerAcquisition), ...
                waitbarHandle, ...
                sprintf('Completed %u buffers', buffersCompleted));


            % Check if waitbar cancel button was pressed
            if getappdata(waitbarHandle, 'canceling')
                break
            end
        end


    end % if bufferFull


end % while ~captureDone
```

```matlab
% Abort the acquisition
retCode = AlazarAbortAsyncRead(boardHandle);
if retCode ~= ApiSuccess
    fprintf('Error:_AlazarAbortAsyncRead_failed_—_%s\n',...
        errorToText(retCode));
end


% Release the buffers
for bufferIndex = 1:bufferCount
    pbuffer = buffers{1, bufferIndex};
    retCode = AlazarFreeBuffer(boardHandle, pbuffer);
    if retCode ~= ApiSuccess
        fprintf('Error:_AlazarFreeBuffer_failed_—_%s\n',...
            errorToText(retCode));
    end
    clear pbuffer;
end


% Display results
if buffersCompleted > 0
    bytesTransferred = double(buffersCompleted) * double(bytesPerBuffer);
    recordsTransferred = recordsPerBuffer * buffersCompleted;

    if transferTime_sec > 0
        buffersPerSec = buffersCompleted / transferTime_sec;
        bytesPerSec = bytesTransferred / transferTime_sec;
        recordsPerSec = recordsTransferred / transferTime_sec;
    else
        buffersPerSec = 0;
        bytesPerSec = 0;
        recordsPerSec = 0.;
    end
```

```matlab
        fprintf('Captured %u buffers in %g sec (%g buffers per sec )\n' ,...
            buffersCompleted , transferTime_sec , buffersPerSec );
        fprintf('Captured %u records (%.4g records per sec )\n' ,...
            recordsTransferred , recordsPerSec );
        fprintf('Transferred %u bytes (%.4g bytes per sec )\n' ,...
            bytesTransferred , bytesPerSec );
    end

    % set return code to indicate success
    result = success ;
end
```